

NORTHWESTERN UNIVERSITY

Synthesis and Surface-Specific Analysis of Terpene-Derived Oxidation Products  
in Biogenic Secondary Organic Aerosol Particles

A DISSERTATION

SUBMITTED TO THE GRADUATE SCHOOL  
IN PARTIAL FULFILLMENT OF THE REQUIREMENTS

for the degree

DOCTOR OF PHILOSOPHY

Field of Chemistry

By

Ariana Gray Bé

EVANSTON, ILLINOIS

MARCH 2020

© Copyright by Ariana Gray Bé 2020

All Rights Reserved

**Abstract**

Synthesis and Surface-Specific Analysis of Terpene-Derived Oxidation Products  
in Biogenic Secondary Organic Aerosol Particles

Ariana Gray Bé

Biogenic secondary organic aerosol (SOA) particles, produced by forest ecosystems across the globe, are principal, yet poorly understood constituents in the climate system. These atmospheric particles form when biogenic volatile organic compounds (BVOCs) react with atmospheric oxidants, leading to increasingly lower volatility oxidation products that partition into the condensed phase through various gas-to-particle conversion pathways. Biogenic SOA particles impact Earth's radiative budget by scattering and absorbing solar radiation as well as serving as seed nuclei that promote cloud formation. However, uncertainties with regard to the climate impacts of biogenic SOA particles remain difficult to constrain due to their inherently diverse sources, formation mechanisms, molecular constituents, properties, and tropospheric lifetimes. Given that heterogeneous phenomena are intrinsically involved SOA processes and interactions and the gas/particle interface is the first point-of-contact for surrounding species, this work focuses on the chemistry occurring at atmospheric surfaces and interfaces.

In this thesis, we investigate the structure, properties, orientation, and reactivity of molecular constituents that partition to atmospherically relevant surfaces with the central goal of gaining molecular-level insights into the surface chemistry of biogenic SOA particles. To do so, we integrate organic synthesis, aerosol generation and collection, and surface science, with an emphasis placed on the utility of nonlinear vibrational spectroscopy and dynamic surface tension measurements. We present syntheses and surface-specific analyses of oxidation products derived

from  $\alpha$ -pinene and  $\beta$ -caryophyllene, the most atmospherically abundant monoterpene and sesquiterpene, respectively.

To explore the influence of various oxidation products on SOA-mediated cloud activation, we describe measurements of the surface tension depression of aqueous droplets containing a suite of synthesized monomeric  $\alpha$ -pinene and  $\beta$ -caryophyllene ozonolysis products. Using vibrational sum frequency generation (SFG) spectroscopy, we report spectroscopic benchmarking experiments aimed at qualitatively investigating the surface spectra of aerosol material generated from the ozonolysis of  $\beta$ -caryophyllene. We also discuss SFG measurements of the  $\beta$ -caryophyllene-derived oxidation products at air/aqueous interfaces in order to further understand their structural organization in conditions applicable to cloud droplet formation scenarios. Expanding beyond the synthesis and analysis of this suite of molecular constituents, we summarize a variety of studies that have laid the groundwork for three main future research avenues towards studying increasingly complex systems relevant to SOA surface science. Specifically, we detail (1) collaborative work utilizing the monomeric oxidation products, (2) efforts to probe atmospheric surfaces under simulated environmental conditions, (3) spectroscopic experiments on field-collected samples, and (4) studies towards the synthesis and analysis of dimeric SOA constituents. The discussed findings overall emphasize the fundamental importance of exploring the molecular surface chemistry of biogenic SOA particles in the atmosphere.

---

Prof. Franz M. Geiger and Prof. Regan J. Thomson  
Research Advisors

## Acknowledgments

I am greatly indebted to many people for enriching this journey and supporting me along the way. I would like to start by sincerely thanking my advisors, Prof. Regan Thomson and Prof. Franz Geiger. Regan, thank you for your constant mentorship and encouragement during my time at Northwestern. Your radiating love of organic chemistry and dedication to pedagogy never cease to inspire me. Franz, thank you for your continuous guidance, optimism, and enthusiasm over the past several years. You encouraged me to pursue opportunities that I never would have imagined possible, and I learned a huge amount from your brilliance as a physical and environmental chemist. You both are incredible scientists, mentors, and people, and I am forever grateful for everything that I learned working with you during my graduate career.

I would like to thank my present and past committee members, Prof. Emily Weiss, Prof. William Dichtel, and Prof. Toru Shiozaki for their time and helpful feedback. I am also extremely appreciative of my undergraduate research advisor, Prof. Joe Reczek, for being a remarkable role model and for invigorating my interest in chemistry. I would definitely not be at this point without his mentorship during my time at Denison. Additionally, I would like to acknowledge the funding sources for my thesis work, particularly the NSF Graduate Research Fellowship Program. I also would like to all of the external collaborators who I had the invaluable opportunity to work with and learn from, with special thanks to: Prof. Scot Martin, Dr. Yue Zhang, Dr. Pengfei Liu, and Yiming Qin (Harvard); Dr. Aashish Tuladhar, Dr. Zheming Wang, Dr. Zizwe Chase, Dr. Hongfei Wang, Dr. Zihua Zhu, and Dr. Nancy Washton (PNNL, EMSL); Prof. Allen Goldstein and Dr. Lindsay Yee (UC Berkeley); Dr. Xuan Zhang and Dr. Manjula Canagaratna (Aerodyne); and Prof. Mijung Song (CBNU).

I would like to thank Dr. Ruth Curry and Dr. Anna Fenton-Hathaway, who I got to know through my experiences with the Center for Civic Engagement. My time in GEO was a period of thoughtful reflection of my sense of place within graduate school, the academy, and society as a whole, and I am grateful to you both for providing me with that opportunity. I would also like to extend my thanks to Susan Mudd, Tiffany Werner, and Lucas Stephens at ELPC. A big thanks to Jonathan Maendel and Madison Schell for their service and dedication to leading, working alongside, and hearing the voices of graduate students in the department. Thank you to the staff in IMSERC for their advice and expertise with MS and NMR experiments. A huge shout out needs to be given to the staff working at the loading dock and mailing room in Tech. You guys were extremely helpful over the years with shipments and gas tank orders, and our chats always cheered me up.

To my friends on the WISER, PLU, and NU BonD boards, thank you so much for your dedication and contributions to the graduate student experience at Northwestern. Past and present members of NU BonD, you all have inspired me with your abilities to question and challenge the system as well as your commitment to advocacy. To the lunch crew, it is amazing how much our friendships (and seats at the table) have grown throughout graduate school! From keeping each other sane on the most challenging of days, to sometimes laughing to tears, to just being down to eat in silence some days, I can't imagine a more incredible group of friends and support system at Northwestern.

To all past and current members of the Geiger and Thomson labs who I was lucky to have worked with – I could not have asked for a better group of people to work alongside in graduate school. I am amazed with how much you all have taught me, and I am looking forward to seeing the exciting things you will all do in your futures. An enormous thank you to my mentor when I

started in the lab, Mary Alice, my mentor thereafter, Hilary, as well as my mentee, Aleia. Thank you to Yangdongling (Dawning), who I had the opportunity to work with throughout graduate school. You are such an amazing friend and labmate, and I couldn't imagine a better person to get to work with through both the successful and failed experiments (because we both know there were a lot). To Naomi, thank you for being my back of the office mate and tea time buddy and for all of your advice as I was job searching and writing up this thesis. Special thanks also to Jen, Marvin, Paul, Alicia, HanByul, Emily R., Johnny, Abdallah, Weiwei, Hudson, and Aidan for their insights in the lab and all of the fun times out of it!

Finally, to my friends and family who supported me throughout this dissertation work: Shaunna, Jen, and Becky, I seriously cannot picture a life where I didn't meet you guys, and I am eternally grateful to Northwestern for bringing us together. Jen – as roommates, labmates, and the best of friends, it is crazy how two people can spend that much time together and not drive each other insane (I must thank U of M and flutes for making our paths cross). To Olivia and Pete, thank you guys for all of the unforgettable memories over the past few years together. Olivia, from your personal recruitment night showing me around Chicago, to being roommates when I first moved, to living down the street from each other the last couple years, we have been so lucky to see each other grow in this time of our lives. I can't even begin to think about what it will be like not having you around the corner pretty soon. To my mom, you are the strongest and most inspiring person in my life, and I want to thank you for everything you have done for me. I would not have been able to accomplish this goal without your endless love and support. Last but not least, to Zack, there is no possible way to capture in words how much I love and appreciate you. Thank you for being my adventure bud, even through this crazy adventure called grad school. I love living life with you and can't wait for our next chapters to come!

**List of Abbreviations**

AcOH	Acetic acid
AFM	Atomic force microscopy
AMAZE	AMazonian Aerosol CharacteriZation Experiment
AMS	Aerosol mass spectrometer
ATR	Attenuated total reflection
B3LYP	Becke, 3-parameter, Lee–Yang–Parr
BEARPEX	Biosphere Effects on Aerosols and Photochemistry Experiment
BHT	Dibutylhydroxytoluene
<i>n</i> BuLi or <i>n</i> -BuLi	<i>n</i> -Butyl lithium
BVOC	Biogenic volatile organic compound
<i>t</i> -Bu or <i>t</i> Bu	<i>tert</i> -Butyl
CCN	Cloud condensation nuclei
CCNC	Cloud condensation nuclei counters
CF	Continuous flow
CPC	Condensation particle counter
DCC	1,3-Dicyclohexylcarbodiimide
DCM	Dichloromethane
DFT	Density functional theory
dH <sub>2</sub> O	Deionized water
DIP	Diisopinocampheyl
DMAP	4-Dimethylaminopyridine
DMS or Me <sub>2</sub> S	Dimethyl sulfide

DMSO	Dimethylsulfoxide
DOE	Department of Energy
DPPC	Dipalmitoylphosphocholine
dr	Diastereomeric ratio
EDL	Electrical double layer
ee	Enantiomeric excess
EI	Electron impact
ELVOCs	Extremely low volatility organic compounds
EMSL	Environmental Molecular Sciences Laboratory
eq or equiv	Equivalents
er	Enantiomeric ratio
ESEM	Environmental scanning electron microscopy
ESI	Electrospray ionization
Et	Ethyl
Et <sub>2</sub> O	Diethylether
EtOAc	Ethyl acetate
EtOH	Ethanol
FT	Fourier transform
FWHM	Full width at half maximum
GC	Gas chromatography
GOAmazon	Green Ocean Amazon
HEC	Harvard Environmental Chamber
HPLC	High pressure liquid chromatography

HOM	Highly oxidized molecules
HR	High resolution
HR-BB	High resolution broadband
HRMS	High resolution mass spectrometry
HTDMA	Hygroscopicity tandem differential mobility analyzer
HUMPPA-COPEC	Hyytiälä United Measurement of Photochemistry and Particles – Comprehensive Organic Particle and Environmental Chemistry
IEPOX	Isoprene epoxydiol
IFT	Interfacial tension
IPCC	Intergovernmental Panel on Climate Change
IR	Infrared
I <sub>SFG</sub>	SFG intensity
J	Coupling constant
LB	Langmuir–Blodgett
LC	Liquid chromatography
LDA	Lithium diisopropylamide
LHMDS	Lithium bis(trimethylsilyl)amide
LLPS	Liquid–liquid phase separation
LRMS	Low resolution mass spectrometry
MD	Molecular dynamics
Me	Methyl
MeOH	Methanol
MMA	Mean molecular area

MOUDI	Micro-orifice uniform deposit impactor
Ms	Methanesulfonyl
MsCl	Methanesulfonyl chloride
MS	Mass spectrometry
MW	Molecular weight
NO <sub>x</sub>	Nitrous oxide
NMR	Nuclear magnetic resonance
NU	Northwestern University
OPA	Optical parametric amplifier
PDT	Pendant drop tensiometry
PEG	Polyethylene glycol
Ph	Phenyl
PM <sub>2.5</sub>	Fine particulate matter (under 2.5 microns)
PM <sub>10</sub>	Course particulate matter (2.5 to 10 microns)
PNNL	Pacific Northwest National Laboratory
POA	Primary organic aerosol
ppb	Parts per billion
ppm	Parts per million
PTFE	Polytetrafluoroethylene (Teflon)
<i>i</i> -Pr or <i>i</i> Pr	<i>iso</i> -Propyl
RF	Radiative forcing
RH	Relative humidity
RO <sub>2</sub>	Peroxy radicals

SD	Static diffusion
SDS	Sodium dodecyl sulfate
SEM	Scanning electron microscopy
SF	Sum frequency
SFG	Sum frequency generation
SLPM	Standard litre per minute
SMPS	Scanning mobility particle sizer
SOA	Secondary organic aerosol
SOM	Secondary organic material
SO <sub>x</sub>	Sulfur oxides
STXM	Scanning transmission x-ray microscopy
SVOCs	Semi-volatile organic compounds
SV-TAG	Semi-volatile thermal desorption aerosol gas chromatography
TBS	<i>tert</i> -Butyldimethylsilyl
TEA	Triethylamine
TAG	Thermal desorption aerosol gas chromatography
Tg C yr <sup>-1</sup>	Teragrams of carbon per year
THF	Tetrahydrofuran
TLC	Thin layer chromatography
TMS	Trimethylsilyl
TMSCl	Trimethylsilyl chloride
ToF	Time of flight
ToF-SIMS	Time-of-flight secondary ion mass spectrometry

TOPAS	Tunable optical parametric amplifier set-up
Ts	Toluenesulfonyl
<i>p</i> TsOH or TsOH	Toluenesulfonic acid
VOC	Volatile organic compound
UV	Ultraviolet
XPS	X-ray photoelectron spectroscopy

## Table of Contents

<b>Abstract</b> .....	3
<b>Acknowledgments</b> .....	5
<b>List of Abbreviations</b> .....	8
<b>Table of Contents</b> .....	14
<b>List of Figures, Schemes, and Tables</b> .....	19
<b>Chapter 1. An Integrated Approach to Probing the Surface Chemistry of Atmospheric Aerosol Particles</b> .....	23
1.1. The role of atmospheric aerosols in the climate system.....	24
1.2. Introduction to biogenic secondary organic aerosol particles.....	25
1.3. Biogenic SOA precursors.....	27
1.4. Importance of surface chemistry for understanding SOA processes.....	28
1.5. Organic synthesis within the field of atmospheric chemistry.....	30
1.6. Thesis scope and organization.....	30
<b>Chapter 2. Cloud Activation Potentials for Atmospheric <math>\alpha</math>-Pinene and <math>\beta</math>-Caryophyllene Ozonolysis Products</b> .....	34
2.1. Introduction and motivation.....	35
2.2. Synthesis of $\alpha$ -pinene and $\beta$ -caryophyllene oxidation products. ....	37
2.3. Stability of aldehyde oxidation products in aqueous media.....	40
2.4. Dynamic interfacial tension measurements.....	41
2.4.1. PDT experimental details.....	41
2.4.2. Interfacial tension measurements.....	44

2.4.3. Kinetics of interfacial tension and equilibration timescales.....	52
2.4.4. Calculation of cloud activation potential.....	54
2.4.5. Atmospheric implications.....	57
2.5. Conclusions.....	60
2.6. Experimental procedures.....	61
2.6.1. General methods.....	61
2.6.2. Synthesis of $\alpha$ -pinene and $\beta$ -caryophyllene oxidation products....	62
<b>Chapter 3. Atmospheric <math>\beta</math>-Caryophyllene-Derived Ozonolysis Products at Interfaces.....</b>	<b>73</b>
3.1. Introduction and motivation.....	74
3.2. Collection of laboratory-derived SOM.....	75
3.2.1. Flow tube reactor experimental details.....	76
3.3. Synthesis of $\beta$ -caryophyllene-derived oxidation products.....	77
3.4. Vibrational SFG spectroscopy.....	77
3.4.1. Introduction to SFG spectroscopy.....	77
3.4.2. Experimental details on sample configurations and SFG set-ups..	80
3.4.3. Comparison of SFG spectra of $\beta$ -caryophyllene-derived SOM and oxidation products: C–H stretches.....	84
3.4.4. Comparison of SFG spectra of $\beta$ -caryophyllene-derived SOM and oxidation products: C=O stretches.....	88
3.4.5. Nonlinear bulk responses from $\beta$ -nocaryophyllinic acid upon crystallization.....	91

3.5. Phase-resolved SFG spectroscopy.....	92
3.5.1. Internal heterodyne SFG introduction and experimental details....	92
3.5.2. Computational methods used to interpret phase-resolved data.....	94
3.5.3. Analysis of phase-resolved spectra.....	95
3.6. Atmospheric implications and conclusions.....	98
<b>Chapter 4. Surface-Active <math>\beta</math>-Caryophyllene Oxidation Products at the</b>	
<b>Air/Aqueous Interface.....</b>	<b>101</b>
4.1. Introduction and motivation.....	102
4.2. Synthesis of oxidation products and preparation of sample solutions.....	104
4.3. SFG spectroscopy at the air/aqueous interface.....	104
4.3.1. Experimental details for SFG spectroscopic measurements.....	104
4.3.2. High resolution SFG spectra of $\beta$ -caryophyllene and its oxidation products at the air/ammonium sulfate (aq) interface.....	107
4.3.3. Probing surface coverage-dependent structural organization of $\beta$ - caryophyllene aldehyde at the air/ammonium sulfate (aq) interface.....	112
4.3.4. Perturbation of the interfacial water structure by $\beta$ -caryophyllene aldehyde suggested by O–H stretches.....	115
4.3.5. Evidence for the “salting out” effect of ammonium sulfate in aqueous environments.....	117
4.4. Attempts to acquire surface pressure–mean molecular area isotherms using a Langmuir-Blodgett trough.....	119
4.4.1. Experimental details.....	120

4.4.2. Discussion of efforts to collect surface pressure–MMA isotherms of $\beta$ -caryophyllene oxidation products.....	121
4.5. Conclusions and future directions.....	123
<b>Chapter 5. Towards Increasingly Complex Systems in the Study of Atmospheric Aerosol Particles.....</b>	<b>126</b>
5.1. Summary and outlook for studying $\alpha$ -pinene and $\beta$ -caryophyllene monomeric constituents.....	127
5.2. Collaborations utilizing $\alpha$ -pinene and $\beta$ -caryophyllene monomeric oxidation products.....	128
5.3. Probing interfacial processes and interactions under varying atmospheric conditions.....	131
5.3.1. Design and assembly of an “all-in-one” flow system for simulating environmental conditions.....	132
5.3.2. Investigating terpene-derived SOM under varying RH.....	134
5.3.3. <i>In situ</i> monitoring of ozonolysis of surface-adsorbed terpenes at solid surfaces.....	137
5.3.4. Studies of BVOCs at SOM surfaces: Adsorption, uptake, and reactions.....	139
5.4. Surface spectroscopic studies of field-derived aerosol.....	142
5.5. Towards dimers and higher order constituents in biogenic SOA particles...	147
5.5.1. Synthesis of $\alpha$ -pinene-derived dimers.....	148
5.5.2. Analytical measurements using dimeric species.....	152

5.5.3. Experimental procedures.....	154
5.5.3.1. General methods.....	154
5.5.3.2. Synthesis of aldol-adduct dimers.....	155
5.5.3.3. Synthesis of ester-adduct dimers.....	162
<b>References</b> .....	169
Chapter 1.....	169
Chapter 2.....	181
Chapter 3.....	188
Chapter 4.....	197
Chapter 5.....	205
<b>Appendices</b> .....	211
Appendix 1.....	211
Appendix 2.....	218
<b>Curriculum Vitae</b> .....	233

## List of Figures, Schemes, and Tables

<b>Figure 1.1.</b> Formation of biogenic SOA particles and their role in the atmosphere.....	26
<b>Figure 1.2.</b> An integrated approach to accessing a molecular view of the surface chemistry of biogenic SOA particles in the atmosphere.....	31
<b>Figure 2.1.</b> Atmospheric monomeric oxidation products derived from $\alpha$ -pinene and $\beta$ -caryophyllene synthesized and measured in this study.....	37
<b>Scheme 2.1.</b> Synthesis of pinonaldehyde and pinic acid.....	38
<b>Scheme 2.2.</b> Synthesis of $\beta$ -caryophyllene-derived aldehydes and monoacids.....	38
<b>Scheme 2.3.</b> Synthetic route to $\beta$ -caryophyllene-derived diacid oxidation products.....	39
<b>Figure 2.2.</b> NMR data showing hydrate formation observed in aldehyde oxidation products.....	41
<b>Figure 2.3.</b> Depiction of PDT experiment.....	43
<b>Figure 2.4.</b> Example of “dipping effect” observed in surface tension data.....	44
<b>Figure 2.5.</b> Comparison of interfacial tension as a function of solute concentration for $\alpha$ -pinene- and $\beta$ -caryophyllene-derived oxidation products.....	45
<b>Figure 2.6.</b> Dynamic surface tension measurements of $\alpha$ -pinene-derived oxidation products.....	47
<b>Figure 2.7.</b> Dynamic surface tension measurements for $\beta$ -caryophyllene oxidation products in water.....	50
<b>Figure 2.8.</b> Dynamic surface tension measurements for $\beta$ -caryophyllene oxidation products in 1 M ammonium sulfate solution.....	51
<b>Figure 2.9.</b> Dynamic surface tension measurements comparing 1 mM solutions.....	52
<b>Table 2.1.</b> Supersaturation ratios for $\alpha$ -pinene-derived oxidation products in water and 1 M ammonium sulfate.....	56
<b>Table 2.2.</b> Supersaturation ratios for $\beta$ -caryophyllene-derived oxidation products in water and 1 M ammonium sulfate.....	57
<b>Table 3.1.</b> Details on $\beta$ -caryophyllene-derived SOM collection in the Harvard flow tube reactor.....	78

<b>Figure 3.1.</b> Schematic of NU Solstice/TOPAS laser set-up.....	84
<b>Figure 3.2.</b> HR SFG spectra in C–H region of SOM compared to $\beta$ -caryophyllene and synthesized compounds spin-coated onto fused silica.....	87
<b>Figure 3.3.</b> SFG spectra of a 1:1 mixture of $\beta$ -caryophyllene aldehyde and $\beta$ -nocaryophyllonic acid versus the individual compounds.....	88
<b>Figure 3.4.</b> SFG spectra in C=O region of SOM compared to $\beta$ -caryophyllene and synthesized compounds spin-coated onto CaF <sub>2</sub> .....	90
<b>Figure 3.5.</b> SFG spectral comparison of spin-coated film of $\beta$ -nocaryophyllonic acid on CaF <sub>2</sub> immediately after prepared and after several hours.....	92
<b>Figure 3.6.</b> Comparison of SFG spectra of $\alpha$ -quartz and the spectrum with $\beta$ -nocaryophyllonic acid spin-coated onto the quartz piece at $\phi=0^\circ$ .....	94
<b>Figure 3.7.</b> Phase-resolved SFG data and proposed orientation of $\beta$ -caryophyllene aldehyde on $\alpha$ -quartz.....	97
<b>Figure 4.1.</b> SFG data showing signal intensity tracking over time.....	106
<b>Figure 4.2.</b> SFG spectra of $\beta$ -caryophyllene oxidation products on 1 M ammonium sulfate (aq) collected in the C–H region.....	109
<b>Figure 4.3.</b> SFG spectra in the C–H stretching region of $\beta$ -caryophyllene aldehyde on 1 M ammonium sulfate (aq) at varying concentrations.....	113
<b>Figure 4.4.</b> HR SFG spectra of $\beta$ -caryophyllene aldehyde on ammonium sulfate (aq) and water in the C–H region.....	114
<b>Figure 4.5.</b> SFG spectra in the O–H stretching region of $\beta$ -caryophyllene aldehyde on 1 M ammonium sulfate (aq).....	116
<b>Figure 4.6.</b> SFG spectra in the C–H and O–H stretching regions of $\beta$ -caryophyllene aldehyde on 1 M ammonium sulfate (aq) and water.....	118
<b>Figure 4.7.</b> Surface pressure–MMA isotherm of neat water.....	121
<b>Figure 4.8.</b> Surface pressure–MMA isotherms of $\beta$ -caryophyllene aldehyde on water and ammonium sulfate (aq) and $\beta$ -caryophyllonic acid on water.....	122

<b>Figure 5.1.</b> Examples of putative $\beta$ -caryophyllene-derived oxidation products and organosulfates not yet synthesized and analyzed by our labs.....	129
<b>Figure 5.2.</b> Visual depiction of possible LLPS morphologies in atmospheric aerosol particles.....	130
<b>Figure 5.3.</b> Diagram of recently built integrated set-up for flowing atmospheric vapors	132
<b>Figure 5.4.</b> % RH as a function of time showing reversible cycling between high and low RH.....	135
<b>Figure 5.5.</b> Preliminary SFG experiment probing $\alpha$ -pinene-derived SOM deposited on $\text{CaF}_2$ under high versus low RH.....	136
<b>Figure 5.6.</b> Preliminary ozonolysis SFG experiment performed using $\alpha$ -pinene and $\beta$ -caryophyllene on a $\text{CaF}_2$ optical window.....	138
<b>Figure 5.7.</b> $\beta$ -Caryophyllene ozonolysis experiment performed using the “all-in-one” flow set-up.....	139
<b>Figure 5.8.</b> HR SFG spectra of vapor-phase $\alpha$ -pinene and isotopologues and SFG spectra of resultant SOM.....	141
<b>Figure 5.9.</b> Maps showing sample sites near Manau and CPC data of the Manaus pollution plume over the T2 and T3 sites.....	144
<b>Figure 5.10.</b> Compiled SFG spectra acquired in the C–H stretching region for filter samples collected during GOAmazon2014/5.....	145
<b>Figure 5.11.</b> SFG spectral overlay of sample collected at T2 site and IEPOX-derived organosulfate standard .....	146
<b>Figure 5.12.</b> Target aldol-adduct and ester-adduct dimers derived from $\alpha$ -pinene.....	149
<b>Scheme 5.1.</b> Synthesis of monomer building blocks for aldol-adduct dimer syntheses..	149
<b>Scheme 5.2.</b> Synthesis of aldol addition dimer.....	150
<b>Scheme 5.3.</b> Synthesis of aldol condensation dimer and acid analogue.....	151
<b>Scheme 5.4.</b> Synthesis of aldehyde ester-adduct dimers.....	151

**Scheme 5.5.** Pinnick oxidation reactions to synthesize acid ester-adduct dimers..... 152

**Figure 5.13.** Preliminary surface tension data for pinonaldehyde and ketone–aldehyde aldol addition dimer at 1 mM in deionized water pendant droplets..... 153

## CHAPTER 1

### An Integrated Approach to Probing the Surface Chemistry of Atmospheric Aerosol Particles

**Portions of this chapter are reproduced in part  
with permission from the American Chemical Society:**

Bé, A. G.; Upshur, M. A.; Liu, P.; Martin, S. T.; Geiger, F. M.; Thomson, R. J., Cloud Activation Potentials for Atmospheric  $\alpha$ -Pinene and  $\beta$ -Caryophyllene Ozonolysis Products. *ACS Cent. Sci.* **2017**, *3* (7), 715–725.

Bé, A. G.; Chase, H. M.; Liu, Y.; Upshur, M. A.; Zhang, Y.; Tuladhar, A.; Chase, Z. A.; Bellcross, A. D.; Wang, H.-F.; Wang, Z.; Batista, V. S.; Martin, S. T.; Thomson, R. J.; Geiger, F. M., Atmospheric  $\beta$ -Caryophyllene-Derived Ozonolysis Products at Interfaces. *ACS Earth Space Chem.* **2019**, *3* (2), 158–169.

**1.1. The role of atmospheric aerosols in the climate system.** The accelerated warming of the Earth's climate has confronted inhabitants across the globe with perhaps the toughest challenge to date.<sup>1-2</sup> The climate system is dynamic in nature, and its components — the atmosphere, hydrosphere, cryosphere, lithosphere, and biosphere — interdependently distribute and govern the flow of energy received from the Sun.<sup>3</sup> Therefore, solving the climate change puzzle requires addressing critical gaps in knowledge with respect to the numerous drivers influencing how the climate system evolves over time.<sup>2-3</sup> To index the degree to which a particular driver alters the Earth's energy budget, radiative forcing (RF) is used in climate prediction and modeling as a measure of the perturbation to the balance of incoming and outgoing energy induced by various agents, both natural and anthropogenic (human-derived).<sup>1-2</sup> RF is formally defined as the rate of change in energy per unit area of the Earth as measured at the top of the atmosphere (tropopause).<sup>4-5</sup> A positive RF value for a given driver indicates that the incoming energy surpasses the outgoing energy (i.e. the particular driver contributes a warming effect), while a negative RF value represents the converse (i.e. a cooling effect).<sup>1</sup> Among the various natural and anthropogenic climate forcing agents within the climate system, atmospheric aerosol particles are an especially poorly understood class of constituents that impact RF.<sup>6-7</sup>

Atmospheric aerosols, defined as suspensions of condensed-phase (i.e. liquid or solid) particles within the gas phase, are ubiquitous airborne constituents primarily abundant in the troposphere.<sup>8-10</sup> Aerosol sizes range across the nanometer to micrometer regime, and fine particulate matter under 2.5 microns (PM<sub>2.5</sub>), in particular, impact public health and the climate.<sup>7</sup> These particles influence RF both through direct effects, via scattering and absorbing radiation, and indirect effects as cloud condensation nuclei (CCN) that promote cloud formation.<sup>7, 11-13</sup> Notably, atmospheric aerosols collectively contribute a net atmospheric cooling effect (i.e.

negative RF value) on Earth's climate.<sup>1, 14-15</sup> In fact, with the exception of the warming RF from anthropogenic black carbon, "aerosols and their interactions with clouds have offset a substantial portion of global mean forcing from well-mixed greenhouse gases," as reported in the 2013 Intergovernmental Panel on Climate Change (IPCC) assessment report.<sup>1</sup> Nonetheless, the IPCC continues to emphasize that atmospheric aerosols "contribute the largest uncertainty" to the total RF estimate.<sup>1</sup> As such, uncertainties in aerosol RF contributions continue to impede the overall accuracy of climate modeling and prediction, yet remain difficult to constrain due to their inherently diverse sources, formation mechanisms, molecular constituents, physicochemical properties, and lifetimes in the troposphere.<sup>1, 3-4, 6, 12, 15-16</sup>

**1.2. Introduction to biogenic secondary organic aerosol particles.** Aerosols are both directly emitted into the atmosphere as condensed-phase particulate matter, and formed via gas-to-particle conversion processes taking place in the atmosphere — termed primary and secondary aerosols, respectively.<sup>7, 16</sup> Both primary and secondary particles can originate from natural sources (e.g. volcanic eruptions, oceanic sea spray, natural wildfires, pollen, and forest ecosystems) or anthropogenic activities, such as car exhaust, factory smokestacks, and burning of agricultural waste.<sup>7, 16</sup> Of the many types of aerosols, organic material constitutes a dominant portion of the aerosol mass in the atmosphere.<sup>6, 12, 15-16</sup> Furthermore, secondary organic aerosol (SOA) particles, are estimated to contribute up to 50–80% of measured PM<sub>2.5</sub> mass in the troposphere depending on season and location.<sup>6, 17-20</sup>

Naturally-derived SOA particles formed from plant-emitted biogenic volatile organic compounds (BVOCs) are of particular importance, as they are estimated to outweigh concentrations of anthropogenic aerosols by a factor of ten,<sup>12</sup> as well as lead to atmospheric cooling predominantly over the world's large forest ecosystems.<sup>17-18</sup> Biogenic SOA particles are

produced when gas-phase BVOCs undergo oxidation in the presence of oxidants (i.e.  $O_3$ ,  $NO_x$ , OH radicals) in the atmosphere, forming increasingly lower volatility oxidation products that partition into the condensed phase through gas-to-particle conversion pathways (**Figure 1.1**).<sup>6, 12, 15, 18, 20-31</sup> The cascades of processes leading to biogenic SOA particles are highly complex, and from mass spectrometry (MS) studies, it has been estimated that greater than 10,000 different organic compounds form within the resulting particles.<sup>15, 30</sup>

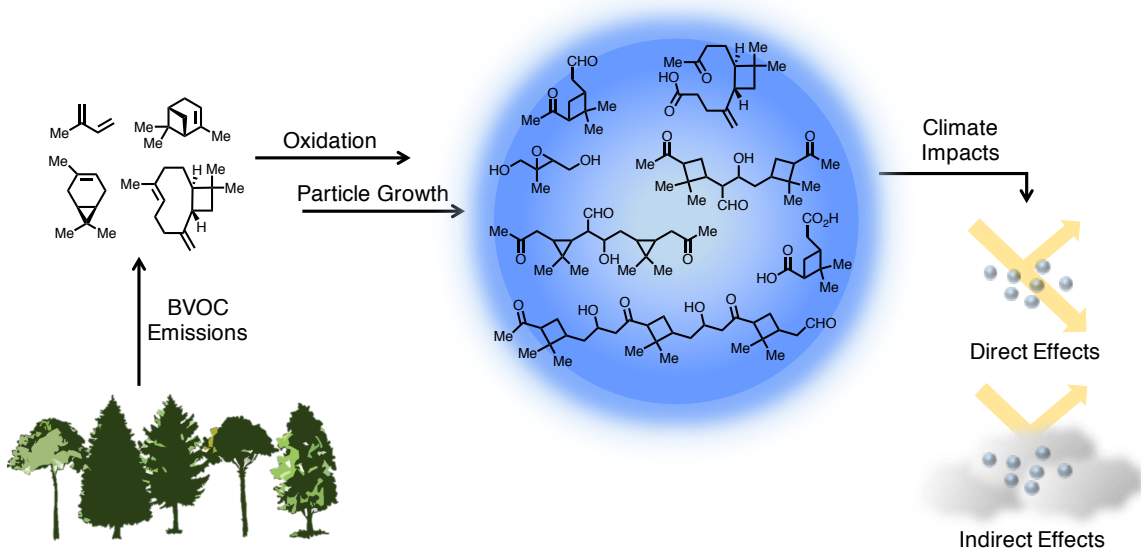


**Figure 1.1.** Formation of biogenic SOA particles and their role in the atmosphere.

Processes leading to SOA particles in the atmosphere include 1) chemical reactions, such as oxidation, dimerization, and oligomerization, 2) nucleation (i.e. particle formation from molecular clustering), and 3) heterogeneous partitioning processes, involving condensation of gaseous precursors onto pre-existing particles and coagulative growth via particle–particle collisions.<sup>6, 15, 32-34</sup> Moreover, SOA formation and growth depend on several factors, including the identities and concentrations of the reacting BVOCs and oxidants, as well as environmental conditions, such as temperature and relative humidity (RH).<sup>8, 12, 20, 25, 35-36</sup> In this thesis, we make

the distinction between SOA and secondary organic material (SOM). SOA refers collectively to all molecular constituents that partition between the gas and particle phases, whereas SOM specifically distinguishes the particle-phase material.

**1.3. Biogenic SOA precursors.** Volatile terpenes primarily produced by different types of trees, flowers, and other plants dominate the pool of BVOCs leading to SOA formation.<sup>15, 37-39</sup> Plants biosynthesize and emit mixtures of volatile terpenes for signalling and defense mechanisms to lower abiotic or biotic stress, leading to a large compositional diversity in terpene emissions based upon the plant species, external stressors, geographical location, and time of year.<sup>40</sup> Despite these variations, a select number of principal terpene BVOCs dominate plant emissions and therefore the resultant formation of biogenic SOA.<sup>40</sup> The work in this thesis chiefly focuses on two prevalent BVOCs,  $\alpha$ -pinene and  $\beta$ -caryophyllene, and several of their proposed and/or detected oxidation products.<sup>41-42</sup>

$\alpha$ -Pinene is the most abundant monoterpene ( $C_{10}$ ) ( $\sim 50 \text{ Tg C y}^{-1}$ )<sup>43-46</sup> in the troposphere and is primarily emitted over the boreal forest ecosystems of the northern hemisphere — the largest terrestrial biome on Earth.<sup>21, 47</sup> While  $\alpha$ -pinene is a canonical system of study in the atmospheric community,  $\beta$ -caryophyllene, the most abundant sesquiterpene (*ca.*  $5\text{--}7 \text{ Tg y}^{-1}$ ),<sup>41, 45, 48-59</sup> remains far less studied to date. Overall, sesquiterpenes ( $C_{15}$ ) are present in lower concentrations in the atmosphere ( $\sim 130$  and  $\sim 15 \text{ Tg C yr}^{-1}$  for total monoterpene and sesquiterpene emission rates, respectively).<sup>44-45, 51, 58, 60</sup> However, they exhibit higher reactivity towards ozone and higher aerosol yields when compared to abundant monoterpenes,<sup>41, 51, 53, 61-64</sup> potentially indicating underestimation of their contribution to SOA formation. Within this thesis, comparisons are made within several chapters between  $C_{10}$  and  $C_{15}$  compounds as well as species derived from isoprene ( $C_5$ ), the most abundant non-methane hydrocarbon ( $\sim 470 \text{ Tg yr}^{-1}$ )<sup>45, 58</sup> that

is the dominantly emitted BVOC over the Amazon rainforest and other tropical forest ecosystems.<sup>28</sup>

**1.4. Importance of surface chemistry for understanding SOA processes.** Despite the abundance and importance of biogenic terpene-derived SOA particles in the climate system, the mechanisms leading to their formation and growth via gas-to-particle conversion as well as their climate-relevant properties, particularly related to cloud formation, remain elusive.<sup>12, 15, 30</sup> MS is the widespread method employed in the aerosol science community, and compositional and mechanistic analyses supported by such studies continue to push forward progress within the field.<sup>15, 40, 65-69</sup> However, much relevant information about the particle sample is often lost upon fragmentation, during the sample preparation process, and due to volatility limitations of MS-based methods, with notable exceptions.<sup>70-71</sup> Additionally, current MS-based techniques have limited applicability for investigating the physicochemical processes occurring at surfaces and interfaces.<sup>18, 37-38, 51, 72-75</sup> Therefore, experimental capabilities that shed light on the molecular-level chemistry of interfacial processes and interactions are needed, as they may play a fundamental role in driving SOA formation, growth, and climate effects in the atmosphere.

Interfaces are the boundaries between regions occupied by two different phase states, and intrinsically, they are the first entities to come into contact with the surrounding environment.<sup>76-77</sup> In the case of SOA particles, the gas/particle interface is first point-of-contact for incoming chemical species, and it is here where important, albeit insufficiently characterized, heterogeneous phenomena take place that lead to particle formation, growth, aging, and climate effects.<sup>14, 78</sup> For instance, adsorption and uptake of gas-phase BVOCs onto pre-existing particle surfaces may lead to condensational growth,<sup>25</sup> while coagulative growth inherently involves surface-to-surface interactions between merging particles.<sup>79</sup> Surface reactions upon exposure to

gas-phase oxidants or other tropospheric reagents may promote SOA growth and aging.<sup>29, 80-81</sup>

Condensation of water vapor onto aerosol seed nuclei, which leads to cloud activation, is believed to be promoted by the presence of surface-active organic species.<sup>82-85</sup> Furthermore, while numerous distinct organic compounds have been detected within the particle bulk as discussed above, only a subset of these compounds may be sufficiently surface-active to reside at the particle surface.<sup>11, 21, 26, 78, 82, 84, 86-95</sup>

Despite the ubiquitous nature of surfaces and interfaces in numerous SOA processes and interactions, progress towards experimentally examining the chemistry of these regions of interest has been slow.<sup>72</sup> Inherent challenges exist with sorting out the interfacial region from the bulk-phase of materials, as the population of bulk species greatly overwhelms the number of interfacial species.<sup>76</sup> As a result, only a handful of techniques that currently exist are adequately equipped to discern the characteristically low surface signal contribution from that of the bulk.<sup>96</sup><sup>97</sup> When considering the application of such surface techniques to SOA analysis, a wide range of analytical tools is required, as no single technique is capable of fully capturing the molecular composition and properties at SOA surfaces and interfaces.<sup>72, 96</sup> Surface-specific methods that have been employed in the SOA field include techniques requiring ultrahigh vacuum conditions, such as x-ray based methods,<sup>98-100</sup> electron microscopies,<sup>101-102</sup> and mass spectrometries configured to ablate surface vs bulk portions of particles,<sup>103-104</sup> as well as ambiently operated scanning probes,<sup>35, 72, 105-106</sup> and surface-specific linear<sup>107-109</sup> and nonlinear spectroscopies.<sup>18, 110-112</sup> These techniques each have their advantages and caveats, and overall, there are several points of concern that must be evaluated when considering analytical tools useful for exploring SOA surface chemistry. Such considerations include, but are not limited to: (1) achieving adequate surface sensitivity in the presence of the bulk phase, (2) offering applicability to different

interfaces of interest, (3) probing samples nondestructively, and ideally with little to no sample manipulation, and (4) operating under environmental conditions relevant to the atmosphere.<sup>72</sup>

**1.5. Organic synthesis within the field of atmospheric chemistry.** An additional challenge in the pursuit to investigating SOA surface physicochemistry is that concrete structural elucidation of proposed oxidation products and investigation of their surface-relevant properties remain indeterminate without access to molecular standards.<sup>29, 41-42, 63, 95</sup> While many terpenes precursors are commercially available, few molecular standards of oxidation products can be readily purchased. The application of organic synthesis to atmospheric aerosol research is therefore powerful, as it allows for access to meaningful quantities of pure standards of molecular constituents that have been proposed or detected, but that without the use of synthesis, would be otherwise difficult to isolate in sufficient amounts or separate from the complex mixtures present in collected samples.<sup>15, 34, 113-114</sup> Historically, however, a relatively scarce number of interactions have taken place between the atmospheric and chemical synthesis communities.<sup>34, 115-119</sup> Yet, given the intrinsic structural complexities of terpene-derived oxidation products, there exists a critical need to synthesize and characterize these molecules with the rigor and methodological toolset established within the field of synthetic organic chemistry.

**1.6. Thesis scope and organization.** As discussed, gaining molecular insights into atmospheric surfaces and interfaces remains challenging, as (1) surfaces are intrinsically difficult to access nondestructively under tropospherically relevant pressures and temperatures, and (2) a lack of existing molecular standards of putative terpene-derived oxidation products continues to hamper progress in identifying and studying the properties of SOA constituents. The work outlined herein seeks to resolve these impediments using a toolbox of approaches that intersect the fields of surface chemistry, organic synthesis, and aerosol science and engineering (**Figure 1.2**).

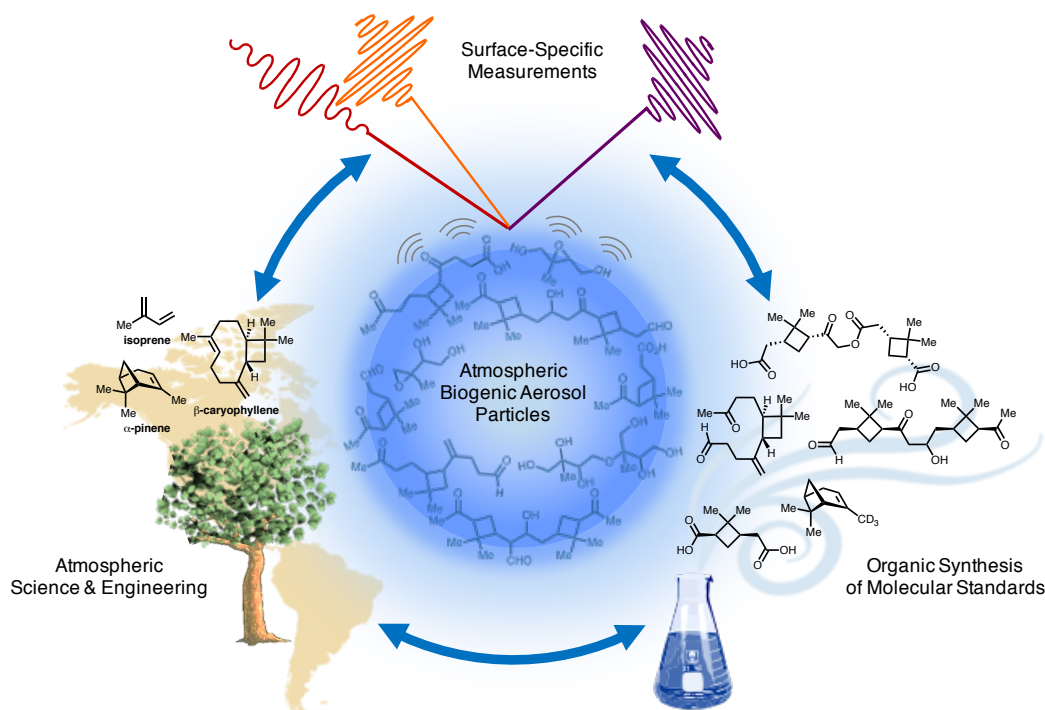


**Figure 1.2.** An integrated approach to accessing a molecular view of the surface chemistry of biogenic SOA particles in the atmosphere.

Ultimately motivated to address the low level of understanding regarding aerosol–cloud–climate interactions, the work presented throughout this thesis takes strides towards understanding the fundamental role of surface-active molecular constituents in SOA processes and interactions in the atmosphere. Focusing on several oxidation products derived from terpene BVOCs,  $\alpha$ -pinene and  $\beta$ -caryophyllene, the work described in this thesis seeks to investigate the relative propensities of these molecules to localize at various atmospheric interfaces and examine their structural organization, orientation, and reactivity within such interfacial environments. These central studies, along with complementary experiments, will be detailed in the chapters that follow. In addition, introductions to techniques and methods employed in these studies, as well as foundational experimental details, will be described throughout the text where appropriate. Taken together, this thesis is organized as follows:

Prompted by field and laboratory studies that report putative oxidation products derived from  $\alpha$ -pinene and  $\beta$ -caryophyllene and the potential role that these species might play in SOA-mediated cloud droplet condensation, Chapter 2 describes the synthesis of a suite of monomer oxidation products that have been proposed to form via ozonolysis of these two precursor terpenes. Chapter 2 also reports subsequent pendant drop tensiometry measurements, which characterize the surface activity of these  $\alpha$ -pinene and  $\beta$ -caryophyllene oxidation products in aqueous droplets, as surface tension depression caused by surface-active organic species is an important parameter driving CCN activation.

Chapter 3 introduces the employment of the surface-selective nonlinear optical method, vibrational sum frequency generation (SFG) spectroscopy, to gain qualitative molecular information on the surface composition of SOA particles. Specifically, Chapter 3 reports SFG benchmarking experiments that compare qualitative matches between the surface vibrational spectrum of laboratory-derived SOM (i.e. particle-phase material) generated from the ozonolysis of  $\beta$ -caryophyllene with that of the  $\beta$ -caryophyllene-derived monomer oxidation products (introduced in Chapter 2). Chapter 3 also provides a brief overview on the use of phase-resolved SFG spectroscopy as a method to gain absolute orientation information about these species at interfaces.

Building on the work detailed in Chapters 2 and 3, Chapter 4 presents vibrational SFG spectroscopy experiments that probe the  $\beta$ -caryophyllene oxidation products at air/aqueous interfaces. Specifically, Chapter 4 expands on the significant cloud activation potentials identified for these oxidation products in Chapter 2 by making connections to molecular structure, surface coverage, and structural organization in interfacial aqueous environments applicable to cloud droplet formation scenarios.

Chapter 5 presents a summary and outlook (Section 5.1) on the work detailed in Chapters 2–4, along with an overview of ongoing work laying the groundwork for several future research avenues that move beyond the synthesis and analysis of monomeric constituents in biogenic SOA (Sections 5.2–5.5). Section 5.2 includes a brief summary of two collaborative studies that have been made possible through the synthesis of the monomer oxidation products derived from  $\alpha$ -pinene and  $\beta$ -caryophyllene. Section 5.3 describes the development of instrumentation and preliminary results that set the stage for probing dynamic atmospheric interfacial processes in real time under varying environmental conditions. Section 5.4 details ongoing data collection that highlights the utility of SFG spectroscopy as a nondestructive and highly sensitive method to fingerprint the surfaces of field-collected SOM. Finally, Section 5.5 focuses on efforts towards the synthesis and analysis of dimeric and oligomeric oxidation products, a potentially important but understudied class of particle-phase accretion oxidation products that may drive SOA formation and growth. Focusing specifically on  $\alpha$ -pinene pathways in the atmosphere, Chapter 5.5 presents modular syntheses for a suite of  $\alpha$ -pinene-derived aldol- and ester-adduct dimers, along with future directions focused on surface tension measurements and MS benchmarking studies.

## CHAPTER 2

### Cloud Activation Potentials for Atmospheric $\alpha$ -Pinene and $\beta$ -Caryophyllene Ozonolysis Products

**Portions of this chapter are reproduced in part  
with permission from the American Chemical Society:**

Bé, A. G.; Upshur, M. A.; Liu, P.; Martin, S. T.; Geiger, F. M.; Thomson, R. J., Cloud Activation Potentials for Atmospheric  $\alpha$ -Pinene and  $\beta$ -Caryophyllene Ozonolysis Products. *ACS Cent. Sci.* **2017**, *3* (7), 715–725.

**2.1. Introduction and motivation.** As introduced in Chapter 1, although biogenic terpene-derived SOA particles are highly abundant in the troposphere and lead to cooling effects over vast forested regions of the globe,<sup>1-6</sup> the mechanisms that drive climate-relevant SOA interactions remain difficult to elucidate.<sup>4, 7-10</sup> A current area of intense research regarding the properties of SOA particles focuses on the role of surface-active organic compounds in cloud formation processes mediated by SOA CCN. Cloud droplet activation refers to the process in which water vapor condenses and forms a growing liquid cloud droplet.<sup>11-12</sup> Cloud activation occurs when the atmospheric RH is at supersaturation (above 100%) and is initiated by the presence of aerosols that serve as CCN.<sup>12</sup> As described by Köhler theory, which is based upon equilibrium thermodynamics, condensational growth of cloud droplets is governed by concurrent, yet competing, changes in saturation vapor pressure that occur due to the droplet curvature of growing droplets (Kelvin effect) and amount of solute species present (Raoult's law).<sup>11-12</sup> While Köhler theory appropriately describes scenarios involving purely inorganic CCN, the effects of organic and mixed organic–inorganic CCN continue to strike debate, as modified forms and alternative representations continue to evolve in attempts to more accurately account for the presence of organic species.<sup>13-18</sup>

In particular, surface-active organic molecules can increase the propensity of SOA particles to nucleate cloud droplets (i.e. their CCN activity) by reducing the surface tension of the forming droplet and thereby lowering the critical supersaturation required for cloud droplet activation.<sup>11, 19-23</sup> A recent publication by Ruehl and coworkers also suggests that the bulk-to-surface partitioning of surface-active organic compounds can result in a concentrated organic film near the gas/particle interface, which can significantly reduce the surface tension and result in a larger droplet diameter before activation.<sup>24</sup> While current models have taken into account the

contribution of organic species to CCN activity through the bulk solubility effect, surface tension depression effects have largely been neglected, in part because of a lack of reliable direct surface tension measurements of relevant individual surface-active organic compounds.<sup>11, 24-27</sup>

Within this context, Chapter 2 investigates the surface tension effects of a suite of ozonolysis oxidation products derived from  $\alpha$ -pinene and  $\beta$ -caryophyllene, which we hypothesized might exhibit higher surface activity than our previously investigated isoprene derivatives.<sup>26</sup> Motivated by studies reporting proposed oxidation products derived from  $\alpha$ -pinene and  $\beta$ -caryophyllene,<sup>28-32</sup> we target here a series of structurally related monomeric ozonolysis products derived from these precursor terpenes (**Figure 2.1**). The specific compounds synthesized in this study have been proposed as constituents relevant to SOM in field and laboratory aerosol studies<sup>30, 33-51</sup> and may therefore serve as homogeneous standards to further corroborate those studies. Following the synthesis of these oxidation products, we present dynamic surface tension measurements of this series of compounds and provide estimations of their individual supersaturation ratios, which allow for prediction of their influences on CCN activity.

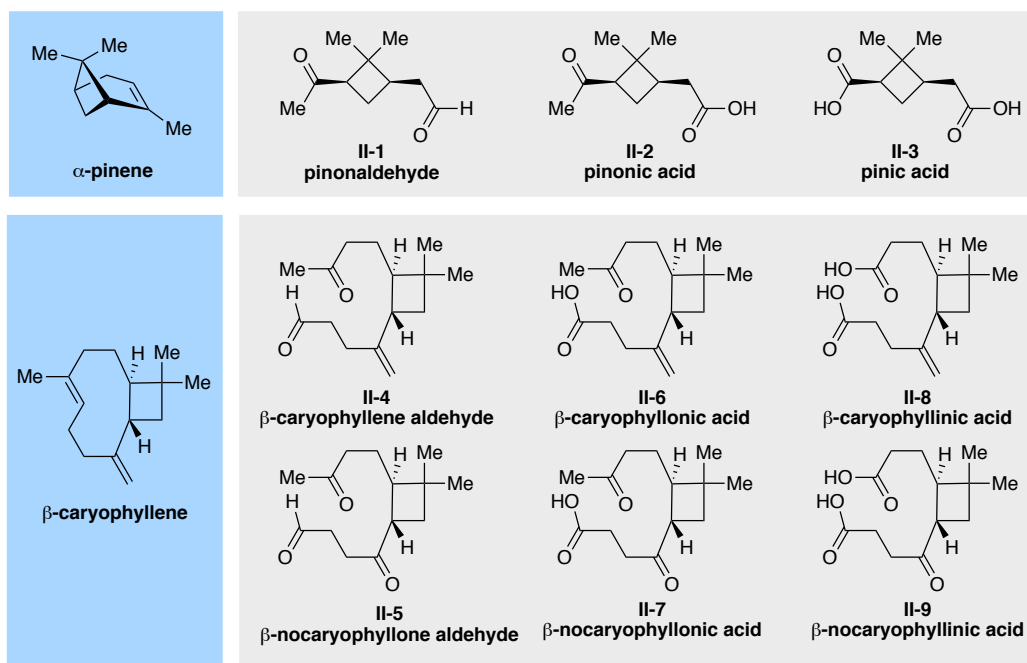
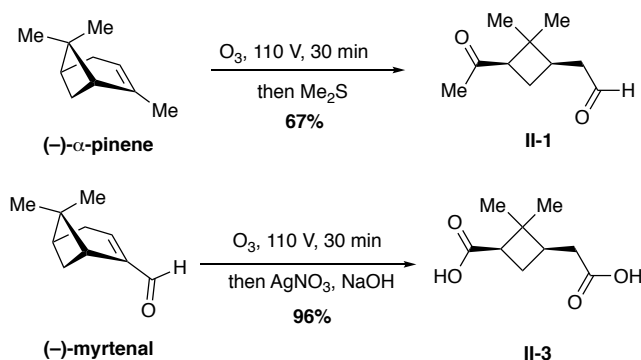


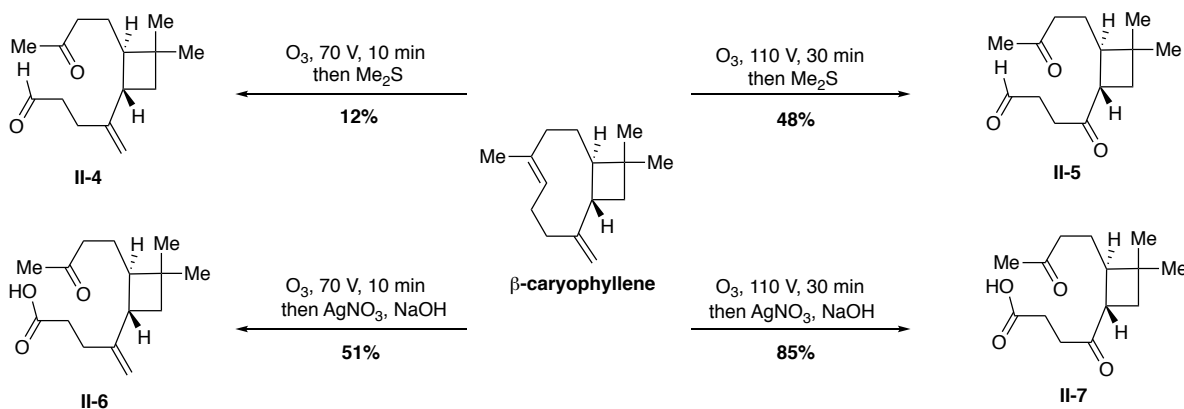
**Figure 2.1.** Atmospheric monomeric oxidation products derived from  $\alpha$ -pinene and  $\beta$ -caryophyllene synthesized and measured in this study.

**2.2. Synthesis of  $\alpha$ -pinene and  $\beta$ -caryophyllene oxidation products.** With the goal of accessing practical quantities of putative SOA constituents derived from  $\alpha$ -pinene and  $\beta$ -caryophyllene for subsequent surface activity measurements, we set out to accomplish the synthesis of a suite of oxidation products proposed to form via ozonolysis, the kinetically favored initial oxidation pathway for these two BVOCs in the atmosphere. All compounds were prepared synthetically, with the exception of pinonic acid (**II-2**), which was purchased from Sigma-Aldrich and used as received. Pinonaldehyde (**II-1**) was accessed through ozonolysis of (–)- $\alpha$ -pinene using an ozone generator with a reductive work-up conditions, while pinic acid (**II-3**) was synthesized from ozonolysis of myrtenal under oxidative work-up conditions (**Scheme 2.1**).



**Scheme 2.1.** Synthesis of pinonaldehyde (**II-1**) and pinic acid (**II-3**).

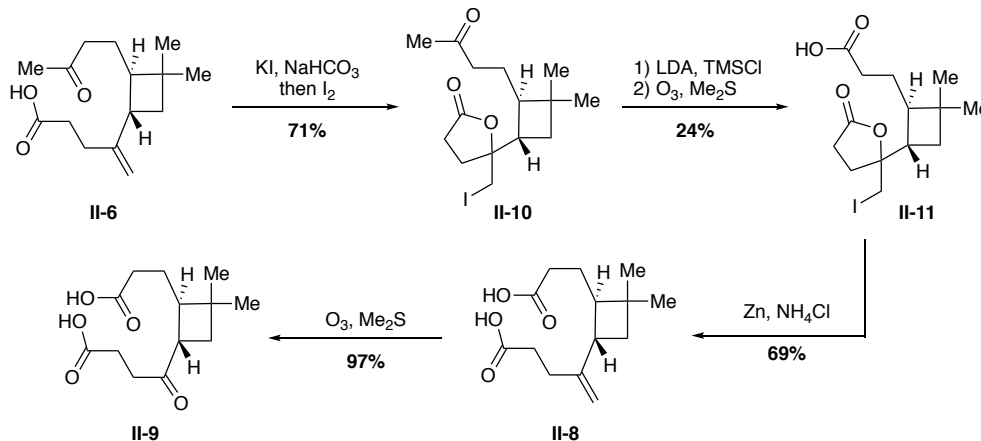
$\beta$ -Caryophyllene aldehyde (**II-4**) and  $\beta$ -nocaryophyllone aldehyde (**II-5**) were synthesized using adapted approaches to procedures reported by Parshintsev and coworkers.<sup>37</sup> Additionally,  $\beta$ -caryophyllonic acid (**II-6**) and  $\beta$ -nocaryophyllonic acid (**II-7**) were prepared analogously to procedures reported by van Eijck and coworkers.<sup>40</sup> In brief, these aldehyde and monoacid oxidation products (**II-4–II-7**) were isolated from ozonolysis of  $\beta$ -caryophyllene under varied reaction times and ozone generator voltage, followed by either oxidative or reductive work-up conditions to access the desired product carbonyl functionality (**Scheme 2.2**).



**Scheme 2.2.** Synthesis of aldehydes, **II-4** and **II-5**, and monoacids, **II-6** and **II-7**.

Attempts to synthesize  $\beta$ -caryophyllinic acid (**II-8**) according to procedures published by van Eijck and coworkers<sup>40</sup> were unsuccessful, however. As such, we developed an alternative

approach for preparing compounds **II-8** and **II-9** from  $\beta$ -caryophyllonic acid (**II-6**) (**Scheme 2.3**). An iodolactonization reaction of monoacid **II-6** simultaneously protected the carboxylic acid and alkene moieties, yielding **II-10**. Silyl enol ether formation and a subsequent ozonolysis converted the methyl ketone to the desired carboxylic acid **II-11**. Subsequently, **II-11** was subjected to iodolactone removal, which revealed the desired acid product,  $\beta$ -caryophyllinic acid (**II-8**). Finally,  $\beta$ -nocaryophyllinic acid (**II-9**) was accessed through a final ozonolysis of diacid **II-8** with oxidative work-up conditions. With the exception of  $\beta$ -caryophyllinic acid (**II-8**) and  $\beta$ -nocaryophyllinic acid (**II-9**), all synthesized compounds required iterative purification using silica gel chromatography until determined to be  $\geq 95\%$  pure by the  $^1\text{H}$  NMR spectroscopy prior to performing the subsequent analytical measurements. Compound-specific purification procedures are included in the experimental procedures described in Section 2.6.



**Scheme 2.3.** Synthetic route to diacid oxidation products, **II-8** and **II-9**, from  $\beta$ -caryophyllonic acid (**II-6**).

By isolating molecular standards of this suite of oxidation products, information about their phase states was also obtained. Such information can disclose insights into viscosities, vapor pressures, and consequently qualitative information on the likelihood for the presence of these species in the SOA particle phase. With this in mind, pinonaldehyde (**II-1**), pinonic acid

(**II-2**), and pinic acid (**II-3**) were present as a low viscosity oil, powdery solid, and highly viscous oil, respectively, from  $-30$ – $25$  °C. At the same temperatures, the synthetic  $\beta$ -caryophyllene oxidation products existed as highly viscous oils, with the exception of  $\beta$ -nocaryophyllinic acid (**II-9**), which was isolated as a powdery solid.

**2.3. Stability of aldehyde oxidation products in aqueous media.** In aqueous environments, aldehydes may readily react with water and thus exist in equilibrium with the hydrate (i.e. geminal diol) form (**Figure 2.2**). In order to monitor the potential formation of the hydrate in aqueous solutions of pinonaldehyde (**II-1**),  $\beta$ -caryophyllene aldehyde (**II-4**), and  $\beta$ -nocaryophyllone aldehyde (**II-5**), solutions ( $2 \text{ mg mL}^{-1}$ ) of each compound in  $\text{D}_2\text{O}$  were prepared and monitored by  $^1\text{H}$  and  $^{13}\text{C}$  NMR spectroscopy for 72 hours. The presence of the hydrate in  $\text{D}_2\text{O}$  was observed for all three aldehyde oxidation products by  $^1\text{H}$  and  $^{13}\text{C}$  NMR spectroscopic data collected after only ten minutes (**Figure 2.2A**, hydrates **II-12**, **II-13**, and **II-14** were formed from aldehydes **II-1**, **II-4**, and **II-5**, respectively). Hydrate formation resulted in a mixture containing approximately 55% hydrate and 45% aldehyde for both pinonaldehyde (**II-1**) and  $\beta$ -nocaryophyllone aldehyde (**II-5**) in  $\text{D}_2\text{O}$  (**Figure 2.2B**). The ratio of aldehyde-to-hydrate did not change any further over the course of days, revealing that an aldehyde–hydrate equilibrium is rapidly reached before ten minutes for these compounds. In addition, the ratio of aldehyde-to-hydrate did not change with the addition of ammonium sulfate ( $100 \text{ mM}$  in  $\text{D}_2\text{O}$ ) over 72 hours. Note that the solubility of  $\beta$ -caryophyllene aldehyde (**II-4**) in  $\text{D}_2\text{O}$  was insufficient for accurate quantification of an aldehyde–hydrate ratio and therefore hydrate formation from this compound was only qualitatively observed.

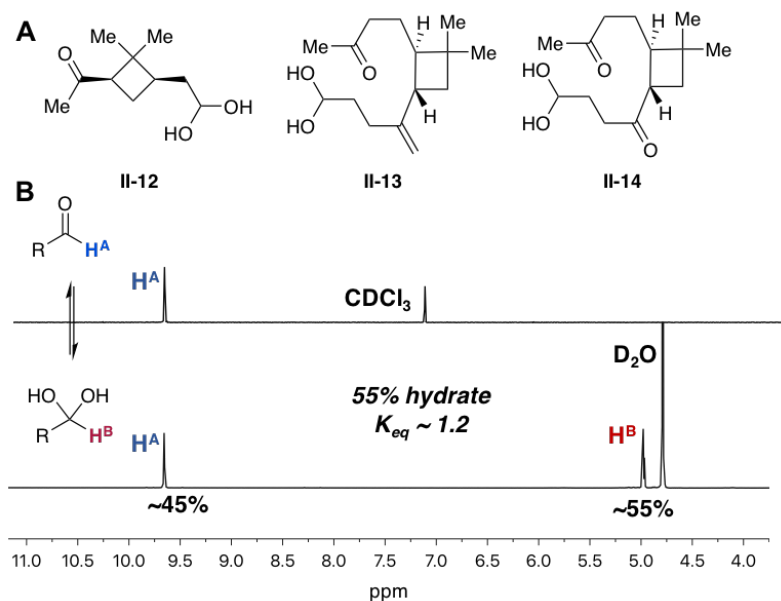


**Figure 2.2.** (A) In aqueous solution, aldehydes **II-1**, **II-4**, and **II-5** exist in equilibrium with their hydrate forms **II-12**, **II-13**, and **II-14**, respectively. (B)  $^1\text{H}$  NMR spectroscopic data taken in  $\text{D}_2\text{O}$  reveals an aldehyde–hydrate mixture containing approximately 55% of the hydrate form for both pinonaldehyde (**II-1**, **II-12**) and  $\beta$ -nocaryophyllone aldehyde (**II-5**, **II-14**). The shown spectra are for pinonaldehyde (**II-1**, **II-12**). Note that the sparing solubility of  $\beta$ -caryophyllene aldehyde (**II-4**) in  $\text{D}_2\text{O}$  resulted in poor signal-to-noise in the NMR spectra and hydrate formation (i.e., **II-13**) from this compound was only qualitatively observed.

**2.4. Dynamic interfacial tension measurements.** The surface tension of suspended aqueous droplets was measured using pendant drop tensiometry (PDT) in order to investigate the surface activity of the  $\alpha$ -pinene- and  $\beta$ -caryophyllene-derived ozonolysis products at various concentrations in aqueous environments. The procedure and experimental setup for interfacial tension measurements using PDT have been described in detail previously, but a brief description follows.<sup>26</sup>

**2.4.1. PDT experimental details.** Surface tension was measured on a FTA125 goniometer by capturing images of droplets at  $20 \pm 2$  °C and 30–40% RH for solutions prepared in either deionized  $\text{H}_2\text{O}$  or 1 M  $(\text{NH}_4)_2\text{SO}_4$  solution (**Figure 2.3**). Specifically, a 1 mL syringe (see below for more details) with a flat stainless steel needle was mounted on the PDT instrument and

inserted ~1 cm into a quartz cuvette containing ~0.2 mL of the solution under measurement. A droplet of the solution (~7  $\mu\text{L}$  in volume, 2.0–2.3 mm in diameter) being measured was then carefully formed at the tip of the needle and was subsequently allowed to stabilize. Images were then immediately captured within 3 s of droplet formation and were taken over 0.3 s intervals for 10 min for a total of 1500 images for each experiment. Images were captured using a RS170 CCD camera equipped with a microscope lens. Surface tension values were determined by fitting the shape of the droplet image to a variation of the Young–Laplace equation using the FTA32 v2.0 software (**Figure 2.3**).

Measurements are reported as an average of 3–5 successive runs (replicates). Measurements were taken over the course of ten minutes, as values were found to maintain steady state during this acquisition time. Similar equilibration times have also been reported for dynamic surface tension studies of  $\text{PM}_{10}$  size fraction of aerosol particles collected in an urban setting.<sup>27</sup> The pH of the  $(\text{NH}_4)_2\text{SO}_4$  solutions were approximately 5.0–6.0 and the pH of solutions prepared in water were approximately 6.0–7.5. All solutions for were measured within 48 hours of their preparation and samples were stored at 4 °C in sealed glass vials when not being measured.

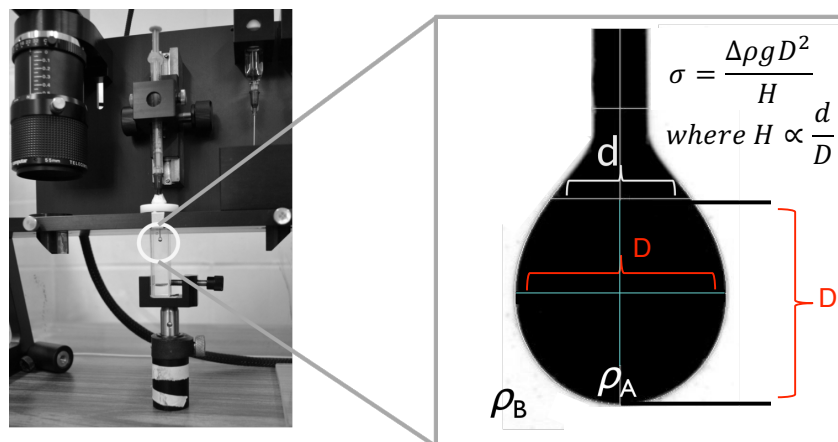


**Figure 2.3.** Depiction of PDT experiment. Interfacial tension (IFT) of the suspended droplet is calculated according to the drop shape ( $H$ ) and the density difference between the drop and surrounding air.

We note that interfacial tension measurements reported previously from our labs were performed using a 1 mL plastic syringe.<sup>26</sup> However, due to the increased hydrophobicity of compounds measured here relative to those studied previously, a consistent reduction in surface tension was noticed when comparing successive data acquisitions on the same solution collected using a plastic syringe without refreshing the solution volume in the syringe between runs (**Figure 2.4**). Potentially due to the solute molecules partitioning to the interior walls of the plastic syringe over time, this “dipping effect” was first noticed for oxidation products derived from  $\beta$ -caryophyllene and was especially pronounced for the more hydrophobic compounds that exhibit lower solubility in water and 1 M  $(\text{NH}_4)_2\text{SO}_4$ . This “dipping effect” was not observed in our previous study,<sup>26</sup> likely due to the highly hydrophilic nature of the isoprene-derived oxidation products compared to the compounds analysed in this study. The use of a clean and oven-dried 1 mL glass syringe eliminated the “dipping effect” for all compounds studied here in the data that follows.

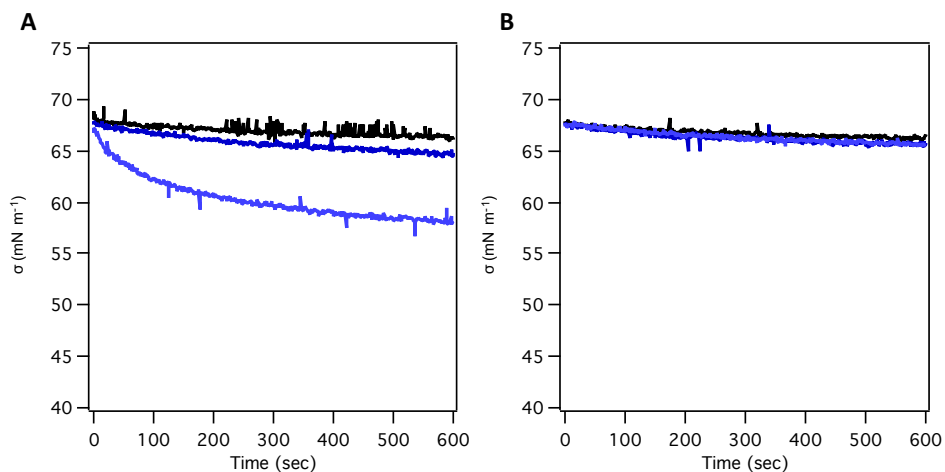


**Figure 2.4.** (A) Example of “dipping effect” in surface tension data observed upon measuring a  $\beta$ -caryophyllene-derived oxidation product when volume in syringe was not refreshed and a plastic syringe was used (3 consecutive runs are shown). (B) “Dipping effect” not observed when volume in syringe was refreshed each time using a plastic syringe and when volume in syringe was not refreshed using a glass syringe.

Concentrations of  $\alpha$ -pinene-derived compounds in water solutions ranged from 0–30 mM for pinonic acid (**II-2**) and pinic acid (**II-3**) and 0–10 mM for pinonaldehyde (**II-1**) due to insolubility above 10 mM. All  $\beta$ -caryophyllene oxidation products (i.e., compounds **II-4–II-9**) were insoluble above 1 mM and therefore 0–1 mM concentrations were measured for these compounds. Solutions in 1 M ammonium sulfate were prepared using the same solute concentrations as those measured in water. Concentrations that could not be measured due to compound insolubility in 1 M ammonium sulfate are noted where applicable. With the exception of pinonic acid (**II-2**),<sup>23, 52-53</sup> we report unprecedented dynamic surface tension experiments for the presented series of compounds.

**2.4.2. Interfacial tension measurements.** In **Figure 2.5**, the interfacial tension ( $\sigma$ ) is plotted as a function of solute concentration on a logarithmic scale for suspended drops of solutions containing the synthesized four-membered ring oxidation products derived from  $\alpha$ -pinene and  $\beta$ -caryophyllene in deionized water and 1 M ammonium sulfate, and the data are fitted to the

Szyszkowski–Langmuir equation.<sup>11, 54-56</sup> The Szyszkowski–Langmuir equation is expressed as follows:

$$\sigma = \sigma_{blank} - RT/\omega \ln(1 + K_{ads}C) \quad (2.1)$$

where  $\omega$  represents the cross-sectional area of surfactant molecules at the surface,  $T$  is the laboratory temperature,  $\sigma_{blank}$  is the average surface tension of the blank solution, and  $\sigma$  is the minimum surface tension at each concentration  $C$  (in mM) measured (see Appendix 1). Below we present the observations of droplets formed using water and 1 M ammonium sulfate for the  $\alpha$ -pinene oxidation products, and then discuss our findings for the  $\beta$ -caryophyllene oxidation products.

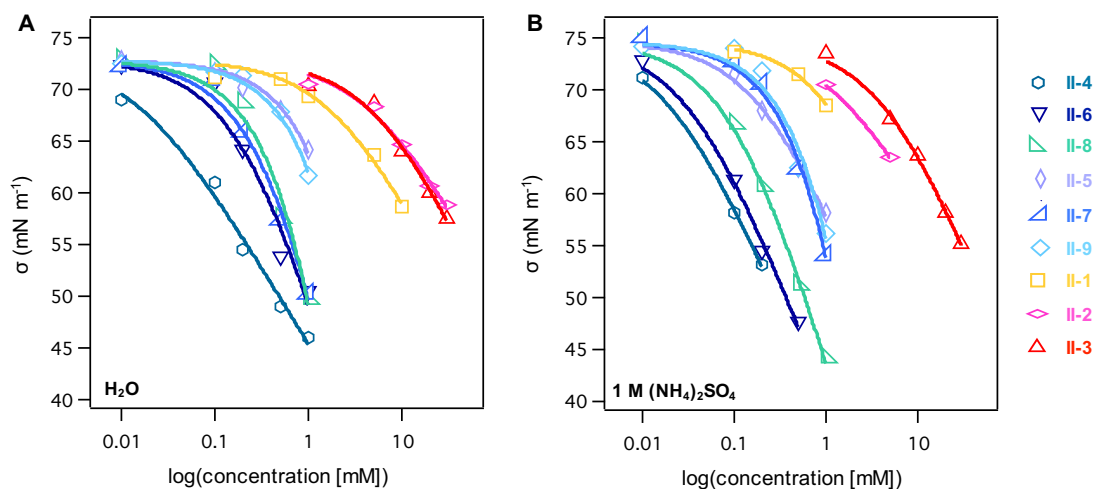


**Figure 2.5.** Comparison of interfacial tension ( $\sigma$ ) as a function of solute concentration and Szyszkowski–Langmuir fitted curves for  $\alpha$ -pinene- and  $\beta$ -caryophyllene-derived oxidation products in (A) water and (B) 1 M ammonium sulfate. [Pinonaldehyde (**II-1**), pinonic acid (**II-2**), pinic acid (**II-3**),  $\beta$ -caryophyllene aldehyde (**II-4**),  $\beta$ -nocaryophyllone aldehyde (**II-5**),  $\beta$ -caryophyllonic acid (**II-6**),  $\beta$ -nocaryophyllonic acid (**II-7**),  $\beta$ -caryophyllinic acid (**II-8**),  $\beta$ -nocaryophyllinic acid (**II-9**)]. All error values range from 0.06 to 0.69  $\text{mN m}^{-1}$ .

The surface tension measurements for the  $\alpha$ -pinene-derived oxidation products in water reveal that pinonaldehyde (**II-1**) is the most surface active of the three compounds measured, reaching a 20% decrease relative to the interfacial tension of water at the highest measured

concentration (10 mM) after 10 minutes (**Figure 2.6**). The surface tension depression caused by pinonaldehyde (**II-1**) at 10 mM in water is comparable to that exhibited by pinonic acid (**II-2**) and pinic acid (**II-3**) present at three times that concentration in water (**Figure 2.5A**). The substantially higher surface tension depression of pinonaldehyde (**II-1**) relative to pinonic acid (**II-2**) and pinic acid (**II-3**) highlights a considerable dependence of surface activity on structural functionality, as pinonic acid (**II-2**) and pinic acid (**II-3**) bear highly polar carboxylic acid moieties while pinonaldehyde (**II-1**) exists as an aldehyde–hydrate mixture with **II-12** in the aqueous droplets measured (**Figure 2.2**).

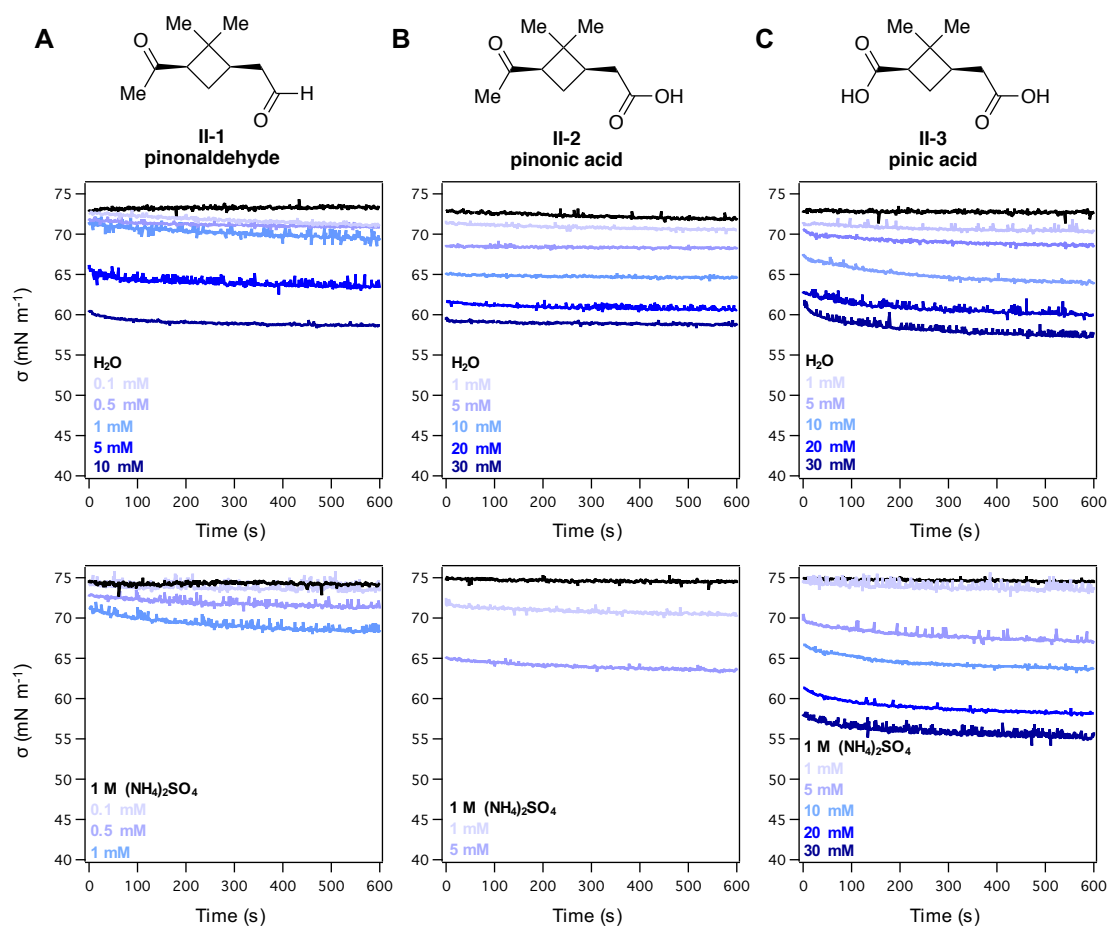


**Figure 2.6.** Dynamic surface tension measurements for (A) pinonaldehyde (**II-1**), (B) pinonic acid (**II-2**), and (C) pinic acid (**II-3**) in water (top) and 1 M ammonium sulfate (bottom). (A) Pinonaldehyde **II-1** was insoluble at concentrations greater than 10 mM in H<sub>2</sub>O. Pinonaldehyde (**II-1**) and pinonic acid (**II-2**) were insoluble at concentrations greater than 1 mM and 5 mM in 1 M ammonium sulfate, respectively.

As reported previously, the surface tension of the droplets is raised by approximately 3% upon addition of 1 M ammonium sulfate in water.<sup>26</sup> The results obtained for the  $\alpha$ -pinene-derived oxidation products in 1 M ammonium sulfate (**Figure 2.5B**) show that pinonaldehyde (**II-1**) and pinonic acid (**II-2**) exhibit enhanced surface activity likely caused by a “salting out” effect in the presence of ammonium sulfate, which increases the solute concentration at the droplet surface due to decreased solubility with the addition of inorganic salt.<sup>26</sup> The influence of “salting out” effects on surface activity of organic species may have a significant influence on the overall

surface tension of atmospheric aerosols, as a substantial portion of the aerosol bulk contains inorganic salts such as  $(\text{NH}_4)_2\text{SO}_4$ .<sup>16, 57-58</sup> For example, 1 mM solutions of pinonaldehyde (**II-1**) and pinonic acid (**II-2**) in 1 M ammonium sulfate each resulted in respective surface tension decreases of 8% and 6% compared to 5% and 2%, respectively, at the same concentration in water after 10 minutes, while a slight decrease in the surface activity of pinic acid (**II-3**) was observed at 1 mM in 1 M ammonium sulfate compared to in water (**Figure 2.6**). Slight enhancement of the surface tension lowering effects was only observed at the higher concentrations measured for pinic acid (**II-3**) in the presence of 1 M ammonium sulfate.

Turning to the  $\beta$ -caryophyllene oxidation products, we reemphasize that surface tension was measured between 0.01 mM and 1 mM due to their low solubility in water at concentrations above 1 mM (**Figure 2.5A**). Of the six  $\beta$ -caryophyllene oxidation products,  $\beta$ -caryophyllene aldehyde (**II-4**) was found to exhibit the highest surface activity in water solutions at all concentrations measured, resulting in an overall 37% decrease at 1 mM compared to the interfacial tension of water (**Figure 2.7**), the greatest surface tension depression we have observed for all oxidation products we have studied to date.<sup>26</sup> Unexpectedly,  $\beta$ -nocaryophyllone aldehyde (**II-5**) exhibited the least surface activity of all six derivatives. This result for nocaryophyllone aldehyde (**II-5**) is potentially attributed to an interdependent decrease in surface activity and increase in solubility, which may be modulated by the existence of a hydrate–aldehyde mixture containing 55% of the hydrate (i.e., **II-14**) in water rather than pure aldehyde content (**Figure 2.2**). The hydrate form of  $\beta$ -nocaryophyllone aldehyde is likely to increase its propensity to hydrogen bond with solvent water molecules within the bulk of the droplet, causing lower surface activity than anticipated. In contrast,  $\beta$ -caryophyllene aldehyde (**II-4**) is substantially more hydrophobic than  $\beta$ -nocaryophyllone aldehyde (**II-5**), due to the presence of

an intact C=C double bond adjacent to the four-membered ring rather than a ketone, and therefore the hydrate form of  $\beta$ -caryophyllene aldehyde (i.e., **II-13**) is unlikely to enhance its bulk aqueous solubility to the same extent. Of the  $\beta$ -caryophyllene oxidation products containing carboxylic acid functional groups, the most polar of the four compounds,  $\beta$ -nocaryophyllinic acid (**9**), is the least surface active, likely due to its higher solubility in water.

In the presence of 1 M ammonium sulfate, all six  $\beta$ -caryophyllene oxidation products exhibited “salting out” effects (**Figure 2.8**),<sup>26</sup> which were most pronounced for the oxidation products that retain the exocyclic C=C double bond of  $\beta$ -caryophyllene compared to those bearing a ketone at that same position. For example, the two monoacid  $\beta$ -caryophyllene oxidation products,  $\beta$ -caryophyllonic acid (**II-6**) and  $\beta$ -nocaryophyllonic acid (**II-7**) exhibited comparable surface activity at 1 mM in water; however, upon addition of 1 M ammonium sulfate, “salting out” effects were much more pronounced for  $\beta$ -caryophyllonic acid (**II-6**) than for  $\beta$ -nocaryophyllonic acid (**II-7**).

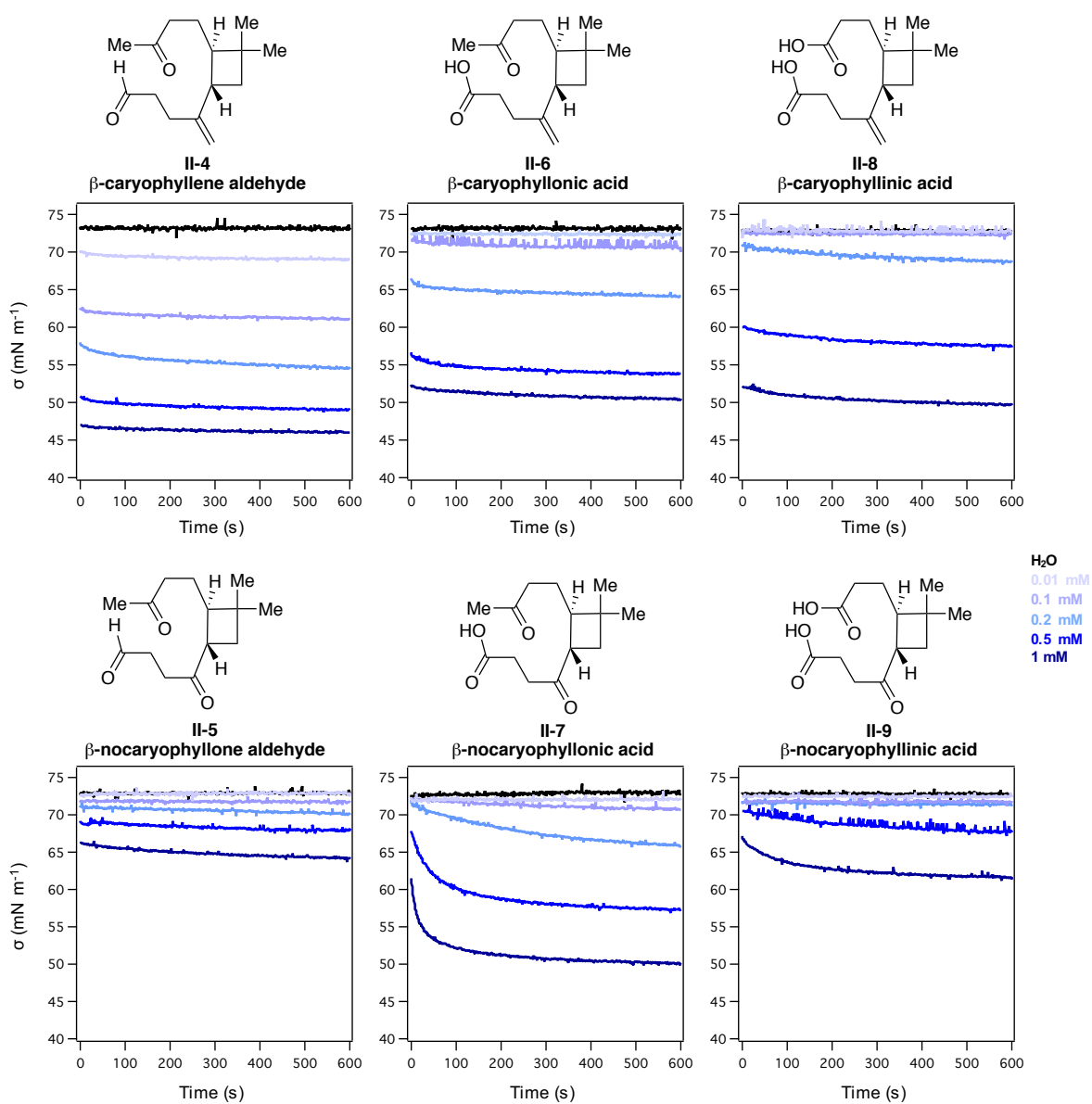


**Figure 2.7.** Dynamic surface tension measurements for  $\beta$ -caryophyllene oxidation products (II-4–II-9) in water.

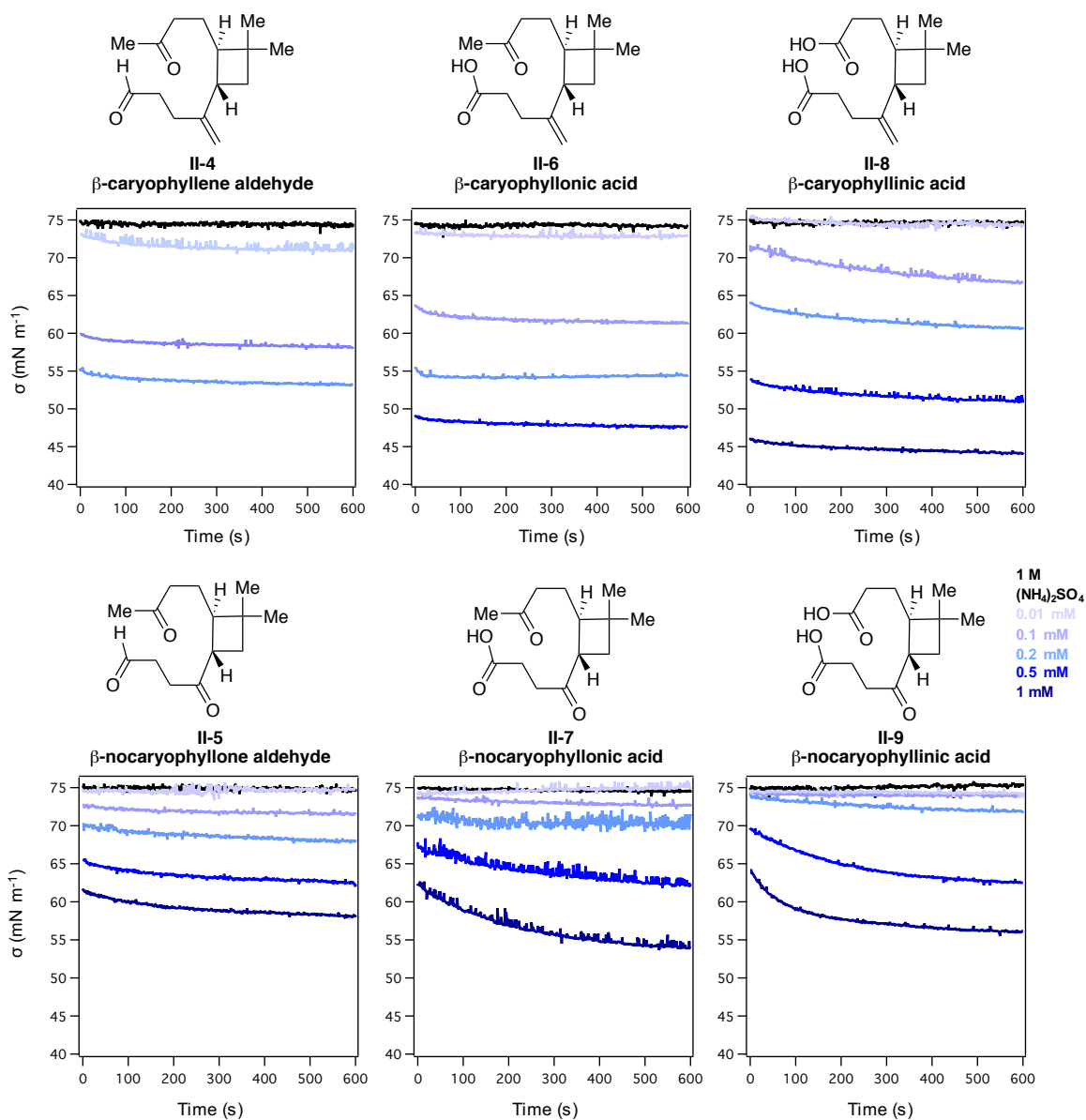


**Figure 2.8.** Dynamic surface tension measurements for  $\beta$ -caryophyllene oxidation products (II-4–II-9) in 1 M ammonium sulfate solution.

Comparing the surface activity of all compounds studied at 1 mM concentration, **Figure 2.9** highlights that the  $\beta$ -caryophyllene oxidation products are significantly more surface active than the measured  $\alpha$ -pinene-derived oxidation products. The stark difference emphasizes that the surface depression behavior exhibited by the monoterpene ( $\text{C}_{10}$ ) and sesquiterpene ( $\text{C}_{15}$ ) ozone-mediated oxidation products studied here depends on carbon chain length and degree of

oxidation. Yet, even the two least surface active compounds studied here, pinonic acid (**II-2**) and pinic acid (**II-3**), still exhibit larger surface tension depression than  $\alpha$ -IEPOX, the most surface active of the IEPOX and tetraol oxidation products derived from isoprene.<sup>26</sup>

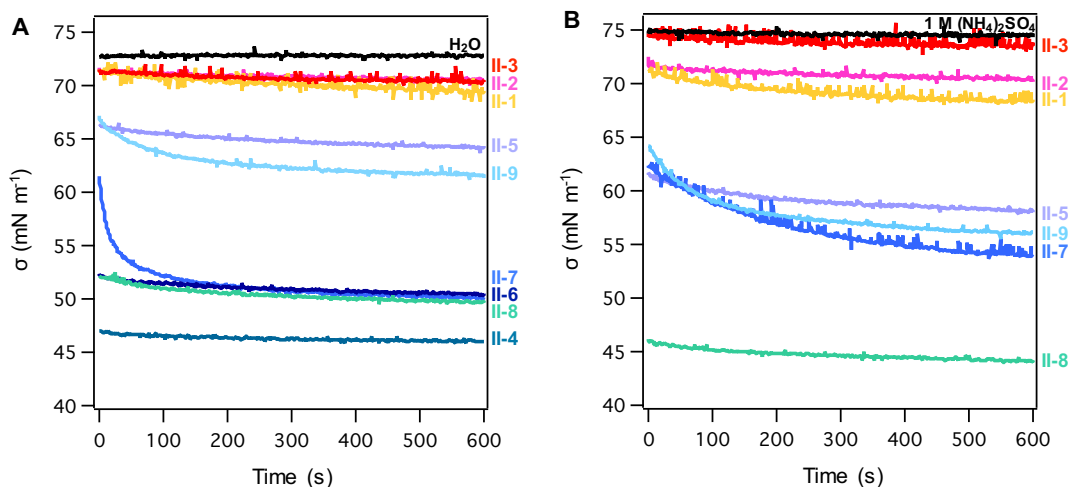


**Figure 2.9.** Dynamic surface tension measurements comparing 1 mM solutions in (A) water and (B) 1 M ammonium sulfate for all compounds in this study. Note:  $\beta$ -Caryophyllene aldehyde (**II-4**) and  $\beta$ -caryophyllonic acid (**II-6**) were insoluble at 1 mM in 1 M ammonium sulfate and therefore are not shown.

**2.4.3. Kinetics of interfacial tension and equilibration timescales.** The values of dynamic surface tension  $\sigma(t)$  are time dependent, and estimations of the kinetics of interfacial tension and equilibration timescales were performed by Dr. Pengfei Liu, a graduate of the laboratory of Prof. Scot Martin at Harvard University. Curves of  $\sigma(t)$  presented in **Figure 2.5** can be typically divided into three kinetic regions: (I) rapid fall region where  $\sigma$  rapidly decreases from the value of pure water ( $72.8 \text{ mN m}^{-1}$ ) to  $\sigma_0$  within the initial time step of the measurement; (II) meso-equilibrium region, in which  $\sigma(t)$  slowly decreases with a characteristic timescale of  $t_m$ ; and (III) equilibrium region where the minimum value  $\sigma_m$  is reached. The time-dependent curve can be described by the following equation.<sup>27, 59</sup>

$$\sigma(t) = \sigma_m + \frac{\sigma_0 - \sigma_m}{1 + \left(\frac{t}{t_m}\right)^n} \quad (2.2)$$

where  $\sigma_0$ ,  $\sigma_m$ ,  $t_m$  and  $n$  are fitting parameters. The optimized values of these parameters are listed in Appendix 1 (**Table A1.1**) for the obtained  $\sigma(t)$  dataset.

For most of the compounds studied, a significant depression in surface tension was achieved in the rapid fall region, as indicated by the lower values of  $\sigma_0$  than that of pure water (**Table A1.1**). This surface tension depression can be treated as instantaneous in any aerosol and cloud process in the atmosphere. Further decrease of  $\sigma(t)$  occurred in the meso-equilibrium region, with a characteristic time  $t_m$  of equilibration that ranged from 10 to 1000 s (**Table A1.1**). At  $t_m$ ,  $\sigma(t_m) = (\sigma_0 + \sigma_m) / 2$ , meaning that equilibration was not yet reached. The final equilibration time was about twice of  $t_m$  ( $t_{eq} = 2 \times t_m$ ).<sup>27</sup> Note that these timescales were measured for aqueous pendant droplets with diameters of 1.9–2.1 mm in the PDT laboratory experiments. These droplets were therefore much larger than typically sized aerosol and cloud droplets in the atmosphere. To estimate the surface tension effect for cloud activation, we calculated the equilibration timescale for a 1  $\mu\text{m}$  droplet using the following equation:

$$t_{\text{eq}_1 \mu\text{m}} = 2 \times t_{\text{m\_lab}} \times \left( \frac{1 \mu\text{m}}{D_{\text{drop}}} \right)^2 \quad (2.3)$$

where  $D_{\text{drop}}$  represents the average diameter of droplets used in the laboratory experiments (**Table A1.1**). The droplet diameter of 1  $\mu\text{m}$  is a typical size of activated aerosol particles. As reference, a particle with a 200 nm dry diameter has an activation diameter of 1.07  $\mu\text{m}$ , assuming a hygroscopic parameter  $\kappa$  of 0.1 and a surface tension equal to that of pure water. The calculated equilibration timescales for 1  $\mu\text{m}$  droplets were on the order of  $10^{-5}$  to  $10^{-4}$  s (**Table A1.1**). These results indicate that the surface tension depression observed in the laboratory experiments can occur instantaneously in the cloud activation processes in both online instruments and in the

atmosphere, given that the surfactant concentrations are similar to those measured in the laboratory.

Nozière and coworkers suggested that the equilibration timescale can steeply increase with a decreasing surfactant concentration.<sup>27</sup> Ambient particles having a low concentration of strong surfactant might exhibit delayed equilibrium. In the present study, we do not intend to extrapolate the results to a lower concentration because this extrapolation may have a large uncertainty.

**2.4.4. Calculation of cloud activation potential.** Cloud droplet formation via water vapor condensation onto SOA particles is known to be heavily influenced by concentration-dependent surface tension depression effects caused by surface-active species, which can reduce the critical supersaturation at the moment of cloud droplet activation.<sup>11</sup> As described in our previous study<sup>26</sup> and by the McNeill laboratory,<sup>11, 57</sup> the critical supersaturation ratio ( $s_c^*/s_c$ ) for cloud activation can be determined using Köhler theory<sup>11-12</sup> from the equilibrium surface tension of a given solute concentration in water ( $\sigma$ ) and the surface tension of water ( $\sigma_w$ ) (72.8 mN m<sup>-1</sup>),<sup>60</sup> and is expressed as follows:

$$(s_c^*/s_c) = (\sigma/\sigma_w)^{3/2} \quad (2.4)$$

Equation 2.4 assumes that the effect of surface-active organic species on equilibrium CCN activity is purely surface tension if the bulk solute concentration remains constant.<sup>57</sup> We note, however, that the critical supersaturation ratio calculated by Equation 2.4 neglects the effect of surfactant partitioning on the Raoult effect,<sup>15, 61</sup> which may potentially increase the critical supersaturation ratio for small particles by reducing the bulk solute concentration and therefore partially counteract the effect of surface tension depression. However, as noted by Sareen and coworkers previously, under heterogeneous SOA formation conditions the bulk solute

composition of the particle is expected to be dominated by salt, and this solute content is expected to remain constant if gas-phase species are continuously taken up at the aerosol surface as they partition to the particle phase.<sup>57</sup> Therefore, we make the assumption that the effect of organic species on equilibrium CCN activity is purely surface tension based in the present study. From the equilibrium surface tension (calculated as the average of the final 20 values of 3–5 10 min acquisitions) (**Tables A1.2** and **A1.3**),  $s_c^*/s_c$  was calculated at all concentrations measured for each compound in both water and 1 M ammonium sulfate (**Tables 2.1** and **2.2**). The equilibrium results were reported herein because such equilibrium can be reached instantaneously in a typically sized particle at activation point (see above). The concentrations of 0.01 to 30 mM are relevant to the total surfactant concentrations in ambient conditions.<sup>62</sup> As an estimate, a particle comprised of 20% to 100% mass fraction of secondary organic material has a total organic concentration of 1–10 M at dry condition. The hygroscopic growth of a particle from dry to cloud activation corresponds to a volume dilution factor of 20 to 1000. The activated particle thus has a total organic concentration of 1 to 500 mM, and the concentration of an individual compound can be much lower. Even so, the studied individual compounds can serve as representatives of a broad spectrum of monomeric carboxylic acids and aldehydes produced from the ozonolysis of  $\alpha$ -pinene and  $\beta$ -caryophyllene precursors, and the total concentrations can be sufficiently high, thus having a significant effect on cloud activation. Similar calculations indicate that a typically sized ammonium sulfate particle (30–500 nm dry diameter) has an ammonium sulfate concentration of 1 to 100 mM. The effect of adding 1 M ammonium sulfate observed in the present study can thus serve as an upper limit estimate for the presence of salts in organic particles.

We previously reported  $s_c^*/s_c$  of 0.90 (10% decrease) for 10 mM *trans*- $\beta$ -IEPOX in water.<sup>26</sup> As shown in **Table 2.1**, a comparable  $s_c^*/s_c$  value of 0.93 was calculated for pinonaldehyde (**II-1**) in water at 1 mM. Additionally, **Table 2.2** shows a similar  $s_c^*/s_c$  value of 0.92 for  $\beta$ -caryophyllene aldehyde (**II-4**) at a concentration of 0.01 mM in water, which is 1000 times lower than the concentration producing a comparable supersaturation ratio (10 mM) for *trans*- $\beta$ -IEPOX in water.<sup>26</sup> Of all the oxidation products we have studied to date,  $\beta$ -caryophyllene aldehyde (**II-4**) was shown to decrease  $s_c^*/s_c$  by the largest extent (50% in water), highlighting the highly amphiphilic and surfactant-like nature of this compound as well as the other monomeric sesquiterpene oxidation products studied relative to monomeric oxidation products derived from  $\alpha$ -pinene and isoprene.

**Table 2.1.** Supersaturation ratios ( $s_c^*/s_c$ ) for  $\alpha$ -pinene-derived oxidation products at 0–30 mM in water and 1 M ammonium sulfate (values in parentheses). Asterisk (\*) notes that value was not obtained due to insolubility at the indicated concentration. Note pinonaldehyde (**II-1**) exists in equilibrium with its hydrate form as described in the text.

Conc. (mM)	pinonaldehyde II-1	pinonic acid II-2	pinic acid II-3
0	1.010±0.003 (1.028±0.003)	0.982±0.002 (1.036±0.002)	0.997±0.006 (1.036±0.002)
1	0.931±0.007 (0.914±0.007)	0.954±0.002 (0.951±0.003)	0.949±0.002 (1.015±0.006)
5	0.817±0.006 (N/A*)	0.908±0.002 (0.814±0.002)	0.915±0.003 (0.886±0.006)
10	0.723±0.002 (N/A*)	0.836±0.002 (N/A*)	0.824±0.003 (0.819±0.002)
20	N/A* (N/A*)	0.761±0.003 (N/A*)	0.749±0.002 (0.714±0.002)
30	N/A* (N/A*)	0.726±0.004 (N/A*)	0.701±0.005 (0.660±0.005)

**Table 2.2.** Supersaturation ratios ( $s_c^*/s_c$ ) for  $\beta$ -caryophyllene-derived oxidation products at 0–1 mM in water and 1 M ammonium sulfate (values in parentheses). Asterisk (\*) notes that value was not obtained due to insolubility at the indicated concentration. Note aldehyde compounds **II-4** and **II-5** exist in equilibrium with hydrate forms as described in the text.

Conc. (mM)	$\beta$ -caryophyllene aldehyde II-4	$\beta$ -nocaryophyllone aldehyde II-5	$\beta$ -caryophyllonic acid II-6	$\beta$ -nocaryophyllonic acid II-7	$\beta$ -caryophyllinic acid II-8	$\beta$ -nocaryophyllinic acid II-9
0	1.007±0.004 (1.032±0.005)	1.002±0.003 (1.041±0.004)	1.006±0.008 (1.028±0.003)	1.004±0.004 (1.036±0.002)	1.000±0.004 (1.038±0.003)	0.999±0.002 (1.052±0.004)
0.01	0.923±0.002 (0.966±0.007)	1.001±0.004 (1.041±0.002)	0.990±0.002 (1.001±0.002)	0.986±0.002 (1.045±0.006)	0.999±0.003 (1.032±0.003)	0.993±0.003 (1.029±0.005)
0.1	0.768±0.002 (0.714±0.001)	0.978±0.002 (0.974±0.003)	0.957±0.008 (0.774±0.002)	0.958±0.002 (0.998±0.002)	0.990±0.003 (0.877±0.002)	0.977±0.003 (1.024±0.003)
0.2	0.649±0.001 (0.624±0.001)	0.946±0.003 (0.902±0.003)	0.827±0.002 (0.647±0.001)	0.861±0.003 (0.953±0.014)	0.917±0.002 (0.761±0.002)	0.972±0.003 (0.981±0.002)
0.5	0.553±0.001 (N/A*)	0.902±0.003 (0.795±0.003)	0.636±0.001 (0.529±0.001)	0.699±0.002 (0.792±0.007)	0.702±0.002 (0.589±0.006)	0.900±0.008 (0.797±0.003)
1	0.502±0.001 (N/A*)	0.828±0.003 (0.713±0.002)	0.577±0.001 (N/A*)	0.571±0.001 (0.640±0.005)	0.564±0.002 (0.472±0.001)	0.778±0.002 (0.676±0.002)

**2.4.5. Atmospheric implications.** As discussed in Chapter 1, according to the 2013 Intergovernmental Panel on Climate Change Report,<sup>6</sup> atmospheric aerosol–cloud interactions remain among the least understood of processes within the climate system. Investigation of sesquiterpenes in the context of SOA–cloud interactions have been particularly rare, in part due to experimental shortcomings related to measuring SOA cloud activation properties coupled with the characteristic complexity and sparse level of chemical understanding regarding sesquiterpenes and their oxidation products compared to other SOA precursors. Comparison of CCN activity of sesquiterpene- and monoterpene-derived SOA samples using cloud condensation nuclei counters (CCNC) has demonstrated that CCN activity of SOA from  $\beta$ -caryophyllene and other sesquiterpenes is lower than that of monoterpene SOA as quantified by CCNC detection.<sup>60, 63-64</sup> However, CCN activity of  $\beta$ -caryophyllene SOA, for example, was reported to be greater when measured using a static diffusion (SD) CCNC than when measured with a continuous flow (CF) CCNC, highlighting a possibility for measurement variability by

CCNC detection.<sup>63, 65</sup> Additionally,  $\beta$ -caryophyllene contributions to secondary organic CCN were revisited by Asa-Awuku and coworkers in 2012,<sup>66</sup> who measured higher CCN activity and hygroscopicity than reported previously and concluded that  $\beta$ -caryophyllene-derived SOA formed in the presence of ozone may be a potentially important source of biogenic CCN.<sup>63-64, 66</sup> CCN activity experiments performed using cloud condensation nuclei counters (CCNC) and related hygroscopicity tandem differential mobility analyzers (HTDMA) indirectly quantify CCN activity by measuring population or growth of nucleated droplets rather than Raoult's term and surface tension, which are key parameters related to cloud activation outlined by Köhler theory.<sup>11-12, 27</sup> Additionally, HTDMA and CCNC instruments typically collect measurements in a time regime on the order of seconds to minutes. In their 2014 publication, Nozière and coworkers suggested that bulk-to-surface partitioning of low concentration surface-active organic compounds may reach equilibrium beyond timescales detectable by these instruments.<sup>27</sup> The experimental results and calculations in the present study, however, suggest that such a delayed equilibrium might be less important for abundant oxidation products at conditions relevant to cloud activation. Nevertheless, Nozière and coworkers highlighted the importance of using bulk surface tension studies of SOA samples as an alternative approach to CCNC and HTDMA experiments to gain a more comprehensive understanding of the role of surface-active organic species in SOA particle CCN activity.<sup>27</sup> Our findings improve upon the growing insight obtained from surface tension studies related to atmospheric aerosol by providing molecule-specific insight into the aqueous surface tension depression induced by pure standards of oxidation products relevant to terpene-derived SOA material.

Oxidation of  $\alpha$ -pinene and  $\beta$ -caryophyllene in the atmosphere generates a plethora of products of different molecular weight and containing diverse sets of functional groups that

impact their surface activities. In order to deconvolute the complexity associated with analyzing this mixture, we focused on several abundant monomeric acid- and aldehyde-containing ozonolysis products. As shown in **Figure A1.1** (Appendix 1), molecular properties such as the surface area per molecule adsorbed at the air/water interface of the pendant drop correlate seemingly well with the free energy of adsorption, at least for the  $\beta$ -caryophyllene oxidation product series examined here. Moreover, our analysis indicates that for the  $\beta$ -caryophyllene oxidation products, free energies of adsorption larger than  $\sim 25$  kJ/mol (just one hydrogen bond equivalent) coincide with considerable reductions in supersaturation ratios, depending on ammonium sulfate and oxidation product concentration in solution.

We expect that molecular-level measurements such as the ones presented here could be useful for developing structure–function relationships across atmospheric organic species. Moreover, these measurements could serve as benchmarks for future studies involving recently developed complementary surface tension measurements in more atmospherically transferrable droplet-size regimes<sup>67-68</sup> as well as other surface-specific climate-relevant aerosol techniques.<sup>69-71</sup> Ultimately, given the inherent complexity of studying the surface tension of SOA-related systems in the context of cloud droplet condensation, we take the specific approach of cataloging the relative surface tension depression exhibited by individual  $\alpha$ -pinene and  $\beta$ -caryophyllene oxidation products in order to gain chemical insight into the correlation between surface activity and molecular structure and reactivity. Among the series of compounds studied,  $\beta$ -caryophyllene aldehyde (**II-4**) shows significant cloud activation potentials indicating that it might play a substantial role in the atmosphere. Our investigations also reveal that aqueous solutions of terpene oxidation products containing aldehyde functional groups exist in equilibrium with hydrated forms, which may modulate their bulk solubility and surface activity. Overall, our

findings highlight substantial differences in surface tension to consider for this given series of monomeric terpene-derived ozonolysis products, and the data obtained in this study should prove valuable for future comparison to laboratory and field CCN studies.

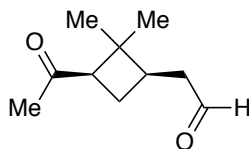
**2.5. Conclusions.** In summary, Chapter 2 presents dynamic surface tension measurements of synthetically prepared homogeneous oxidation products derived from  $\alpha$ -pinene and  $\beta$ -caryophyllene and provides calculated equilibration timescales and supersaturation ratios of relevance to predicting CCN activity. Equilibration timescales calculated for a 1  $\mu\text{m}$  aerosol particle provide an estimate of the surface tension depression effect on cloud activation for typically sized atmospheric particles. The results of these experiments also demonstrate that the oxidation products derived from  $\beta$ -caryophyllene exhibit significantly greater surface tension depression behavior, and, consequently, cloud activation potentials, than those prepared from  $\alpha$ -pinene.  $\beta$ -Caryophyllene aldehyde (**II-4**) was found to be the most surface active of all compounds we have studied to date, with a calculated supersaturation ratio of 50% at 1 mM concentration, and 8% at 10  $\mu\text{M}$  concentration. We also revealed that hydrate formation from oxidation products containing aldehydes was rapid, leading to approximately equal mixtures of the aldehyde and hydrate forms within aqueous solutions of the compounds investigated. Our findings provide specific molecular-level understanding of the relative surface tension effects exhibited by  $\alpha$ -pinene and  $\beta$ -caryophyllene oxidation products towards investigating their role as surface-active organic compounds in SOA–cloud interactions. Given the notable surface activities observed for the  $\beta$ -caryophyllene oxidation products, we expand upon this work in Chapters 3 and 4 by probing this molecular suite at various atmospherically relevant interfaces using surface-selective nonlinear spectroscopy.

## 2.6. Experimental procedures.

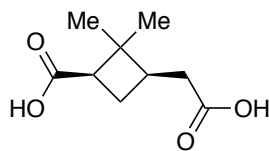
### 2.6.1. General methods.

All reactions were carried out under nitrogen atmosphere in flame-dried glassware unless otherwise stated. Anhydrous solvents (DCM, methanol, THF, Et<sub>2</sub>O) were purified by passage through a bed of activated alumina.<sup>1</sup> Reagents were purified prior to use unless otherwise stated following the guidelines of Armarego and Chai.<sup>2</sup> Purification of reaction products was carried out by flash chromatography using SiliCycle silica gel F60, 40-63 μm (230-400 mesh). Analytical thin-layer chromatography (TLC) was performed using Merck Silica Gel 60 Å F-254 precoated plates (0.25 mm thickness) or EM Reagent 0.25mm silica gel 60-F plates. Visualization was accomplished with p-anisaldehyde stain. <sup>1</sup>H-NMR spectra were recorded on a Varian Inova 500 (500 MHz), Agilent DD2 (500MHz), Agilent DD MR-400 (400MHz), or Bruker Advance III 500 (500 MHz) spectrometer and are reported in ppm using solvent as an internal standard (CDCl<sub>3</sub> at 7.26 ppm). Data are reported as (app = apparent, obs = obscured, s = singlet, d = doublet, t = triplet, q = quartet, p = pentet, h = hextet, sep = septet, o = octet, m = multiplet, b = broad; integration; coupling constant(s) in Hz. <sup>13</sup>C-NMR spectra were recorded on a Bruker Advance III 500 spectrometer equipped with DCH CryoProbe, and are reported in ppm using solvent as an internal standard (CDCl<sub>3</sub> at 77.16 ppm, except where noted). Optical rotation was determined using a Rudolph Research Analytical Autopol IV, Series #82239 with either a 10 cm or 5 cm pathlength cell at the sodium D line. High resolution mass spectra were collected on a Thermo Q-Exactive orbitrap mass spectrometer in ESI mode. Diamond ATR infrared spectra were obtained on a ThermoNicolet iS10 FT-IR spectrometer. Germanium ATR infrared spectra were recorded using a Bruker Tensor 37.

### 2.6.2. Synthesis of $\alpha$ -pinene and $\beta$ -caryophyllene oxidation products.

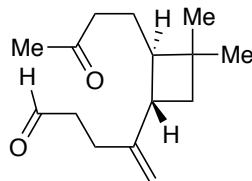


**2-((1*R*,3*R*)-3-Acetyl-2,2-dimethylcyclobutyl)acetaldehyde (II-1):** Ozone (generated at 110 V) was bubbled through a solution of (–)- $\alpha$ -pinene (10.0 g, 73.4 mmol) in dichloromethane (250 mL) at  $-78$  °C for 35 minutes. At this time,  $O_2$  was bubbled through solution for an additional 20 minutes. After addition of dimethyl sulfide (60 mL, 832 mmol), mixture was then allowed to warm to room temperature and stirred for an additional 16 hours. The mixture was then diluted with  $H_2O$  (100 mL) and transferred to a separatory funnel. The resulting mixture was extracted with  $CH_2Cl_2$  (3 x 100 mL) and washed with brine (100 mL). The combined organics were dried using  $MgSO_4$  and solvent concentrated under reduced pressure to afford the crude product as a light yellow oil. Flash column chromatography on silica gel using 10% to 30% EtOAc in hexanes as the eluent afforded the title compound (8.3 g, 49.3 mmol, 67% yield) as a clear oil. A small amount of material (1.19 g, 7.07 mmol) was further purified by distillation (80 to 120 °C) under reduced pressure to obtain higher purity samples for analytical measurements: IR (neat) 2954, 2826, 2724, 1720, 1701, 1369, 1181  $cm^{-1}$ ;  $^1H$  NMR (500 MHz,  $CDCl_3$ )  $\delta$  9.74 (s, 1H), 2.92 (dd,  $J = 10.0, 7.7$  Hz, 1H), 2.53 – 2.37 (m, 3H), 2.04 (s, 3H), 2.02 – 1.90 (m, 2H), 1.34 (s, 3H), 0.84 (s, 3H);  $^{13}C$  NMR (125 MHz,  $CDCl_3$ )  $\delta$  207.5, 201.5, 54.5, 45.3, 43.4, 35.9, 30.5, 30.3, 22.9, 17.8; HRMS (ESI): Exact mass calcd for  $C_{10}H_{16}O_2 [M+H]^+$ , 169.1229. Found 169.1223.

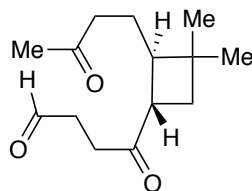


**(1'*R*,3'*R*)-2-(3'-Carboxy-2',2'-dimethylcyclobutyl)acetic acid (II-3):** Ozone (generated at 110 V) was bubbled through a solution of (-)-myrtenal (2.1 g, 14.0 mmol) in dichloromethane (125 mL) at  $-78\text{ }^{\circ}\text{C}$  for 30 minutes. At this time,  $\text{O}_2$  was bubbled through solution for an additional 20 minutes. The resulting reaction mixture was then allowed to warm to room temperature and solvent concentrated under reduced pressure. After diluting with EtOH (100 mL),  $\text{AgNO}_3$  (2.7 g, 15.9 mmol) added and mixture was allowed to stir at room temperature until  $\text{AgNO}_3$  was dissolved. At this time, aqueous NaOH solution (4.6 M, 15 mL) was added dropwise and mixture was then allowed to stir at room temperature for an additional 16 hours. The reaction mixture was then vacuum filtered, rinsing with EtOH (25 mL), and filtrate concentrated under reduced pressure. Resulting residue was then diluted with EtOAc (100 mL) and 2 M HCl (100 mL) and transferred to a separatory funnel. The mixture was extracted with EtOAc (3 x 100 mL) and dried over  $\text{MgSO}_4$ . Subsequent concentration under reduced pressure afforded the crude product as a light yellow oil. Flash column chromatography on silica gel using 50% EtOAc in hexanes as the eluent afforded the title compound (2.50 g, 13.4 mmol, 96% yield). A small amount of material (90 mg, 0.48 mmol) was further purified via flash column chromatography on silica gel with 5% MeOH in  $\text{CH}_2\text{Cl}_2$  as the eluent to obtain higher purity samples for analytical measurements: IR (neat) 3384-2537, 2962, 1719, 1689, 1407, 1246, 906  $\text{cm}^{-1}$ ;  $^1\text{H}$  NMR (500 MHz,  $\text{CD}_3\text{OD}$ )  $\delta$  2.75 (dd,  $J = 10.4, 7.8$  Hz, 1H), 2.41 – 2.31 (m, 2H), 2.31 – 2.21 (m, 1H), 2.11 – 2.02 (m, 1H), 1.91 – 1.83 (m, 1H), 1.23 (s, 3H), 0.98 (s, 3H);  $^{13}\text{C}$  NMR (125 MHz,  $\text{CD}_3\text{OD}$ )  $\delta$

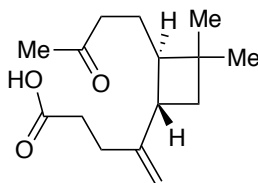
176.6, 176.5, 47.3, 43.4, 39.6, 36.2, 30.3, 25.6, 17.9; HRMS (ESI): Exact mass calcd for  $C_9H_{14}O_4 [M+Na]^+$ , 209.0790. Found 209.0786.



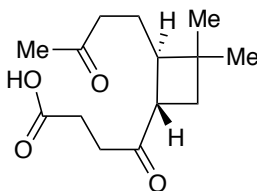
**4-((1*S*,2*R*)-3,3-Dimethyl-2-(3-oxobutyl)cyclobutyl)pent-4-enal (II-4):** Ozone (generated at 70 V) was bubbled through a solution of  $\beta$ -caryophyllene (3.0 g, 14.7 mmol) in dichloromethane (250 mL) at -78 °C for 10 minutes. At this time,  $O_2$  was bubbled through solution for an additional 20 minutes. After addition of dimethyl sulfide (18 mL, 250 mmol), mixture was then allowed to warm to room temperature and stirred for an additional 16 hours. The mixture was then diluted with  $H_2O$  (100 mL) and transferred to a separatory funnel. The resulting mixture was extracted with  $CH_2Cl_2$  (3 x 100 mL) and washed with brine (100 mL). The combined organics were dried using  $MgSO_4$  and solvent concentrated under reduced pressure to afford the crude product as a light yellow oil. Flash column chromatography on silica gel using 10% EtOAc in hexanes as the eluent afforded the title compound (422 mg, 1.8 mmol, 12% yield) as a clear oil: IR (neat) 3082, 2950, 2863, 2721, 1714, 1643, 1364, 889  $cm^{-1}$ ;  $^1H$  NMR (500 MHz,  $CDCl_3$ )  $\delta$  9.77 (s, 1H), 4.80 – 4.76 (m, 1H), 4.68 (d,  $J = 1.7$  Hz, 1H), 2.56 (td,  $J = 7.8, 7.4, 1.7$  Hz, 2H), 2.45 – 2.27 (m, 5H), 2.11 (s, 3H), 1.88 (dt,  $J = 9.6, 7.6$  Hz, 1H), 1.81 (dd,  $J = 10.4, 8.5$  Hz, 1H), 1.67 – 1.60 (m, 2H), 1.44 (t,  $J = 10.2$  Hz, 1H), 1.05 (s, 3H), 1.04 (s, 3H);  $^{13}C$  NMR (125 MHz,  $CDCl_3$ )  $\delta$  208.9, 202.3, 150.8, 107.7, 47.9, 42.1, 42.0, 41.8, 39.9, 33.8, 31.2, 30.1, 26.7, 24.7, 22.5. HRMS (ESI): Exact mass calcd for  $C_{15}H_{24}O_2 [M+H]^+$ , 237.1855. Found 237.1851.



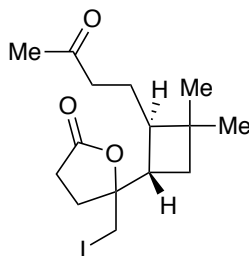
**4-[(1*S*,2*R*)-3,3-Dimethyl-2-(3-oxidanylidenebutyl)cyclobutyl]-4-oxidanylidene-butanal (II-5):** Ozone (generated at 110 V) was bubbled through a solution of  $\beta$ -caryophyllene (6.3 g, 24.5 mmol) in methanol (85 mL) at -78 °C for 30 minutes. At this time, O<sub>2</sub> was bubbled through solution for an additional 20 minutes. After addition of dimethyl sulfide (26.3 g, 31 mL, 0.423 mol), mixture was then allowed to warm to room temperature and stirred for an additional 16 hours. The mixture was then diluted with H<sub>2</sub>O (100 mL) and transferred to a separatory funnel. The resulting mixture was extracted with CH<sub>2</sub>Cl<sub>2</sub> (3 x 100 mL) and washed with brine (100 mL). The combined organics were dried using MgSO<sub>4</sub> and solvent concentrated under reduced pressure to afford the crude product as a light yellow oil. Flash column chromatography on silica gel using 20% EtOAc in hexanes as the eluent afforded the title compound (2.8 g, 11.7 mmol, 48% yield) as a clear oil. A small amount of material (0.763 g, 3.20 mmol) was further purified by flash column chromatography on silica gel using 10% to 30% EtOAc in hexanes as the eluent to obtain higher purity samples for analytical measurements: IR (neat) 2951, 2865, 2727, 1703, 1363, 1165, 1113 cm<sup>-1</sup>; <sup>1</sup>H NMR (500 MHz, CDCl<sub>3</sub>)  $\delta$  9.80 (s, 1H), 2.89 – 2.58 (m, 5H), 2.42 – 2.30 (m, 2H), 2.17 – 2.12 (m, 1H), 2.11 (s, 3H), 1.88 (ddd,  $J$  = 10.7, 9.0, 0.8 Hz, 1H), 1.74 (t,  $J$  = 10.2 Hz, 1H), 1.70 – 1.56 (m, 2H), 1.06 (s, 3H), 1.04 (s, 3H); <sup>13</sup>C NMR (125 MHz, CDCl<sub>3</sub>)  $\delta$  210.0, 208.9, 200.6, 46.9, 46.0, 41.7, 37.5, 36.9, 34.1, 32.9, 30.2, 30.1, 23.9, 22.6; HRMS (ESI): Exact mass calcd for C<sub>14</sub>H<sub>22</sub>O<sub>3</sub> [M+H]<sup>+</sup>, 239.1647. Found 239.1644.



**4-((1S,2R)-3,3-Dimethyl-2-(3-oxobutyl)cyclobutyl)pent-4-enoic acid (II-6):** Ozone (generated at 70 V) was bubbled through a solution of  $\beta$ -caryophyllene (3.0 g, 14.7 mmol) in dichloromethane (250 mL) at  $-78\text{ }^{\circ}\text{C}$  for 10 minutes. At this time,  $\text{O}_2$  was bubbled through solution for an additional 20 minutes. Resulting reaction mixture was then allowed to warm to room temperature and solvent concentrated under reduced pressure. After diluting with EtOH (200 mL),  $\text{AgNO}_3$  (3.0 g, 17.6 mmol) added and mixture was allowed to stir at room temperature until  $\text{AgNO}_3$  was dissolved. At this time, aqueous NaOH solution (4.6 M, 17 mL) was added dropwise and mixture was then allowed to stir at room temperature for an additional 16 hours. The reaction mixture was then vacuum filtered, rinsing with EtOH (50 mL), and filtrate concentrated under reduced pressure. The resulting residue was then diluted with EtOAc (150 mL) and 1 M HCl (150 mL) and transferred to a separatory funnel. The mixture was extracted with EtOAc (3 x 100 mL) and dried over  $\text{MgSO}_4$ . Subsequent concentration under reduced pressure afforded the crude product as a viscous yellow oil. Flash column chromatography on silica gel using 20% EtOAc in hexanes as the eluent afforded the title compound (1.9 g, 7.5 mmol, 51% yield): IR (neat) 3100-2665, 3081, 2950, 1707, 1643, 1382, 1161, 887  $\text{cm}^{-1}$ ;  $^1\text{H}$  NMR (500 MHz,  $\text{CDCl}_3$ )  $\delta$  4.78 (s, 1H), 4.71 (s, 1H), 2.52 – 2.47 (m, 2H), 2.41 – 2.27 (m, 5H), 2.11 (s, 3H), 1.88 (dt,  $J = 9.6, 7.7$  Hz, 1H), 1.81 (dd,  $J = 2.0, 1.5, 1.3$  Hz, 1H), 1.69 – 1.59 (m, 2H), 1.45 (t,  $J = 10.2$  Hz, 1H), 1.05 (s, 3H), 1.04 (s, 3H);  $^{13}\text{C}$  NMR (125 MHz,  $\text{CDCl}_3$ )  $\delta$  209.1, 178.8, 150.7, 107.5, 47.9, 42.1, 41.8, 39.8, 33.8, 32.5, 31.2, 30.0, 29.1, 24.7, 22.5; HRMS (ESI): Exact mass calcd for  $\text{C}_{15}\text{H}_{24}\text{O}_3$   $[\text{M}+\text{Na}]^+$ , 275.1623. Found 275.1626.



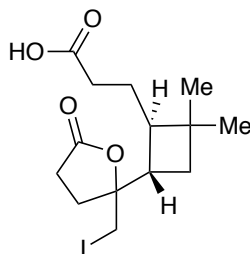
**4-Oxo-4-[(1S)-3,3-dimethyl-2t-(3-oxo-butyl)-cyclobutyl-(r)]-butyric acid (II-7):** Ozone (generated at 110 V) was bubbled through a solution of  $\beta$ -caryophyllene (3.5 g, 17.1 mmol) in dichloromethane (250 mL) at  $-78\text{ }^{\circ}\text{C}$  for 1 hour. At this time,  $\text{O}_2$  was bubbled through solution for an additional 20 minutes. Resulting reaction mixture was then allowed to warm to room temperature and solvent concentrated under reduced pressure. After diluting with EtOH (60 mL),  $\text{AgNO}_3$  (3.4 g, 19.8 mmol) added and mixture was allowed to stir at room temperature until  $\text{AgNO}_3$  was dissolved. At this time, aqueous NaOH solution (4.6 M, 13 mL) was added dropwise and mixture was then allowed to stir at room temperature for an additional 16 hours. Reaction mixture was then vacuum filtered, rinsing with EtOH (50 mL), and filtrate concentrated under reduced pressure. The resulting residue was then diluted with EtOAc (150 mL) and 1 M HCl (150 mL) and transferred to a separatory funnel. The mixture was extracted with EtOAc (3 x 100 mL) and dried over  $\text{MgSO}_4$ . Subsequent concentration under reduced pressure afforded the crude product as a highly viscous oil. Flash column chromatography on silica gel using 20% to 40% EtOAc in hexanes as the eluent afforded the title compound (3.9 g, 14.5 mmol, 85% yield): IR (neat) 3038-2654, 2951, 2865, 1737, 1701, 1366, 1163  $\text{cm}^{-1}$ ;  $^1\text{H}$  NMR (500 MHz,  $\text{CDCl}_3$ )  $\delta$  2.83 – 2.57 (m, 5H), 2.41 – 2.27 (m, 2H), 2.15 – 2.10 (m, 1H), 2.09 (s, 3H), 1.85 (dd,  $J = 10.7, 9.1$  Hz, 1H), 1.71 (t,  $J = 10.2$  Hz, 1H), 1.67 – 1.52 (m, 2H), 1.04 (s, 3H), 1.02 (s, 3H);  $^{13}\text{C}$  NMR (125 MHz,  $\text{CDCl}_3$ )  $\delta$  210.1, 209.3, 178.6, 46.8, 45.9, 41.7, 36.8, 35.0, 34.0, 30.2, 30.1, 27.8, 23.9, 22.6; HRMS (ESI): Exact mass calcd for  $\text{C}_{14}\text{H}_{22}\text{O}_4$   $[\text{M}+\text{Na}]^+$ , 277.1416. Found 277.1413.



**5-[(1S,2R)-3,3-dimethyl-2-(3-oxobutyl)cyclobutyl](iodomethyl)oxolan-2-one (II-10):** To a solution of KI (7.9 g, 47.6 mmol) and NaHCO<sub>3</sub> (2.0 g, 23.8 mmol) in H<sub>2</sub>O (40 mL) at room temperature was added dropwise 4-((1S,2R)-3,3-dimethyl-2-(3-oxobutyl)cyclobutyl)pent-4-enoic acid (II-6) (2.0 g, 7.9 mmol) in CH<sub>2</sub>Cl<sub>2</sub> (8 mL) by cannula. Reaction mixture was allowed to stir vigorously for 20 minutes and then I<sub>2</sub> (1.2 g, 9.5 mmol) was added. After 10 minutes, an additional portion of I<sub>2</sub> (0.50 g, 2.0 mmol) was added and reaction was allowed to stir at room temperature for 16 hours. The reaction mixture was then transferred to a separatory funnel. The organic phase was collected and the aqueous layer extracted with dichloromethane (3 x 50 mL). The combined organics were washed with 10% Na<sub>2</sub>S<sub>2</sub>O<sub>3</sub> (3 x 50 mL) and dried with MgSO<sub>4</sub>. Concentration under reduced pressure and flash column chromatography on silica gel using 20% EtOAc in hexanes as the eluent afforded the corresponding compound (2.1 g, 5.6 mmol, 71% yield) as a viscous yellow oil. The product was isolated as a mixture of diastereomers and both diastereomers were carried forward to the subsequent reaction: IR (neat) 2952, 2864, 1764, 1702, 1245, 1159, 915 cm<sup>-1</sup>; <sup>1</sup>H NMR (500 MHz, CDCl<sub>3</sub>, mixture of diastereomers) δ <sup>1</sup>H NMR (500 MHz, CDCl<sub>3</sub>, mixture of diastereomers) δ 3.43 (d, *J* = 10.7 Hz), 3.32 (d, *J* = 10.6 Hz), 3.25 (d, *J* = 10.7 Hz), 3.21 (d, *J* = 10.6 Hz), 2.78 – 2.61 (m), 2.60 – 2.50 (m), 2.47 – 2.28 (m), 2.27 – 2.14 (m), 2.12 (s), 2.11 – 1.99 (m), 1.92 (td, *J* = 9.2, 6.2 Hz), 1.78 (dt, *J* = 9.2, 7.4 Hz), 1.73 – 1.54 (m), 1.41 (t, *J* = 10.2 Hz), 1.07 (s), 1.04 (s); <sup>13</sup>C NMR (125 MHz, CDCl<sub>3</sub>, mixture of diastereomers) δ 208.3, 208.1, 176.5, 176.4, 86.7, 86.2, 44.6, 44.6, 42.3, 42.2, 41.9, 41.7, 34.3,

34.0, 33.7, 33.5, 31.2, 31.0, 30.3, 30.2, 30.1, 29.7, 29.6, 29.5, 25.1, 25.0, 22.7, 22.6, 14.0, 13.4;

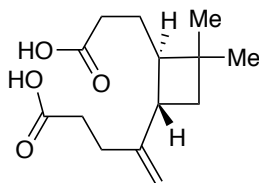
HRMS (ESI): Exact mass calcd for  $C_{15}H_{23}IO_3$   $[M+H]^+$ , 379.0770. Found 379.0771.



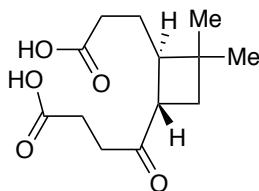
**3-[(1R,4S)-4-[2-iodomethyl]-5-oxoxolan-2-yl]-2,2-dimethylcyclobutyl]propanoic acid (II-11):**

To a solution of freshly distilled diisopropylamine (1.0 mL, 7.4 mmol) in THF (30 mL) at 0 °C was added *n*-BuLi (3.6 mL, 5.9 mmol, 1.62 M in hexanes, titrated using BHT) under  $N_2$ . After 5 minutes, reaction was cooled to  $-20$  °C and distilled TMSCl (1.3 mL, 9.8 mmol) was added. 5-[(1S,2R)-3,3-dimethyl-2-(3-oxobutyl)cyclobutyl](iodomethyl)oxolan-2-one (II-10) (1.9 g, 4.9 mmol) in THF (20 mL) was then added dropwise via cannula. After stirring at  $-20$  °C for 2 hours, the reaction was quenched with triethylamine (5 mL) and diluted with  $NaHCO_3$  (50 mL). After transferring to a separatory funnel, the mixture was extracted with EtOAc (3 x 100 mL) and washed with brine (50 mL). The combined organics were dried using  $MgSO_4$  and solvent concentrated under reduced pressure to afford crude 5-[(1S,2R)-3,3-dimethyl-2-{(3-[(trimethylsilyl)oxy]but-3-en-1-yl)}cyclobutyl](iodomethyl)oxolan-2-one (2.2 g, 4.9 mmol) as a light yellow oil, which was directly carried over to the next step without further purification. Ozone (generated at 110 V) was bubbled through a solution of 5-[(1S,2R)-3,3-dimethyl-2-{(3-[(trimethylsilyl)oxy]but-3-en-1-yl)}cyclobutyl](iodo-methyl)oxolan-2-one (2.2 g, 4.9 mmol) in dichloromethane (125 mL) at  $-78$  °C for 6 minutes. At this time,  $O_2$  was bubbled through solution for an additional 15 minutes. After addition of dimethyl sulfide (3.9 mL, 53.7 mmol),

mixture was then allowed to warm to room temperature and stir for an additional 16 hours. The mixture was then diluted with H<sub>2</sub>O (75 mL) and transferred to a separatory funnel. The resulting mixture was extracted with CH<sub>2</sub>Cl<sub>2</sub> (3 x 75 mL) and washed with brine (75 mL). The combined organics were dried using MgSO<sub>4</sub> and solvent concentrated under reduced pressure to afford the crude product as a light yellow oil. Flash column chromatography on silica gel using 10% to 15% EtOAc in hexanes as the eluent afforded the title compound (444.2 mg, 1.2 mmol, 24% yield over the two steps) as a light yellow oil. Due to incomplete conversion, the original starting material, 5-[(1S,2R)-3,3-dimethyl-2-(3-oxobutyl)cyclobutyl](iodomethyl)oxolan-2-one (**II-10**), was recovered (1.35 g, 3.57 mmol) and subsequently cycled through the reaction sequence a second time for an overall yield of the product (**II-11**) of 39% (655 mg, 1.7 mmol) over the two steps. The product was isolated as a mixture of diastereomers and both diastereomers were carried forward to the subsequent reaction: IR (neat) 3358-2553, 2951, 2864, 1770, 1706, 1154, 915, 729 cm<sup>-1</sup>; <sup>1</sup>H NMR (500 MHz, CDCl<sub>3</sub>, mixture of diastereomers) δ 3.43 (d, *J* = 10.7 Hz), 3.33 (d), 3.25 (d, *J* = 10.7 Hz), 3.21 (d, *J* = 10.6 Hz), 2.79 – 2.60 (m), 2.58 – 2.47 (m), 2.43 – 2.30 (m), 2.30 – 1.95 (m), 1.91 – 1.69 (m), 1.68 – 1.57 (m), 1.44 (t, *J* = 10.2 Hz), 1.09 (s), 1.08 (s); <sup>13</sup>C NMR (125 MHz, CDCl<sub>3</sub>, mixture of diastereomers) δ 178.2, 178.1, 176.5, 176.4, 86.8, 86.2, 77.2, 44.4, 44.3, 42.2, 42.0, 34.3, 34.1, 33.8, 33.5, 32.3, 32.2, 31.1, 31.0, 30.2, 29.7, 29.7, 29.5, 26.3, 26.2, 22.6, 22.6, 13.6, 13.3; HRMS (ESI): Exact mass calcd for C<sub>14</sub>H<sub>21</sub>IO<sub>4</sub> [M+H]<sup>+</sup>, 381.0563. Found 381.0560.



**4-[(1*S*,2*R*)-2-(3-Hydroxy-3-oxopropyl)-3,3-dimethyl-cyclobutyl]pent-4-enoic acid (II-8):** Zn dust (1.2 g, 17.8 mmol) and NH<sub>4</sub>Cl (0.95 g, 17.8 mmol) were added to a solution of 3-[(1*R*,4*S*)-4-[2-iodomethyl]-5-oxoxolan-2-yl]-2,2-dimethylcyclobutyl]propanoic acid (II-11) (444.2 mg, 1.2 mmol) in EtOH (19 mL). The reaction mixture was heated under reflux for 1 hour. After cooling to room temperature, the reaction mixture was vacuum filtered, rinsing with acetone (25 mL), and solvent concentrated under reduced pressure to afford the crude product as a dark yellow oil. The reaction was repeated on the same scale and crude products were combined prior to purification. Flash column chromatography on silica gel with 5% MeOH and 0.1% AcOH in CH<sub>2</sub>Cl<sub>2</sub> as the eluent afforded the title compound (383.2 mg, 1.5 mmol, 69% yield from combined crude product) as a yellow oil: IR (neat) 3391-2344, 3080, 2950, 2864, 1704, 1644, 1438, 888 cm<sup>-1</sup>; <sup>1</sup>H NMR (500 MHz, CD<sub>3</sub>OD) δ 4.81 (s, 1H), 4.74 (s, 1H), 2.51 – 2.38 (m, 3H), 2.35 – 2.15 (m, 4H), 1.98 (dt, *J* = 9.6, 7.6 Hz, 1H), 1.83 (dd, *J* = 10.4, 8.5 Hz, 1H), 1.76 – 1.63 (m, 2H), 1.46 (t, *J* = 10.2 Hz, 1H), 1.08 (s, 3H), 1.07 (s, 3H); <sup>13</sup>C NMR (125 MHz, CD<sub>3</sub>OD) δ 177.4, 177.1, 152.5, 107.8, 42.7, 40.8, 34.6, 33.6, 33.4, 31.5, 30.5, 27.1, 22.7; HRMS (ESI): Exact mass calcd for C<sub>14</sub>H<sub>22</sub>O<sub>4</sub> [M+Na]<sup>+</sup>, 277.1416. Found 277.1421.



**4-[(1*S*,2*R*)-2-(2-Carboxyethyl)-3,3-dimethylcyclobutyl]-4-oxobutanoic acid (II-9):** Ozone (generated at 110 V) was bubbled through a solution of 4-[(1*S*,2*R*)-2-(3-hydroxy-3-oxopropyl)-3,3-dimethyl-cyclobutyl]pent-4-enoic acid (#) (121.2 mg, 0.5 mmol) in MeOH (22 mL) at  $-78\text{ }^{\circ}\text{C}$  for 5 minutes. At this time,  $\text{O}_2$  was bubbled through solution for an additional 15 minutes. After addition of dimethyl sulfide (385  $\mu\text{L}$ , 5.2 mmol), the mixture was allowed to warm to room temperature and stir for an additional 16 hours. The mixture was then diluted with 2 M HCl (10 mL) and transferred to a separatory funnel. The resulting mixture was extracted with EtOAc (3 x 25 mL). The combined organics were dried using  $\text{MgSO}_4$  and solvent concentrated under reduced pressure to afford the crude product as a light yellow oil. Flash column chromatography on silica gel with 5% MeOH in  $\text{CH}_2\text{Cl}_2$  as the eluent afforded the title compound (118 mg, 0.5 mmol, 97% yield) as a white solid: IR (neat) 2955-2561, 2917, 2866, 1696, 1384, 1286, 951  $\text{cm}^{-1}$ ;  $^1\text{H}$  NMR (500 MHz,  $\text{CD}_3\text{OD}$ )  $\delta$  2.97 – 2.86 (m, 1H), 2.78 – 2.61 (m, 2H), 2.59 – 2.45 (m, 2H), 2.28 – 2.13 (m, 3H), 1.86 (dd,  $J = 10.7, 9.0$  Hz, 1H), 1.78 – 1.60 (m, 3H), 1.09 (s, 3H), 1.06 (s, 3H);  $^{13}\text{C}$  NMR (125 MHz,  $\text{CD}_3\text{OD}$ )  $\delta$  212.6, 177.2, 176.4, 47.5, 47.2, 37.3, 36.3, 34.7, 33.2, 30.6, 28.6, 26.6, 22.7. HRMS (ESI): Exact mass calcd for  $\text{C}_{13}\text{H}_{20}\text{O}_5$   $[\text{M}+\text{H}]^+$ , 257.1389. Found 257.1384 .

## CHAPTER 3

### Atmospheric $\beta$ -Caryophyllene-Derived Ozonolysis Products at Interfaces

**Portions of this chapter are reproduced in part  
with permission from the American Chemical Society:**

Bé, A. G.; Chase, H. M.; Liu, Y.; Upshur, M. A.; Zhang, Y.; Tuladhar, A.; Chase, Z. A.; Bellcross, A. D.; Wang, H.-F.; Wang, Z.; Batista, V. S.; Martin, S. T.; Thomson, R. J.; Geiger, F. M., Atmospheric  $\beta$ -Caryophyllene-Derived Ozonolysis Products at Interfaces. *ACS Earth Space Chem.* **2019**, 3 (2), 158–169.

**3.1. Introduction and motivation.** As highlighted in the previous chapters, acquiring chemical information about atmospherically relevant interfaces is important for understanding cloud activation,<sup>1-13</sup> particle growth,<sup>8, 14-16</sup> heterogeneous chemistry,<sup>17</sup> and aerosol optical properties.<sup>18-19</sup> In Chapter 2, we reported the development of synthetic routes to access a suite of monomeric oxidation products believed to form via atmospheric ozonolysis of  $\alpha$ -pinene and  $\beta$ -caryophyllene. With the goal of shedding light on the influence that these molecules might have on SOA CCN activity, dynamic surface tension measurements were also performed on this molecular suite, revealing considerable differences in the surface tension depression of pendant droplets containing each of these species. Notably, the surface tension depression of aqueous droplets containing the  $\beta$ -caryophyllene oxidation products was found to exceed those of SDS<sup>20</sup> at equivalent concentrations.<sup>21</sup> These oxidation products produced from  $\beta$ -caryophyllene ozonolysis have also been foci in recent field<sup>22-25</sup> and laboratory<sup>26-29</sup> studies examining atmospheric oxidation of sesquiterpenes. Therefore, we expand upon our studies on these  $\beta$ -caryophyllene-derived constituents in Chapters 3 and 4 by gaining spectroscopic insights into the interfacial molecular composition of SOM derived from  $\beta$ -caryophyllene.

Oxidation products have been observed at the surfaces of isoprene- and  $\alpha$ -pinene-derived SOM,<sup>6, 8, 12, 18, 30</sup> however, Chapter 3 takes the first steps towards elucidating the interfacial structure and orientation of  $\beta$ -caryophyllene-derived oxidation products benchmarked to the surface of SOM synthesized from the ozonolysis of  $\beta$ -caryophyllene. As introduced in Chapter 1, probing the interfacial composition of SOM remains challenging, as few techniques are appropriate for interfacial analysis with chemical bond specificity and under conditions relevant to the atmosphere. Vibrational nonlinear spectroscopy<sup>30-35</sup> offers the prospect of probing SOM interfacial chemistry under ambient conditions, nondestructively, and with capabilities for

observing constituents present on the surfaces of SOM as well as obtaining molecular orientation information. Previous work in this area reported on the observation of organic molecules at the interface of aerosol particles deposited on or in contact with solid substrates,<sup>14, 30-31, 36-41</sup> and more recently suspended in air.<sup>18, 42</sup> Here, we combine vibrational sum frequency generation (SFG) spectroscopy, organic synthesis, and density functional theory (DFT) calculations to probe the surface composition of  $\beta$ -caryophyllene-derived SOM and to obtain detailed structural and orientation information of individual molecular constituents on the particle surfaces. By comparing the spectra from the synthesized reference compounds with those observed from the  $\beta$ -caryophyllene-derived SOM in both the C–H and C=O stretching frequency regions, we identify  $\beta$ -caryophyllene aldehyde (**III-1**), along with  $\beta$ -caryophyllonic acid (**III-3**), as the most likely surface-localized species. These same species were also found to exhibit the highest and second highest surface activities (and thus estimated cloud activation potentials), respectively, of the oxidation products we investigated in Chapter 2.<sup>21, 43</sup>

**3.2 Collection of laboratory-derived SOM.** SOM samples collected directly from the field are highly complex in composition, and therefore information about individual BVOC sources, oxidation pathways, and physicochemical properties can often be difficult to disentangle. Consequently, methods and instrumentation used to generate model aerosol samples in the laboratory have been developed to supplement field observations, study fundamental SOA formation and growth pathways, and collect samples for offline analyses. Synthesis and collection of aerosol material in laboratory settings is advantageous in that the BVOC precursor, oxidant, RH, temperature, and other factors can be controlled. In collaboration with the research group of Prof. Scot Martin at Harvard University, SOM derived from the ozonolysis of  $\beta$ -caryophyllene was produced in a home-built flow tube reactor housed in their lab. All SOM

samples collected and analyzed in this study were collected with help from Dr. Yue Zhang, a graduate of the Martin lab. In contrast to other chambers built for SOA production, the Harvard flow tube reactor can generate SOA particles in larger quantities over much faster timescales and fluctuations in temperature and RH are minimal.

**3.2.1. Flow tube reactor experimental details.** A comprehensive description of the Harvard flow tube reactor used in this work can be found in our previously published work.<sup>14, 44</sup> Briefly,  $\beta$ -caryophyllene was introduced into the flow tube as a solution of  $\beta$ -caryophyllene ( $\geq 98.5\%$ , Sigma-Aldrich Inc.) diluted in 1-butanol (1:625 v/v)<sup>14, 45-46</sup> at selected injection rates that altered the gas-phase concentration in the range of 300–500 ppb, which subsequently changed the organic particle mass loading in the flow tube. 1-Butanol was used as an OH scavenger to ensure that ozonolysis products were generated. Excess ozone (53 ppm) was passed through the reactor with a flow rate of 4 SLPM to ensure  $\beta$ -caryophyllene was fully reacted. Aerosol particle samples were nucleated in the absence of seed particles and collected on Teflon filters (PTFE-47 membrane, pore size 0.45  $\mu\text{m}$ , Z269425, Sigma-Aldrich Inc.) for 7–10 hr, or until saturated, for subsequent SFG analysis.

From the flow rate, collection time, collection efficiency, and particle mass concentration (obtained from a scanning mobility particle sizer), the mass of the particles collected on the filters was estimated in the range of 5–14 mg. The SOM generated had mode diameters of 66–80 nm during the course of the flow tube experiment, with an average mass loading of 7 mg m<sup>-3</sup> (**Table 3.1**). Previous chamber and flow tube studies of sesquiterpene ( $\beta$ -caryophyllene) and monoterpene SOM suggest that the chemical composition of the  $\beta$ -caryophyllene SOM in this study is likely to be similar to those performed under low volatile organic compound (VOC) concentrations, due to a low effective saturation concentration of  $\beta$ -caryophyllene SOM.<sup>44, 46-48</sup>

All filter samples were sealed using Teflon tape and parafilm, stored in a  $-20\text{ }^{\circ}\text{C}$  freezer, and warmed to room temperature before breaking the sealant for SFG measurements. No spectral changes were observed over the course of approximately 1.5 years, suggesting the high stability of the SOM once formed, at least as detected by SFG spectroscopy.

**Table 3.1.** Details on  $\beta$ -caryophyllene-derived SOM collection in the Harvard flow tube reactor.

Sample #	Mass loading ( $\text{mg m}^{-3}$ )	Collection time (hr)	Mode diameter (nm)	Number concentration ( $\# \text{ cm}^{-3}$ )	Mass collected (mg)
1	$6 \pm 1$	10	$66 \pm 8$	$(9 \pm 2) \times 10^6$	7
2	$5.6 \pm 0.2$	9	$68 \pm 3$	$(9.7 \pm 0.3) \times 10^6$	6
3	$5.6 \pm 0.2$	9	$66 \pm 3$	$(1.0 \pm 0.1) \times 10^7$	6
4	$5 \pm 2$	9	$62 \pm 4$	$(8 \pm 3) \times 10^6$	5
5	$10 \pm 5$	9	$75 \pm 5$	$(1.5 \pm 0.8) \times 10^7$	11
6	$8 \pm 1$	8	$70 \pm 4$	$(1.4 \pm 0.2) \times 10^7$	8
7	$13 \pm 2$	9	$80 \pm 9$	$(1.7 \pm 0.2) \times 10^7$	14
8	$7.6 \pm 0.5$	7	$72 \pm 5$	$(1.2 \pm 0.1) \times 10^7$	6

**3.3. Synthesis of  $\beta$ -caryophyllene-derived oxidation products.** The  $\beta$ -caryophyllene-derived oxidation products measured in this study (i.e.  $\beta$ -caryophyllene aldehyde (**III-1**),  $\beta$ -nocaryophyllone aldehyde (**III-2**),  $\beta$ -caryophyllonic acid (**III-3**),  $\beta$ -nocaryophyllonic acid (**III-4**),  $\beta$ -caryophyllinic acid (**III-5**), and  $\beta$ -nocaryophyllinic acid (**III-6**)) were prepared following the synthetic routes outlined in Section 2.2 of Chapter 2.

### 3.4. Vibrational SFG spectroscopy.

**3.4.1 Introduction to SFG spectroscopy.** SFG spectroscopy is a second-order nonlinear optical technique that is capable of selectively probing vibrational modes at surfaces and interfaces. Among the various surface science techniques that have been applied to studying SOA chemistry, SFG spectroscopy offers several aforementioned advantages due to its versatile applicability, chemical bond-specificity, and practical considerations as a nondestructive and ambiently

operated technique. To provide context of its applicability to atmospherically relevant interfaces, a brief introduction to the technique follows, as more comprehensive accounts of SFG theory can be found elsewhere in the literature. In second-order nonlinear processes, two photons combine to generate a single photon at the sum of their two frequencies. The inherent surface selectivity of second-order processes, results from the asymmetry present at surfaces or interfaces. Under the electric-dipole approximation, SFG is not allowed in media with inversion symmetry, such as in the centrosymmetric bulk of most materials. However, centrosymmetry is inherently broken when a plane of asymmetry is introduced by an interface, allowing for SFG signal to be generated.

In the case of SFG spectroscopy, a visible up-converter beam at a fixed frequency ( $\omega_{\text{vis}}$ ) and a pulsed infrared (IR) beam with a tunable frequency ( $\omega_{\text{IR}}$ ) are spatially and temporally overlapped on the sample to generate an SFG signal ( $\omega_{\text{SFG}} = \omega_{\text{IR}} + \omega_{\text{vis}}$ ). The SFG signal is enhanced as the IR frequency is tuned into resonance with the vibrational transitions at the interface. Thus, detecting the SFG light as a function of the IR frequency results in an interfacial vibrational spectrum, where modes must be simultaneously IR and Raman active to be SFG active. The SFG signal intensity ( $I_{\text{SFG}}$ ) produced in asymmetric environments is directly proportional to the square modulus of the second-order susceptibility of the interface ( $\chi^{(2)}$ ) and the intensity of the electric fields of the incident IR ( $I_{\text{IR}}$ ) and visible ( $I_{\text{vis}}$ ) beams, according to

$$I_{\text{SFG}} \propto \left| \chi_{\text{eff}}^{(2)} \right|^2 I_{\text{IR}} I_{\text{vis}} \quad (3.1)$$

The second order susceptibility,  $\chi^{(2)}$ , of the sample contains resonant,  $\chi_{\text{R}}^{(2)}$ , and nonresonant,  $\chi_{\text{NR}}^{(2)}$ , components. Increased SFG signal intensity is observed from the resonant enhancement of

$\chi_{\text{R}}^{(2)}$ , while  $\chi_{\text{NR}}^{(2)}$  has minimal contributions for the low dielectric surfaces and molecules relevant to this research.<sup>49</sup>

Varied polarization combinations of the input and signal beams can be used to measure different tensor components in  $\chi^{(2)}$ , and therefore orientation information at the interface can be deduced. Unlike traditional Raman or IR spectroscopy methods, only those transition dipole moment components that point along the direction probed by chosen polarization combination contribute to the SFG signal intensity. As such, SFG spectra are often better resolved and contain more orientational information than their Raman and IR counterparts. There are two different polarizations, one for the electric field vector perpendicular to the plane of incidence, labeled S, and one for the electric field vector parallel to the plane of incidence, labeled P. Four polarization combinations are typically used – *ppp*, *ssp*, *sps*, *pss* – where the letters are listed for beams of decreasing frequency (i.e. sum frequency (SF), visible, and IR) and each beam is either plane-polarized parallel (*s*) or perpendicular (*p*) to the surface. In this work, we predominantly use the polarization combinations *ssp* and *ppp*. The *ssp* polarization combination probes the components of the vibrational transition dipole moments that are oriented perpendicular to the solid substrate,<sup>40</sup> whereas the *ppp* polarization combination, needed for detailed orientational analysis,<sup>50</sup> probes off-diagonal elements of the  $\chi^{(2)}$  tensor.

In this thesis work, several SFG set-ups were used to obtain spectra across the C–H (2700–3200  $\text{cm}^{-1}$ ), C=O (1600–1800  $\text{cm}^{-1}$ ), and O–H stretching regions (3200–3800  $\text{cm}^{-1}$ ): two standard resolution broadband SFG systems at Northwestern (NU) as well as a scanning SFG system and a high resolution-broadband (HR-BB) system at Pacific Northwest National Lab (PNNL). In the case of picosecond (ps) scanning systems, the spectral bandwidths for the overlapped IR and visible beams are narrow and the vibrational spectrum of the interfacial region

can be collected by scanning across IR frequencies of interest in a piecewise fashion. Femtosecond (fs) broadband spectrometers differ in that the spectral bandwidth of the IR pulse is sufficiently broad that it can cover wider ranges of the spectral window of interest, typically allowing for spectra to be acquired much faster. All measurements collected at PNNL were carried out with help from Dr. Aashish Tuladhar and Dr. Zizwe Chase at Environmental Molecular Sciences Laboratory (EMSL), a Department of Energy (DOE) Office of Science user facility.

**3.4.2. Experimental details on sample configurations and SFG set-ups.** In the present study, the synthesized standards, along with  $\beta$ -caryophyllene ( $\geq 98.5\%$ , Sigma-Aldrich Inc.), were measured in both the condensed and vapor phases in contact with solid fused silica or calcium fluoride substrates at laboratory ambient temperature and RH in near total internal reflection geometry. Vapor-phase spectra were taken by exposing an optical window with the equilibrium vapor pressure of the compound being measured, and condensed-phase spectra were obtained by measuring a window containing a spin-coated sample. Samples were prepared for measurement by spin-coating the compound, dissolved in a deuterated solvent ( $\text{CDCl}_3$  and/or  $\text{CD}_3\text{OD}$ ), at 3000 rpm onto an optical window. Synthetic SOM was analyzed by pressing an optical window against a Teflon filter containing the collected material. Spectra were measured with *ssp* and *ppp* polarization combinations. The standard (NU,  $10\text{--}15\text{ cm}^{-1}$ )<sup>31, 51-52</sup> and high (PNNL,  $0.6\text{ cm}^{-1}$ )<sup>32, 53-55</sup> spectral resolution broadband SFG laser systems used herein for obtaining spectra in the C–H region have been detailed in previous work.

The standard resolution system used for obtaining C–H data uses an 800 nm regeneratively amplified Ti:sapphire laser (Spectra Physics, Spitfire Pro) that operates at a 1 kHz repetition rate and produces  $\sim 100$  fsec pulses. The output beam is split by a 50/50 beam splitter,

where half of the beam is used to pump an optical parametric amplifier (OPA 800C, Spectra Physics) to produce the broadband IR ( $\sim 150 \text{ cm}^{-1}$  FWHM) tuned to the C–H stretching region. The other half of the output light is used as a visible up-converter beam that passes through a bandpass filter to achieve a resolution of  $\sim 10 \text{ cm}^{-1}$ . The temporal overlap between these two beams is achieved using a home-built delay stage for the visible beam. The IR beam and the up-converter pulse were directed onto the sample at  $60^\circ$  and  $45^\circ$  from the surface normal, respectively. The beams are refracted in the substrate and therefore incident at the substrate/sample surface at  $\sim 38^\circ$  and  $\sim 30^\circ$  for the IR and visible, respectively. For the standard resolution SFG laser system, vapor-phase spectra of the synthesized compounds were taken by adding 1–2 drops of viscous liquid compound to the bottom of a fused silica window, which was then sealed with a Viton O-ring to a home-built Teflon cell and placed on a sample stage. The vapor was allowed to equilibrate for  $\sim 10$ –45 minutes before spectral acquisition. The visible and IR beams were aligned above the sample droplet to probe the vapor/solid (as opposed to liquid/solid) interface. Windows containing spin-coated sample were sealed with a Viton O-ring to the Teflon cell and clamped onto the sample stage prior to measuring condensed-phase compound spectra. All optical windows were plasma cleaned for 10–15 minutes prior to sample exposure. The spectra reported here are an average of 4–7 individual spectra each taken for 2 minutes each. Spectra were referenced to the *ppp*-polarized nonresonant SFG response of gold deposited on fused silica to account for the incident IR energy distribution, and frequencies were calibrated using a polystyrene film.<sup>40, 44, 56-57</sup>

In contrast to the standard resolution system, the HR-BB SFG system utilizes two pairs of electronically synchronized (Synchrolock-AP, Coherent Inc.) Ti:sapphire oscillators/amplifiers to generate 800-nm beams with different pulse widths — one at  $\sim 40$  fs (Micra-5/Legend Elite

DUO, Coherent Inc.), which produces a broadband IR beam through an optical parametric amplifier (OPA, OPERA-Solo, Coherent Inc.), and the other at  $\sim 100$  ps (TIGER/Legend Elite HE-ps, Coherent Inc.) as the visible up-converter to provide sub-wavenumber spectral resolution ( $\sim 0.6$   $\text{cm}^{-1}$ ). The incident angles of the IR beam and the visible beam are  $55^\circ$  and  $45^\circ$ , respectively. Vapor-phase compound spectra were acquired by placing 1–2 drops of liquid sample at the edge of a shallow Teflon beaker that was then capped with a fused silica optical window. The vapor was allowed to equilibrate for  $\sim 10$ –45 minutes before spectral data acquisition. For spectra of spin-coated compounds, samples were prepared using the same procedure as stated above. All fused silica windows were placed in an ozone cleaner (Novascan Technologies) for  $\sim 10$  minutes, and plasma cleaned (PDC-001-HP, Harrick Plasma) for  $\sim 15$  minutes before depositing sample. The spectra reported are an average of 2–3 individual acquisitions each recorded for 5–10 minutes. SFG intensities were normalized to the *ppp*-polarized nonresonant SFG profile of clean z-cut  $\alpha$ -quartz, and frequencies were calibrated to a polystyrene film. Although the data was experimentally obtained using  $0.6$   $\text{cm}^{-1}$  resolution, we note that the spectra were subsequently binned to improve signal to noise. The data points in the HR SFG spectra were binned by 5 points, or by  $1.73$   $\text{cm}^{-1}$ , in Igor Pro Version 6.11 (WaveMetrics, Lake Oswego, OR, USA).

SFG spectra collected in the C=O region were measured using a TOPAS (TOPAS-C, Light Conversion) tunable optical parametric amplifier set-up that has been described in detail previously.<sup>58</sup> Though the set-up is analogous to that described above for the standard resolution system used for collecting the C–H data, a 795 nm regeneratively amplified laser system (Solstice, Spectra Physics) operating at 1 kHz repetition rate produces 100 fs pulses that are split by a 90:10 beam splitter, where 90% pumps the TOPAS to generate the broadband IR and 10%

is used as a visible up-converter beam. The incident angles arriving at the sample were  $45^\circ$  for the visible beam and  $60^\circ$  for IR beam, and therefore the beams are refracted in the substrate and therefore incident at the substrate/sample surface at  $\sim 30^\circ$  and  $\sim 38^\circ$ , respectively. Sample preparation and data collection for obtaining condensed-phase spectra in the C=O region were carried out under the same protocol as described above for the standard resolution SFG laser system used for obtaining spectra in the C–H region. All spectra in the C=O region were measured using calcium fluoride optical windows. Spectra were recorded using an automated Python script to measure the IR center wavelengths (5500–6300 nm with 695 nm as the spectrograph center wavelength) that cover the frequency range of interest ( $\sim 1590$ – $1820$   $\text{cm}^{-1}$ ). Spectra were normalized to the incident IR energy profile by recording a *ppp*-polarized nonresonant spectrum from a gold film deposited on calcium fluoride, and frequencies were calibrated to a polystyrene film measured in the C–H region.<sup>59</sup> A visual representation of this optical set-up is shown in **Figure 3.1** to provide an example of the described SFG optical set-ups.

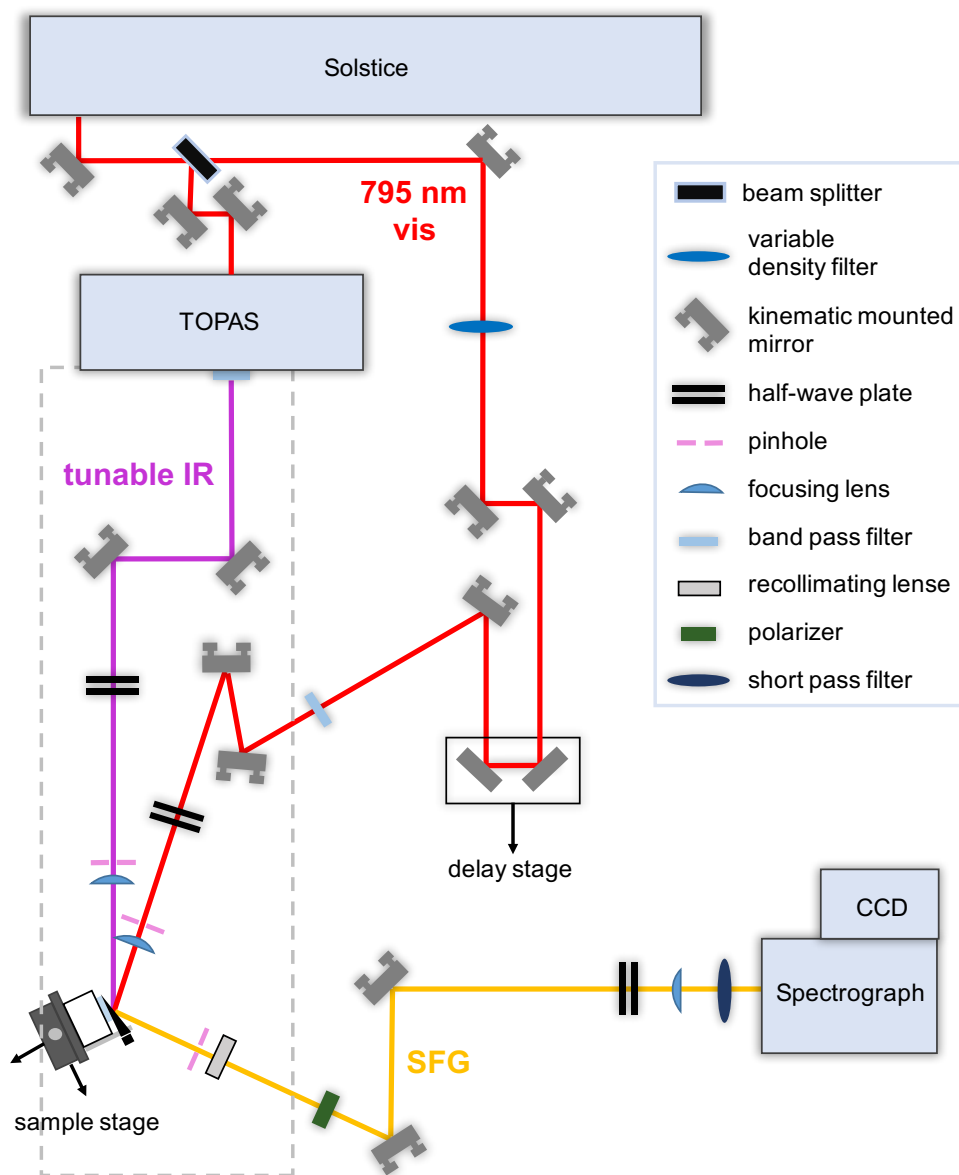


**Figure 3.1.** Schematic of NU Solstice/TOPAS laser set-up.

### 3.4.3. Comparison of SFG spectra of $\beta$ -caryophyllene-derived SOM and oxidation

**products: C–H stretches.** Polarization-resolved SFG spectra were recorded in the C–H stretching region for the  $\beta$ -caryophyllene oxidation products in both the condensed and vapor phases and the  $\beta$ -caryophyllene-derived SOM surfaces in contact with fused silica. The phase state of SOA particles remains difficult to experimentally probe and little is known about

molecular environment changes that may lead to phase behavior differences at the surface versus in the bulk. Indeed, surface-induced melting has been observed in a range of systems, from metal nanoparticles to ice for instance.<sup>60-61</sup> Therefore, we provide both the vapor and condensed-phase spectra for compounds **III-1–III-6**, though we expect the condensed-phase spectra to more accurately reflect the phase states of the compounds present in the collected particle-phase SOM (see Appendix 2, **Figure A2.4** for vapor-phase spectra).<sup>40</sup>

We now compare the condensed-phase HR-BB spectra of the  $\beta$ -caryophyllene oxidation products and the  $\beta$ -caryophyllene-derived SOM surfaces in the *ssp* versus *ppp* polarization combinations collected in the C–H region (**Figure 3.2**). The *ssp*-polarized SFG spectrum of  $\beta$ -caryophyllene-derived SOM contains two distinct peaks around 2943  $\text{cm}^{-1}$  and 2860  $\text{cm}^{-1}$ . Comparison to the *ssp*-polarized spectra of the oxidation products reveals that all compound spectra also display these two peaks at approximately  $2940 \pm 5 \text{ cm}^{-1}$  and  $2860 \pm 5 \text{ cm}^{-1}$ . An additional peak centered between 2902 and 2912  $\text{cm}^{-1}$ , which is not present in the SOM spectrum, is observed in the spectra of  $\beta$ -caryophyllene,  $\beta$ -nocaryophyllone aldehyde (**III-2**),  $\beta$ -nocaryophyllonic acid (**III-4**), and both diacid compounds **III-5** and **III-6**. The spectra of  $\beta$ -nocaryophyllone aldehyde (**III-2**) and  $\beta$ -nocaryophyllonic acid (**III-6**) also contain a 2963  $\text{cm}^{-1}$  peak not observed in the other spectra. In contrast to the other compounds, the *ssp*-polarized SFG spectra of  $\beta$ -caryophyllene aldehyde (**III-1**) and  $\beta$ -caryophyllonic acid (**III-3**) contain only two prominent peaks near 2943  $\text{cm}^{-1}$  and 2860  $\text{cm}^{-1}$ , though  $\beta$ -caryophyllonic acid (**III-3**) shows a small peak around 2902  $\text{cm}^{-1}$ . The HR-BB *ppp*-polarized SFG spectrum of  $\beta$ -caryophyllene-derived SOM contains one distinct peak centered at 2947  $\text{cm}^{-1}$ , while the *ppp*-polarized SFG spectra of compounds **III-2** and **III-6** contain an additional prominent peak around 2964  $\text{cm}^{-1}$ .

The *ppp*-polarized spectra of compounds **III-1**, **III-3**, **III-4**, and **III-5** as well as  $\beta$ -caryophyllene, however, also contain one identifiable peak, though the spectra of  $\beta$ -caryophyllene and compound **III-4** contain a possible shoulder near 2920  $\text{cm}^{-1}$ . As in the *ppp*-polarized SFG spectrum of  $\beta$ -caryophyllene-derived SOM, one prominent peak centered at 2947  $\text{cm}^{-1}$  is observed in the *ppp*-polarized SFG spectra of compounds **III-1** and **III-3**.

The *ssp*- and *ppp*-polarized SFG spectra in the C–H stretching region show a best match for  $\beta$ -caryophyllene aldehyde (**III-1**), as it most closely resembles the *ssp*- and *ppp*-polarized SFG spectra of the  $\beta$ -caryophyllene-derived SOM.  $\beta$ -Caryophyllonic acid (**III-3**) is an additional close spectral match. As discussed earlier, we recently found that  $\beta$ -caryophyllene aldehyde (**III-1**) exhibits the highest surface activity in aqueous droplets within the synthesized suite of  $\beta$ -caryophyllene oxidation products, with  $\beta$ -caryophyllonic acid (**III-3**) as the second most surface-active compound in the series.<sup>21</sup> While surface-specific measurements of aqueous media are not directly comparable to those in organic SOM, it may be speculated, based on our SFG results, that compounds **III-1** and **III-3** exhibit a higher propensity to populate the surface of SOM than the other compounds studied. Additionally, a condensed-phase spectrum of a 1:1 mixture of compounds **III-1** (best spectral match) and **III-4** (poor spectral match) was collected to compare the mixture to the spectra of the individual compounds (**Figure 3.3**). The mixture spectrum differs significantly from that of both **III-1** in the condensed phase and the  $\beta$ -caryophyllene-derived SOM, indicating that (1) the SOM sample contains a complex mixture of  $\beta$ -caryophyllene-derived oxidation products with relative surface vs. bulk compositions that cannot be replicated by simply combining oxidation products, and (2) the spectral match observed between the SOM and  $\beta$ -caryophyllene aldehyde (**III-1**) appears to indicate that **III-1** may reside

at the SOM surface while this is not the case for the 1:1 oxidation product mixture. We caution, however, that these comparisons are merely preliminary, and future work aims to focus on measurements on multi-constituent samples.

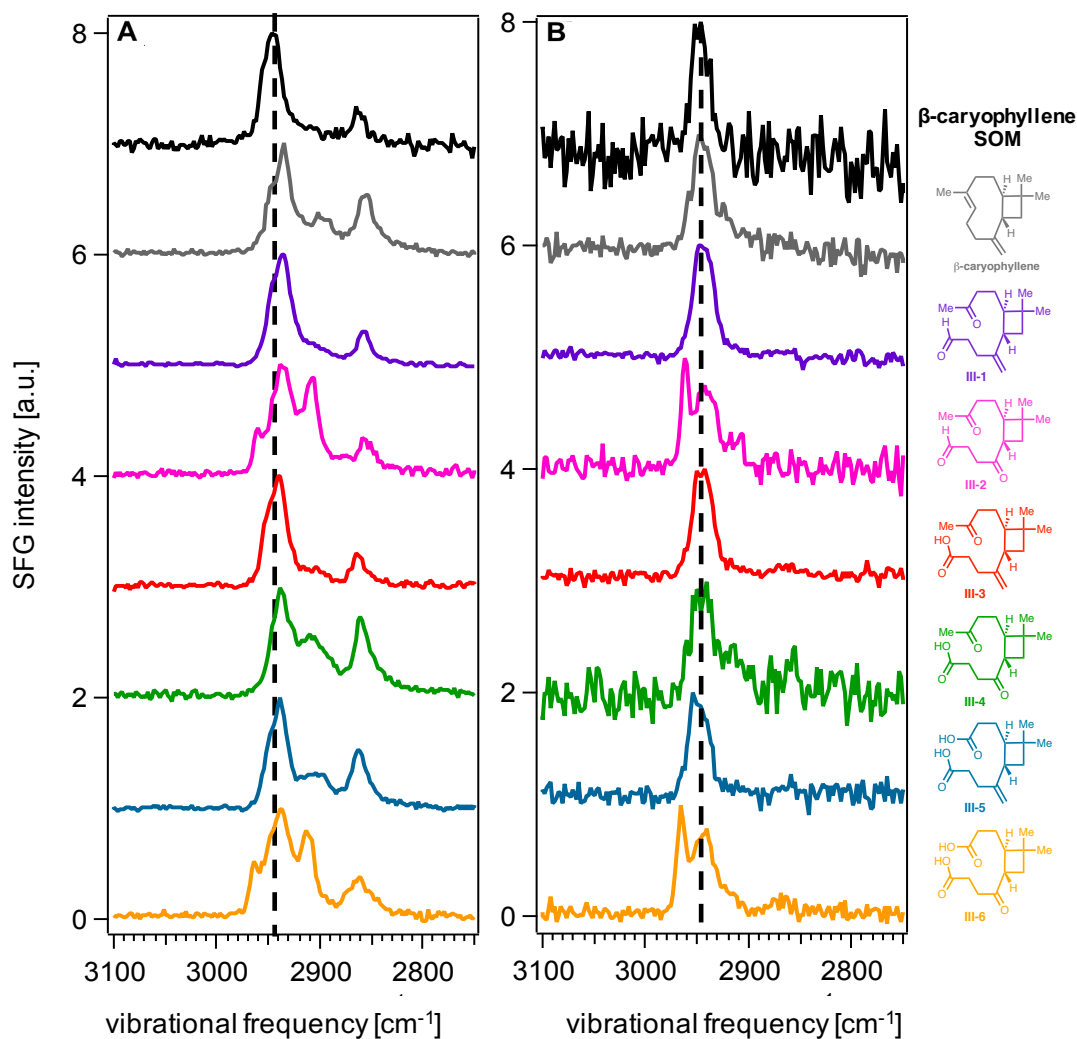


**Figure 3.2.** HR (A) *ssp*- and (B) *ppp*-polarized SFG spectra of synthetic  $\beta$ -caryophyllene-derived SOM pressed against fused silica (black trace) compared to  $\beta$ -caryophyllene and synthesized  $\beta$ -caryophyllene oxidation products (III-1–III-6) spin-coated onto fused silica. All maximum SFG intensities have been normalized to 1 and offset for clarity.

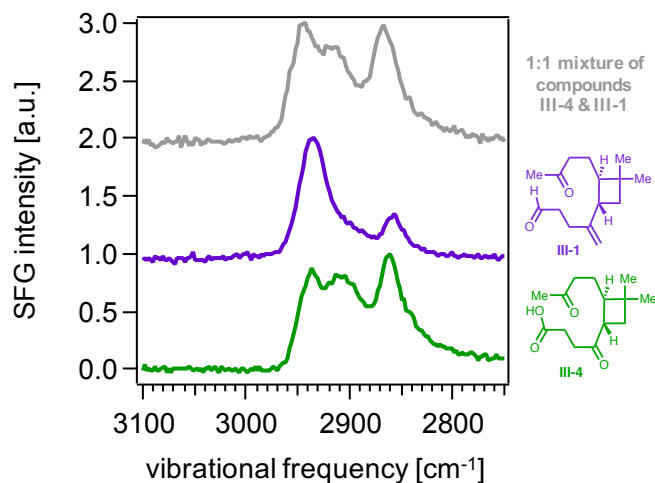


**Figure 3.3.** Standard resolution *ssp*-polarized SFG spectrum of a 1:1 mixture of compounds **III-1** and **III-4** spin-coated onto fused silica compared to the standard resolution *ssp*-polarized SFG spectra of the spin-coated individual compounds. Maximum intensities have been normalized to 1 and offset for clarity.

**3.4.4. Comparison of SFG spectra of  $\beta$ -caryophyllene-derived SOM and oxidation products: C=O stretches.** We next discuss the SFG spectra collected in the C=O stretching region, which were acquired with help from a fellow graduate student, Yangdongling Liu. Applying our spectral analysis to the C=O region (**Figure 3.4**), albeit on calcium fluoride (given its transparency in this infrared region), we find the following: The SFG spectrum of the  $\beta$ -caryophyllene-derived SOM is remarkably simple, as it contains only one broad peak centered at  $\sim 1730\text{ cm}^{-1}$ . Few spectral differences are observed in the oxidation product spectra compared to that of the  $\beta$ -caryophyllene-derived SOM, with the exception of a slight mismatch between the spectral shape and center peak frequency in the SOM and compound **III-4** spectra in the C=O region. Additionally, the SFG spectrum of diacid compound **III-6** contains a possible shoulder around  $1690\text{ cm}^{-1}$ , which is in contrast to the other spectra. These spectral differences suggest that compounds **III-4** and **III-6** may not populate the surface of  $\beta$ -caryophyllene-derived SOM,

lending further support to our conclusions from the interfacial tension measurements and the *ssp*- and *ppp*-polarized SFG spectra we collected in the C–H stretching region (*vide supra*).

The SFG spectra of compounds **III-1**, **III-2**, **III-3**, and **III-5** all contain a broad peak centered near  $1730\text{ cm}^{-1}$ , which matches closely to the SFG spectrum of  $\beta$ -caryophyllene-derived SOM. The absence of prominent spectral differences in the C=O region suggests the insensitivity of this region for identifying carbonyl groups on secondary organic material derived from  $\beta$ -caryophyllene with chemical specificity. Yet, this same insensitivity offers the opportunity to test generically for the presence of carbonyl groups at the interface by SFG spectroscopy. While the C=O data alone cannot help to distinguish which oxidation products may populate the surface of the SOM, the SFG spectra in the C–H region reveal more notable spectral variances in the oxidation products compared to the SOM.

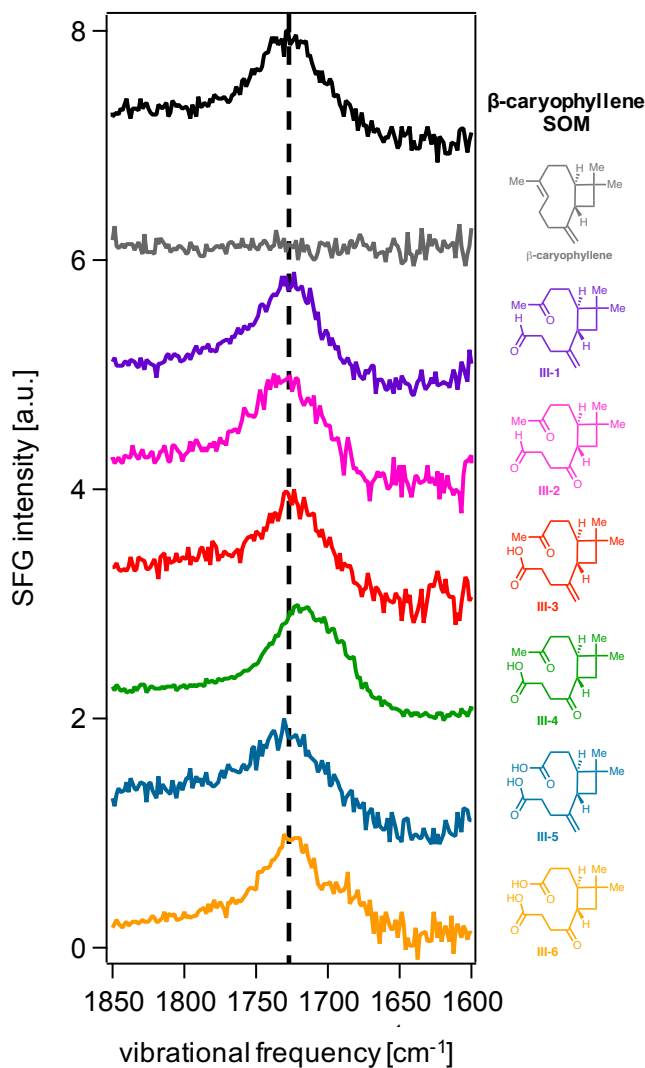


**Figure 3.4.** Standard resolution *ssp*-polarized SFG spectra of synthetic  $\beta$ -caryophyllene-derived SOM on calcium fluoride (black trace) in the carbonyl stretching region compared to those obtained from  $\beta$ -caryophyllene and several synthesized  $\beta$ -caryophyllene oxidation products (**III-1–III-6**) spin-coated onto calcium fluoride. All maximum SFG intensities have been normalized to 1 and offset for clarity.

A thorough analysis of spectral assignments in the C=O region that is based on comparison to carbonyl standards is forthcoming.  $\beta$ -Caryophyllene was also measured as a control and showed no C=O signal by SFG, as expected. We note that the oxidation products gave negligible signal in the *ppp* polarization combination in the C=O region. We caution that

the *ppp* signal may have an incident angle dependence<sup>62</sup> and indeed in forward scattering geometries, for instance, non-zero *ppp* signal intensities may be detected, though such additional orientational analyses are beyond the scope herein. Taken together, the C–H and C=O data together reveal that the spectrum of  $\beta$ -caryophyllene aldehyde (**III-1**), as well as that of  $\beta$ -caryophyllonic acid (**III-3**), spectrally resemble the  $\beta$ -caryophyllene-derived SOM surface to a largest degree out of the suite of compounds studied herein.

**3.4.5. Nonlinear bulk responses from  $\beta$ -nocaryophyllinic acid upon crystallization.** We also note that large nonlinear bulk responses from  $\beta$ -nocaryophyllinic acid (**III-6**) were observed upon slow crystallization of the sample (**Figure 3.5**), which is consistent with our earlier reports on molecular chirality in field-collected and synthetic atmospheric aerosol particles.<sup>30, 63-64</sup> Upon leaving a sample of  $\beta$ -nocaryophyllinic acid (**III-6**) spin-coated for  $\sim 1$  hour at ambient lab conditions (22°C, 30% RH), the compound film on the window, which originally appeared as a uniform, transparent condensed-phase film, revealed patchy crystalline regions. Interestingly, extremely large SFG signal intensities were observed for the crystalline material compared to the SFG signal intensities of the condensed-phase  $\beta$ -nocaryophyllinic acid (**III-6**) film prepared immediately after spin-coating. The observed SFG response of the crystallized sample was approximately 10-fold larger than that of the freshly prepared sample. We propose that, over time,  $\beta$ -nocaryophyllinic acid (**III-6**) slowly crystallizes to form a chiral crystalline material, thereby giving strong bulk SFG responses that surpass the even *ppp*-polarized nonresonant response of gold and the bulk SFG signal of  $\alpha$ -quartz.

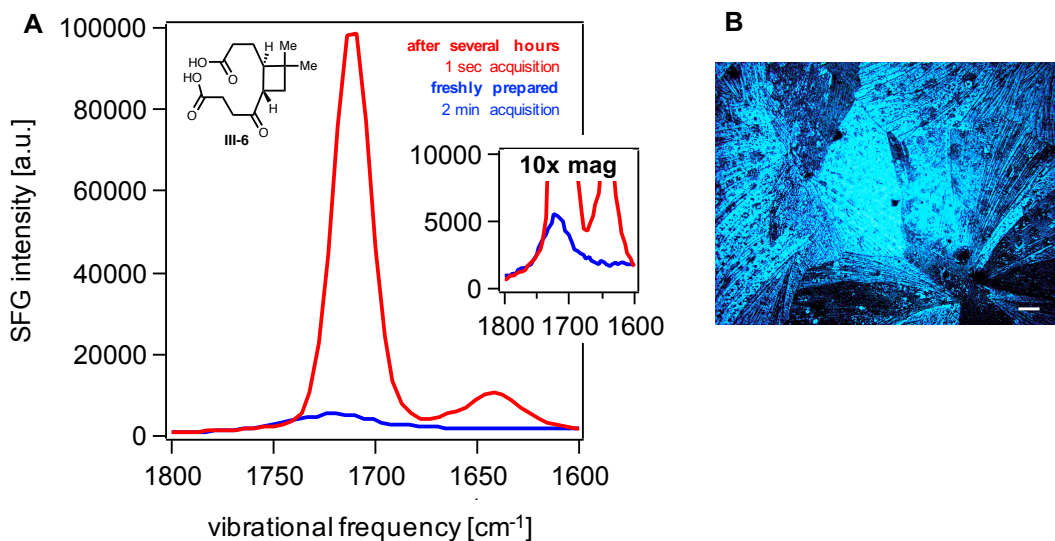


**Figure 3.5.** (A) *ssp*-Polarized SFG spectra of a spin-coated film of  $\beta$ -nocaryophyllinic acid (**III-6**) on  $\text{CaF}_2$  in the carbonyl region, immediately after prepared (blue) and after several hours (red). Red spectrum shows signal intensity over 90,000 counts in 1 second acquisitions, while blue trace shows signal intensity at  $\sim 5,000$  counts in 2 minutes. (B) An optical image of the spin-coated window taken with a 10X objective (Ziess), reveals that  $\beta$ -nocaryophyllinic acid (**III-6**) crystallizes slowly over time, forming a chiral crystalline material with a strong nonlinear bulk SFG response. The white scale bar represents  $20 \mu\text{m}$ .

### 3.5. Phase-resolved SFG spectroscopy.

**3.5.1. Internal heterodyne SFG introduction and experimental details.** We employ a recently established<sup>32, 65-67</sup> internal heterodyne method to obtain phase-resolved SFG spectra of, and thus structural information on, the  $\beta$ -caryophyllene oxidation products spin-coated on *z*-cut  $\alpha$ -quartz.

The phase-resolved SFG measurements discussed herein were collected with Dr. Hilary Chase, a recent graduate of our lab. Phase-resolved SFG responses are obtained directly, and without the need of an additional external local oscillator as seen in conventional heterodyne SFG set-ups.<sup>68-</sup>

<sup>70</sup> Briefly, when measuring an SFG spectrum of a sample deposited onto *z*-cut  $\alpha$ -quartz, the resulting SFG response contains contributions from (A) the bulk quartz and (B) the molecules adsorbed on the quartz. The nonlinear susceptibility contribution from the adsorbed layer

contains both real and imaginary components. The intensity of the SFG spectrum,  $I$ , that is directly measured is given by equation 3.2:

$$I \propto \left| \chi_{S,eff}^{(2)} \right|^2 = \left| \chi_{S,Re}^{(2)} + i\chi_{S,Im}^{(2)} + i\chi_{Quartz}^{(2)} \right|^2 \quad (3.2)$$

Here,  $\chi_{S,eff}^{(2)}$  is the effective nonlinear susceptibility from the surface,  $\vec{\chi}_{S,Re}^{(2)}$  is the real part of the nonlinear susceptibility from the adlayer,  $\vec{\chi}_{S,Im}^{(2)}$  is the imaginary component of the nonlinear susceptibility, and  $\vec{\chi}_{Quartz}^{(2)}$  is the nonlinear response from the quartz bulk. The  $\vec{\chi}_{Quartz}^{(2)}$  term is assumed to be off-resonance, therefore remaining a constant throughout the experiment, and  $\chi_{S,eff}^{(2)}$  is assumed to contribute much less than  $\vec{\chi}_{Quartz}^{(2)}$ . Therefore, equation 1 can be reduced down to following expressions, equation 2 and equation 3.

$$I = \left| \vec{\chi}_{Quartz}^{(2)} \right|^2 + 2\vec{\chi}_{Quartz}^{(2)} \cdot \vec{\chi}_{S,Im}^{(2)} + \left| \vec{\chi}_S^{(2)} \right|^2 \quad (3.3)$$

$$\approx \left| \vec{\chi}_{Quartz}^{(2)} \right|^2 + 2\vec{\chi}_{Quartz}^{(2)} \cdot \vec{\chi}_{S,Im}^{(2)} \quad (3.4)$$

Thus, as long as the azimuthal angle ( $\phi$ ) of the quartz substrate is known, the sign of  $\vec{\chi}_{S,Im}^{(2)}$  is readily obtained directly. A brief experimental description for phase-resolved measurements using quartz follows. Synthetic standards **III-1–III-4** were selected as representatives within our available molecular suite for phase-resolved measurements, and all samples were spin-coated onto z-cut  $\alpha$ -quartz (right-handed, size 12.7 x 12.7 x 5 mm, Conex System Technology) analogous to what is described in Section 3.3.2. The incident visible and IR beams were focused onto the top side of the quartz piece. Spectra reported herein are an average of 5 individual spectra each acquired for 5 minutes. *ssp*-Polarized spectra of the quartz were obtained at azimuthal angles of  $\phi = 0^\circ$  and  $\phi = 180^\circ$ . The individual spectra were normalized to the spectrum

of clean  $\alpha$ -quartz at the same azimuthal angle. **Figure 3.6** shows an example of the *ssp*-Polarized SFG spectra of clean  $\alpha$ -quartz compared to a spectrum of an oxidation product spin-coated onto the quartz piece at  $\phi=0^\circ$ , which shows clear peaks that are in- and out-of-phase with respect to the quartz.

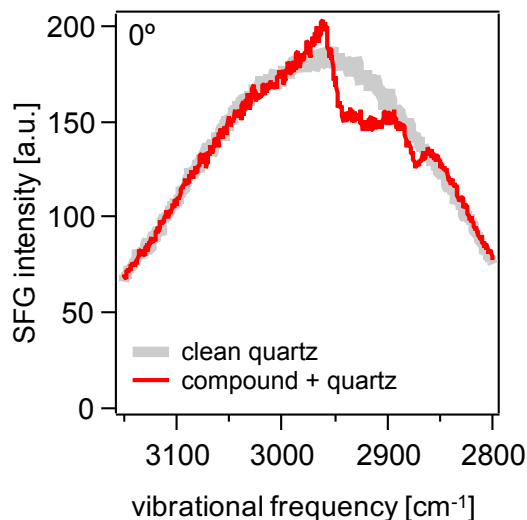


**Figure 3.6.** Comparison of *ssp*-Polarized SFG spectrum of clean  $\alpha$ -quartz (gray trace) and the spectrum with  $\beta$ -nocaryophyllonic acid (**III-4**) spin-coated onto the quartz piece at  $\phi=0^\circ$ .

**3.5.2. Computational methods used to interpret phase-resolved data.** All DFT calculations were performed by Dr. Hilary Chase to aid in spectral analysis of the phase-resolved data. Similar to our previous work,<sup>71-72</sup> geometries for a number of different conformers of each oxidation product were optimized by using B3LYP<sup>73-75</sup>/6-311G(d,p)<sup>76</sup> via the Gaussian '09 software package located at Yale University.<sup>77</sup> Upon optimization, the harmonic and anharmonic frequencies were calculated in addition to the dipole and polarizability derivatives with respect to each normal mode. We identified Fermi resonances through a previously described procedure<sup>71-72, 78</sup> that employs a multi-mode Fermi resonance Hamiltonian with a frequency cutoff of 10  $\text{cm}^{-1}$ . According to this model, if an overtone or combination band is within 10  $\text{cm}^{-1}$  of a fundamental

vibrational mode, the modes couple and result in a shift in frequencies and intensities dependent on the coupling constant. Additional frequency cutoffs were tested, however, a  $10\text{ cm}^{-1}$  cutoff appeared to result in the closest spectral matches across all of the oxidation products.

**3.5.3. Analysis of phase-resolved spectra.** Accounting for Fermi resonances as determined by the DFT calculations of Dr. Hilary Chase, we obtain similar mode assignments for the dominant peaks in the experimental SFG spectra of the oxidation products studied here. The Fermi resonance-corrected DFT calculations indicate that the two largest signal intensities at  $\sim 2940$  and  $\sim 2860\text{ cm}^{-1}$  are from the  $\text{CH}_2$ -symmetric and the  $\text{CH}_3$ -symmetric stretches present on the four-membered ring motif, respectively. These assignments resemble those of  $\alpha$ -pinene, a molecule that has some similar structural motifs (geminal methyl groups on a four-membered ring) to the compounds studied here.<sup>78-79</sup> Specifically, by SFG and DFT, it was found that a majority of the peak intensity in the SFG spectrum of  $\alpha$ -pinene was due to contributions of the methylene group within the four-membered ring, which also exhibited the longest vibrational decoherence lifetimes.<sup>54</sup> There are likely some lower intensity vibrational modes present in the spectrum, but the general assignment holds for the compounds studied here for the dominant peaks.

The phase-resolved SFG spectra are rather similar across oxidation products **III-1–III-4**, therefore we include a representative *ssp*-polarized phase-resolved SFG spectrum of  $\beta$ -caryophyllene aldehyde (**III-1**) on  $\alpha$ -quartz at an azimuthal angle of  $0^\circ$  in **Figure 3.7A**. The interference (difference) SFG spectrum shows a positive peak at  $2950\text{--}2960\text{ cm}^{-1}$ , a negative peak from  $2910\text{--}2940\text{ cm}^{-1}$ , and a small negative peak near  $2850\text{--}2880\text{ cm}^{-1}$ . Based on the vibrational mode assignments and the azimuthal angle of quartz, we identify the sign of  $\vec{\chi}_{S,Im}^{(2)}$ , and therefore deduce the orientation of four-membered ring on  $\beta$ -caryophyllene aldehyde (**III-1**)

(and by extension that of the other oxidation products) at the quartz surface (please see Appendix 2, Section A2.1). The analysis indicates that the negative interference peak indicates that the CH<sub>3</sub> groups on the cyclobutane ring face away from the surface, just like its methylene group.

In addition to an “up” versus “down” determination of the discussed stretches on the cyclobutane ring given by the phase-resolved SFG results, a hybrid experimental/DFT method previously published for simulating SFG spectra and carrying out conformational analysis<sup>71-72</sup> was used to determine the molecular orientation that gives the best matched SFG spectrum (**Figure 3.7B**) to the spectrum of compound **III-1** spin-coated on fused silica in the C–H region. With this information in mind, the probable orientation of  $\beta$ -caryophyllene aldehyde (**III-1**), and by extension, the remaining oxidation products studied, is given in **Figure 3.7C**. This orientation is reasonable for a somewhat amphiphilic molecule as it enables hydrogen bonding of the oxygenated groups to the Si–OH groups on the quartz surface. We were unable to obtain phase-resolved spectra within the C=O stretching region; however, the negligible *ppp*-polarized signal intensities suggest that the C=O functional groups within the molecule are aligned nearly perpendicular to the surface, resulting in strong *ssp*-polarized signal intensities. Note that polarization intensity ratio analyses<sup>50</sup> using the *ssp*- and *ppp*-polarized spectra in **Figure 3.2** were unsuccessful due to minimal *ppp* signal for the isolated 2860 cm<sup>-1</sup> CH<sub>3</sub>-symmetric (ring) stretch (see **Figure A2.2** in Appendix 2). Altogether, the orientation analysis of complex molecules on a model surface enabled here by phase-resolved SFG measurements opens the possibility to carry out such analyses on the surfaces of synthetic and field-derived SOM.

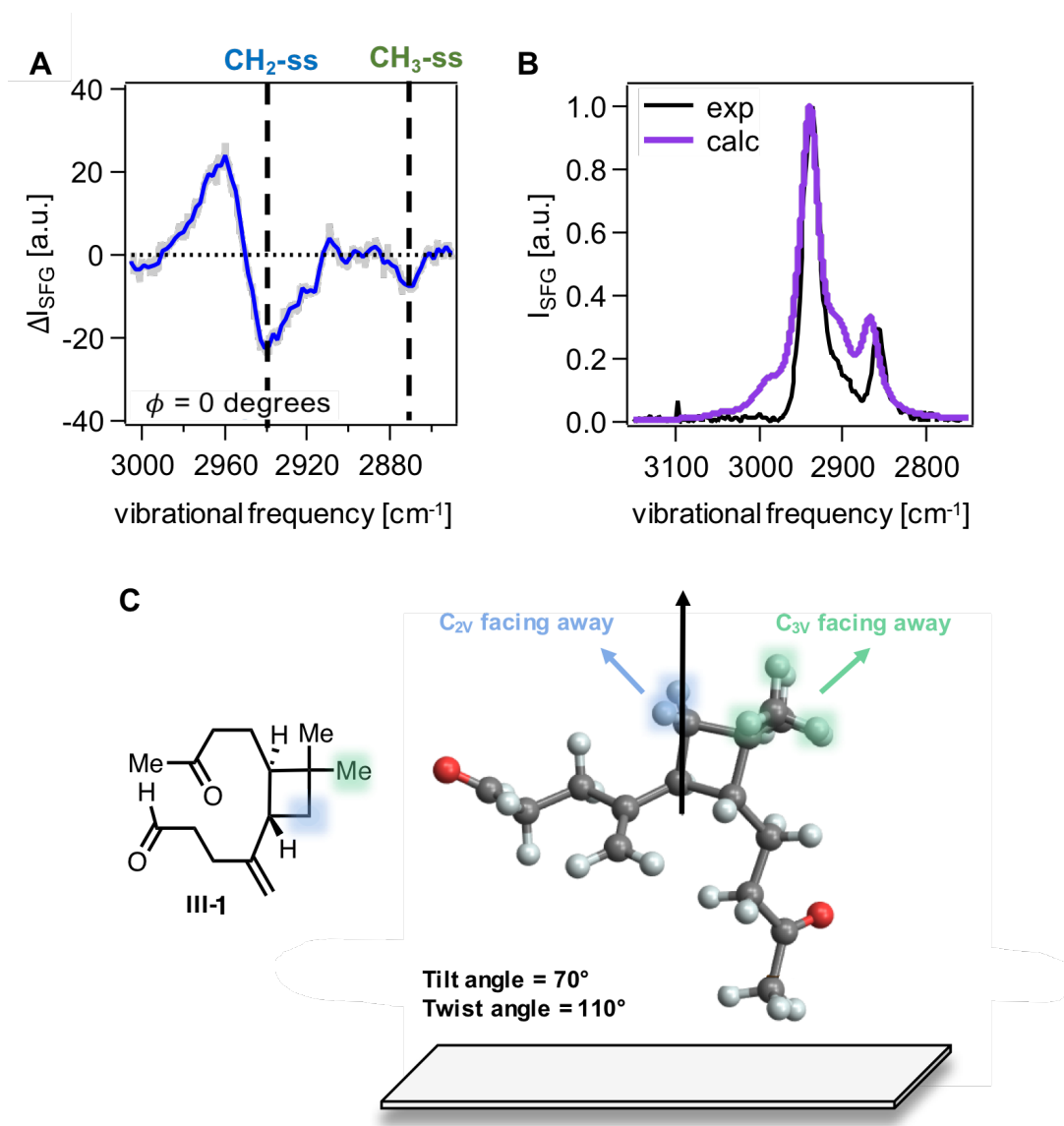


**Figure 3.7.** (A) Phase-resolved *ssp*-polarized SFG spectrum of  $\beta$ -caryophyllene aldehyde (**III-1**) on  $\alpha$ -quartz with quartz oriented at  $\phi = 0^\circ$ ; (B) Best matched SFG simulation (purple trace) overlaid to experimental HR spectrum (black trace) of compound 1 (spin-coated on fused silica); (C) Proposed orientation of  $\beta$ -caryophyllene aldehyde (**III-1**) on the  $\alpha$ -quartz surface based on phase-resolved data and comparison of calculated vs. experimental SFG spectra (tilt and twist angles of the assigned Z-axis with respect to surface normal (black arrow) are  $70^\circ$  and  $110^\circ$ , respectively).

**3.6. Atmospheric implications and conclusions.** This work integrates organic synthesis, aerosol generation and collection, DFT calculations, and SFG spectroscopy to search for the presence of sesquiterpene-derived oxidation products, specifically those derived from  $\beta$ -caryophyllene, on the surfaces of synthetic  $\beta$ -caryophyllene-derived SOM. Polarization-resolved SFG spectra of  $\beta$ -caryophyllene aldehyde (**III-1**), along with  $\beta$ -caryophyllonic acid (**III-3**), most closely match those of the  $\beta$ -caryophyllene-derived SOM, both in the C–H and the C=O stretching regions, but especially the former. These two compounds also appear to be the most surface active out of the series based on our previously reported dynamic surface tension measurements, as they lead to the largest depressions of interfacial tension in aqueous droplets.<sup>21</sup>

The present study cannot unequivocally identify the oxidation products on the  $\beta$ -caryophyllene-derived SOM surface, though a comprehensive compositional analysis of the SOM examined herein is forthcoming in future work. Nevertheless,  $\beta$ -caryophyllene aldehyde (**III-1**) and  $\beta$ -caryophyllonic acid (**III-3**) have previously been positively identified in several non-surface-specific ambient field SOM<sup>25, 29</sup> and laboratory  $\beta$ -caryophyllene ozonolysis<sup>26-27, 80</sup> studies. Considering thermal methods such as GC/MS<sup>26, 29</sup> and SV-TAG<sup>25</sup> may cause decomposition,<sup>81</sup> one possible caveat is that compounds **III-1** and **III-3** could have actually formed as analytical artifacts in such studies. Yet, these compounds have also been detected using ESI-MS coupled with liquid chromatography,<sup>27, 80</sup> which does not rely on high temperature conditions, supporting their existence as  $\beta$ -caryophyllene oxidation products detected in SOM. Furthermore, we note that compounds **III-1** and **III-3** bear an intact alkene adjacent to the cyclobutane ring, allowing them to potentially further react in the presence of atmospheric ozone. Indeed, the rate constant of the endocyclic alkene is  $\sim 100$  times greater than that of the exocyclic

double bond.<sup>27</sup> We presume that  $\beta$ -caryophyllene aldehyde (**III-1**) and  $\beta$ -caryophyllonic acid (**III-3**) may still serve as important SOM constituents given their high surface activities, even considering their likely limited lifetimes as first generation products in the atmosphere. We note that the potential presence of highly oxidized molecules (HOMs), an important yet elusive class of SOA constituents,<sup>82-86</sup> was not considered because of (1) the likelihood of decomposition of HOMs in the SOM upon shipping, handling, and spectroscopic analysis, and (2) the significant challenges that would arise in the synthesis of such standards given their reported instabilities and relatively short lifetimes.<sup>87-89</sup>

Our current and recent studies<sup>21</sup> provide concrete lines of evidence supporting that SOM surfaces may be disproportionately populated by a minority subset of compounds that exhibit amphiphilic or surfactant-like properties. We caution that mismatches between the spectra of the other compounds and that of the SOM may be due to a lack of surface activity of these molecules and therefore a propensity to sit in the bulk of the particles. Although mismatches presumably could be due to surface oscillator orientation changes within the SOM, we do not expect diffusion that may cause molecular orientation changes within the  $\beta$ -caryophyllene-derived particles to be likely at the ambient laboratory RH conditions (~40% RH) used in this study.<sup>90</sup>

Additionally, orientation analysis by phase-resolved SFG spectroscopy reveals a “pincer-like” configuration of the  $\beta$ -caryophyllene oxidation products, albeit on a model quartz surface, that somewhat resembles the orientation of double-tailed surfactants at the surfaces biological systems. This configuration orients the cyclobutane moiety away from the surface, enabling hydrogen bonding of the terminal oxygenated functional groups to the quartz substrate. Though quartz serves as a distant model system for an actual aerosol particle surface, an analogous orientation at a particle surface may be promoted by the presence of water, inorganic salts,

highly oxidized molecules, or any other plausible constituents that could induce polarity, charge density, or hydrogen bonding capabilities at the particle surface. Moreover, the “pincer-like” configuration adopted by the  $\beta$ -caryophyllene oxidation products suggests that the less polar moiety of a surface-localized oxidation product, such as those studied here, may be the first site-of-contact for a gas-phase molecule approaching an aerosol particle. Yet, similar investigations of additional SOM constituents are needed in order to fully realize the implications of understanding interfacial structure and orientation on the heterogeneous chemistry leading to particle growth, cloud activation, and other aerosol processes in the atmosphere.

The observed close spectral matches between  $\beta$ -caryophyllene-derived SOM surfaces and  $\beta$ -caryophyllene aldehyde (**III-1**) and  $\beta$ -caryophyllonic acid (**III-3**) presented herein, and the high surface tension depression described previously<sup>21</sup> for these same oxidation products open the possibility for revealing an intrinsically chemical origin for cloud activation. Indeed, the considerable surface activity points to a high likelihood that these molecules may occupy the surfaces of SOA particles formed from  $\beta$ -caryophyllene oxidation in the atmosphere. Taken together, the discussed interfacial tension and SFG results in Chapters 2 and 3, respectively, also suggest that the terpene-derived surfactant pool at SOA particle surfaces may be far less chemically complex than that present in the particle bulk. Such findings on the structure and orientation of terpene-derived oxidation products and their corresponding SOM at interfaces may improve our understanding of the drivers of heterogeneous processes at SOM surfaces containing such species. With the goal of moving towards interfacial conditions more closely applicable to cloud droplet-forming scenarios, Chapter 4 will next expand upon the work highlighted in Chapters 2 and 3 by describing SFG spectroscopy experiments on this same suite of  $\beta$ -caryophyllene-derived ozonolysis products at air/aqueous interfaces.

## CHAPTER 4

### Surface-Active $\beta$ -Caryophyllene Oxidation Products at the Air/Aqueous Interface

**Portions of this chapter are reproduced in part  
with permission from the American Chemical Society:**

Bé, A. G.; Liu, Y.; Tuladhar, A.; Bellcross, A. D.; Wang, Z.; Thomson, R. J.; Geiger, F. M., Surface-Active  $\beta$ -Caryophyllene Oxidation Products at the Air/Aqueous Interface. *ACS Earth Space Chem.* **2019**, 3 (9), 1740–1748.

**4.1. Introduction and motivation.** The interactions between particulate matter and ambient water in the atmosphere remain central to elucidating the evolution and fate mechanisms, physicochemical properties, as well as both direct and indirect effects of atmospheric aerosols on the climate system.<sup>1-2</sup> Modulations of the viscosity,<sup>3-6</sup> diffusivity,<sup>7</sup> chemical reactivity,<sup>8-9</sup> as well as liquid-liquid phase separation exhibited by aerosol particles<sup>6, 10-14</sup> have been revealed under varying RH scenarios, for instance. Additionally, as detailed in Chapter 2, aerosol particles can serve as CCN that activate cloud droplet formation,<sup>15-21</sup> and the presence of surface-active organic constituents that localize at the air/aqueous interface can reduce the surface tension of forming droplets containing aerosol nuclei.<sup>15, 17-18, 20, 22-25</sup> Moreover, such surface-active molecules may play an important role in cooperative adsorption processes, where the presence of an adsorbed insoluble monolayer at the vapor/aqueous interface may further promote the surface enrichment of soluble organic species in the aerosol bulk, thereby influencing aerosol-mediated cloud droplet nucleation.<sup>26-28</sup> Numerous studies have provided estimates for the relative aqueous surface activities of several organic species likely present within aerosol mixtures,<sup>17, 29-34</sup> along with laboratory and field aerosol samples themselves.<sup>19, 35-37</sup> Yet, establishing how the interfacial organization of such compounds on an aqueous subphase alters aerosol surface properties, and thus CCN activities, remains challenging.<sup>38-41</sup> Therefore, molecular-level insights into the organization of surface-active molecules at atmospherically relevant air/aqueous interfaces are needed to reveal the molecular origins of CCN-driven cloud activation.

Chapter 2 investigated the surface tension of mm-sized aqueous droplets containing a suite of structurally related monomeric oxidation products that were previously reported to be present in biogenic SOM derived from ozonolysis of  $\beta$ -caryophyllene.<sup>17</sup> Following the synthesis of authentic standards of these  $\beta$ -caryophyllene-derived ozonolysis products, surface tension

measurements revealed their higher surface activities relative to other oxidation products derived from  $\alpha$ -pinene<sup>17</sup> and isoprene,<sup>34</sup> with the highest surface activity exhibited by  $\beta$ -caryophyllene aldehyde (**IV-1**) within the entire suite.<sup>17</sup> Following the work outlined in Chapter 2, Chapter 3 reported on our attempts to spectroscopically benchmark these  $\beta$ -caryophyllene-derived molecules to the surface of laboratory particle-phase  $\beta$ -caryophyllene-derived SOM.<sup>42</sup> Using vibrational nonlinear spectroscopy, namely SFG spectroscopy, to probe the interfacial structure and orientation of this molecular suite, we provided a qualitative SFG analysis of the surface composition of the SOM using our synthetic standards.<sup>42</sup>

In this chapter, we expand upon the aforementioned work in Chapters 2 and 3 by probing this same suite of  $\beta$ -caryophyllene-derived ozonolysis products at the interface between ambient air and liquid water as well as aqueous solutions of ammonium sulfate with the goal of studying their interfacial molecular coverage and structural organization under conditions broadly applicable to cloud-forming droplet scenarios. We present spectral differences in polarization-resolved HR-BB SFG spectra recorded in the C–H stretching region across the full series of  $\beta$ -caryophyllene-derived oxidation products at high surface coverages. We also explore the SFG response of the most surface-active compound in the series,  $\beta$ -caryophyllene aldehyde (**IV-1**), over a broad range of surface coverages, at both the water and ammonium sulfate (aq) subphases across the C–H and the O–H stretching continuum using a standard resolution scanning SFG spectrometer. Moreover, the SFG experiments presented herein represent the first of several ongoing studies to probe the structure, orientation, and reactivity of surface-active organic species within interfacial environments relevant for understanding aerosol–cloud–climate interactions in the atmosphere.

**4.2. Synthesis of oxidation products and preparation of sample solutions.** The synthesis and characterization of the  $\beta$ -caryophyllene-derived oxidation products **IV-1–IV-6** are detailed in Section 2.2 of Chapter 2.<sup>17, 42</sup> We note that aldehydes **IV-1** and **IV-2** each readily react with water and there exist in equilibrium with their hydrate form under the conditions studied in this work.<sup>17</sup> However, for simplicity, we refer here to compounds **IV-1** and **IV-2** as caryophyllene aldehyde and  $\beta$ -nocaryophyllone aldehyde, respectively. To prepare sample solutions of  $\beta$ -caryophyllene ( $\geq 98.5\%$ , Sigma Aldrich Inc.) and the synthesized  $\beta$ -caryophyllene oxidation products, each compound was dissolved in  $\text{CDCl}_3$  at a concentration of 1 mg/mL. Nanopure water produced by an ion exchange system (U.S. Filter) was used as a subphase, as well as for preparing aqueous solutions of 1 M ammonium sulfate  $[(\text{NH}_4)_2\text{SO}_4]$  (99.999%, metal basis, Sigma Aldrich).

### **4.3. SFG spectroscopy at the air/aqueous interface.**

**4.3.1. Experimental details for SFG spectroscopic measurements.** Measurements were carried out on two SFG spectrometers, a ps scanning system and a fs HR-BB system, which have been described in detail in previous work.<sup>43-46</sup> SFG measurements were collected with a fellow graduate student, Yangdongling Liu, with help from Dr. Aashish Tuladhar at EMSL, a DOE Office of Science user facility at PNNL. On the scanning SFG system (EKSPLA, Lithuania), a tunable IR beam and a 532-nm visible beam are overlapped spatially and temporarily on the air/aqueous interface at incident angles of  $55^\circ$  and  $65^\circ$ , respectively. A brief overview of the HR-BB system can be found in Section 3.4.2 in Chapter 3. All measurements were performed under ambient conditions of laboratory temperature (20–25 °C) and RH (30–40% RH). During the experiment, a 90 mm diameter Pyrex petri dish (Fisher Scientific), which was selected in order to avoid any potential edge meniscus effects that could arise using smaller-sized dishes, was ozone-

cleaned for 30 min, placed on the sample stage, and subsequently filled with 20 mL of 1 M ammonium sulfate (aq) or neat water as the subphase. A selected volume of the 1 mg/mL sample solution was then added dropwise using a flat-tipped microsyringe onto the surface of the subphase gently and slowly so as to allow the sample solution to spread across the air/aqueous interface. Following the addition, the sample was left for 5–10 min to ensure complete evaporation of the  $\text{CDCl}_3$  prior to SFG measurements. The signal intensities at two different frequencies (2850 and 2940  $\text{cm}^{-1}$ ) in the C–H region were recorded over time for varying amounts of  $\beta$ -caryophyllene aldehyde (**IV-1**) on 1 M ammonium sulfate (aq) and neat water subphases to ensure that no significant effects from surface–bulk partitioning and/or subphase evaporation occur during the data collection period (**Figure 4.1**). The signal intensities do not change over the course of the 30 minutes, indicating that equilibrium is rapidly established upon sample addition, and subphase evaporation does not appreciably occur during each single spectral acquisition. Nevertheless, possible water evaporation over the course of lengthier experiments with multiple acquisitions (up to 3–4 hours in total) was compensated for by optimizing the signal intensity between acquisitions via slight adjustment ( $\sim 1$  mm total) of the sample stage height. Yet, monitoring the height of the aqueous surface relative to a reference z-cut quartz crystal surface using a displacement sensor would be a more desirable approach to accurately probing the air/water interface, which could be a focus of future work.<sup>47-48</sup>

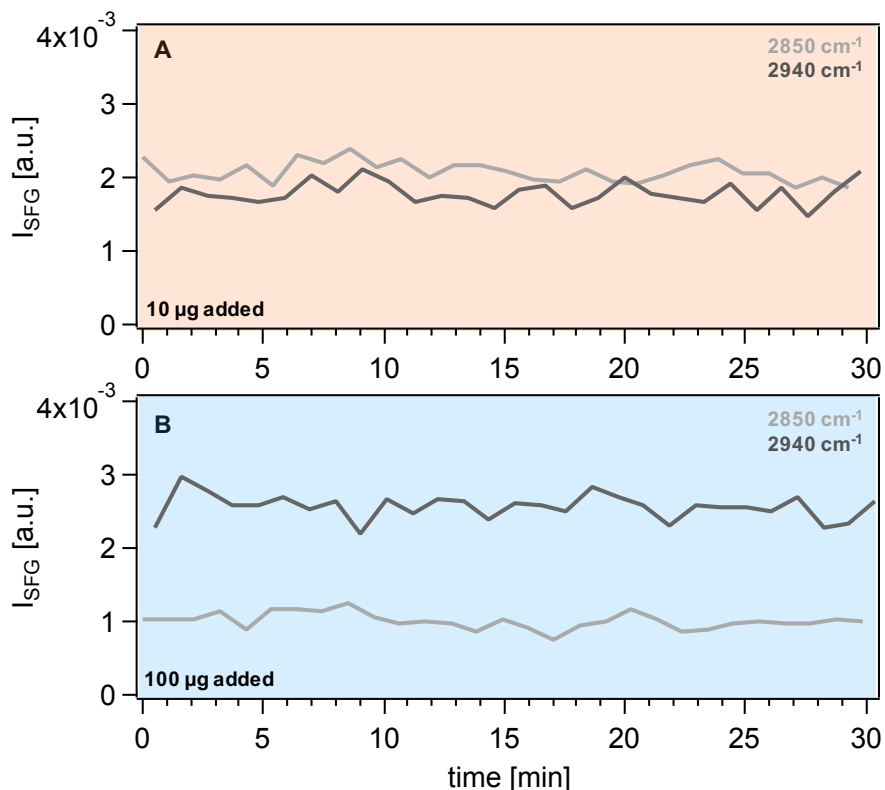


**Figure 4.1.** SFG signal intensity at 2850 and 2940  $\text{cm}^{-1}$  over the course of 30 minutes for (A) 10  $\mu\text{g}$  of  $\beta$ -caryophyllene aldehyde (**IV-1**) on 1 M  $(\text{NH}_4)_2\text{SO}_4$  (aq) and (B) 100  $\mu\text{g}$  of  $\beta$ -caryophyllene aldehyde (**IV-1**) on neat water.

*ssp*- and *ppp*-Polarized HR SFG spectra in the C–H stretching region (2800–3000  $\text{cm}^{-1}$ ) were collected for each sample compound on 1 M ammonium sulfate (aq) at two or more different surface coverages (see Appendix 2, **Figure A2.8** for spectra at all surface coverages measured).  $\beta$ -caryophyllene aldehyde (**IV-1**) was also measured using neat water as the subphase to compare to the 1 M ammonium sulfate (aq) data for this compound. Each spectrum reported is an average of triplicate or quadruplet measurements each recorded for 5 min and subsequently binned over every 5 data points to increase the signal-to-noise ratio. The frequencies were calibrated using DMSO.<sup>45</sup> The intensities were referenced to the *ssp*-polarized non-resonant SFG signal of a 5 mm thick z-cut  $\alpha$ -quartz crystal and then normalized to the maximum peak intensity of each spectrum.

For concentration-dependent experiments with  $\beta$ -caryophyllene aldehyde (**IV-1**), *ssp*-polarized SFG spectra were collected on the scanning system in the C–H (2800–3000  $\text{cm}^{-1}$ ) and O–H (3000–3800  $\text{cm}^{-1}$ ) stretching regions on 1 M ammonium sulfate (aq) at smaller surface coverage increments than those in the aforementioned experiments on the HR-BB system. Each spectrum reported is an average of duplicate or triplicate measurements (See Appendix 2, **Figure A2.9–A2.10** for individual spectra), with signal intensities corrected by the IR and visible beam powers. In the C–H region, the optical alignment was optimized based on the SFG response from a 200  $\mu\text{m}$  thin z-cut  $\alpha$ -quartz crystal at 2950  $\text{cm}^{-1}$ , whereas in the O–H region, the system was aligned based on the signal at 3700  $\text{cm}^{-1}$ . Therefore, the spectra in the C–H and O–H stretching regions presented herein are plotted separately. In addition, in the C–H (2800–3000  $\text{cm}^{-1}$ ) and free O–H (3600–3800  $\text{cm}^{-1}$ ) stretching regions, the spectra were recorded at a step size of 4  $\text{cm}^{-1}$ , and in the hydrogen-bonded O–H stretching region (3000–3600  $\text{cm}^{-1}$ ), the spectra were recorded every 8  $\text{cm}^{-1}$ . Thus, the free O–H and hydrogen-bonded O–H regions are normalized to their own maximum intensities (with relative intensities retained) and plotted separately (a gap inserted in between) to indicate that the two traces were recorded in separate acquisitions. Moreover, because the sample stage height was slightly adjusted between each acquisition to compensate for water evaporation over time, as mentioned above, we avoid quantitatively comparing or interpreting the relative intensities of two different traces. Raw data with absolute intensities, before any normalization, are included in Appendix 2 (**Figures A2.9–A2.11**).

**4.3.2. High resolution SFG spectra of  $\beta$ -caryophyllene and its oxidation products at the air/ammonium sulfate (aq) interface.** The *ssp*- and *ppp*-polarized HR vibrational SFG spectra in the C–H stretching region of  $\beta$ -caryophyllene and its oxidation products at air/ammonium sulfate (aq) interface at high surface coverages are shown in **Figure 4.2**. As mentioned in

Chapter 3, the *ssp* polarization combination probes those components of the transition dipole moments that are oriented perpendicularly to the surface, while the *ppp* polarization combination is sensitive to off-diagonal elements necessary for a molecular orientation analysis.

All *ssp*-polarized spectra contain two prominent peaks at  $2940 \pm 5 \text{ cm}^{-1}$  and  $2860 \pm 5 \text{ cm}^{-1}$ , similar to the SFG responses previously observed in the condensed-phase spectra of these compounds collected in the C–H region.<sup>42</sup> The air/ammonium sulfate (aq) spectra of  $\beta$ -nocaryophyllone aldehyde (**IV-2**) and  $\beta$ -nocaryophyllinic acid (**IV-6**) both show a dominant peak around  $2880 \text{ cm}^{-1}$ , while the rest of the  $\beta$ -caryophyllene oxidation products show a weak peak at that frequency. This  $\sim 2880 \text{ cm}^{-1}$  peak is absent in the air/ ammonium sulfate (aq) spectrum of the precursor,  $\beta$ -caryophyllene, as well as previously reported condensed-phase spectra.<sup>42</sup> A small peak between  $2900 \text{ cm}^{-1}$  and  $2910 \text{ cm}^{-1}$  is also observed in the air/ ammonium sulfate (aq) spectra of  $\beta$ -caryophyllene,  $\beta$ -caryophyllonic acid (**IV-3**),  $\beta$ -nocaryophyllonic acid (**IV-4**),  $\beta$ -caryophyllinic acid (**IV-5**), and  $\beta$ -nocaryophyllinic acid (**IV-6**).

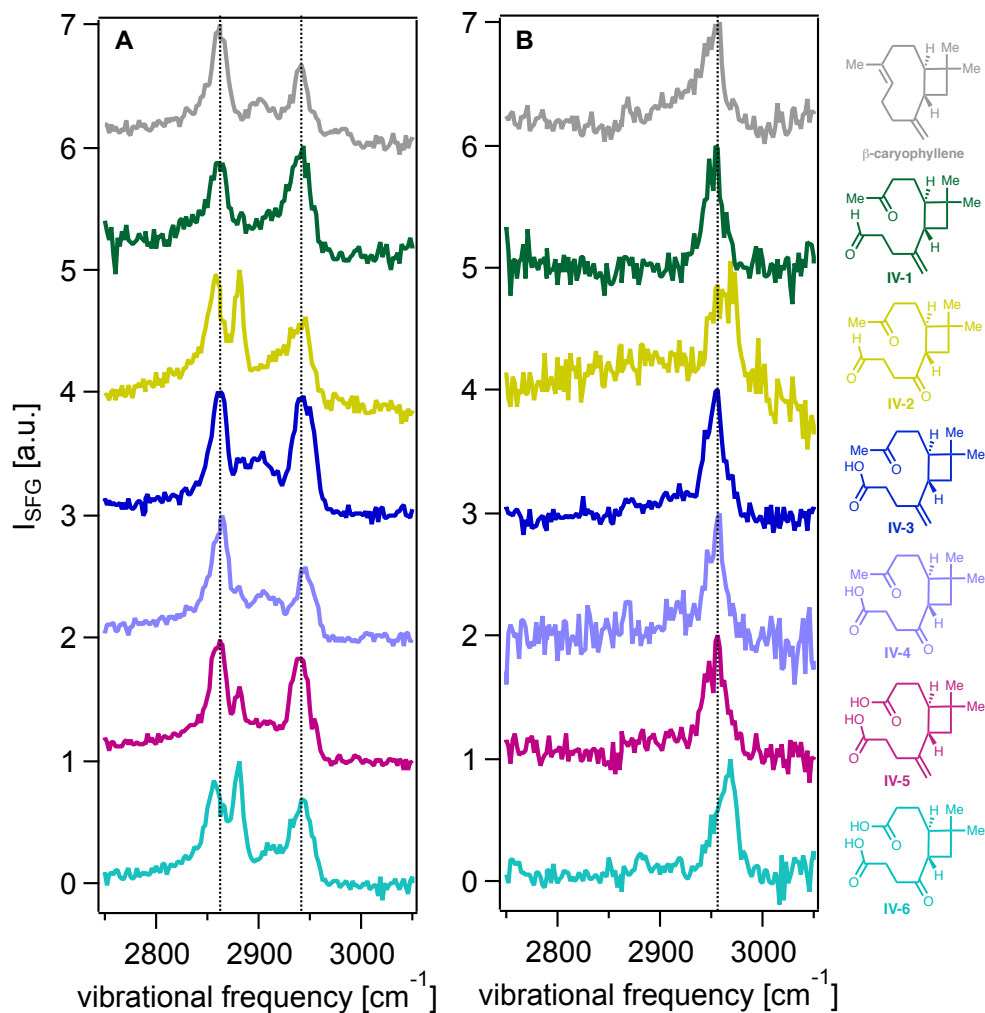


**Figure 4.2.** (A) *ssp*- and (B) *ppp*-polarized SFG spectra of  $\beta$ -caryophyllene oxidation products on 1 M ammonium sulfate (aq) collected in the C–H region. Each sample was dissolved in  $\text{CDCl}_3$  at a concentration of 1 mg/mL, and the spectra were collected with 100  $\mu\text{L}$  of the solution (100  $\mu\text{g}$  of the sample) spread on the surface of 1 M ammonium sulfate (aq), except for  $\beta$ -caryophyllene (gray trace, 2 mg added) and  $\beta$ -nocaryophyllone aldehyde (**IV-2**) (yellow trace, 250  $\mu\text{g}$  added).

Overall, the *ssp*-polarized spectra in the C–H region of  $\beta$ -caryophyllene and  $\beta$ -caryophyllene aldehyde (**IV-1**) at air/ ammonium sulfate (aq) interface share common vibrational features with their condensed-phase counterparts,<sup>42</sup> despite the notable differences in relative peak intensities. These spectral similarities observed at the two different interfaces probed may

arise as a result of the relatively weak interactions of these two molecules with both the aqueous subphase and the fused silica substrate used in our earlier work,<sup>42</sup> which may be reasonable given the high surface activity of  $\beta$ -caryophyllene aldehyde (**IV-1**) as well as the (nominally apolar) hydrocarbon skeleton of  $\beta$ -caryophyllene.<sup>17</sup> The spectra of  $\beta$ -caryophyllonic acid (**IV-3**),  $\beta$ -nocaryophyllonic acid (**IV-4**), and  $\beta$ -caryophyllinic acid (**IV-5**) in both environments also consist of similar features, except that the spectra obtained at the air/ammonium sulfate (aq) interface exhibit a small peak around  $2880\text{ cm}^{-1}$ . In contrast,  $\beta$ -nocaryophyllone aldehyde (**IV-2**) and  $\beta$ -nocaryophyllinic acid (**IV-6**) show distinctly different spectra at the air/ammonium sulfate (aq) interface compared to in the condensed phase, which implies relatively strong perturbations of the molecular structure or orientation by the aqueous subphase. This interpretation is consistent with the previous finding that  $\beta$ -nocaryophyllone aldehyde (**IV-2**) and  $\beta$ -nocaryophyllinic acid (**IV-6**) are the least surface-active molecules in the suite of  $\beta$ -caryophyllene oxidation products studied. The *ppp*-polarized spectra of  $\beta$ -caryophyllene,  $\beta$ -caryophyllene aldehyde (**IV-1**),  $\beta$ -caryophyllonic acid (**IV-3**),  $\beta$ -nocaryophyllonic acid (**IV-4**), and  $\beta$ -caryophyllinic acid (**IV-5**) all consist of a single distinct peak centered around  $2955\text{ cm}^{-1}$ , which is slightly blue-shifted compared to the condensed-phase spectra.<sup>42</sup> In contrast, the spectrum of  $\beta$ -nocaryophyllinic acid (**IV-6**) contains a single peak around  $2968\text{ cm}^{-1}$ , and  $\beta$ -nocaryophyllone aldehyde (**IV-2**) shows two peaks around  $2955\text{ cm}^{-1}$   $2968\text{ cm}^{-1}$ .

Each spectrum shown in **Figure 4.2** was obtained after adding  $100\text{ }\mu\text{L}$  of the  $1\text{ mg/mL}$  sample solution ( $100\text{ }\mu\text{g}$  of the sample) to the surface of  $1\text{ M}$  ammonium sulfate (aq), except for  $\beta$ -caryophyllene (gray trace) and  $\beta$ -nocaryophyllone aldehyde (**IV-2**) (yellow trace). When  $100\text{ }\mu\text{L}$  of  $\beta$ -caryophyllene solution or  $\beta$ -nocaryophyllone aldehyde (**IV-2**) solution was spread onto

the surface in the same way as for the other samples, both the *ssp*- and *ppp*-polarized SFG signals were too low to be distinguished from noise. This observation could be explained by two hypotheses: these two molecules are completely disordered on the surface and therefore no break of symmetry exists, which is necessary for there to be SFG signal, or a significant portion of the population of molecules partitions to the bulk phase, resulting in low surface coverage at equilibrium. For  $\beta$ -caryophyllene, which is a bicyclic hydrocarbon, the former hypothesis is reasonable because it likely does not exhibit a significant preference in molecular conformations or orientations on the aqueous surface, nor does it partition to an aqueous bulk phase. After 2 mg of  $\beta$ -caryophyllene was directly added to the surface, a comparable signal-to-noise ratio was achieved (**Figure 4.2**), presumably because of the formation of a new air/neat  $\beta$ -caryophyllene interface and a net ordering of the interfacial species. Similar surface organization for molecules lacking strong polarity has been observed and interpreted in the literature.<sup>49-50</sup> For  $\beta$ -nocaryophyllone aldehyde (**IV-2**), the former hypothesis is unlikely, considering its structural similarity to the other  $\beta$ -caryophyllene oxidation products in the suite. The latter hypothesis, however, is consistent with our previous report of  $\beta$ -nocaryophyllone aldehyde (**IV-2**) being the least surface active among the  $\beta$ -caryophyllene oxidation products.<sup>17</sup> A distinguishable signal intensity was observed upon the addition of 250  $\mu$ L of  $\beta$ -nocaryophyllone aldehyde (**IV-2**) solution (250  $\mu$ g) to the air/ ammonium sulfate (aq) interface. In other words, an addition of 2.5 times more  $\beta$ -nocaryophyllone aldehyde (**IV-2**) was required to achieve a surface coverage comparable to those of the other  $\beta$ -caryophyllene oxidation products after the surface–bulk partitioning equilibrium was reached.

**4.3.3. Probing surface coverage-dependent structural organization of  $\beta$ -caryophyllene aldehyde at the air/ammonium sulfate (aq) interface.** The average orientation of a molecule at the air/aqueous interface can be influenced by its surface coverage.<sup>51-52</sup> It is expected that crowding at the air/aqueous interface may force each molecule to adopt a preferential alignment, whereas at low surface coverage, the molecules may orient themselves more freely. Here, we expand upon the aforementioned experiments conducted at high surface coverages by more closely examining the SFG response of the most surface-active compound,  $\beta$ -caryophyllene aldehyde (**IV-1**), at the air/aqueous interface across a broader range of surface coverages using the scanning system.

The C–H stretching spectra collected upon the addition of 0, 1, 5, 10, 15, 20, 25, and 100  $\mu\text{g}$  of  $\beta$ -caryophyllene aldehyde (**IV-1**) at the air/ammonium sulfate (aq) interface are displayed in **Figure 4.3A**. Despite the much lower resolution of the scanning system data, the overall spectral lineshapes remain consistent with those obtained using the HR spectrometer, with two prominent peaks around  $2940\text{ cm}^{-1}$  and  $2860\text{ cm}^{-1}$  and a small peak around  $2880\text{ cm}^{-1}$  that is distinguishable at higher surface coverages.

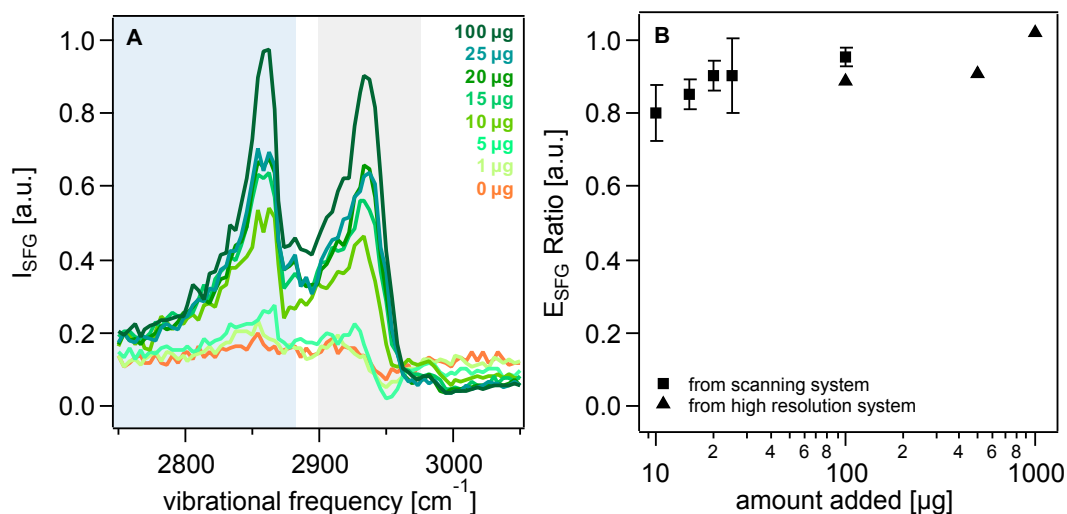


**Figure 4.3.** (A) *ssp*-polarized SFG spectra in the C–H stretching region of  $\beta$ -caryophyllene aldehyde (**IV-1**) on 1 M ammonium sulfate (aq) at varying concentrations. The spectra were collected with different amounts of the sample spread on the surface of 1 M ammonium sulfate (aq). (B) The ratios of SFG E-field of the two major vibrational bands (shaded in gray vs. shaded in blue) as a function of the amount of  $\beta$ -caryophyllene aldehyde added. Square symbols represent data from triplicate experiments on the scanning system and triangle symbols represent averaged triplicate data each from one experiment on the HR system (spectra shown in **Figure A2.8**).

We note that the spectra collected when only 1  $\mu\text{g}$  and 5  $\mu\text{g}$  of the sample were added contain a dip around 2950  $\text{cm}^{-1}$  that does not show up at higher surface coverages. This dip is likely to stem from an oscillator with opposite phase to the vibrational mode around 2940  $\text{cm}^{-1}$ . At low surface coverages, the amplitude of the vibrational mode around 2950  $\text{cm}^{-1}$  increases to a larger extent than the one around 2940  $\text{cm}^{-1}$ , leading to a significant cancellation of the two elements and thus the presence of a spectral dip. However, as the surface coverage increases upon the addition of 10  $\mu\text{g}$  of  $\beta$ -caryophyllene aldehyde (**IV-1**), the amplitude of the vibrational mode around 2940  $\text{cm}^{-1}$  increases much more than that of the 2950  $\text{cm}^{-1}$  mode, leading to the apparent disappearance of the spectral dip. Further experimental and computational investigation is needed to unveil the origin of this dip, yet the obvious difference of the spectral lineshapes

before and after 10  $\mu\text{g}$  of the sample was added reveals an orientation distribution change from the low to high surface coverage regime.

With 10  $\mu\text{g}$  or more of  $\beta$ -caryophyllene aldehyde (**IV-1**) added, the lineshape of the spectra does not change significantly. In order to more quantitatively assess the lineshape change, the E-field magnitude ratio of the two dominant peaks was plotted, though we caution that the two signals may be attributed to delocalized vibrational modes (**Figure 4.3B**).<sup>53</sup> The E-field ratio does not change considerably up to 1000  $\mu\text{g}$  added, indicating that the average molecular orientation of  $\beta$ -caryophyllene aldehyde (**IV-1**) remains largely invariant with increasing surface coverage beyond the addition of 10  $\mu\text{g}$  to the air/ammonium sulfate (aq) interface.  $\beta$ -Caryophyllene aldehyde (**IV-1**) was also measured using neat water as the subphase to compare to the 1 M ammonium sulfate (aq) data for this compound (**Figure 4.4**).

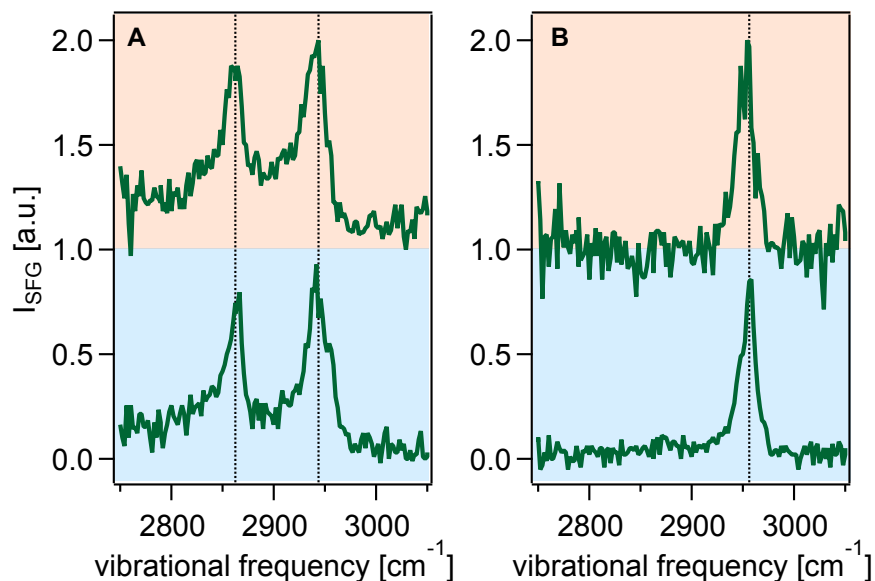


**Figure 4.4.** (A) *ssp*- and (B) *ppp*-Polarized HR SFG spectra of  $\beta$ -caryophyllene aldehyde (**IV-1**) on 1 M  $(\text{NH}_4)_2\text{SO}_4$  (aq) (orange, top trace) and water (blue, bottom trace) in the C–H region.  $\beta$ -caryophyllene aldehyde was dissolved in  $\text{CDCl}_3$  at a concentration of 1mg/mL, and the spectra were obtained 100  $\mu\text{L}$  (100  $\mu\text{g}$ ) of the solution spread on the surface of each subphase.

#### 4.3.4. Perturbation of the interfacial water structure by $\beta$ -caryophyllene aldehyde

**suggested by O–H stretches.** The SFG response in the O–H stretching region of  $\beta$ -caryophyllene aldehyde (**IV-1**) at different surface coverages was also recorded so as to investigate the consequence of molecular adsorption on the hydrogen bonding network at the aqueous/air interface (**Figure 4.5**). Given the high ionic strength of 1 M ammonium sulfate (aq),<sup>54-56</sup> the electrical double layer (EDL) is compressed enough that the  $\chi^{(2)} : \chi^{(3)}$  phase mismatch is negligible under these conditions.<sup>38, 56-57</sup> In other words, the DC phase angle is close to zero and  $\chi^{(2)}$  and  $\chi^{(3)}\Phi(0)$  simply add.<sup>58-59</sup> Given that the surface-localized molecules are electrostatically neutral under our experimental conditions, we do not expect the  $\chi^{(3)}$  effect to impact our interpretation of the data collected in the O–H region under high ionic strength unless the dipole potential of the surface species are sizeable.<sup>56</sup> The relatively narrow peak centered around  $3700\text{ cm}^{-1}$ , which is due to the free O–H oscillators present at the aqueous interface,<sup>60-63</sup> decreases as the amount of the sample added increases. This result indicates that the water molecules with dangling O–H bonds present at the topmost layer become displaced by or hydrogen-bonded to the adsorbed  $\beta$ -caryophyllene aldehyde (**IV-1**) on the surface. Moreover, the spectrum obtained when  $10\text{ }\mu\text{g}$  of sample was added reveals a possible shoulder around  $3670\text{ cm}^{-1}$ . Upon addition of  $100\text{ }\mu\text{g}$  of the sample, the peak around  $3670\text{ cm}^{-1}$  appears to be more prominent. Moreover, a possible peak around  $3760\text{ cm}^{-1}$  shows up, which has been observed for neat water or aqueous solutions of alkali salts.<sup>64-68</sup> The pair of two vibrational bands around  $3670\text{ cm}^{-1}$  and  $3760\text{ cm}^{-1}$  have been assigned to symmetric and asymmetric stretching modes of “vapor-phase” water molecules.<sup>61, 65</sup>

As explained in Section 2.2, for a given set of two spectra, we compare the lineshapes rather than their absolute intensities. In the spectrum of the air/ammonium sulfate (aq) interface without any sample added, the two broad bands around  $3200\text{ cm}^{-1}$  and  $3400\text{ cm}^{-1}$  (**Figure 4.5**, orange trace) are consistent with the rich literature precedent on the SFG spectra of air/water and air/salt (aq) interfaces.<sup>60, 63, 69-71</sup> The addition of  $\beta$ -caryophyllene aldehyde (**IV-1**) to the surface causes the relative intensity of the band around  $3400\text{ cm}^{-1}$  to decrease significantly (**Figure 4.4**, green traces) whereas the  $3200\text{ cm}^{-1}$  band remains largely unchanged, which can be interpreted as a preferential perturbation to the more weakly hydrogen-bonded water molecules, even though the exact origin of the two bands continues to remain enigmatic and controversial.<sup>62-63, 68, 70</sup>

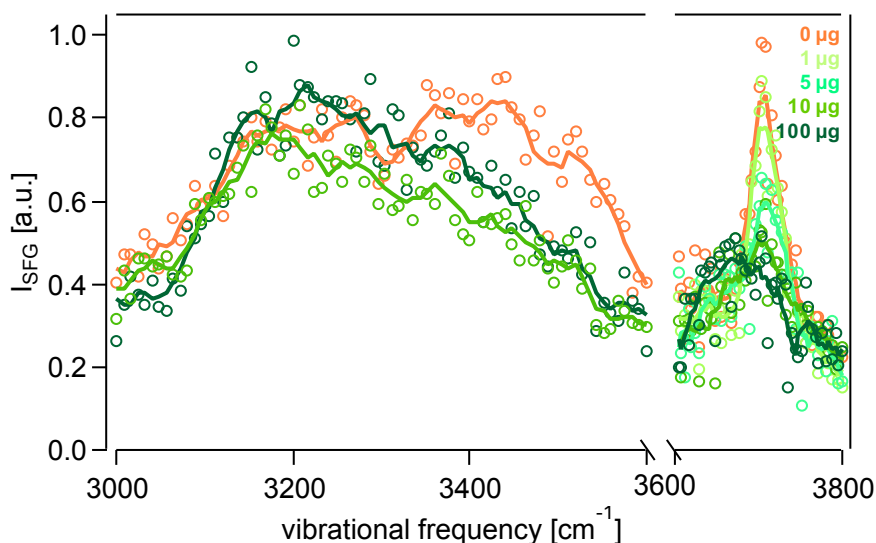


**Figure 4.5.** *ssp*-Polarized SFG spectra in the O–H stretching region of  $\beta$ -caryophyllene aldehyde (**IV-1**) on 1 M ammonium sulfate (aq). Solid traces represent spectra boxcarred over every 5 data points for clarity. The free O–H and hydrogen-bonded O–H regions were normalized to their own maximum intensities (with relative intensities retained) and plotted separately, denoted by a gap inserted in between, to indicate that the two regions were recorded in separate acquisitions.

#### 4.3.5. Evidence for the “salting out” effect of ammonium sulfate in aqueous environments.

The presence of ammonium sulfate in aqueous droplets containing surfactant-like organic species has been reported to increase the surface activity of such compounds, leading to an overall surface tension reduction exhibited by the droplets.<sup>17, 34</sup> This enhancement of surface activity of organic species results from a “salting out” effect, whereby the salt ions “push” the organic solutes to the surface by lowering their solubility in the bulk phase. The following comparison of the SFG responses of  $\beta$ -caryophyllene aldehyde (**IV-1**) at the air/ammonium sulfate (aq) interface versus the air/water interface provides additional evidence to the “salting out” role of inorganic salts in aqueous droplets containing dissolved surface-active species from aerosol CCN.

With 20  $\mu\text{g}$  of  $\beta$ -caryophyllene aldehyde (**IV-1**) added to the surface of the 1 M ammonium sulfate subphase, the SFG signal obtained is slightly lower than, yet comparable to, the signal intensity upon 100  $\mu\text{g}$  of the sample added (**Figure 4.6A**, top traces). However, the spectrum collected when 20  $\mu\text{g}$  of  $\beta$ -caryophyllene aldehyde (**IV-1**) was added to a neat water subphase reveals a nearly flat line (negligible SFG signal), except for the presence of a small dip around 2950  $\text{cm}^{-1}$  (**Figure 4.6A**, bottom traces), which is comparable to the spectra with 1  $\mu\text{g}$  and 5  $\mu\text{g}$  of the sample at the air/ammonium sulfate (aq) interface (**Figure 4.3**). This result is consistent with our hypothesis that a larger portion of  $\beta$ -caryophyllene aldehyde (**IV-1**) localizes at the interface in the presence of ammonium sulfate in the bulk solution, thus leading to higher SFG signal intensity.

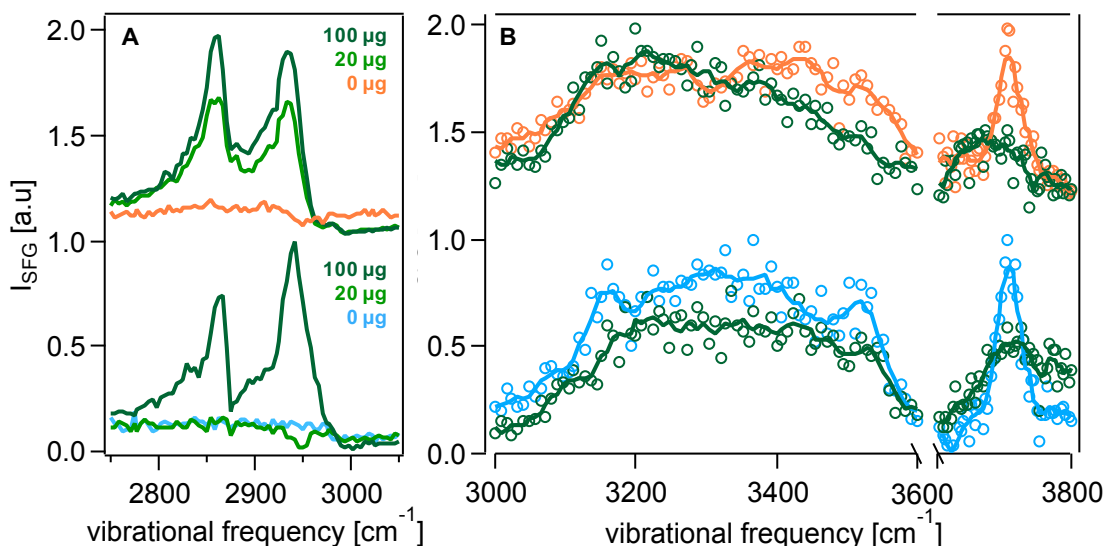


**Figure 4.6.** *ssp*-Polarized SFG spectra in the (A) C–H and (B) O–H stretching regions of  $\beta$ -caryophyllene aldehyde (**IV-1**) on 1 M ammonium sulfate (aq) (top trace) and pure water (bottom trace). Solid traces represent spectra boxcarred over every 5 data points for clarity. The free O–H and hydrogen-bonded O–H regions were normalized to their own maximum intensities (with relative intensities retained) and plotted separately, denoted by a gap inserted in between, to indicate that the two regions were recorded in separate acquisitions.

In contrast to the spectra in the O–H region of  $\beta$ -caryophyllene aldehyde (**IV-1**) on an ammonium sulfate (aq) subphase, the spectra in the hydrogen-bonded O–H region with or without  $\beta$ -caryophyllene aldehyde (**IV-1**) added to the water surface do not show significant lineshape changes. Instead, the entire trace decreases to a comparable extent, which suggests a possible non-preferential perturbation of the hydrogen-bond network in the presence of  $\beta$ -caryophyllene aldehyde (**IV-1**). As expected, the free O–H signal from the neat water surface centered at  $3700\text{ cm}^{-1}$  exhibits lower intensity upon the addition of  $\beta$ -caryophyllene aldehyde (**IV-1**). Additionally, the small peak around  $3770\text{ cm}^{-1}$  appears to slightly increase, along with an apparent rise in the baseline in the region of  $3600\text{--}3800\text{ cm}^{-1}$ . We note that the  $\chi^{(3)}$  effect may need to be considered here due to the longer Debye length present at the very low ionic strength conditions studied here.<sup>55-56</sup> Given that the  $\beta$ -caryophyllene aldehyde (**IV-1**) molecules are

neutral under the conditions of the experiment, the Coulombic potential is negligible. Yet, the dipole potential originating from net-aligned bonds could optically mix with the second-order contribution to the SFG signal, provided it were sizeable enough. Further work focusing on determining the currently unknown dipole potential of aldehyde **IV-1** at the air/water interface using, for instance, surface potentiometry, as previously outlined by Allen and co-workers,<sup>72</sup> or heterodyne-detected off-resonant second harmonic generation<sup>73-74</sup> is needed to address this question in detail.

**4.4. Attempts to acquire surface pressure–mean molecular area isotherms using a Langmuir-Blodgett trough.** Langmuir-Blodgett (LB) trough experiments were performed in an attempt to generate surface pressure–mean molecular area (MMA) isotherms for the synthesized  $\beta$ -caryophyllene-derived oxidation products on neat water and 1 M ammonium sulfate (aq) subphases. By compressing monolayers of surfactants on the surface of a given subphase, LB experiments enable one to measure surface coverage-dependent interfacial organization of molecules at air/aqueous interfaces. Using surface pressure–MMA isotherms to inform our subsequent air/aqueous SFG measurements at selected molecular “footprints”, we hoped to probe the structural organization of the  $\beta$ -caryophyllene oxidation products at quantified surface coverages. However, the extent of surface–bulk partitioning of these molecules into the aqueous subphase that was observed during the course of the LB experiments prohibited the employment of this technique for obtaining reliable surface pressure–MMA isotherms. Despite the notable surface activities of  $\beta$ -caryophyllene-derived ozonolysis products compared to other terpene-derived SOM constituents we had identified using pendant drop tensiometry,<sup>17</sup> the observed surface–bulk partitioning phenomena in the LB experiments indicate that these compounds do not behave as traditional surfactants used in these measurements upon compression on an

aqueous subphase. This result likely arises because these molecules do not structurally resemble non-ionic amphiphilic surfactants (i.e. long hydrophobic tails and hydrophilic head groups), making their solubility in the aqueous subphase considerably higher than what is known from the relatively bulk-insoluble surfactants required for LB experiments. Our attempts to perform LB experiments are described in detail below. Taken together, the surface coverages relevant for the experimental conditions here are best determined using the interfacial tension measurements we reported earlier in Chapter 2.<sup>17</sup>

**4.4.1. Experimental details.** The LB trough (KSV Instruments) was placed on a vibrational isolation table and enclosed in a glass chamber. The ambient temperature of the lab was maintained at 20–22 °C. Before the first use of the instrument, the trough and the barriers were cleaned thoroughly with detergent and ion exchanged nanopure water. Subsequently, before each experiment, the trough, the barriers, and the Wilhelmy plate were rinsed with ethanol and ion exchanged nanopure water. In each experiment, nanopure water or 1 M (NH<sub>4</sub>)<sub>2</sub>SO<sub>4</sub> (aq) was added to the trough until the surface of the subphase was a couple of millimeters above the edge of the trough, and the topmost layer of the subphase was subsequently cleaned using a home-built aspirator. The cleanness of the surface was checked by compressing the barriers together while monitoring the surface pressure to ensure that the pressure did not exceed 0.3 mN/m. Additionally, the surface pressure-mean molecular area (MMA) isotherm of neat water shows a flat line (**Figure 4.7**), which indicates the absence of contaminants on the water surface after the cleaning procedure.

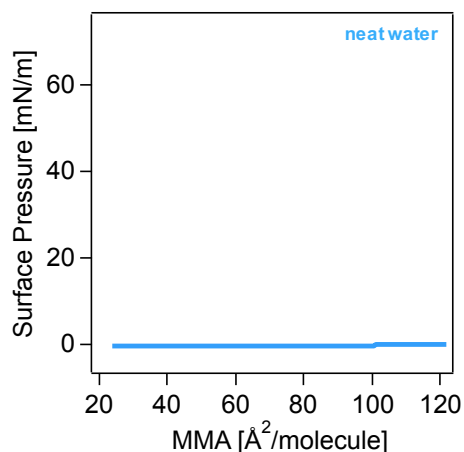


**Figure 4.7.** Surface pressure–MMA isotherm of neat water.

Each sample was dissolved in  $\text{CDCl}_3$  at a concentration of 1 mg/mL. A selected volume of the solution was gently spread onto the surface of the subphase using a flat-tipped glass microsyringe, which was cleaned using  $\text{CDCl}_3$  and left to dry, and the sample/subphase were left for 10 min to allow the solvent to evaporate completely. Subsequently, the barriers were closed at a rate of either 5 or 10 mm/min, and the surface pressure increase was recorded as the MMA of the surface molecules decreased. The resulting isotherm was then plotted to extract information regarding the surface tension depression and surface organization of the sample.

**4.4.2. Discussion of efforts to collect surface pressure–MMA isotherms of  $\beta$ -caryophyllene oxidation products.** The surface pressure-MMA isotherm of  $\beta$ -caryophyllene aldehyde (**IV-1**) on neat water does not show a significant surface pressure increase even when the MMA reaches below  $10 \text{ \AA}^2/\text{molecule}$ , and the barrier closing rate does not seem to play an important role (**Figure 4.8**). In another attempt using  $\beta$ -caryophyllonic acid (**3**), the second most surface-active molecule studied,<sup>75</sup> an increase in surface pressure is observed when the MMA reaches below  $5 \text{ \AA}^2/\text{molecule}$ , which is a physically unrealistic value given that the C–C bond length is generally  $1.54 \text{ \AA}$  (**Figure 4.8**). Note that the MMA is calculated based on the total amount of the sample

added and the assumption that all of the molecules stay on the surface. Therefore, a reasonable explanation to this outcome is that a significant portion of the sample partitions to the bulk phase, which results in the MMA calculation overestimating the exact number of surface molecules, and thus the molecular areas reported are lower than the actual values.

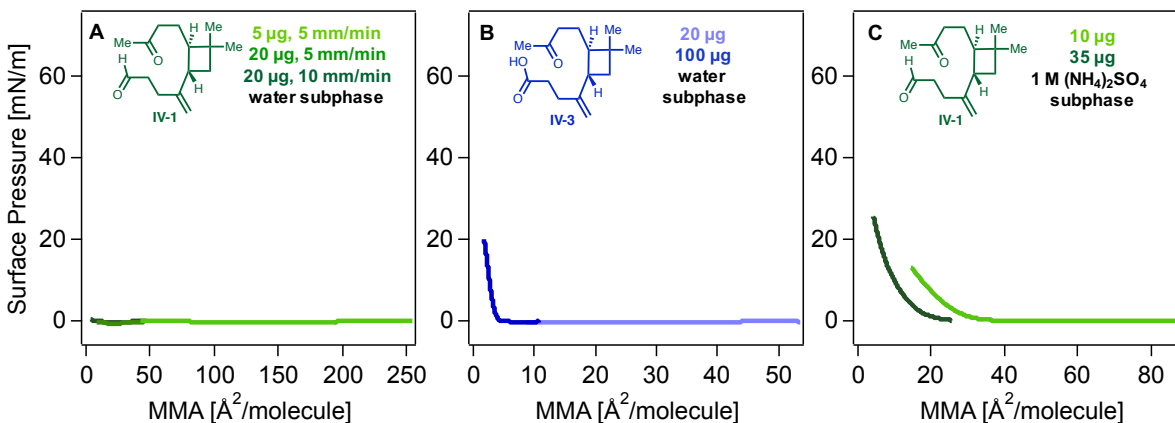


**Figure 4.8.** Surface pressure–MMA isotherms of (A)  $\beta$ -caryophyllene aldehyde (IV-1) on water, (B)  $\beta$ -caryophyllonic acid (IV-3) on water, and (C)  $\beta$ -caryophyllene aldehyde (IV-1) on 1 M  $(\text{NH}_4)_2\text{SO}_4$  (aq). In (B) and (C), the barrier closing rates were 10 mm/min.

When 1 M  $(\text{NH}_4)_2\text{SO}_4$  (aq) is used as the subphase, the surface pressure shows an increase at about  $35 \text{ \AA}^2/\text{molecule}$  (Figure 4.8), indicating that the surface-bulk partitioning of  $\beta$ -caryophyllene aldehyde (IV-1) is hindered to some degree by the presence of  $(\text{NH}_4)_2\text{SO}_4$ . This is an example of the “salting out” effect (more discussion in the main text), whereby organic solutes are “pushed” to the surface due to lower solubility in salt solutions. However, when a different initial amount of  $\beta$ -caryophyllene aldehyde (IV-1) is added, the isotherm is significantly shifted (Figure 4.8), likely because a considerably different surface-bulk partition equilibrium is established depending on the total amount of sample.

All molecules undergo surface–bulk partitioning to some extent. Conventional amphiphilic surfactants with long hydrocarbon tails, such as stearic acid and

dipalmitoylphosphocholine (DPPC), exhibit a much stronger propensity to remain on the surface than in the bulk aqueous phase, and thus are ideal sample molecules for LB trough measurements. In contrast, even though  $\beta$ -caryophyllene oxidation products have demonstrated comparable surface tension depression capabilities, they do not possess typical amphiphilic structures. Upon surface compression in LB trough experiments, they are likely to continuously partition to the large bulk phase that acts as a reservoir, which leads to considerable variations and misrepresentations in results. We expect that the observation of this phenomenon may be relevant for numerous other surface-active SOA oxidation products that do not structurally resemble the relatively bulk-insoluble amphiphilic molecules containing long hydrocarbon tails that are required for LB experiments.

**4.5. Conclusions and future directions.** The experiments reported herein examined the surface vibrational spectral responses of synthesized standards of structurally related  $\beta$ -caryophyllene ozonolysis products at the air/aqueous interface. We described spectral differences across polarization-resolved HR SFG spectra of  $\beta$ -caryophyllene and its oxidation products at high surface coverages on an ammonium sulfate (aq) subphase, and made spectral comparisons to our previously reported condensed-phase spectra for this molecular suite.<sup>42</sup> Despite the importance of elucidating the surface activity and interfacial organization of individual molecules in aqueous media, the combinatorial effects of several surface-active constituents likely dictate overall cloud activation potentials of aerosol particles. Future work expanding upon the reported initial air/aqueous experiments could investigate the SFG responses of varying mixtures of the synthesized  $\beta$ -caryophyllene-derived oxidation products, along with extracted and re-dissolved laboratory and field SOM. Moreover, the possibility for cooperative surface adsorption of these

various oxidation products to be modulated in the presence of an insoluble adsorbed overlayer could be explored.

Given that orientation distributions of molecules at the air/aqueous interface are expected to be surface coverage-dependent, we examined the SFG response of  $\beta$ -caryophyllene aldehyde (**IV-1**), the most surface-active molecule in the suite, across different coverages at the air/ammonium sulfate (aq) interface in the C–H and O–H stretching regions. Spectra recorded in the C–H stretching region for at increasing relative surface coverages on the ammonium sulfate (aq) subphase suggest a modulation in orientation distribution between low to high surface coverage regimes, followed by an average molecular orientation that remains largely invariant with increasing surface coverage beyond 10  $\mu\text{g}$  of  $\beta$ -caryophyllene aldehyde (**IV-1**) added to the surface. In the future, orientation distribution information at air/aqueous interfaces could be obtained using peak fitting analyses across different polarization combinations,<sup>76-78</sup> density functional theory (DFT) calculation-based spectral matching procedures<sup>42, 53, 79</sup> and/or heterodyne (phase-resolved) methods.<sup>42-43, 80-81</sup>

The structural organization of the interfacial water network in the presence and absence of  $\beta$ -caryophyllene aldehyde (**IV-1**) was also investigated and compared between the air/ammonium sulfate (aq) and air/water interfaces. Our findings indicate that the water molecules present at the outermost layer of the aqueous interface are displaced by  $\beta$ -caryophyllene aldehyde (**IV-1**) on both the ammonium sulfate (aq) and water subphases. Additionally, the more weakly hydrogen-bonded water network seems to be perturbed more by  $\beta$ -caryophyllene aldehyde (**IV-1**) than the more strongly hydrogen-bonded population as suggested by the air/ammonium sulfate (aq) spectra, while this effect is not observed in the air/water data. Moreover, when comparing the SFG spectra of  $\beta$ -caryophyllene aldehyde (**IV-1**)

collected in the C–H stretching region of at the air/ammonium sulfate (aq) versus air/water interfaces, we find surface spectroscopic evidence for a “salting out” effects of ammonium sulfate (aq), which has direct implications for understanding the organization of surface-localized molecules present in aqueous cloud-forming droplets containing dissolved aerosol CCN in the atmosphere. Additional studies focusing on the potential ion-specific Hofmeister “salting out” effects<sup>82-84</sup> of various atmospherically relevant aqueous salt subphases could be explored. Future efforts could also involve studies aimed towards probing other surface-active organic species and their chemical reactivity within interfacial aqueous environments relevant for understanding aerosol formation and growth mechanisms, atmospheric lifetimes, and climate interactions. Chapter 5 will next summarize the surface-specific studies on the monomeric  $\beta$ -caryophyllene- and  $\alpha$ -pinene-derived oxidation products detailed in Chapters 2–4 and outline additional research avenues in which these molecular standards are being utilized. Expanding beyond this molecular suite, Chapter 5 will also describe ongoing work focusing on studying various systems of increasing complexity within the study of SOA particle interactions and processes in the atmosphere.

## CHAPTER 5

### Towards Increasingly Complex Systems in the Study of Atmospheric Aerosol Particles

**Portions of this chapter are reproduced in part with permission from the European Geosciences Union and the Royal Society of Chemistry:**

Yee, L. D.; Isaacman-VanWertz, G.; Wernis, R. A.; Meng, M.; Rivera, V.; Kreisberg, N. M.; Hering, S. V.; Bering, M. S.; Glasius, M.; Upshur, M. A.; Bé, A. G.; Thomson, R. J.; Geiger, F. M.; Offenberg, J. H.; Lewandowski, M.; Kourtchev, I.; Kalberer, M.; de Sá, S.; Martin, S. T.; Alexander, M. L.; Palm, B. B.; Hu, W.; Campuzano-Jost, P.; Day, D. A.; Jimenez, J. L.; Liu, Y.; McKinney, K. A.; Artaxo, P.; Viegas, J.; Manzi, A.; Oliveira, M. B.; de Souza, R.; Machado, L. A. T.; Longo, K.; Goldstein, A. H.; Observations of sesquiterpenes and their oxidation products in central Amazonia during the wet and dry seasons. *Atmos. Chem. Phys.* **2018**, *18*, 10433–10457.

Upshur, M. A.; Vega, M. M.; Bé, A. G.; Chase, H. M.; Zhang, Y.; Tuladhar, A.; Chase, Z. A.; Fu, L.; Ebben, C. J.; Wang, Z.; Martin, S. T.; Geiger, F. M.; Thomson, R. J., Synthesis and surface spectroscopy of  $\alpha$ -pinene isotopologues and their corresponding secondary organic material. *Chem. Sci.* **2019**, *10* (36), 8390–8398.

**5.1. Summary and outlook for studying  $\alpha$ -pinene and  $\beta$ -caryophyllene monomeric constituents.** The interfacial physicochemical nature of biogenic SOA particles may play an essential role in the formation, composition, properties, and climate effects of this elusive class of atmospheric particulates.<sup>1-4</sup> Additionally, limited parameters to investigate the chemistry of SOA particles, such as oxygen-to-carbon elemental ratio (O:C) of the organic material, have been historically used throughout the atmospheric research community.<sup>5-9</sup> As such, molecular-level measurements, such as those described herein, can aid in more rigorous investigations of the structure–property–function relationships of constituent molecules that are related to SOA processes and interactions. Taken together, the work detailed in this thesis seeks to access a molecular view of the surface chemistry of biogenic SOA particles by combining organic synthesis, surface science techniques (i.e. pendant drop tensiometry and vibrational nonlinear spectroscopy), and aerosol synthesis and collection. Chapters 2–4 of this thesis focused on efforts to elucidate the relative affinities of oxidation products derived from  $\alpha$ -pinene and  $\beta$ -caryophyllene for various interfaces of atmospheric relevance. Specifically, a suite of  $\alpha$ -pinene- and  $\beta$ -caryophyllene-derived monomeric oxidation products were synthetically prepared for subsequent surface-specific analyses. Fundamental insights into the structure, properties, orientation, and reactivity of this series of molecules within interfacial environments were then gained through (1) dynamic surface tension measurements on pendant aqueous droplets (Chapter 2), (2) surface benchmarking to laboratory-synthesized SOM using SFG spectroscopy (Chapter 3), and (3) SFG spectroscopy experiments performed at the air/aqueous interface (Chapter 4).

While specific future directions to address the current limitations of these studies are discussed at the conclusion of each chapter, Chapter 5 will focus specifically on ongoing studies that build upon the work detailed in Chapters 2–4 and lay the groundwork for moving towards

increasingly complex systems relevant to atmospheric SOA surface science. In Chapter 5, we discuss the following future research directions and preliminary work in each of these areas:

- (1) Collaborative studies utilizing  $\alpha$ -pinene and  $\beta$ -caryophyllene monomeric oxidation products;
- (2) Probing interfacial processes and interactions under varying atmospheric conditions;
- (3) Surface spectroscopic studies of field-derived aerosol samples; and
- (4) Efforts toward the synthesis and analysis of new dimers and higher order SOA constituents.

## **5.2. Collaborations utilizing $\alpha$ -pinene and $\beta$ -caryophyllene monomeric oxidation products.**

Efforts to identify and unambiguously elucidate SOA constituents as well as study their physicochemical properties require the synthesis of pure and homogeneous molecular standards prepared on a preparative scale.<sup>2</sup> As such, there exists a critical need for more cross-disciplinary interactions between the atmospheric and synthetic organic communities. With this objective in mind, several collaborative studies have been initiated in order to utilize the molecular standards synthesized in our labs. We briefly highlight below some ongoing collaborations using the  $\alpha$ -pinene and  $\beta$ -caryophyllene monomeric oxidation products synthesized in this thesis work.

$\beta$ -Caryophyllene oxidation products synthesized by our group were recently used as tracer standards to identify these compounds in samples collected during the Green Ocean Amazon (GOAmazon2014/5) field campaign the Central Amazon region. In collaboration with our labs, Dr. Lindsay Yee, from the laboratory of Prof. Allen Goldstein at University of California Berkeley, carried this work out using semi-volatile thermal desorption aerosol gas chromatography (SV-TAG). Employing the six standards whose synthesis is outlined in Chapter 2, several of  $\beta$ -caryophyllene oxidation products were identified in both the gas and particle phases in the GOAmazon2014/5 SOA samples. However, over 40 other sesquiterpene-derived species were also found to be present in the Amazonian samples that could not be unequivocally

elucidated, due to a lack of available standards for these putative compounds. Synthetic standards of proposed oxidation products derived  $\beta$ -caryophyllene and other sesquiterpenes are therefore needed for more comprehensive structural identification and quantification of sesquiterpene oxidation products in Amazonian aerosol particles.<sup>10</sup> Moreover, access to  $\beta$ -caryophyllene-derived molecular markers for interactions between BVOCs and anthropogenic emissions, such as organosulfates and organonitrates, would corroborate these field studies.<sup>10</sup> To our knowledge, the synthesis of  $\beta$ -caryophyllene-derived organosulfates has only been reported once in the literature.<sup>11</sup> However, we suspect these organosulfates to exhibit higher surface activities than the  $\beta$ -caryophyllene-derived oxidation products studied in Chapter 2, because the sulfate group confers structural resemblance to ionic surfactants (e.g. sodium dodecyl sulfate (SDS)). To this end, the potentially high surface activities of  $\beta$ -caryophyllene-derived organosulfates make them attractive target molecules to synthesize and probe with our surface-specific toolset. **Figure 5.1** provides some examples of putative oxidation products and organosulfates that could be target molecules of study in future endeavors.<sup>11-13</sup> Related work focusing on organosulfate markers and SOA interactions with anthropogenic emissions during the GOAmazon2014/5 field campaign will also be described in Section 5.4.

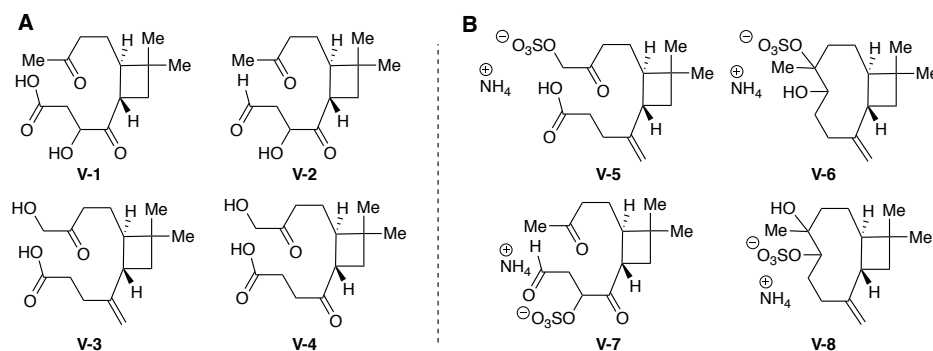


**Figure 5.1.** Examples of putative  $\beta$ -caryophyllene-derived (A) oxidation products and (B) organosulfates not yet synthesized and analyzed by our labs.

Another collaboration made possible through our expertise in synthesizing  $\alpha$ -pinene and  $\beta$ -caryophyllene monomeric oxidation products centers around using these molecular standards to investigate liquid–liquid phase separation (LLPS) under conditions of high RH. This work is currently being carried out in collaboration with the laboratory of Prof. Mijung Song at Chonbuk National University in Jeonju, South Korea. Under increasing % RH, LLPS has been observed in SOM both with and without the presence of inorganic salts.<sup>7-8, 14</sup> As depicted in **Figure 5.2**, LLPS is characterized by the formation of two distinct, immiscible phases — one hydrophilic, containing liquid water and water-soluble inorganic or organic species, and the other hydrophobic and organic-rich.<sup>15</sup> It has been proposed that the occurrence of LLPS may be an initial step in lowering the barrier to CCN activation under relevant % RH ranges, given that the water-rich phase can increase water uptake while the organic-rich phase simultaneously lowers the surface tension of the forming cloud droplets (introduced in Chapter 2).<sup>7</sup>

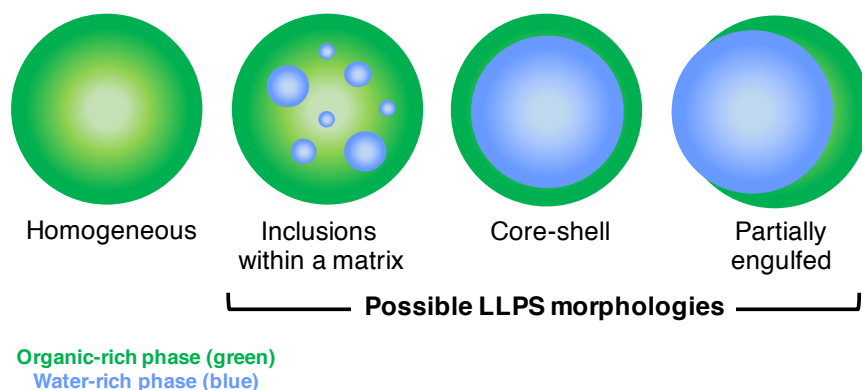


**Figure 5.2.** Visual depiction of possible LLPS morphologies in atmospheric aerosol particles (Adapted from ref. 15).<sup>15</sup>

LLPS was recently observed by Song and coworkers to occur in laboratory-produced SOM derived from  $\alpha$ -pinene, limonene, and  $\beta$ -caryophyllene, but not in SOM derived from isoprene or toluene.<sup>8</sup> With the goal of gaining additional insight into LLPS in particles derived

from  $\alpha$ -pinene and  $\beta$ -caryophyllene, the present collaboration investigates LLPS in nebulized particles generated directly from our oxidation product standards (i.e. single component systems) and dual component systems. Dual component experiments refer to 1:1 mixtures generated from each of the synthesized oxidation products with a commercially available standard, namely PEG-400, diethyl L-tartrate, and pyruvic acid. The results of this study are preliminary at this stage and therefore will not be further discussed here. Note these LLPS experiments are performed using optical reflectance microscopy, which requires the use of particles greater than 20  $\mu\text{m}$  in size. Given that LLPS morphologies may be size dependent, future LLPS studies could address this caveat by imaging more atmospherically relevant particle-size regimes using microscopy techniques with resolution limits on the nm-scale, such as environmental scanning electron microscopy (ESEM) and scanning transmission x-ray microscopy (STXM).<sup>15-16</sup>

### **5.3. Probing interfacial processes and interactions under varying atmospheric conditions.**

Chapters 3 and 4 highlighted the utility of SFG spectroscopy as a nondestructive nonlinear optical probe to study the surfaces of both SOM and air/aqueous interfaces, respectively. While these chapters specifically focused on using SFG spectroscopy to examine  $\beta$ -caryophyllene-derived oxidation products, in the following two sections (Sections 5.3 and 5.4), we move beyond probing this molecular suite to discuss additional applications of this technique to atmospherically relevant surfaces. We begin by discussing the development of “all-in-one” flow set-up to design and carry out a wide range of experiments using both aerosol samples and model substrates to investigate both the separate and integrated effects of various environmental conditions on the gas/particle interface.

**5.3.1. Design and assembly of an “all-in-one” flow system for simulating environmental conditions.** SOA surfaces encounter numerous surrounding gas-phase species in the atmosphere, and adsorption, uptake, and reactions of these gaseous molecules at particle surfaces may serve as important initial steps in several SOA processes and interactions in the atmosphere.<sup>3, 17-19</sup> Section 5.3 therefore focuses on developing experimental capabilities to simulate and probe these atmospherically relevant surface processes *in situ* and in real time. To accomplish this goal, we discuss efforts to design and assemble flow instrumentation capable of exposing a given surface to changes in various gaseous environments, which can be coupled to our SFG spectroscopy set-ups. Working with a fellow graduate student, Yangdongling Liu, we developed a home-built set-up that can control varying conditions of RH, BVOC partial pressure, ozone partial pressure, and temperature with the goal of creating a proxy for the real atmosphere (**Figure 5.3**). The preliminary experiments discussed in the subsequent sections demonstrate the versatility of this flow set-up for probing a variety of interfacial processes and interactions under changing atmospheric conditions.

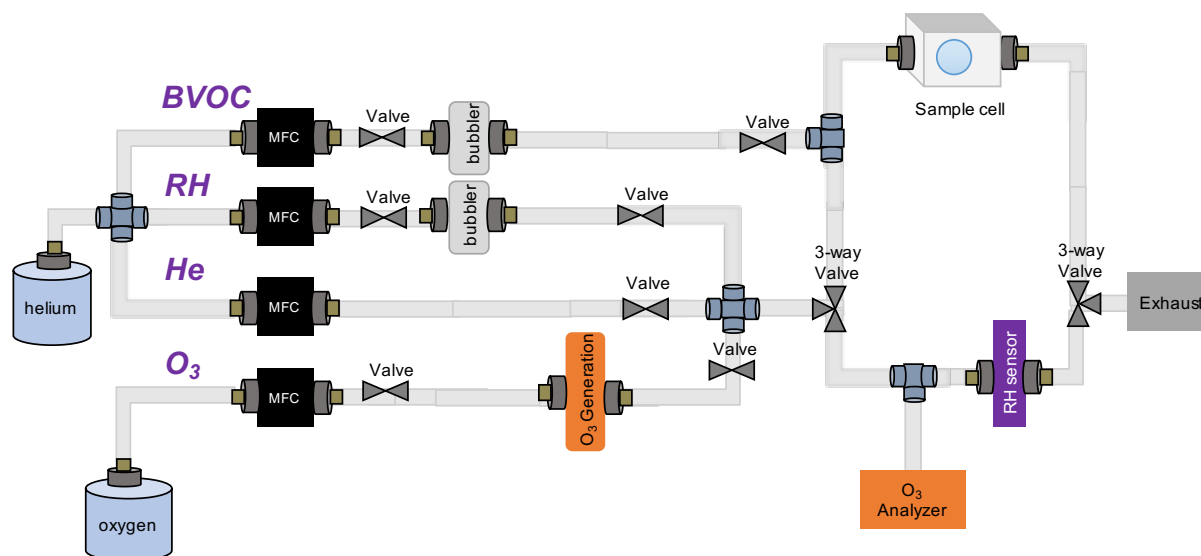


**Figure 5.3.** Diagram of recently built integrated set-up for flowing atmospheric vapors.

The multi-path flow system was adapted from previously described flow systems.<sup>18, 20-22</sup> Each vapor (namely, water vapor, BVOC, dry He, and ozone) was passed through its respective line and subsequently sent across the sample surface of interest, which was sealed with a Viton O-ring to two different home-built Teflon flow-cells, one built for near internal reflection geometry and the other for external reflection geometry configurations. The external reflection geometry flow cell was designed and built with help from a recent graduate, Dr. Paul Ohno. Ultra-high purity He (Airgas, 99.999%) was used as the carrier gas. Helium was sent directly to the sample in the dry line, while the BVOC and RH paths each consisted of a bubbler containing roughly 10 mL of the molecule of interest or Millipore water, respectively, to flow the vapor of interest to the sample cell using He as a carrier gas. For the ozone line, ultra-high purity oxygen (Airgas, 99.999%) was passed through a line containing an ozone generator (Oxidation Technologies, ZO-30, air pump disabled and bypassed). All flow rates were regulated using electronic mass flow controllers (MFCs) (Alicat Scientific). Through a separate line that bypassed the sample cell, the % RH was measured using an RH meter (Omega Engineering, RH-USB) and the ozone concentration (in ppb to ppm amounts) was measured using a UV ozone analyzer (EcoSensors, UV-100). All vapors were directed into the exhaust following sample exposure. Upon switching between flow conditions, the system was allowed to stabilize for approximately 5 min before data acquisition was started. All SFG measurements were performed in the C–H or O–H stretching regions using the Solstice laser system equipped with the TOPAS tunable optical parametric amplifier set-up described in Section 3.4.2 in Chapter 3.

**5.3.2. Investigating terpene-derived SOM under varying RH.** Studying the structure and ordering of water molecules at the surface of SOA particles at a molecular level may have implications for the understanding RH-dependent physicochemical processes in SOA formation, growth, and CCN activation.<sup>23</sup> For instance, previous studies have shown that water can act as a plasticizer, changing the viscosity of SOA particles between “honey-like” at high RH and “marble-like” at low RH.<sup>14, 18, 24</sup> A previous study in our lab focused on using SFG spectroscopy to probe  $\alpha$ -pinene-derived SOM under high versus low RH in the C–H region, and revealed that the “honey-like” state may be associated with surface disordering, allowing for the chemical exchange between gas and particle phases.<sup>18</sup> We aim to expand upon this study by investigating the hydrogen bonding network (CH–OH continuum) over various biogenic and anthropogenic SOM surfaces under high versus low RH using the “all-in-one” flow set-up.

For a preliminary set of experiments, SOM samples derived from  $\alpha$ -pinene were generated using an analogous protocol to that described in Section 3.2 of Chapter 3. In collaboration with Yiming Qin, a graduate student in the laboratory of Prof. Scot Martin (Harvard University), particles were generated from the ozonolysis of (–)- $\alpha$ -pinene (99%, optical purity ee: 97%, Sigma-Aldrich Inc.) in an oxidation flow reactor and were collected onto CaF<sub>2</sub> optical windows (ISP Optics) using an electrostatic precipitator (TSI 3089). Using our flow instrumentation,  $\alpha$ -pinene-derived SOM deposited on a CaF<sub>2</sub> window was exposed to alternating high humidity (80–95% RH) and dry (<0.5% RH) conditions (**Figure 5.4**) and probed in the C–H and O–H vibrational stretching regions.

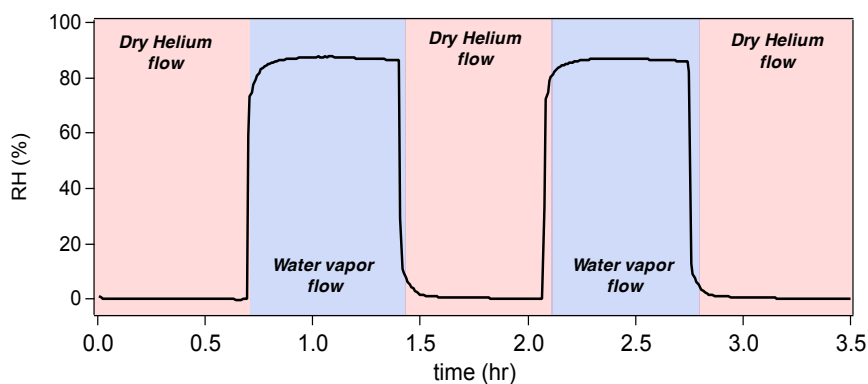


**Figure 5.4.** % RH as a function of time showing reversible cycling between high and low RH.

**Figure 5.5** shows initial spectra of  $\alpha$ -pinene-derived SOM collected in near internal reflection geometry in the C–H and O–H regions under high versus low RH. Three consecutive runs between high and low RH are displayed, revealing that changes in the CH–OH spectra are reversible upon alternation between dry and humid conditions. Moreover, signal intensity in the C–H region is lower under high RH than low RH, which indicates a decrease in surface ordering, as shown previously.<sup>18</sup> Under high RH conditions, the increased signal intensity in O–H region indicates the presence of an interfacial hydrogen-bonded water network over the SOM surface. Overlaying the spectral lineshapes observed in the O–H region with the bulk IR spectra of water in the liquid and solid phases<sup>25</sup> reveals that the center frequency of the O–H continuum matches that of ice. From this comparison, it may be speculated that strong hydrogen bonding of water molecules on the SOA surface occurs under high RH conditions, similar to that of ice water. However, upon replicating the experiment using a blank control calcium fluoride substrate, the SOM/H<sub>2</sub>O SFG spectrum in the O–H region was found to closely resemble the CaF<sub>2</sub>/H<sub>2</sub>O interface. Although we have traditionally probed samples using near internal reflection geometry, this finding led us to design an external reflection geometry flow cell to be able to directly probe the SOM/H<sub>2</sub>O interface.

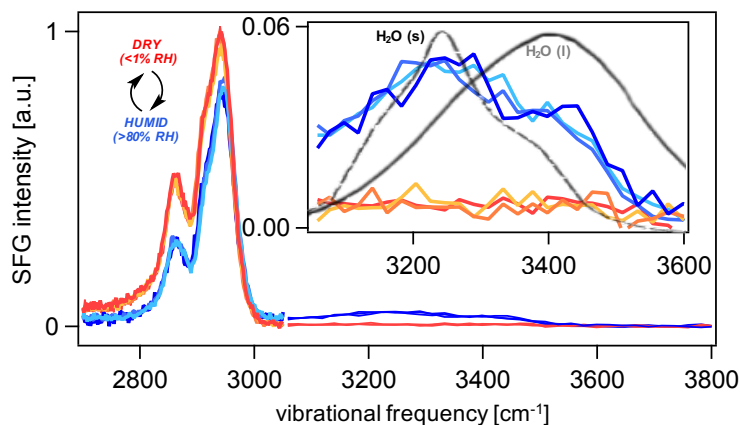


**Figure 5.5.** Preliminary SFG experiment probing  $\alpha$ -pinene-derived SOM deposited on  $\text{CaF}_2$  under high versus low RH (color shades represent different runs alternating between high and low RH). Inset shows zoomed in spectra ( $3050\text{--}3550\text{ cm}^{-1}$ ) collected in the O–H stretching region overlaid to the bulk IR spectra of liquid and solid water.<sup>25</sup> The flow rates for both the dry and humid lines was 1 SLPM. Maximum intensities for spectra collected under dry conditions are normalized to 1 and intensities for spectra collected under humid conditions are scaled based the highest intensity observed in the “dry” spectra.

Additionally, characterization of the SOM films is crucial to interpreting the external versus internal spectra and determining if the desired interface (SOM/ $\text{H}_2\text{O}$  vs.  $\text{CaF}_2/\text{H}_2\text{O}$ ) is in fact being probed. For instance, if the film does not sufficiently cover the solid substrate underneath, it is possible that the  $\text{CaF}_2/\text{H}_2\text{O}$  interface could still be probed in external reflection geometry at a given spot in the sample. Therefore, we set out to characterize the SOM films using a number of methods, namely atomic force microscopy (AFM), x-ray photoelectron spectroscopy (XPS), scanning electron microscopy (SEM), and ellipsometry film analysis. The results for characterizing the SOM films remain inconclusive thus far, and therefore more measurements are needed to determine if a uniform film is present on the substrates. More SOM samples, collected over longer length scales, may be needed to guarantee that a film forms on the solid substrates. Once it has been determined that a film exists on the SOM/optical window samples, work continued on by Yangdongling Liu will focus on continuing these RH-dependent SFG studies on various SOM surfaces using the external reflection geometry flow cell.

**5.3.3. *In situ* monitoring of ozonolysis of surface-adsorbed terpenes at solid surfaces.** The traditional approaches used to study SOA formation mechanisms, properties, and composition in laboratory settings uses flow tubes and chambers with certain residence times (msec to hours)<sup>26-32</sup> to generate particles from gas-phase chemical reactions, as described in Section 3.2 of Chapter 3. However, heterogeneous physical and chemical transformations leading to SOA particles remain challenging to detect using techniques relying on these chamber systems. Previous studies in the Geiger lab have focused on *in situ* monitoring oxidation reactions of immobilized olefinic species capable of undergoing ozonolysis.<sup>20-21</sup> To avoid evaporation, tailored oxide surfaces containing cyclohexene, cyclopentene, and a menthenyl derivative were prepared by using covalent silane-based linkers. More recently, our labs have reported on the partial reversibility of adsorption of various terpenes onto solid substrates.<sup>20-21</sup> This finding opens up the opportunity to directly probe the reactivity of adsorbed species that are “immobilized” solely via adsorption on a solid substrate through real-time measurements.

Towards this end, ongoing work has been carried out with the goal of performing chemical reactions on adsorbed terpene molecules that are irreversibly adsorbed on model surfaces using the “all-in-one” flow instrumentation and characterizing these reactions *in situ* using SFG spectroscopy. As a first experiment, two CaF<sub>2</sub> optical windows were exposed to  $\alpha$ -pinene and  $\beta$ -caryophyllene vapors, respectively. After allowing the loosely bound molecules to desorb over the course of 10 mins in ambient conditions, the sample was placed in an ozone chamber for ozonolysis of the remaining tightly bound molecules. The SFG spectra of the samples were taken before and after ozonolysis, as shown in **Figure 5.6**. The results are in agreement with the previously collected vapor-phase spectra of these two molecules and their corresponding SOM, as the spectra taken post-ozone exposure spectrally match that of the SOM

derived from each of the BVOC molecules. In the case of  $\alpha$ -pinene ozonolysis, a blue shift in the spectrum marked the reaction progress, while  $\beta$ -caryophyllene ozonolysis results in a loss of the middle peak in the spectrum (around  $2900\text{ cm}^{-1}$ ).

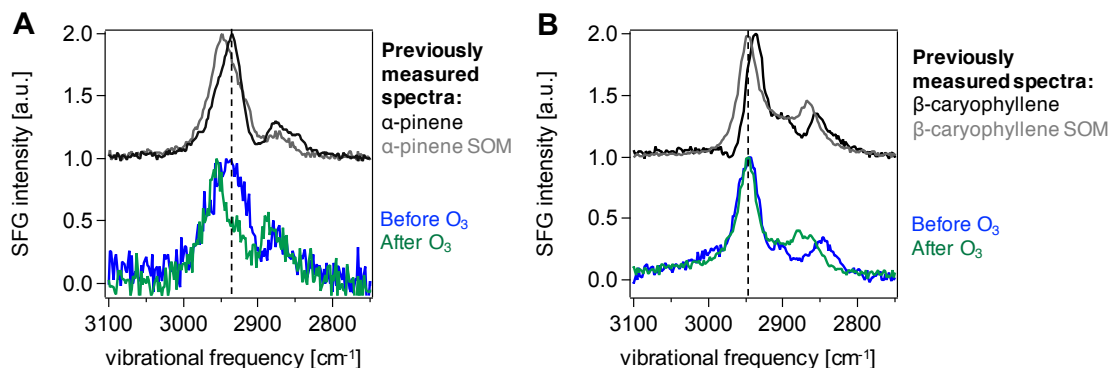


**Figure 5.6.** Preliminary ozonolysis SFG experiment performed using (A)  $\alpha$ -pinene and (B)  $\beta$ -caryophyllene on a calcium fluoride optical window. Maximum intensities are normalized to 1 and offset for clarity.

Using the all-in-one flow set-up, we then designed and carried out experiments to perform the ozonolysis of  $\alpha$ -pinene and  $\beta$ -caryophyllene adsorbed to an optical window while monitoring the C–H spectra using our SFG set-up. Specifically, the BVOC of interest was flowed onto the substrate for 5 min at a flow rate of 0.5 SLPM before “rinsing” with helium flow over the course of 10 min at a flow rate of 1 SLPM. Subsequently, the sample containing adsorbed BVOC molecules was exposed to ozone (1–2 SLPM). To our dismay, we did not observe any spectral shift upon ozonolysis of  $\alpha$ -pinene on  $\text{CaF}_2$ . Numerous experiments are being performed to determine if the spectral shift is dependent on optical substrate, external vs. internal reflection geometry, or ozone concentration. In the case of  $\beta$ -caryophyllene ozonolysis, preliminary results show the loss of the middle peak “marker” upon both 10 and 20 min exposure to ozone (**Figure 5.7**). However, in these studies,  $\sim 500$  ppm of ozone was used. Future studies will focus on carrying out these ozonolysis experiments under more atmospherically relevant

ozone concentrations in the ppb to sub-ppm regime. Moreover, these reactions will be carried out and monitored under varying conditions of atmospherically relevant RH and temperature.

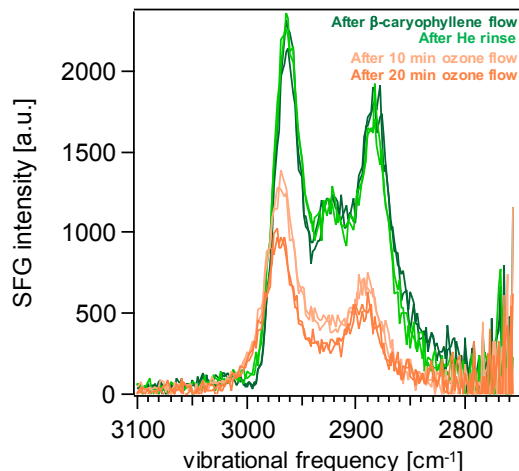


**Figure 5.7.**  $\beta$ -Caryophyllene ozonolysis experiment performed using the “all-in-one” flow set-up to flow  $\beta$ -caryophyllene (0.5 SLPM), He (1 SLPM), and ozone (1–2 SLPM,  $\sim$ 500 ppm) onto a  $\text{CaF}_2$  window. After exposure to each condition, spectra were collected with the flow stopped.

While this data is preliminary, ongoing experiments demonstrating that oxidation reactions relevant to SOA particle formation and growth may be performed on adsorbed terpene molecules that are immobilized on model surfaces, and the reaction products may be characterized *in situ* using SFG spectroscopy. Other future directions could include probing other vibrational modes such as the C=O and O–H regions, developing simulated dynamic environments using the “all-in-one” flow set-up, and ultimately expanding these studies from probing model surfaces to real aerosol surfaces. The latter is further described in the following section.

**5.3.4. Studies of BVOCs at SOM surfaces: Adsorption, uptake, and reactions.** The initial studies using the developed flow instrumentation focused on probing the gas/particle interface under varying conditions of RH (Section 5.3.2) and monitoring the oxidative cleavage of BVOCs at model surfaces (Section 5.3.3) *in situ* by SFG spectroscopy. The “all-in-one” flow set-up also

unlocks the prospect of using SFG spectroscopy to track the dynamics of BVOC uptake onto or into the particle phase under varying RH and temperature (and consequently particle viscosity) as well as study subsequent oxidation reactions on these BVOCs at these surfaces. Unfortunately, spectroscopically tracking such dynamic interactions is not as straightforward as one might assume, given that the SFG signal frequencies and intensities obtained from SOM derived from a particular terpene overlap significantly with those of its precursors. For instance, the highest SFG signal intensity obtained from  $\alpha$ -pinene-derived SOM occurs at  $2950\text{ cm}^{-1}$ , shifted only by  $15\text{ cm}^{-1}$  from the otherwise similarly shaped SFG spectrum of  $\alpha$ -pinene itself.

Deuterium labeling offers the opportunity to address these limitations by “silencing” SFG signal intensity generating C–H oscillators in the SFG spectra of both the precursor terpene and its corresponding SOM, thereby enabling vibrational mode elucidation of the highly congested SFG spectra. Using deuterium labeling strategies, future work could therefore center on studying the interactions between unlabeled VOCs and labeled particle surfaces using deuterated precursors and their subsequent SOM to distinguish the unlabeled gas-phase molecules from those in the particle phase. Under this scenario, BVOC–SOM interactions would be probed in the C–H stretching region. Alternatively, monitoring could be performed in the C–D stretching region, requiring the use of labeled VOCs and unlabeled particle surfaces.

With such goals in mind, we recently carried out detailed isotope-labeling studies in which several  $\alpha$ -pinene isotopologues and their corresponding SOM were synthesized and characterized using SFG spectroscopy. This work was carried out with major contributions from previous graduate students in our labs, Dr. Mary Alice Upshur, Dr. Marvin Vega, and Dr. Hilary Chase, along with Dr. Yue Zhang from the Martin lab (Harvard), and our PNNL EMSL collaborators, Dr. Aashish Tuladhar and Dr. Zizwe Chase. The SFG spectra of the isotopologues

at vapor/solid interfaces were collected to investigate contributions from such C–H stretches on the complex SFG spectrum of  $\alpha$ -pinene in the pursuit of identifying high signal intensity generating oscillators. While our previous work on methyl C–D  $\alpha$ -pinene isotopologues did not reveal significant decreases in signal intensity in the C–H region,<sup>33</sup> our recent study on three new analogues with methylene bridge, bridgehead methine, allylic, and vinyl deuteration shows that the ring-substituted isotopologues revealed significant reduction of the dominant peak in this region of interest (**Figure 5.8**).

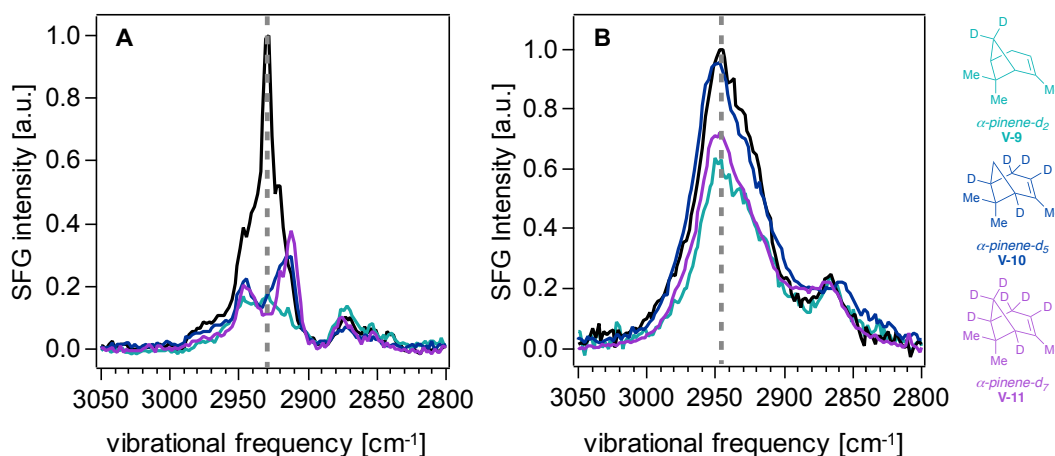


**Figure 5.8.** (A) Sub 1  $\text{cm}^{-1}$ -resolution *ssp*-polarized SFG spectra of vapor-phase (–)- $\alpha$ -pinene (black trace) and isotopologues **V-9–V-11** in contact with fused silica. Intensities are scaled based the highest intensity peak of the vapor (–)- $\alpha$ -pinene spectrum collected on the same day as each of the isotopologues. (B) Standard resolution *ssp*-polarized SFG spectra of SOM produced from (–)- $\alpha$ -pinene (black trace) and isotopologues **V-9–V-11** in contact with fused silica. Intensities are scaled based the highest intensity peak of the (–)- $\alpha$ -pinene SOM SFG spectrum collected on the same day as each of the isotopologue SOM samples. Note standard resolution spectra were collected for the SOM because our previous work comparing the spectra of  $\alpha$ -pinene-derived SOM using standard versus high resolution SFG systems indicates that no gain in spectral resolution is observed despite the increased spectral resolving power.<sup>18</sup>

Specifically, the ring-substituted isotopologues revealed a 50–80% suppression of the SFG signal intensity in the broad band (centered around  $2930\text{ cm}^{-1}$ ) that is emblematic of unlabeled  $\alpha$ -pinene (**Figure 5.8A**). By subsequently preparing and collecting SFG spectra of

SOM derived from the  $\alpha$ -pinene isotopologues, we then made the first attempts thus far towards identifying the surface oscillators in  $\alpha$ -pinene-derived SOM. The SFG spectra of the SOM prepared from the ozonolysis of the two isotopologues featuring a deuterated bridge methylene group show up to 40% less signal intensity than that of the unlabeled SOM (**Figure 5.8B**). While these results are promising, further efforts towards the synthesis and SFG spectroscopy of other isotopologues and their corresponding SOM are needed to achieve adequate signal intensity suppression for the planned flow studies using the “all-in-one” set-up. Nevertheless, these initial studies open the door to future investigations of the dynamics of gas-phase BVOC adsorption on and/or uptake into the particle phase and subsequent surface oxidation reactions under varying tropospherically realistic conditions.

**5.4. Surface spectroscopic studies of field-derived aerosol.** While the thesis work presented thus far primarily utilizes laboratory-produced SOM derived from a given BVOC precursor, it is also important to corroborate these more fundamental studies with observations of particle samples collected from the natural environment. As such, this section presents ongoing work focusing on using SFG spectroscopy as a nondestructive, highly sensitive offline tool to probe the surfaces of field-derived aerosol particles in tandem with the other online and offline analytical techniques to study SOA particle and gas phases. Our labs have previously published several analyses of field aerosol particles,<sup>17, 34</sup> including samples collected in the central Amazon Basin during the wet season of the AMAZE-08 field campaign, pine forests in Blodgett Forest, California during the BEARPEX-2009 field campaign, and Finnish boreal forests during the HUMPPA-COPEC-2010 field campaign.

To expand upon these studies, Dr. Mary Alice Upshur travelled to the central Amazon Basin during the dry season in the year 2014 to collect several particle samples for future SFG

analysis. This particle collection activity was carried out during the GOAmazon2014/5 campaign, previously mentioned in Section 5.2. Often called the “lungs of the planet,” the Amazon rainforest is the largest and most biodiverse tropical ecosystem, spanning over 2 million square miles in South America. A variety of field campaigns continue to take place in the Amazon rainforest, as it is one of the last remaining locations where “pristine” samples containing almost no anthropogenic components can be collected during certain times of the raining season. Under certain conditions of meteorology, however, natural–anthropogenic interactions can be probed.<sup>35</sup> <sup>36</sup> This project therefore aims to characterize the surface vibrational spectra of samples collected at various locations in the Amazon Rainforest within an 80 km radius of the city of Manaus to investigate the impacts of urban pollution on the surface chemistry of pristine organic particles from the Amazon.

Over 100 samples were collected using teflon filters (37 mm diameter, 1  $\mu\text{m}$  pore size). Filter samples were obtained using a portable  $\text{PM}_{2.5}$  particle sampler during periods over varying amounts of time when particle concentrations were relatively low ( $\sim 10 \mu\text{g}/\text{m}^3$  as detected by aerosol mass spectrometry (AMS)). Two control samples were collected at a control site located  $>50$  km north from Manaus, named ZF2, and all other samples were collected at either the T2 Tiwa site, 8 km from Manaus, or the T3 Manacapuru site, 70 km from Manaus. **Figure 5.9A** shows the locations of the three sample sites and their relative distances from Manaus, while **Figure 5.9B** shows condensation particle counter (CPC) data taken in an aircraft above the sample collection sites. The CPC data shows that particle number and mass concentrations are 10–100 times higher in the urban outflow pollution plume compared to in pristine conditions, and the T2 and T3 sites for sample collection are located in the region of the plume activity, while the ZF2 site is largely unaffected.

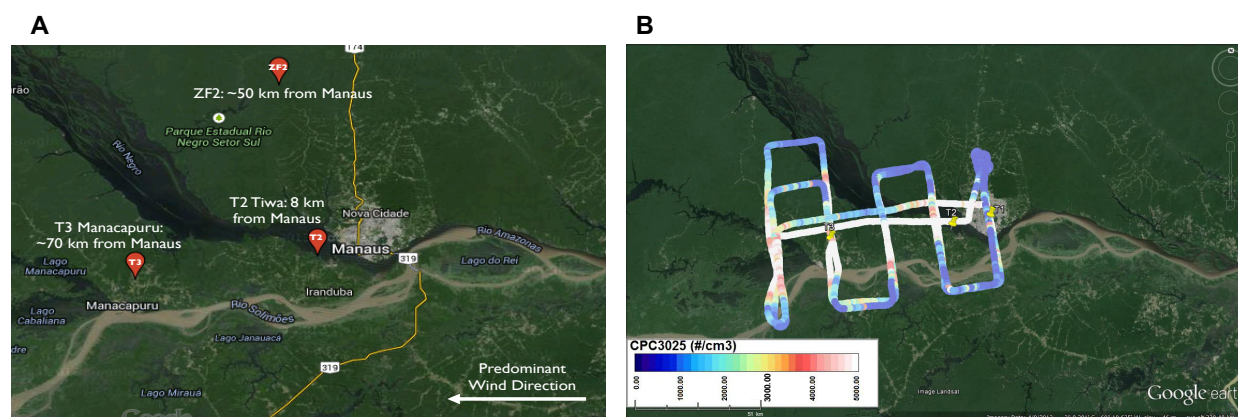


**Figure 5.9.** Maps showing (A) all three sample sites and their locations relative to the city of Manaus, and (B) CPC data of the Manaus pollution plume over the T2 and T3 sites.

Working with a fellow graduate student, Yangdongling Liu, all samples collected by Dr. Mary Alice Upshur during the GOAmazon2014/5 campaign have recently been examined by SFG spectroscopy in the C–H stretching region. **Figure 5.10** displays a summary of the comprehensive compilation of SFG spectra, in which duplicate to triplicate spots on each sample were measured.

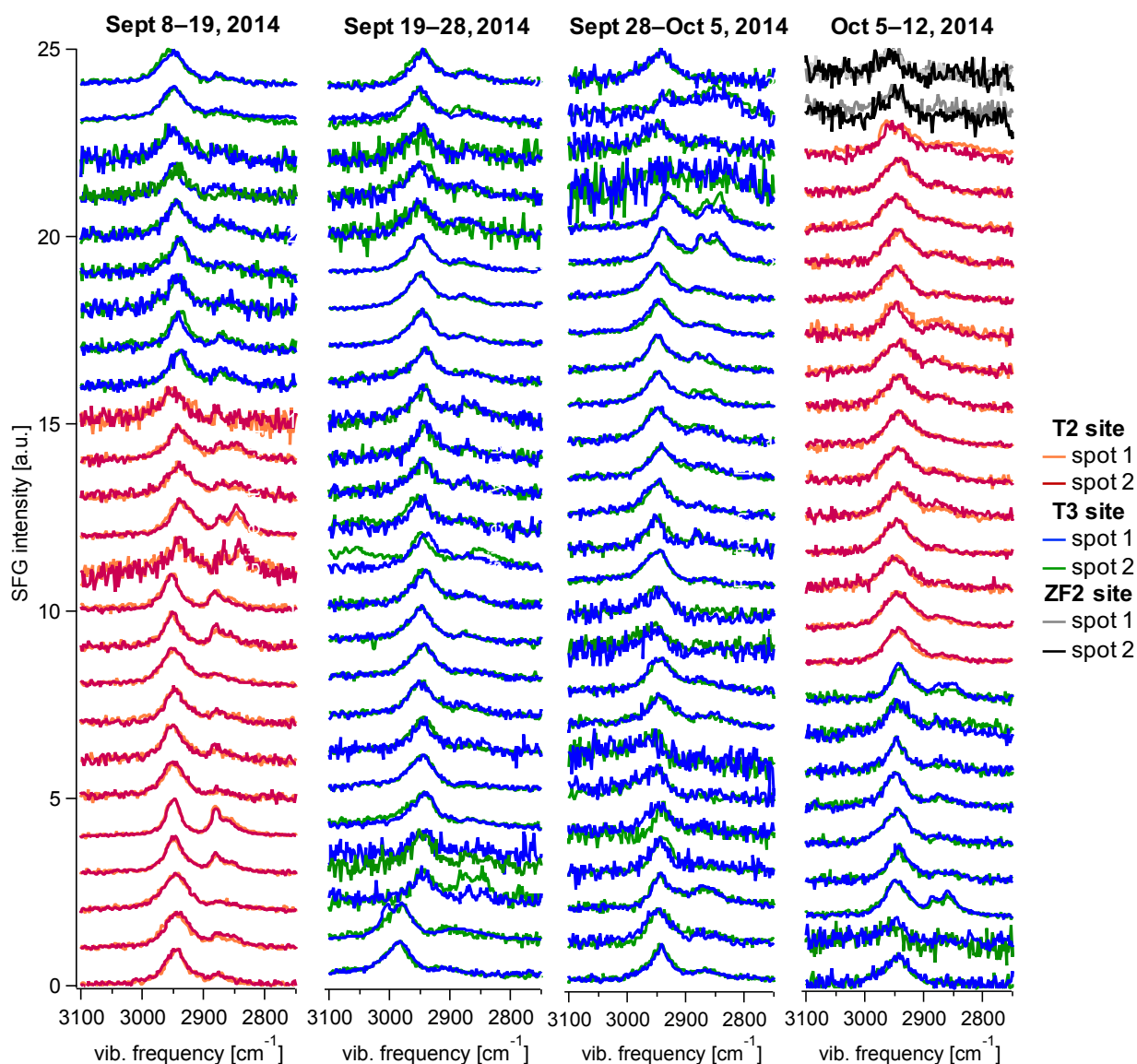


**Figure 5.10.** Compiled SFG spectra acquired in the C–H stretching region for filter samples collected during GOAmazon2014/5.

Given that aerosol samples from tropical rainforest ecosystems are well known to be dominated by products formed from isoprene emissions, the spectra are currently being compared to molecular standards of hydroxyl-mediated isoprene-derived oxidation products and organosulfates, which were synthesized by a fellow student, Jonathan Varelas, and a recent graduate, Dr. Marvin Vega. Interestingly, several of the spectra contain three distinct peaks in the

C–H region that resemble preliminary spectra of molecular standards of organosulfates derived from isoprene epoxy diol (IEPOX). Additionally, a large portion of the spectra obtained spectrally resemble that of  $\alpha$ -pinene- and  $\beta$ -caryophyllene-derived SOM collected in the Harvard flow tube reactor. **Figure 5.11** shows an example of the spectral resemblance observed between the IEPOX-derived organosulfates.

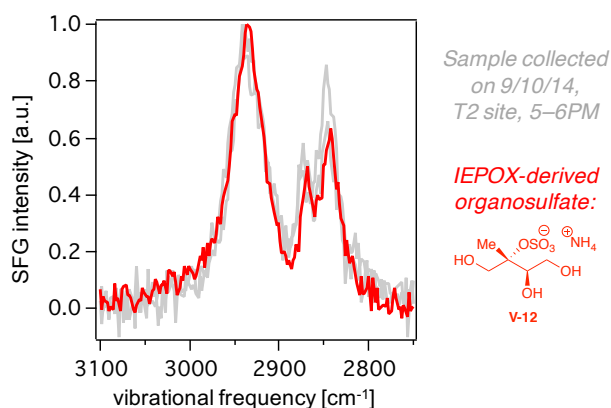


**Figure 5.11.** Example spectral overlay of sample collected at T2 site and IEPOX-derived organosulfate standard showing the spectral resemblance qualitatively observed.

We caution that in the absence of additional data, our qualitative comparisons are merely empirical. Ongoing work carried out by Yangdongling Liu focuses on fitting the SFG spectra to more rigorously compare our data to trends in several factors. These considerations include wind speed, wind direction, temperature, RH AMS data, temperature, concentration of relevant gases (e.g. ozone, CO, NO<sub>x</sub>, and SO<sub>2</sub>), RH, time of day/week/year (e.g. day vs. night, weekend vs. weekday, holidays), distance from Manaus, sample collection length, precipitation, and solar radiation.

**5.5. Towards dimers and higher order constituents in biogenic SOA particles.** In the following section, we discuss ongoing studies aimed at expanding our current suite of molecular standards to include dimers and higher order species, an emergent class of SOA constituents predicted to form via coupling reactions between earlier generation monomeric products of BVOC oxidation. In the previous chapters of this thesis, we outlined the synthesis and analysis of monomeric oxidation products that form when biogenic terpenes,  $\alpha$ -pinene and  $\beta$ -caryophyllene, undergo rapid gas-phase oxidation in the presence of ozone. These monomeric oxidation products are believed to facilitate transitions from the gas phase to the particle phase of SOA particles. Later-stage dimerization and oligomerization accretion reactions have also been proposed to take place, yielding higher molecular weight species that drive particle formation and growth.<sup>37-40</sup> Accretion of early-generation monomer oxidation products has been speculated to occur in both the gas and particle phases as well as via reactive heterogeneous processes.<sup>2, 41-42</sup> Moreover, such reactions can also occur during aging of aerosols leading to increased viscosity, which can influence the physicochemical properties of particles.<sup>41</sup> It is also speculated that dimers and oligomers may have a higher propensity to populate the particle surface than their monomer counterparts, and therefore their surface activity may have effects on the kinetics of SOA growth and evaporation, along with CCN activity. For instance, recent studies have observed a “crusting effect,” wherein oligomers populate the surface of particles and over time form a shell-like structure.<sup>43-44</sup> Due to the low volatility and high viscosity of these compounds, this shell is thought to both limit diffusion of adsorbed molecules into the bulk as well as the evaporation of less volatile species.<sup>45-46</sup>

An increasing number of field and laboratory studies have reported that the higher order oxidation products formed from these accretion reactions may make up a significant portion of

the total organic mass present in atmospheric aerosol.<sup>47-50</sup> However, the diversity of monomer precursors and the chemical transformations that couple them together presents a great challenge for structural elucidation and analysis of their relevant properties. Therefore, the identification and investigation of these species represents an enigmatic, yet important area within atmospheric processes. In this section, we describe ongoing work focused on the synthesis and analysis of a suite of dimeric and oligomeric species that have been putatively identified by MS studies in order to both confirm their structures and to provide sufficient material to investigate their atmospherically relevant physicochemical properties.

Specifically, we focus on dimers derived from  $\alpha$ -pinene, given the existing literature precedent for this BVOC. We discuss synthetic routes that have been established to couple monomer building blocks together via esterification<sup>38, 40, 48, 50-51</sup> and aldol addition and condensation,<sup>48-49, 52-55</sup> which are among the various postulated reactions leading to dimerization of early-generation monomers. Such studies could enable access to a diverse suite of dimers and higher order species, bringing the field a step closer to elucidating key structure–property relationships for this currently elusive class of molecules. We also describe preliminary data and future plans for subsequent measurements utilizing these dimer molecular standards. This project is being carried out with help from a fellow graduate student, Aleia Bellcross.

**5.5.1. Synthesis of  $\alpha$ -pinene-derived dimers.** Our synthetic approach towards accessing putative dimeric and oligomeric SOA particle constituents utilizes a modular strategy starting from monomeric building blocks. **Figure 5.12** displays the initial suite of aldol-adduct and ester-adduct dimers that were targeted.

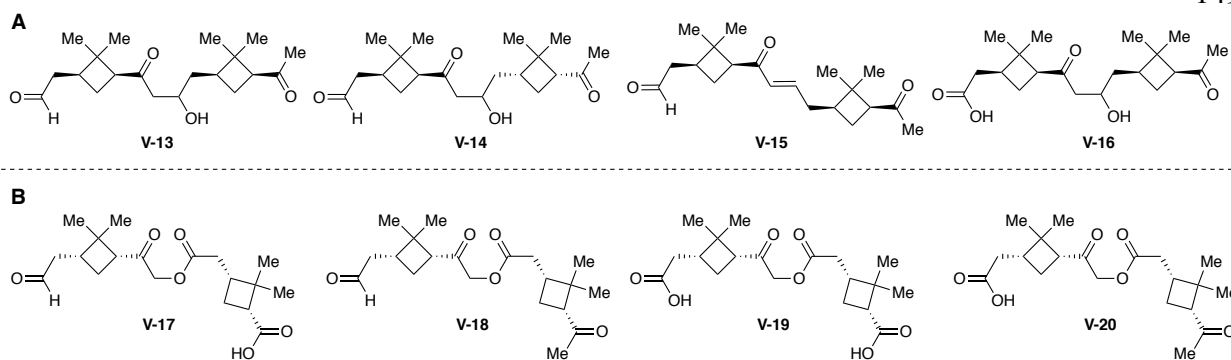
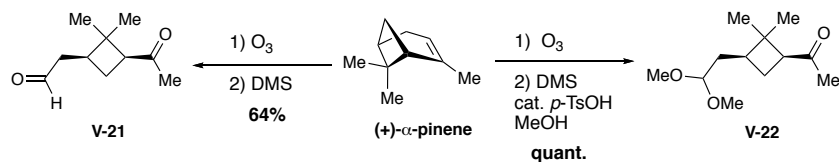


**Figure 5.12.** Target (A) aldol-adduct and (B) ester-adduct dimers derived from  $\alpha$ -pinene.

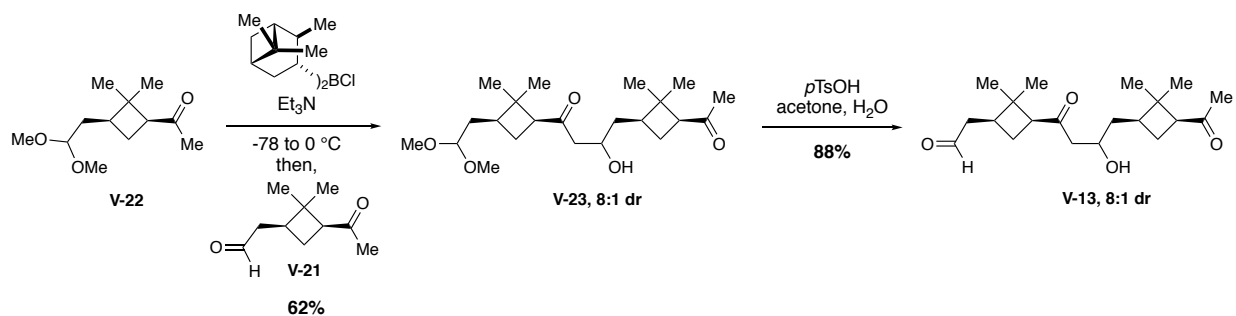
We first discuss efforts towards the synthesis of the aldol-adduct dimers derived from pinonaldehyde (**V-21**) shown in **Figure 5.12A**. The expected stability of these aldol adduct dimers made them a promising starting point for the synthesis of these higher order SOA constituents. When considering aldol addition of pinonaldehyde (**V-21**) with itself, regioisomeric adducts could arise because pinonaldehyde (**V-21**) contains both an aldehyde and ketone that may participate in aldol chemistry. Therefore, in order to access the ketone–aldehyde adduct in particular, two monomer building blocks were synthesized. Pinonaldehyde (**V-21**) was synthesized analogous as described in Chapter 2, via ozonolysis of  $\alpha$ -pinene with reductive work-up conditions. To synthesize a monomer building block in which the aldehyde is masked, acetal **V-22** was synthesized using Schreiber conditions.<sup>56</sup>



**Scheme 5.1.** Synthesis of monomer building blocks for aldol-adduct dimer syntheses.

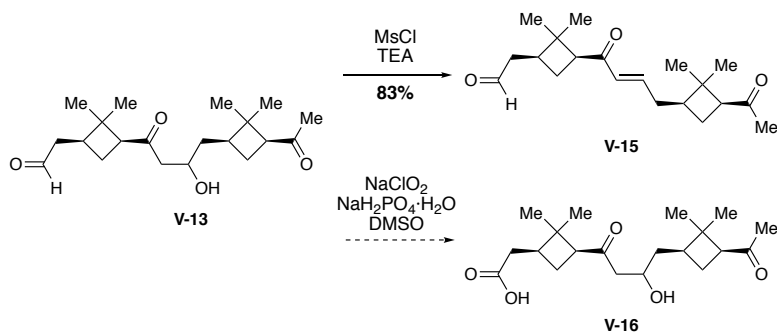
With these two monomers in hand, we next turned our attention to dimerization of building blocks, **V-21** and **V-22**, under aldol addition conditions. Initial efforts using LDA to form a lithium enolate were generally low yielding and inherently non-diastereoselective, and

thus, an alternate strategy employing a chiral boron reagent was explored. Coupling together **V-21** and **V-22**, synthesized from (+)- $\alpha$ -pinene, using (-)-diisopinocampheyl chloroborane ((-)-DIP-chloride) yielded the desired acetal-protected ketone–aldehyde dimer **V-23** in 64% yield and ~8:1 dr. Subsequent deprotection of acetal **V-23** afforded compound **V-13**. The moderate diastereoselectivity observed under these reaction conditions prompted investigation into potentially accessing stereochemical diversity via varied combinations of the enantiomers of the two monomer building blocks and DIP-chloride. To our dismay, subjecting the enantiomers of **V-21** and **V-22** (*ent*-**V-21** and *ent*-**V-22**, respectively) produced from (-)- $\alpha$ -pinene to aldol conditions with (-)-DIP-chloride yielded the corresponding acetal-protected ketone–aldehyde dimer in 1:1 dr. Initial efforts to assign the absolute configuration of the formed stereogenic center by Mosher Ester analysis were unsuccessful and could be a subject of future work.



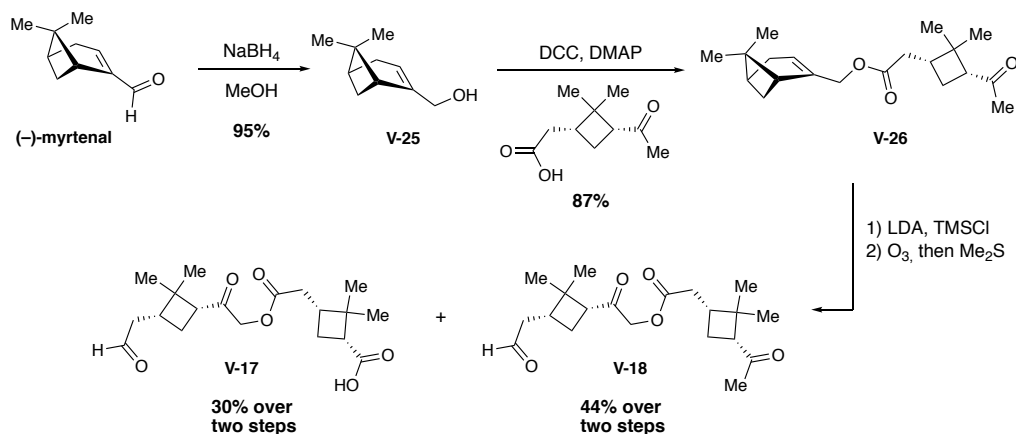
**Scheme 5.2.** Synthesis of aldol addition dimer **V-13**.

Acetal-protected dimer **V-24** was accessed in an analogous fashion to that discussed for **V-23**, but using the enantiomer of **V-21** (*ent*-**V-21**) as the electrophilic partner. Subsequent acetal deprotection afforded dimer **V-14**. Additionally, aldol condensation dimer **V-15** was synthesized via a mesylate-mediated dehydration of **V-13** under basic conditions. Efforts to synthesize acid **V-16** using Pinnick oxidation conditions are also currently underway.



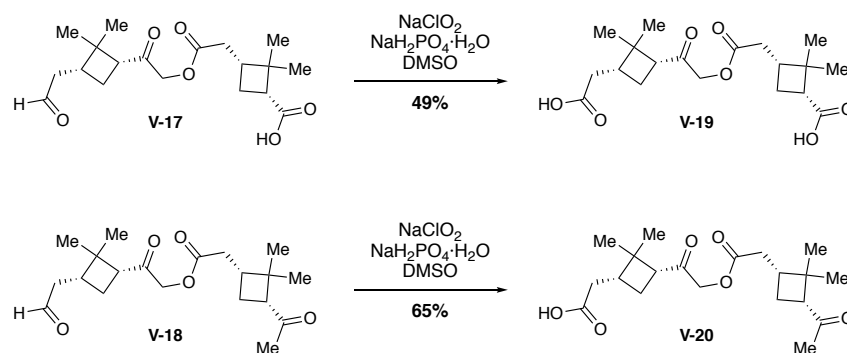
**Scheme 5.3.** Synthesis of aldol condensation dimer **V-15** and acid analogue **V-16**.

We subsequently turned our attention to synthesizing a suite of ester-adduct dimers. (–)-Myrtenol (**V-25**) was synthesized from a NaBH<sub>4</sub> reduction of (–)-myrtenal, which was then subjected to esterification with commercially available *cis*-pinonic acid (racemate) to yield myrtenol–pinonyl ester **V-26** as an equal mixture of diastereomers. Subsequently, formation of the silyl enol ether and ozonolysis using reductive work-up conditions afforded product **V-17**. A low yield was obtained due to incomplete conversion of the methyl ketone to the silyl enol ether, which also led to the simultaneous isolation of another desired analogue, **V-18**, following ozone-mediated oxidative cleavage with the methyl ketone still intact. To our delight, compounds **V-17** and **V-18** could be easily separated via flash column chromatography.



**Scheme 5.4.** Synthesis of ester-adduct dimers **V-17** and **V-18**.

Additionally, dimers **V-17** and **V-18** were each subjected to Pinnick oxidation conditions to afford the desired acids **V-19** and **V-20**, respectively (**Scheme 5.5**). Once practical quantities of all eight aldol- and ester-adduct dimers have been synthesized, we aim to carry out subsequent analytical measurements using these species for both MS studies (for possible structural elucidation in laboratory and SOM samples), and for characterization of their climate-relevant physicochemical properties. Future synthetic efforts could focus on applying this modular aldol addition methodology towards the synthesis of aldol-adduct trimers, tetramers, and higher order oligomers. Furthermore, we could further expand the scope of this work to synthesize dimers from building blocks derived from other abundant terpenes, including 3-carene and  $\beta$ -caryophyllene, as well as crossed-products from these different species. Further studies could also explore other dimerization pathways, including anhydride formation,<sup>57</sup> that have been proposed as relevant transformations for SOA formation and growth.



**Scheme 5.5.** Pinnick oxidation reactions of **V-17** and **V-18** to synthesize **V-19** and **V-20**, respectively.

**5.5.2. Analytical measurements using dimeric species.** Investigation of these dimeric molecular standards by MS benchmarking studies, as well as surface-specific analyses, would yield insight into the composition and surface chemistry of biogenic SOA particles. With this goal in mind, dynamic surface tension measurements are being carried out to further investigate

the surface activity of these dimers, and therefore their potential impacts on cloud activation, as compared to their monomer counterparts. In fact, preliminary experiments reveal that these dimers may be significantly more surface active than their monomer building blocks, despite their identical O:C ratios (**Figure 5.13**).

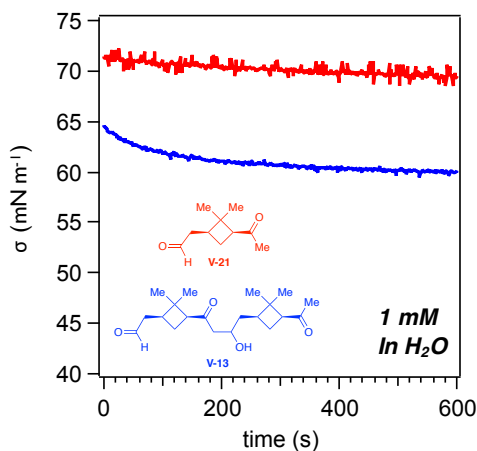


**Figure 5.13.** Preliminary surface tension data for pinonaldehyde (V-21) and ketone–aldehyde aldol addition dimer V-13 at 1 mM in water pendant droplets.

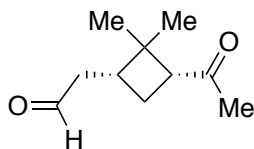
In addition, we have begun to explore the utility of time-of-flight secondary ion mass spectrometry (ToF-SIMS) as a surface-sensitive technique for exploring the composition of secondary organic aerosols.<sup>58</sup> To complement such studies, ESI-MS benchmarking studies are also currently underway towards possible identification of these standards in laboratory and field SOM samples. These analyses will be continued by Aleia Bellcross. Overall, gaining access to dimer and oligomer standards such as these is essential for both understanding their physical properties as well as the accurate elucidation of SOA particle composition.

### 5.5.3. Experimental procedures.

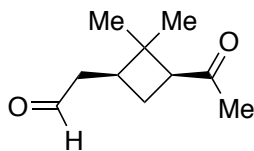
#### 5.5.3.1. General methods.

All reactions were carried out under nitrogen atmosphere in flame-dried glassware unless otherwise stated. Anhydrous solvents (DCM, methanol, THF, Et<sub>2</sub>O) were purified by passage through a bed of activated alumina.<sup>1</sup> Reagents were purified prior to use unless otherwise stated following the guidelines of Armarego and Chai.<sup>2</sup> Purification of reaction products was carried out by flash chromatography using SiliCycle silica gel F60, 40-63 μm (230-400 mesh). Analytical TLC was performed using Merck Silica Gel 60 Å F-254 precoated plates (0.25 mm thickness) or EM Reagent 0.25mm silica gel 60-F plates. Visualization was accomplished with p-anisaldehyde stain. <sup>1</sup>H-NMR spectra were recorded on a Varian Inova 500 (500 MHz), Agilent DD2 (500MHz), Agilent DD MR-400 (400MHz), or Bruker Advance III 500 (500 MHz) spectrometer and are reported in ppm using solvent as an internal standard (CDCl<sub>3</sub> at 7.26 ppm). Data are reported as (app = apparent, obs = obscured, s = singlet, d = doublet, t = triplet, q = quartet, p = pentet, h = hextet, sep = septet, o = octet, m = multiplet, b = broad; integration; coupling constant(s) in Hz. <sup>13</sup>C-NMR spectra were recorded on a Bruker Advance III 500 spectrometer equipped with DCH CryoProbe, and are reported in ppm using solvent as an internal standard (CDCl<sub>3</sub> at 77.16 ppm, except where noted). Optical rotation was determined using a Rudolph Research Analytical Autopol IV, Series #82239 with either a 10 cm or 5 cm pathlength cell at the sodium D line. HR mass spectra were collected on a Thermo Q-Exactive orbitrap mass spectrometer in ESI mode. Diamond ATR infrared spectra were obtained on a ThermoNicolet iS10 FT-IR spectrometer. Germanium ATR infrared spectra were recorded using a Bruker Tensor 37.

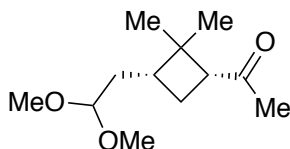
### 5.5.3.2. Synthesis of aldol-adduct dimers.



**2-((1*R*,3*R*)-3-Acetyl-2,2-dimethylcyclobutyl)acetaldehyde (*ent*-V-21).** (–)- $\alpha$ -Pinene (10.0 g, 73.4 mmol, 1.0 eq) and  $\text{CH}_2\text{Cl}_2$  (250 mL) were added to a flame-dried round bottom flask. Ozone (generated at 110 V) was bubbled through the solution at  $-78\text{ }^\circ\text{C}$  for 35 minutes or until observation of the characteristic pale blue color of ozone. At this time,  $\text{O}_2$  was bubbled through solution for an additional 10 minutes. After addition of dimethyl sulfide (60 mL, 832 mmol), the reaction was allowed to warm to room temperature and stirred overnight for an additional 16 hours. The reaction was then diluted with  $\text{H}_2\text{O}$  and extracted with  $\text{CH}_2\text{Cl}_2$ . The combined organic layers were washed with brine, dried using  $\text{MgSO}_4$ , and solvent concentrated under reduced pressure to afford the crude product as a light yellow oil. Flash column chromatography on silica gel using a gradient of 10% to 30% EtOAc in hexanes as the eluent afforded the title compound (8.17 g, 48.6 mmol, 66% yield) as a clear oil:  $[\alpha]_{\text{D}} = -5.1$  ( $c$  1.00,  $\text{CHCl}_3$ ); IR (Germanium ATR): 2954, 2826, 2724, 1720, 1701, 1369, 1181  $\text{cm}^{-1}$ ;  $^1\text{H}$  NMR (500 MHz,  $\text{CDCl}_3$ )  $\delta$  9.74 (s, 1H), 2.92 (dd,  $J = 10.0, 7.7$  Hz, 1H), 2.53 – 2.37 (m, 3H), 2.04 (s, 3H), 2.02 – 1.90 (m, 2H), 1.34 (s, 3H), 0.84 (s, 3H);  $^{13}\text{C}$  NMR (126 MHz,  $\text{CDCl}_3$ )  $\delta$  207.5, 201.5, 54.5, 45.3, 43.4, 35.9, 30.5, 30.3, 23.0, 17.8; HRMS (ESI): Exact mass calc'd for  $\text{C}_{10}\text{H}_{17}\text{O}_2$   $[\text{M}+\text{H}]^+$ , 169.1229. Found 169.1223.

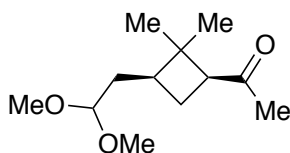


**2-((1*S*,3*S*)-3-Acetyl-2,2-dimethylcyclobutyl)acetaldehyde (V-21).** Compound **V-21** was prepared as described for compound *ent*-**V-21** above, using (+)- $\alpha$ -pinene. The title compound (7.88 g, 46.8 mmol, 64% yield) was isolated as a clear oil:  $[\alpha]_D = +11.3$  ( $c$  1.00,  $\text{CHCl}_3$ ); IR (Germanium ATR): 2956, 2875, 1703, 1370, 1225, 1183, 802  $\text{cm}^{-1}$ ;  $^1\text{H}$  NMR (500 MHz,  $\text{CDCl}_3$ )  $\delta$  9.73 (s, 1H), 2.91 (dd,  $J = 10.1, 7.6$  Hz, 1H), 2.57 – 2.33 (m, 1H), 2.04 (s, 3H), 2.02 – 1.90 (m, 2H), 1.33 (s, 3H), 0.84 (s, 3H);  $^{13}\text{C}$  NMR (126 MHz,  $\text{CDCl}_3$ )  $\delta$  207.5, 201.5, 54.5, 45.3, 43.4, 35.9, 30.5, 30.3, 23.0, 17.8; All spectroscopic data for this compound agrees with previously reported values for *ent*-**V-21**.<sup>59</sup>

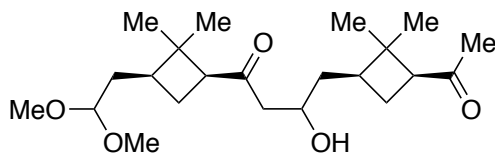


**1-((1*R*,3*R*)-3-(2,2-Dimethoxyethyl)-2,2-dimethylcyclobutyl)ethan-1-one (*ent*-**V-22**).** (–)- $\alpha$ -Pinene (2.00 g, 14.7 mmol, 1.0 eq) and 1:1 DCM:MeOH (120 mL) were added to a flame-dried round bottom flask. Ozone (generated at 110 V) was bubbled through the solution at  $-78$  °C for 35 minutes or until observation of the characteristic pale blue color of ozone.  $\text{O}_2$  was then bubbled through solution for an additional 15 minutes. At  $-78$  °C, *p*-toluenesulfonic acid monohydrate (0.196 g, 1.03 mmol, 0.07 eq) and dimethyl sulfide (3.00 mL, 41.1 mmol, 2.8 eq) in MeOH (20 mL) was added dropwise (10 mL rinse), and the reaction was then allowed to warm to 0 °C over the course of 1 hour. At this time, the reaction was warmed to room temperature, and stirred overnight for an additional 16 hours. The mixture was then diluted with  $\text{H}_2\text{O}$  and extracted with  $\text{CH}_2\text{Cl}_2$ . The combined organic layers were washed with brine, dried

using  $\text{MgSO}_4$ , and solvent concentrated under reduced pressure to afford the crude product as a light yellow oil. Flash column chromatography on silica gel using 20% EtOAc in hexanes as the eluent afforded the title compound (3.04 g, 14.2 mmol, 97% yield) as a clear pale yellow oil:  $[\alpha]_D = -3.4$  ( $c$  1.00,  $\text{CHCl}_3$ ); IR (Germanium ATR): 2949, 2830, 1704, 1355, 1122, 1052, 808  $\text{cm}^{-1}$ ;  $^1\text{H}$  NMR (400 MHz,  $\text{CDCl}_3$ )  $\delta$  4.28 (dd,  $J = 6.2, 5.3$  Hz, 1H), 3.30 (s, 3H), 3.29 (s, 3H), 2.82 (dd,  $J = 9.9, 7.4$  Hz, 1H), 2.03 (s, 3H), 2.02 – 1.80 (m, 3H), 1.63 – 1.55 (m, 1H), 1.55 – 1.44 (m, 1H), 1.28 (s, 3H), 0.85 (s, 3H);  $^{13}\text{C}$  NMR (101 MHz,  $\text{CDCl}_3$ )  $\delta$  208.0, 103.6, 54.7, 53.0, 52.8, 43.4, 37.9, 32.9, 30.4, 30.2, 23.4, 17.5; HRMS (ESI): Exact mass calc'd for  $\text{C}_{12}\text{H}_{22}\text{O}_3$   $[\text{M}+\text{Na}]^+$ , 237.1467. Found 237.1459.

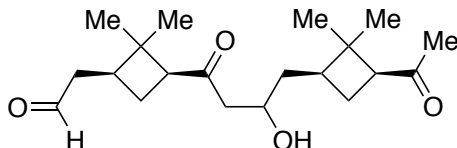


**1-((1S,3S)-3-(2,2-Dimethoxyethyl)-2,2-dimethylcyclobutyl)ethan-1-one (V-22).** Compound **V-22** was prepared as described for compound *ent-V-22* above, using (+)- $\alpha$ -pinene. The title compound (3.14 g, 14.7 mmol, quant. yield) was isolated a clear pale yellow oil:  $[\alpha]_D = +7.3$  ( $c$  1.00,  $\text{CHCl}_3$ ); IR (Germanium ATR): 2951, 2830, 1705, 1354, 1121, 1053, 819  $\text{cm}^{-1}$ ;  $^1\text{H}$  NMR (400 MHz,  $\text{CDCl}_3$ )  $\delta$  4.29 (dd,  $J = 6.2, 5.3$  Hz, 1H), 3.30 (s, 3H), 3.30 (s, 3H), 2.82 (dd,  $J = 9.9, 7.4$  Hz, 1H), 2.03 (s, 3H), 2.03 – 1.80 (m, 3H), 1.69 – 1.55 (m, 1H), 1.55 – 1.42 (m, 1H), 1.28 (s, 3H), 0.86 (s, 3H);  $^{13}\text{C}$  NMR (101 MHz,  $\text{CDCl}_3$ )  $\delta$  208.0, 103.6, 54.7, 53.0, 52.8, 43.4, 37.9, 33.0, 30.4, 30.3, 23.4, 17.5; HRMS (ESI): Exact mass calc'd for  $\text{C}_{12}\text{H}_{22}\text{O}_3$   $[\text{M}+\text{Na}]^+$ , 237.1467. Found 237.1461.

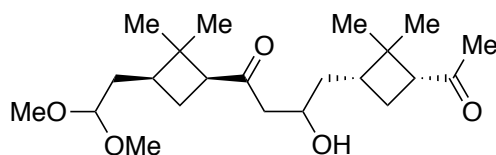


**4-((1*S*,3*S*)-3-Acetyl-2,2-dimethylcyclobutyl)-1-((1*S*,3*S*)-3-(2,2-dimethoxyethyl)-2,2-dimethylcyclobutyl)-3-hydroxybutan-1-one (V-23).** To a flame-dried round bottom flask was added (–)-DIP-chloride (65 wt % in hexanes, 0.121 mL, 1.4 eq) and Et<sub>2</sub>O (3 mL). The solution was cooled to -78 °C and freshly distilled TEA (0.039 mL, 0.278 mmol, 1.7 eq) was added. A solution of compound **V-22** (0.035 g, 0.163 mmol, 1.0 eq) in Et<sub>2</sub>O (1 mL) was then added (with 2 additional 0.5 mL rinses) via cannula, and the reaction was brought to 0 °C to stir for 1 hour. At this time, the reaction was brought to -78 °C and compound **V-21** (0.036 g, 0.212 mmol, 1.3 eq) in Et<sub>2</sub>O (1 mL) was then added (with 2 additional 0.5 mL rinses) via cannula. The reaction was stirred at -78 °C for 2 hours, at which time the reaction was quenched by slowly adding a 2:1:1 solution of pH 7 phosphate buffer: MeOH:30% H<sub>2</sub>O<sub>2</sub> (114 mL). The mixture was stirred at room temperature for 30 minutes, diluted with H<sub>2</sub>O, and extracted with Et<sub>2</sub>O. The combined organic layers were washed with saturated NaHCO<sub>3</sub>, dried over Na<sub>2</sub>SO<sub>4</sub>, and concentrated under reduced pressure. The crude material was purified by flash column chromatography on silica gel (30 to 100% EtOAc in hexanes solvent gradient) to afford the desired dimer (0.039 g, 0.101 mmol, 62% yield, ~8:1 mixture of diastereomers) as a viscous clear oil: IR (Germanium ATR): 3482, 2948, 1700, 1462, 1369, 1123, 1050 cm<sup>-1</sup>; Major diastereomer (89%): <sup>1</sup>H NMR (400 MHz, CDCl<sub>3</sub>) δ 4.31 – 4.25 (m, 1H), 3.96 – 3.81 (m, 1H), 3.29 (s, 6H), 2.92 – 2.73 (m, 2H), 2.43 – 2.33 (m, 2H), 2.19 – 2.07 (m, 1H), 2.03 (s, 3H), 2.01 – 1.82 (m, 6H), 1.72 – 1.57 (m, 2H), 1.56 – 1.44 (m, 2H), 1.28 (s, 3H), 1.27 (s, 3H), 0.84 (s, 3H), 0.83 (s, 3H); <sup>13</sup>C NMR (101 MHz, CDCl<sub>3</sub>) δ 211.6, 208.1, 103.5, 65.8, 54.5, 54.4, 53.0, 52.9, 49.8, 44.0, 43.3, 38.5, 37.9, 37.9, 36.8, 32.9,

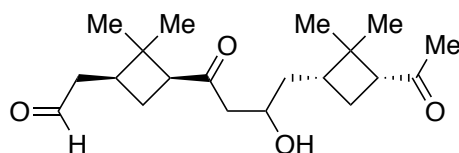
30.5, 30.3, 23.3, 23.0, 17.8, 17.5; HRMS (ESI): Exact mass calc'd for  $C_{22}H_{38}O_5$   $[M+Na]^+$ , 405.2617. Found 405.2611.



**2-((1S,3S)-3-(4-((1S,3S)-3-Acetyl-2,2-dimethylcyclobutyl)-3-hydroxybutanoyl)-2,2-dimethylcyclobutyl)acetaldehyde (V-13):** To a solution of the crude material (0.039 g, 0.101 mmol, 1.0 eq) and a 2:2:1 solution of acetone:H<sub>2</sub>O:EtOAc (5 mL) was added *p*-toluenesulfonic acid monohydrate (0.019 g, 0.101 mmol, 1.0 eq) at room temperature. The reaction was stirred overnight for 16 hours at room temperature, at which time the reaction was diluted with H<sub>2</sub>O, extracted with Et<sub>2</sub>O, dried over Na<sub>2</sub>SO<sub>4</sub>, and concentrated under reduced pressure. The crude product was purified by flash column chromatography on silica gel using a 30% EtOAc in hexanes to 100% EtOAc solvent gradient, followed by subsequent purification by flash column chromatography on silica gel using 2.5 to 5% MeOH in DCM to afford the title compound (0.030 g, 0.088 mmol, 88% yield, ~8:1 mixture of diastereomers) as a viscous clear oil: IR (Germanium ATR): 3437, 2952, 2729, 1696, 1369, 1146, 750 cm<sup>-1</sup>; Major diastereomer (89%): <sup>1</sup>H NMR (400 MHz, CDCl<sub>3</sub>) δ 9.73 (s, 1H), 4.01 – 3.79 (m, 1H), 3.28 (s, 1H), 2.94 – 2.79 (m, 2H), 2.53 – 2.32 (m, 5H), 2.20 – 2.07 (m, 1H), 2.03 (s, 3H), 2.01 – 1.82 (m, 4H), 1.52 (ddd, *J* = 13.6, 8.8, 4.8 Hz, 1H), 1.32 (s, 3H), 1.28 (s, 3H), 1.24 – 1.13 (m, 1H), 0.83 (s, 3H), 0.82 (s, 3H); <sup>13</sup>C NMR (101 MHz, CDCl<sub>3</sub>) δ 211.1, 208.1, 201.3, 65.8, 54.4, 54.3, 49.9, 45.2, 43.9, 43.3, 38.4, 36.8, 35.9, 30.6, 30.3, 23.3, 22.6, 18.1, 17.5; HRMS (ESI): Exact mass calc'd for  $C_{20}H_{32}O_4$   $[M+Na]^+$ , 359.2198. Found 359.2194.

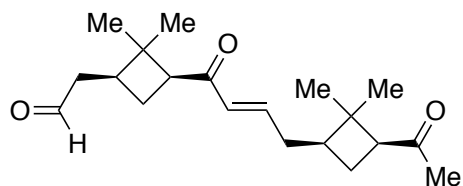


**4-((1R,3R)-3-Acetyl-2,2-dimethylcyclobutyl)-1-((1S,3S)-3-(2,2-dimethoxyethyl)-2,2-dimethylcyclobutyl)-3-hydroxybutan-1-one (V-24).** Acetal **V-22** (0.250 g, 1.17 mmol) was coupled to aldehyde *ent*-**V-21** (0.255 g, 1.52 mmol) following the procedure for aldol addition described for compound **V-23** to afford the title compound (0.322 g, 0.840 mmol, 72% yield, ratio of diastereomers not detectable by NMR) as a viscous clear oil: IR (Germanium ATR): 2966, 2923, 2861, 1724, 1702, 1386, 1028  $\text{cm}^{-1}$ ;  $^1\text{H}$  NMR (400 MHz,  $\text{CDCl}_3$ )  $\delta$  4.34 – 4.21 (m, 1H), 4.02 – 3.92 (m, 1H), 3.30 (s, 6H), 2.88 – 2.76 (m, 2H), 2.53 – 2.24 (m, 2H), 2.03 (s, 3H), 2.01 – 1.82 (m, 6H), 1.67 – 1.58 (m, 1H), 1.54 – 1.46 (m, 2H), 1.45 – 1.36 (m, 2H), 1.27 (s, 3H), 1.26 (s, 3H), 0.85 (s, 3H), 0.84 (s, 3H);  $^{13}\text{C}$  NMR (126 MHz,  $\text{CDCl}_3$ )  $\delta$  211.5, 208.1, 103.5, 66.6, 54.7, 53.0, 52.9, 49.5, 43.9, 43.6, 38.3, 37.9, 36.9, 32.9, 30.7, 30.3, 29.8, 24.1, 23.1, 17.9, 17.4; HRMS (ESI): Exact mass calc'd for  $\text{C}_{22}\text{H}_{38}\text{O}_5$   $[\text{M}+\text{Na}]^+$ , 405.2617. Found 405.2618.



**2-((1R,3R)-3-(4-((1S,3S)-3-Acetyl-2,2-dimethylcyclobutyl)-3-hydroxybutanoyl)-2,2-dimethylcyclobutyl)acetaldehyde (V-14):** Compound **V-14** (0.322 g, 0.840 mmol) was prepared following the procedure for acetal deprotection described above for compound **V-13** to afford the title compound (0.233 g, 0.692 mmol, 82% yield, ratio of diastereomers not detectable by NMR) as a viscous clear oil: IR (Germanium ATR): 3453, 2952, 2861, 1722, 1696, 1369, 1181  $\text{cm}^{-1}$ ;  $^1\text{H}$  NMR (400 MHz,  $\text{CDCl}_3$ )  $\delta$  9.73 (s, 1H), 4.02 – 3.84 (m, 1H), 3.11 (s, 1H), 2.93 – 2.78 (m, 2H), 2.57 – 2.22 (m, 5H), 2.15 – 2.07 (m, 1H), 2.03 (s, 3H), 2.00 – 1.76 (m, 4H), 1.45 – 1.36 (m, 2H),

1.32 (s, 3H), 1.31 (s, 3H), 0.84 (s, 3H), 0.82 (s, 3H);  $^{13}\text{C}$  NMR (126 MHz,  $\text{CDCl}_3$ )  $\delta$  210.9, 208.0, 201.3, 66.6, 60.5, 54.7, 54.3, 49.6, 45.2, 43.9, 43.6, 38.3, 36.9, 35.9, 30.6, 30.3, 24.1, 22.7, 18.1, 17.4; HRMS (ESI): Exact mass calc'd for  $\text{C}_{20}\text{H}_{32}\text{O}_4$   $[\text{M}+\text{Na}]^+$ , 359.2198. Found 359.2189.

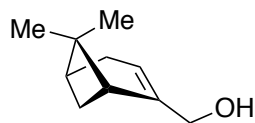


**2-((1*S*,3*S*)-3-((*E*)-4-((1*R*,3*S*)-3-Acetyl-2,2-dimethylcyclobutyl)but-2-enoyl)-2,2-**

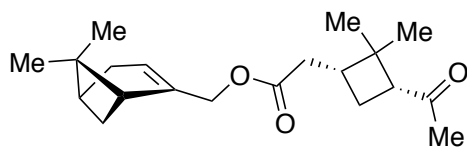
**dimethylcyclobutyl)acetaldehyde (V-15).** To a solution of compound **V-13** (0.030 g, 0.089 mmol, 1.0 eq) in  $\text{CH}_2\text{Cl}_2$  (1 mL) at 0 °C was added freshly distilled triethylamine (0.037 mL, 0.267 mmol, 3.0 eq). Distilled methanesulfonyl chloride (0.008 mL, 0.107 mmol, 1.2 eq) was then added dropwise. After stirring for 5 minutes at 0 °C, the reaction mixture was allowed to warmed to room temperature to stir for 24 hours. The reaction was then diluted with  $\text{H}_2\text{O}$  and extracted with  $\text{CH}_2\text{Cl}_2$ . The combined organic layers were washed with saturated  $\text{NaHCO}_3$ , dried over  $\text{Na}_2\text{SO}_4$ , and concentrated under reduced pressure. The crude product was purified by flash column chromatography on silica gel using a 20 to 30% EtOAc in hexanes solvent gradient, followed by subsequent purification by flash column chromatography to afford the desired compound (0.0236 g, 0.074 mmol, 83% yield) as a viscous clear oil: IR (Germanium ATR) 2968, 2861, 1703, 1660, 1624, 1368, 1156  $\text{cm}^{-1}$ ,  $^1\text{H}$  NMR (500 MHz,  $\text{CDCl}_3$ )  $\delta$  9.74 (s, 1H), 6.68 (dt,  $J = 15.8, 7.1$  Hz, 1H), 6.06 (d,  $J = 15.8$  Hz, 1H), 3.14 (dd,  $J = 9.9, 7.5$  Hz, 1H), 2.85 (dd,  $J = 9.9, 7.5$  Hz, 1H), 2.51 – 2.41 (m, 2H), 2.30 – 2.19 (m, 1H), 2.16 – 2.08 (m, 2H), 2.04 (s, 3H), 2.02 – 1.91 (m, 2H), 1.86 (dt,  $J = 11.1, 7.6$  Hz, 1H), 1.31 (s, 6H), 1.28 – 1.23 (m, 2H), 0.88 (s, 3H), 0.77 (s, 3H);  $^{13}\text{C}$  NMR (126 MHz,  $\text{CDCl}_3$ )  $\delta$  207.6, 201.7, 198.8, 145.2, 131.4, 54.2, 51.6,

45.4, 43.6, 43.5, 41.0, 36.0, 33.5, 30.7, 30.5, 30.4, 23.1, 22.6, 18.0, 17.5; HRMS (ESI): Exact mass calc'd for C<sub>20</sub>H<sub>30</sub>O<sub>3</sub> [M+Na]<sup>+</sup>, 341.2093. Found 341.2093.

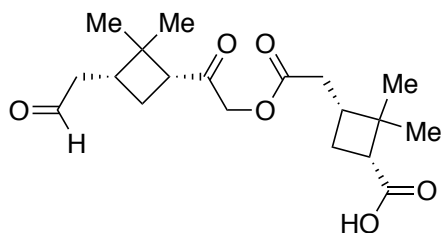
### 5.5.3.3. Synthesis of ester-adduct dimers.



**(1R)-(-)-Myrtenol (V-25).** (1R)-(-)-Myrtenal (2.16 g, 14.4 mmol, 1.0 eq) and MeOH (80 mL) were added to a flame-dried round bottom flask. NaBH<sub>4</sub> was slowly added portion-wise at 0 °C, and the reaction was stirred at 0 °C for 1 hour. The reaction was quenched using excess H<sub>2</sub>O (~20 mL) at 0 °C, and the reaction was warmed to room temperature. The reaction mixture was concentrated under reduced pressure, and extracted with DCM. The combined organic layers were washed with brine, dried over MgSO<sub>4</sub>, and the solvent evaporated under reduced pressure. The crude material was purified by flash column chromatography using silica gel (30% Et<sub>2</sub>O in pentanes), which afforded the title compound as a clear oil (2.08 g, 13.7 mmol, 95% yield): IR (Germanium ATR): 3309, 2986, 2912, 2832, 1655, 1449, 1331, 800 cm<sup>-1</sup>; <sup>1</sup>H NMR (500 MHz, CDCl<sub>3</sub>) δ 5.49 – 5.47 (m, 1H), 4.11 – 3.88 (m, 2H), 2.49 – 2.36 (m, 1H), 2.36 – 2.28 (m, 1H), 2.28 – 2.21 (m, 1H), 2.19 – 2.08 (m, 2H), 1.30 (s, 3H), 1.22 (t, J = 5.6 Hz, 1H), 1.18 (d, J = 8.6 Hz, 1H), 0.84 (s, 3H); <sup>13</sup>C NMR (126 MHz, CDCl<sub>3</sub>) δ 147.9, 118.1, 66.2, 43.5, 41.1, 38.1, 31.8, 31.3, 26.3, 21.3; All spectroscopic data matches previously reported data for myrtenol.<sup>60</sup>



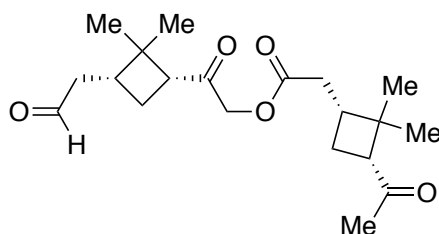
**((1R)-6,6-Dimethylbicyclo[3.1.1]hept-2-en-2-yl)methyl-2-((1R,3R)-3-acetyl-2,2-dimethylcyclobutyl)acetate (V-26).** Compound V-25 (1.00 g, 6.57 mmol, 1.0 eq) and CH<sub>2</sub>Cl<sub>2</sub> (110 mL) were added to a flame-dried round bottom flask. To the solution, *N,N'*-dicyclohexylcarbodiimide (1.49 g, 7.23 mmol, 1.1 eq) and *cis*-pinonic acid (1.33 g, 7.23 mmol, 1.1 eq) were added and the reaction mixture was stirred for 5 minutes at room temperature. At this time, 4-dimethylaminopyridine (DMAP) (0.080 g, 0.657 mmol, 0.1 eq) was added and the reaction was stirred at room temperature for 24 hours. The reaction mixture was then filtered through Celite rinsing with EtOAc and the filtrate was concentrated under reduced pressure. Any remaining dicyclohexyl urea byproduct was precipitated from cold EtOAc and removed via vacuum filtration. Subsequent purification by flash column chromatography with silica gel (10% EtOAc in hexanes) afforded the title compound as a 1:1 diastereomeric mixture (1.82 g, 5.72 mmol, 87% yield) as a viscous clear oil: IR (Germanium ATR): 2922, 1734, 1706, 1661, 1453, 1165, 803 cm<sup>-1</sup>; Due to overlapping signals, NMR data is reported for a single diastereomer for simplicity: <sup>1</sup>H NMR (400 MHz, CDCl<sub>3</sub>) δ 5.67 – 5.41 (m, 1H), 4.43 (dp, *J* = 3.0, 1.5 Hz, 2H), 2.87 (dd, *J* = 10.1, 7.6 Hz, 1H), 2.50 – 2.17 (m, 6H), 2.14 – 2.07 (m, 2H), 2.04 (s, 3H), 2.01 – 1.84 (m, 2H), 1.32 (s, 3H), 1.29 (d, *J* = 1.6 Hz, 3H), 1.17 (d, *J* = 8.7 Hz, 1H), 0.86 (s, 3H), 0.82 (s, 3H); <sup>13</sup>C NMR (101 MHz, CDCl<sub>3</sub>) δ 207.6, 172.8, 143.1, 121.8, 67.1, 54.4, 43.7, 43.4, 40.8, 38.1, 35.3, 31.6, 31.4, 30.4, 30.3, 26.3, 23.3, 23.2, 21.2, 17.4; HRMS (ESI): Exact mass calc'd for C<sub>20</sub>H<sub>30</sub>O<sub>3</sub> [M+Na]<sup>+</sup>, 341.2093. Found 341.2089.



**(1*R*,3*R*)-3-(2-(2-((1*R*,3*R*)-2,2-Dimethyl-3-(2-oxoethyl)cyclobutyl)-2-oxoethoxy)-2-oxoethyl)-2,2-dimethylcyclobutane-1-carboxylic acid (V-17).** To a solution of freshly distilled diisopropylamine (0.99 mL, 7.07 mmol, 1.5 eq) in THF (28 mL) in a flame-dried round bottom flask at 0 °C was added *n*-BuLi (3.02 mL, 5.65 mmol, 1.87 M in hexanes) to prepare a solution of LDA. After 5 minutes, reaction was cooled to –20 °C and distilled TMSCl (1.19 mL, 9.42 mmol, 2.0 eq) was added. Compound **V-26** (1.50 g, 4.71 mmol, 1.0 eq) in THF (13 mL) was then added (with 2 additional 3 mL rinses) dropwise via cannula. After stirring at –20 °C for 2 hours, the reaction was quenched with triethylamine and diluted with saturated NaHCO<sub>3</sub>. The mixture was warmed to room temperature, extracted with EtOAc, and washed with brine. The combined organic layers were dried using MgSO<sub>4</sub> and solvent concentrated under reduced pressure to afford crude product mixture as a light yellow oil, which was immediately carried over to the next step without further purification due to instability of the silyl enol ether.

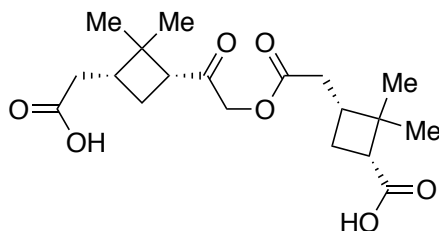
Ozone (generated at 110 V) was then bubbled through a solution of crude product (1.84 g, 4.71 mmol, 1.0 eq) in CH<sub>2</sub>Cl<sub>2</sub> (100 mL) in a flame-dried round bottom flask at –78 °C for 20 minutes, at which time the characteristic blue color of ozone was observed. O<sub>2</sub> was then bubbled through solution for an additional 10 minutes. After addition of dimethyl sulfide (3.80 mL, 51.8 mmol), mixture was allowed to warm to room temperature and stir overnight for an additional 16 hours. The mixture was then diluted with H<sub>2</sub>O, extracted with CH<sub>2</sub>Cl<sub>2</sub>, and the combined organic layers were washed with brine. The combined organic layers were then dried

using  $\text{MgSO}_4$  and the solvent concentrated under reduced pressure. Flash column chromatography on silica gel using 30% EtOAc in hexanes to 100% EtOAc solvent gradient, followed by subsequent purification by flash column chromatography on silica gel using 2.5% MeOH in DCM, afforded the desired compound (0.502 g, 1.43 mmol, 30% yield, equal mixture of diastereomers) as a clear viscous oil. Loss of product yield occurred due to incomplete conversion of the methyl ketone to the silyl enol ether, which led to the isolation of compound, **V-18**, 2-((1R,3R)-2,2-dimethyl-3-(2-oxoethyl)cyclobutyl)-2-oxoethyl-2-((1R,3R)-3-acetyl-2,2-dimethylcyclobutyl)acetate (0.732 g, 2.09 mmol, 44% yield) following oxidative cleavage under exposure to ozone. Compound **V-17** data: IR (Germanium ATR) 2958, 2926, 2863, 1721, 1692, 1369, 11147  $\text{cm}^{-1}$ ; Due to overlapping signals, NMR data is reported for a single diastereomer for simplicity:  $^1\text{H}$  NMR (500 MHz,  $\text{CDCl}_3$ )  $\delta$  9.73 (s, 1H), 4.66 – 4.45 (m, 2H), 3.00 – 2.86 (m, 1H), 2.84 – 2.75 (m, 1H), 2.55 – 2.36 (m, 6H), 2.20 – 2.11 (m, 1H), 2.09 – 2.02 (m, 1H), 1.99 – 1.90 (m, 2H), 1.32 (s, 3H), 1.25 (s, 3H), 1.02 (s, 3H), 0.87 (s, 3H);  $^{13}\text{C}$  NMR (126 MHz,  $\text{CDCl}_3$ )  $\delta$  201.9, 201.3, 178.4, 171.9, 68.3, 50.1, 46.2, 45.2, 44.0, 43.1, 38.3, 36.1, 35.0, 30.7, 30.0, 24.4, 22.2, 17.9, 17.7; HRMS (ESI): Exact mass calc'd for  $\text{C}_{19}\text{H}_{28}\text{O}_6$   $[\text{M}+\text{NH}_4]^+$ , 370.2230. Found 370.2235.



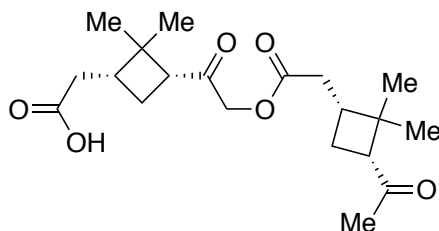
**2-((1R,3R)-2,2-Dimethyl-3-(2-oxoethyl)cyclobutyl)-2-oxoethyl-2-((1R,3R)-3-acetyl-2,2-dimethylcyclobutyl)acetate (V-18)**. As described above, compound **V-18** was isolated, along with the desired compound **V-17**, due to incomplete conversion of the methyl ketone to the silyl

enol ether and subsequent exposure to ozone. Separation of compounds **V-17** and **V-18** via flash column chromatography on silica gel using 30% EtOAc in hexanes to 100% EtOAc solvent gradient afforded compound **V-18** (0.732 g, 2.09 mmol, 44% yield) as a clear viscous oil: IR (Germanium ATR) 2953, 2863, 1738, 1721, 1453, 1147, 729  $\text{cm}^{-1}$ ; Due to overlapping signals, NMR data is reported for a single diastereomer for simplicity:  $^1\text{H}$  NMR (500 MHz,  $\text{CDCl}_3$ )  $\delta$  9.73 (s, 1H), 4.60 – 4.45 (m, 2H), 3.00 – 2.82 (m, 2H), 2.54 – 2.25 (m, 6H), 2.10 – 2.05 (m, 1H), 2.03 (s, 3H), 2.01 – 1.90 (m, 3H), 1.32 (s, 3H), 1.31 (s, 3H), 0.88 (s, 3H), 0.88 (s, 3H);  $^{13}\text{C}$  NMR (126 MHz,  $\text{CDCl}_3$ )  $\delta$  207.7, 201.9, 201.3, 172.0, 68.3, 54.3, 50.1, 45.2, 44.0, 43.4, 37.9, 36.1, 34.8, 30.7, 30.3, 23.2, 22.2, 17.9, 17.4; HRMS (ESI): Exact mass calc'd for  $\text{C}_{20}\text{H}_{30}\text{O}_5$   $[\text{M}+\text{Na}]^+$ , 373.1991. Found 373.1986.



**(1R,3R)-3-(2-(2-((1R,3R)-3-(Carboxymethyl)-2,2-dimethylcyclobutyl)-2-oxoethoxy)-2-oxoethyl)-2,2-dimethylcyclobutane-1-carboxylic acid (V-19).** Compound **V-17** (0.050 g, 0.142 mmol, 1 eq), a 0.7 M aqueous solution of  $\text{H}_2\text{PO}_4\cdot\text{H}_2\text{O}$ , and DMSO (1.4 mL) were added to a flame-dried flask. At room temperature, a 1 M aqueous solution of 80 wt%  $\text{NaClO}_2$  (0.023 g, 0.199 mmol, 1.4 eq) was added slowly via dropwise addition into the reaction flask, which was vented to release evolved gas during the addition. The reaction mixture was stirred at room temperature for 12 hours. Saturated  $\text{Na}_2\text{SO}_3$  was then added dropwise to the reaction mixture, followed by 1 M HCl until pH 2 was reached. The reaction mixture was then extracted using EtOAc, dried over  $\text{Na}_2\text{SO}_4$ , and concentrated. Subsequent purification by flash column

chromatography with silica gel (5% MeOH in CH<sub>2</sub>Cl<sub>2</sub>) afforded the title compound as an equal mixture of diastereomers (0.0261 g, 0.071 mmol, 49% yield) as a viscous clear oil: IR (Germanium ATR) 2958, 2916, 2848, 1698, 1412, 1158, 730 cm<sup>-1</sup>; Due to overlapping signals, NMR data is reported for a single diastereomer for simplicity: <sup>1</sup>H NMR (500 MHz, CD<sub>3</sub>OD) δ 4.75 – 4.54 (m, 2H), 3.00 (ddd, *J* = 10.2, 7.6, 1.4 Hz, 1H), 2.74 (dd, *J* = 10.3, 7.8 Hz, 1H), 2.53 – 2.44 (m, 1H), 2.43 – 2.35 (m, 3H), 2.34 – 2.26 (m, 1H), 2.24 – 2.16 (m, 1H), 2.13 – 2.05 (m, 1H), 2.03 – 1.96 (m, 1H), 1.96 – 1.81 (m, 2H), 1.32 (s, 3H), 1.23 (s, 3H), 1.01 (s, 3H), 0.89 (s, 3H); <sup>13</sup>C NMR (126 MHz, CD<sub>3</sub>OD) δ 204.3, 204.2, 176.9, 173.5, 69.4, 45.0, 43.4, 40.4, 39.8, 39.4, 36.6, 35.8, 30.6, 30.4, 25.7, 23.5, 17.9, 17.6; HRMS (ESI): Exact mass calc'd for C<sub>19</sub>H<sub>28</sub>O<sub>7</sub> [M+Na]<sup>+</sup>, 391.1732. Found 391.1734.



**2-((1R,3R)-3-(2-(2-((1R,3R)-3-Acetyl-2,2-dimethylcyclobutyl)acetoxy)acetyl)-2,2-**

**dimethylcyclobutyl)acetic acid (V-20).** Compound **V-18** (0.200 g, 0.571 mmol, 1 eq), a 0.7 M aqueous solution of H<sub>2</sub>PO<sub>4</sub>•H<sub>2</sub>O, and DMSO (5.7 mL) were added to a flame-dried flask. At room temperature, a 1 M aqueous solution of 80 wt% NaClO<sub>2</sub> (0.867 g, 0.799 mmol, 1.4 eq) was added slowly via dropwise addition into the reaction flask, which was vented to release evolved gas during the addition. The reaction mixture was stirred at room temperature for 12 hours. Saturated Na<sub>2</sub>SO<sub>3</sub> was then added dropwise to the reaction mixture, followed by 1 M HCl until pH 2 was reached. The reaction mixture was then extracted using EtOAc, dried over Na<sub>2</sub>SO<sub>4</sub>, and concentrated. Subsequent purification by flash column chromatography with silica gel (5%

MeOH in CH<sub>2</sub>Cl<sub>2</sub>) afforded the title compound as an equal mixture of diastereomers (0.137 g, 0.373 mmol, 65% yield) as a viscous clear oil: IR (Germanium ATR): 2952, 2874, 1722, 1453, 1703, 1146, 936 cm<sup>-1</sup>; Due to overlapping signals, NMR data is reported for a single diastereomer for simplicity: <sup>1</sup>H NMR (500 MHz, CDCl<sub>3</sub>) δ 4.67 – 4.42 (m, 2H), 3.07 – 2.78 (m, 2H), 2.48 – 2.25 (m, 5H), 2.15 – 2.06 (m, 1H), 2.05 (s, 3H), 2.04 – 1.92 (m, 3H), 1.64 – 1.42 (m, 1H), 1.33 (s, 3H), 1.32 (s, 3H), 0.91 (s, 3H), 0.89 (s, 3H); <sup>13</sup>C NMR (126 MHz, CDCl<sub>3</sub>) δ 207.8, 201.9, 172.1, 68.3, 54.4, 50.0, 44.0, 43.9, 43.5, 38.0, 38.0, 34.8, 30.5, 30.3, 30.3, 23.2, 22.4, 17.5; HRMS (ESI): Exact mass calc'd for C<sub>20</sub>H<sub>30</sub>O<sub>6</sub> [M+Na]<sup>+</sup>, 389.1940. Found 389.1936.

**Chapter 1 references.**

1. IPCC, 2013: Summary for Policymakers. In: *Climate Change 2013: The Physical Science Basis. Contribution of Working Group I to the Fifth Assessment Report of the Intergovernmental Panel on Climate Change* Cambridge University Press: Cambridge, UK, 2013.
2. National Research Council, 2005: *Radiative Forcing of Climate Change: Expanding the Concept and Addressing Uncertainties*. The National Academies Press: Washington, DC, 2005.
3. Myhre, G., D. Shindell, F.-M. Bréon, W. Collins, J. Fuglestvedt, J. Huang, D. Koch, J.-F. Lamarque, D. Lee, B. Mendoza, T. Nakajima, A. Robock, G. Stephens, T. Takemura and H. Zhang, 2013: Anthropogenic and Natural Radiative Forcing. In: *Climate Change 2013: The Physical Science Basis. Contribution of Working Group I to the Fifth Assessment Report of the Intergovernmental Panel on Climate Change* [Stocker, T.F., D. Qin, G.-K. Plattner, M. Tignor, S.K. Allen, J. Boschung, A. Nauels, Y. Xia, V. Bex and P.M. Midgley (eds.)]. Cambridge University Press, Cambridge, United Kingdom and New York, NY, USA.
4. John H. Seinfeld, S. N. P., *Atmospheric Chemistry and Physics: From Air Pollution to Climate Change*. 3rd ed.; John Wiley & Sons: Hoboken, NJ, 2016.
5. Rockström, J.; Steffen, W.; Noone, K.; Persson, Å.; Chapin, F. S.; Lambin, E. F.; Lenton, T. M.; Scheffer, M.; Folke, C.; Schellnhuber, H. J.; Nykvist, B.; de Wit, C. A.; Hughes, T.; van der Leeuw, S.; Rodhe, H.; Sörlin, S.; Snyder, P. K.; Costanza, R.; Svedin, U.; Falkenmark, M.; Karlberg, L.; Corell, R. W.; Fabry, V. J.; Hansen, J.; Walker, B.; Liverman, D.; Richardson, K.; Crutzen, P.; Foley, J. A., A safe operating space for humanity. *Nature* **2009**, *461* (7263), 472-475.
6. Kroll, J. H.; Seinfeld, J. H., Chemistry of secondary organic aerosol: Formation and evolution of low-volatility organics in the atmosphere. *Atmos. Environ.* **2008**, *42* (16), 3593-3624.
7. Poschl, U., Atmospheric aerosols: composition, transformation, climate and health effects. *Angew. Chem. Int. Ed. Engl.* **2005**, *44* (46), 7520-40.
8. Baltensperger, U.; Prévôt, A. S. H., Chemical analysis of atmospheric aerosols. *Anal. Bioanal. Chem.* **2008**, *390* (1), 277-280.
9. Zahardis, J.; Geddes, S.; Petrucci, G. A., Improved Understanding of Atmospheric Organic Aerosols via Innovations in Soft Ionization Aerosol Mass Spectrometry. *Anal. Chem.* **2011**, *83* (7), 2409-2415.
10. Prather, K. A.; Hatch, C. D.; Grassian, V. H., Analysis of atmospheric aerosols. *Annu Rev Anal Chem (Palo Alto Calif)* **2008**, *1*, 485-514.

11. Levy, H.; Horowitz, L. W.; Schwarzkopf, M. D.; Ming, Y.; Golaz, J.-C.; Naik, V.; Ramaswamy, V., The roles of aerosol direct and indirect effects in past and future climate change. *J. Geophys. Res. Atmos.* **2013**, *118* (10), 4521-4532.
12. Hallquist, M.; Wenger, J. C.; Baltensperger, U.; Rudich, Y.; Simpson, D.; Claeys, M.; Dommen, J.; Donahue, N. M.; George, C.; Goldstein, A. H.; Hamilton, J. F.; Herrmann, H.; Hoffmann, T.; Iinuma, Y.; Jang, M.; Jenkin, M. E.; Jimenez, J. L.; Kiendler-Scharr, A.; Maenhaut, W.; McFiggans, G.; Mentel, T. F.; Monod, A.; Prévôt, A. S. H.; Seinfeld, J. H.; Surratt, J. D.; Szmigielski, R.; Wildt, J., The formation, properties and impact of secondary organic aerosol: current and emerging issues. *Atmos. Chem. Phys.* **2009**, *9* (14), 5155-5236.
13. Lohmann, U.; Feichter, J., Global indirect aerosol effects: a review. *Atmos. Chem. Phys.* **2005**, *5* (3), 715-737.
14. Ebben, C. J.; Strick, B. F.; Upshur, M. A.; Chase, H. M.; Achtyl, J. L.; Thomson, R. J.; Geiger, F. M., Towards the identification of molecular constituents associated with the surfaces of isoprene-derived secondary organic aerosol (SOA) particles. *Atmos. Chem. Phys.* **2014**, *14* (5), 2303-2314.
15. Nozière, B.; Kalberer, M.; Claeys, M.; Allan, J.; D'Anna, B.; Decesari, S.; Finessi, E.; Glasius, M.; Grgić, I.; Hamilton, J. F.; Hoffmann, T.; Iinuma, Y.; Jaoui, M.; Kahnt, A.; Kampf, C. J.; Kourchev, I.; Maenhaut, W.; Marsden, N.; Saarikoski, S.; Schnelle-Kreis, J.; Surratt, J. D.; Szidat, S.; Szmigielski, R.; Wisthaler, A., The Molecular Identification of Organic Compounds in the Atmosphere: State of the Art and Challenges. *Chem. Rev.* **2015**, *115* (10), 3919-3983.
16. Kanakidou, M.; Seinfeld, J. H.; Pandis, S. N.; Barnes, I.; Dentener, F. J.; Facchini, M. C.; Van Dingenen, R.; Ervens, B.; Nenes, A.; Nielsen, C. J.; Swietlicki, E.; Putaud, J. P.; Balkanski, Y.; Fuzzi, S.; Horth, J.; Moortgat, G. K.; Winterhalter, R.; Myhre, C. E. L.; Tsigaridis, K.; Vignati, E.; Stephanou, E. G.; Wilson, J., Organic aerosol and global climate modelling: a review. *Atmos. Chem. Phys.* **2005**, *5* (4), 1053-1123.
17. Williams, J.; Crowley, J.; Fischer, H.; Harder, H.; Martinez, M.; Petäjä, T.; Rinne, J.; Bäck, J.; Boy, M.; Dal Maso, M.; Hakala, J.; Kajos, M.; Keronen, P.; Rantala, P.; Aalto, J.; Aaltonen, H.; Paatero, J.; Vesala, T.; Hakola, H.; Levula, J.; Pohja, T.; Herrmann, F.; Auld, J.; Mesarchaki, E.; Song, W.; Yassaa, N.; Nölscher, A.; Johnson, A. M.; Custer, T.; Sinha, V.; Thieser, J.; Pouvesle, N.; Taraborrelli, D.; Tang, M. J.; Bozem, H.; Hosaynali-Beygi, Z.; Axinte, R.; Oswald, R.; Novelli, A.; Kubistin, D.; Hens, K.; Javed, U.; Trawny, K.; Breitenberger, C.; Hidalgo, P. J.; Ebben, C. J.; Geiger, F. M.; Corrigan, A. L.; Russell, L. M.; Ouwersloot, H. G.; Vilà-Guerau de Arellano, J.; Ganzeveld, L.; Vogel, A.; Beck, M.; Bayerle, A.; Kampf, C. J.; Bertelmann, M.; Köllner, F.; Hoffmann, T.; Valverde, J.; González, D.; Riekkola, M. L.; Kulmala, M.; Lelieveld, J., The summertime Boreal forest field measurement intensive (HUMPPA-COPEC-2010): an overview of meteorological and chemical influences. *Atmos. Chem. Phys.* **2011**, *11* (20), 10599-10618.

18. Ebben, C. J.; Shrestha, M.; Martinez, I. S.; Corrigan, A. L.; Frossard, A. A.; Song, W. W.; Worton, D. R.; Petäjä, T.; Williams, J.; Russell, L. M.; Kulmala, M.; Goldstein, A. H.; Artaxo, P.; Martin, S. T.; Thomson, R. J.; Geiger, F. M., Organic Constituents on the Surfaces of Aerosol Particles from Southern Finland, Amazonia, and California Studied by Vibrational Sum Frequency Generation. *J. Phys. Chem. A* **2012**, *116* (32), 8271-8290.
19. Ng, N. L.; Canagaratna, M. R.; Zhang, Q.; Jimenez, J. L.; Tian, J.; Ulbrich, I. M.; Kroll, J. H.; Docherty, K. S.; Chhabra, P. S.; Bahreini, R.; Murphy, S. M.; Seinfeld, J. H.; Hildebrandt, L.; Donahue, N. M.; DeCarlo, P. F.; Lanz, V. A.; Prévôt, A. S. H.; Dinar, E.; Rudich, Y.; Worsnop, D. R., Organic aerosol components observed in Northern Hemispheric datasets from Aerosol Mass Spectrometry. *Atmos. Chem. Phys.* **2010**, *10* (10), 4625-4641.
20. Baltensperger, U.; Kalberer, M.; Dommen, J.; Paulsen, D.; Alfarra, M. R.; Coe, H.; Fisseha, R.; Gascho, A.; Gysel, M.; Nyeki, S.; Sax, M.; Steinbacher, M.; Prevot, A. S. H.; Sjogren, S.; Weingartner, E.; Zenobi, R., Secondary organic aerosols from anthropogenic and biogenic precursors. *Faraday Discuss.* **2005**, *130* (0), 265-278.
21. Zhang, X.; McVay, R. C.; Huang, D. D.; Dalleska, N. F.; Aumont, B.; Flagan, R. C.; Seinfeld, J. H., Formation and evolution of molecular products in  $\alpha$ -pinene secondary organic aerosol. *Proc. Natl. Acad. Sci.* **2015**, *112* (46), 14168-14173.
22. Virtanen, A.; Joutsensaari, J.; Koop, T.; Kannosto, J.; Yli-Pirila, P.; Leskinen, J.; Makela, J. M.; Holopainen, J. K.; Poschl, U.; Kulmala, M.; Worsnop, D. R.; Laaksonen, A., An amorphous solid state of biogenic secondary organic aerosol particles. *Nature* **2010**, *467* (7317), 824-827.
23. Good, N.; Topping, D. O.; Duplissy, J.; Gysel, M.; Meyer, N. K.; Metzger, A.; Turner, S. F.; Baltensperger, U.; Ristovski, Z.; Weingartner, E.; Coe, H.; McFiggans, G., Widening the gap between measurement and modelling of secondary organic aerosol properties? *Atmos. Chem. Phys.* **2010**, *10* (6), 2577-2593.
24. Wyche, K. P.; Monks, P. S.; Smallbone, K. L.; Hamilton, J. F.; Alfarra, M. R.; Rickard, A. R.; McFiggans, G. B.; Jenkin, M. E.; Bloss, W. J.; Ryan, A. C.; Hewitt, C. N.; MacKenzie, A. R., Mapping gas-phase organic reactivity and concomitant secondary organic aerosol formation: chemometric dimension reduction techniques for the deconvolution of complex atmospheric data sets. *Atmos. Chem. Phys.* **2015**, *15* (14), 8077-8100.
25. Shrestha, M.; Zhang, Y.; Ebben, C. J.; Martin, S. T.; Geiger, F. M., Vibrational sum frequency generation spectroscopy of secondary organic material produced by condensational growth from alpha-pinene ozonolysis. *J. Phys. Chem. A* **2013**, *117* (35), 8427-8436.
26. Iinuma, Y.; Boge, O.; Miao, Y.; Sierau, B.; Gnauk, T.; Herrmann, H., Laboratory studies on secondary organic aerosol formation from terpenes. *Faraday Discuss.* **2005**, *130* (0), 279-294.

27. Griffin, R. J.; Cocker, D. R.; Flagan, R. C.; Seinfeld, J. H., Organic aerosol formation from the oxidation of biogenic hydrocarbons. *J. Geophys. Res. Atmos.* **1999**, *104* (D3), 3555-3567.
28. Carlton, A. G.; Wiedinmyer, C.; Kroll, J. H., A review of Secondary Organic Aerosol (SOA) formation from isoprene. *Atmos. Chem. Phys.* **2009**, *9* (14), 4987-5005.
29. Atkinson, R.; Arey, J., Atmospheric Chemistry of Biogenic Organic Compounds. *Acc. Chem. Res.* **1998**, *31* (9), 574-583.
30. Goldstein, A. H.; Galbally, I. E., Known and Unexplored Organic Constituents in the Earth's Atmosphere. *Environ. Sci. Technol.* **2007**, *41* (5), 1514-1521.
31. Jimenez, J. L.; Canagaratna, M. R.; Donahue, N. M.; Prevot, A. S. H.; Zhang, Q.; Kroll, J. H.; DeCarlo, P. F.; Allan, J. D.; Coe, H.; Ng, N. L.; Aiken, A. C.; Docherty, K. S.; Ulbrich, I. M.; Grieshop, A. P.; Robinson, A. L.; Duplissy, J.; Smith, J. D.; Wilson, K. R.; Lanz, V. A.; Hueglin, C.; Sun, Y. L.; Tian, J.; Laaksonen, A.; Raatikainen, T.; Rautiainen, J.; Vaattovaara, P.; Ehn, M.; Kulmala, M.; Tomlinson, J. M.; Collins, D. R.; Cubison, M. J.; Dunlea, J.; Huffman, J. A.; Onasch, T. B.; Alfarra, M. R.; Williams, P. I.; Bower, K.; Kondo, Y.; Schneider, J.; Drewnick, F.; Borrmann, S.; Weimer, S.; Demerjian, K.; Salcedo, D.; Cottrell, L.; Griffin, R.; Takami, A.; Miyoshi, T.; Hatakeyama, S.; Shimono, A.; Sun, J. Y.; Zhang, Y. M.; Dzepina, K.; Kimmel, J. R.; Sueper, D.; Jayne, J. T.; Herndon, S. C.; Trimborn, A. M.; Williams, L. R.; Wood, E. C.; Middlebrook, A. M.; Kolb, C. E.; Baltensperger, U.; Worsnop, D. R., Evolution of Organic Aerosols in the Atmosphere. *Science* **2009**, *326* (5959), 1525-1529.
32. Abramson, E.; Imre, D.; Beranek, J.; Wilson, J.; Zelenyuk, A., Experimental determination of chemical diffusion within secondary organic aerosol particles. *Phys. Chem. Chem. Phys.* **2013**, *15* (8), 2983-2991.
33. Liu, P.; Song, M.; Zhao, T.; Gunthe, S. S.; Ham, S.; He, Y.; Qin, Y. M.; Gong, Z.; Amorim, J. C.; Bertram, A. K.; Martin, S. T., Resolving the mechanisms of hygroscopic growth and cloud condensation nuclei activity for organic particulate matter. *Nature Commun.* **2018**, *9* (1), 4076.
34. Upshur, M. A.; Vega, M. M.; Bé, A. G.; Chase, H. M.; Zhang, Y.; Tuladhar, A.; Chase, Z. A.; Fu, L.; Ebben, C. J.; Wang, Z.; Martin, S. T.; Geiger, F. M.; Thomson, R. J., Synthesis and surface spectroscopy of  $\alpha$ -pinene isotopologues and their corresponding secondary organic material. *Chem. Sci.* **2019**, *10* (36), 8390-8398.
35. Shrestha, M.; Zhang, Y.; Upshur, M. A.; Liu, P.; Blair, S. L.; Wang, H.-f.; Nizkorodov, S. A.; Thomson, R. J.; Martin, S. T.; Geiger, F. M., On Surface Order and Disorder of  $\alpha$ -Pinene-Derived Secondary Organic Material. *J. Phys. Chem. A* **2015**, *119* (19), 4609-4617.

36. Kristensen, K.; Cui, T.; Zhang, H.; Gold, A.; Glasius, M.; Surratt, J. D., Dimers in  $\alpha$ -pinene secondary organic aerosol: effect of hydroxyl radical, ozone, relative humidity and aerosol acidity. *Atmos. Chem. Phys.* **2014**, *14* (8), 4201-4218.
37. Ebben, C. J.; Martinez, I. S.; Shrestha, M.; Buchbinder, A. M.; Corrigan, A. L.; Guenther, A.; Karl, T.; Petäjä, T.; Song, W. W.; Zorn, S. R.; Artaxo, P.; Kulmala, M.; Martin, S. T.; Russell, L. M.; Williams, J.; Geiger, F. M., Contrasting organic aerosol particles from boreal and tropical forests during HUMPPA-COPEC-2010 and AMAZE-08 using coherent vibrational spectroscopy. *Atmos. Chem. Phys.* **2011**, *11* (20), 10317-10329.
38. Gao, Y.; Hall, W. A.; Johnston, M. V., Molecular Composition of Monoterpene Secondary Organic Aerosol at Low Mass Loading. *Environ. Sci. Technol.* **2010**, *44* (20), 7897-7902.
39. Andersson-Sköld, Y.; Simpson, D., Secondary organic aerosol formation in northern Europe: A model study. *J. Geophys. Res. Atmos.* **2001**, *106* (D7), 7357-7374.
40. Holopainen, J. K.; Kivimäenpää, M.; Nizkorodov, S. A., Plant-derived Secondary Organic Material in the Air and Ecosystems. *Trends Plant Sci.* **2017**, *22* (9), 744-753.
41. Bonn, B.; Moortgat, G. K., Sesquiterpene ozonolysis: Origin of atmospheric new particle formation from biogenic hydrocarbons. *Geophys. Res. Lett.* **2003**, *30* (11), 1585.
42. Goldstein, A. H.; McKay, M.; Kurpius, M. R.; Schade, G. W.; Lee, A.; Holzinger, R.; Rasmussen, R. A., Forest thinning experiment confirms ozone deposition to forest canopy is dominated by reaction with biogenic VOCs. *Geophys. Res. Lett.* **2004**, *31* (22), n/a-n/a.
43. Pathak, R. K.; Presto, A. A.; Lane, T. E.; Stanier, C. O.; Donahue, N. M.; Pandis, S. N., Ozonolysis of  $\alpha$ -pinene: parameterization of secondary organic aerosol mass fraction. *Atmos. Chem. Phys.* **2007**, *7* (14), 3811-3821.
44. Guenther, A.; Hewitt, C. N.; Erickson, D.; Fall, R.; Geron, C.; Graedel, T.; Harley, P.; Klinger, L.; Lerdau, M.; McKay, W. A.; Pierce, T.; Scholes, B.; Steinbrecher, R.; Tallamraju, R.; Taylor, J.; Zimmerman, P., A global model of natural volatile organic compound emissions. *J. Geophys. Res. Atmos.* **1995**, *100* (D5), 8873-8892.
45. Guenther, A. B.; Jiang, X.; Heald, C. L.; Sakulyanontvittaya, T.; Duhl, T.; Emmons, L. K.; Wang, X., The Model of Emissions of Gases and Aerosols from Nature version 2.1 (MEGAN2.1): an extended and updated framework for modeling biogenic emissions. *Geosci. Model Dev.* **2012**, *5* (6), 1471-1492.
46. Watry, M. B., M. G.; Richmond, G. L. Applied Spectroscopy, 55 (321A-340A) 2001., Probing Molecular Structure at Liquid Surfaces with Vibrational Sum Frequency Spectroscopy. *Appl. Spectrosc.* **2001**, *55*, 321A-340A.

47. Hakola, H.; Tarvainen, V.; Laurila, T.; Hiltunen, V.; Hellén, H.; Keronen, P., Seasonal variation of VOC concentrations above a boreal coniferous forest. *Atmos. Environ.* **2003**, *37* (12), 1623-1634.
48. Bouvier-Brown, N. C.; Goldstein, A. H.; Gilman, J. B.; Kuster, W. C.; de Gouw, J. A., In-situ ambient quantification of monoterpenes, sesquiterpenes, and related oxygenated compounds during BEARPEX 2007: implications for gas- and particle-phase chemistry. *Atmos. Chem. Phys.* **2009**, *9* (15), 5505-5518.
49. Chan, M. N.; Surratt, J. D.; Chan, A. W. H.; Schilling, K.; Offenberg, J. H.; Lewandowski, M.; Edney, E. O.; Kleindienst, T. E.; Jaoui, M.; Edgerton, E. S.; Tanner, R. L.; Shaw, S. L.; Zheng, M.; Knipping, E. M.; Seinfeld, J. H., Influence of aerosol acidity on the chemical composition of secondary organic aerosol from beta-caryophyllene. *Atmos. Chem. Phys.* **2011**, *11* (4), 1735-1751.
50. Helmig, D.; Ortega, J.; Duhl, T.; Tanner, D.; Guenther, A.; Harley, P.; Wiedinmyer, C.; Milford, J.; Sakulyanontvittaya, T., Sesquiterpene Emissions from Pine Trees – Identifications, Emission Rates and Flux Estimates for the Contiguous United States. *Environ. Sci. Technol.* **2007**, *41* (5), 1545-1553.
51. Jaoui, M.; Leungsakul, S.; Kamens, R. M., Gas and Particle Products Distribution from the Reaction of  $\beta$ -Caryophyllene with Ozone. *J. Atmos. Chem.* **2003**, *45* (3), 261-287.
52. Kleindienst, T. E.; Jaoui, M.; Lewandowski, M.; Offenberg, J. H.; Lewis, C. W.; Bhave, P. V.; Edney, E. O., Estimates of the contributions of biogenic and anthropogenic hydrocarbons to secondary organic aerosol at a southeastern US location. *Atmos. Environ.* **2007**, *41* (37), 8288-8300.
53. Lee, A.; Goldstein, A. H.; Kroll, J. H.; Ng, N. L.; Varutbangkul, V.; Flagan, R. C.; Seinfeld, J. H., Gas-phase products and secondary aerosol yields from the photooxidation of 16 different terpenes. *J. Geophys. Res. Atmos.* **2006**, *111* (D17).
54. Lewandowski, M.; Jaoui, M.; Offenberg, J. H.; Kleindienst, T. E.; Edney, E. O.; Sheesley, R. J.; Schauer, J. J., Primary and Secondary Contributions to Ambient PM in the Midwestern United States. *Environ. Sci. Technol.* **2008**, *42* (9), 3303-3309.
55. Li, Y. J.; Chen, Q.; Guzman, M. I.; Chan, C. K.; Martin, S. T., Second-generation products contribute substantially to the particle-phase organic material produced by  $\beta$ -caryophyllene ozonolysis. *Atmos. Chem. Phys.* **2011**, *11* (1), 121-132.
56. Parshintsev, J.; Nurmi, J.; Kilpeläinen, I.; Hartonen, K.; Kulmala, M.; Riekkola, M.-L., Preparation of  $\beta$ -caryophyllene oxidation products and their determination in ambient aerosol samples. *Anal. Bioanal. Chem.* **2008**, *390* (3), 913-919.
57. Sakulyanontvittaya, T.; Duhl, T.; Wiedinmyer, C.; Helmig, D.; Matsunaga, S.; Potosnak, M.; Milford, J.; Guenther, A., Monoterpene and Sesquiterpene Emission Estimates for the United States. *Environ. Sci. Technol.* **2008**, *42* (5), 1623-1629.

58. Henrot, A. J.; Stanelle, T.; Schröder, S.; Siegenthaler, C.; Taraborrelli, D.; Schultz, M. G., Implementation of the MEGAN (v2.1) biogenic emission model in the ECHAM6-HAMMOZ chemistry climate model. *Geosci. Model Dev.* **2017**, *10* (2), 903-926.
59. Duhl, T. R.; Helmig, D.; Guenther, A., Sesquiterpene emissions from vegetation: a review. *Biogeosciences* **2008**, *5* (3), 761-777.
60. Henze, D. K.; Seinfeld, J. H.; Ng, N. L.; Kroll, J. H.; Fu, T. M.; Jacob, D. J.; Heald, C. L., Global modeling of secondary organic aerosol formation from aromatic hydrocarbons: high- vs. low-yield pathways. *Atmos. Chem. Phys.* **2008**, *8* (9), 2405-2420.
61. Griffin, R. J.; Cocker, D. R.; Seinfeld, J. H.; Dabdub, D., Estimate of global atmospheric organic aerosol from oxidation of biogenic hydrocarbons. *Geophys. Res. Lett.* **1999**, *26* (17), 2721-2724.
62. Nguyen, T. L.; Winterhalter, R.; Moortgat, G.; Kanawati, B.; Peeters, J.; Vereecken, L., The gas-phase ozonolysis of [small beta]-caryophyllene (C<sub>15</sub>H<sub>24</sub>). Part II: A theoretical study. *Phys. Chem. Chem. Phys.* **2009**, *11* (21), 4173-4183.
63. Shu, Y.; Atkinson, R., Atmospheric lifetimes and fates of a series of sesquiterpenes. *J. Geophys. Res. Atmos.* **1995**, *100* (D4), 7275-7281.
64. Frosch, M.; Bilde, M.; Nenes, A.; Praplan, A. P.; Jurányi, Z.; Dommen, J.; Gysel, M.; Weingartner, E.; Baltensperger, U., CCN activity and volatility of  $\beta$ -caryophyllene secondary organic aerosol. *Atmos. Chem. Phys.* **2013**, *13* (4), 2283-2297.
65. Camredon, M.; Hamilton, J. F.; Alam, M. S.; Wyche, K. P.; Carr, T.; White, I. R.; Monks, P. S.; Rickard, A. R.; Bloss, W. J., Distribution of gaseous and particulate organic composition during dark  $\alpha$ -pinene ozonolysis. *Atmos. Chem. Phys.* **2010**, *10* (6), 2893-2917.
66. Heaton, K. J.; Dreyfus, M. A.; Wang, S.; Johnston, M. V., Oligomers in the Early Stage of Biogenic Secondary Organic Aerosol Formation and Growth. *Environ. Sci. Technol.* **2007**, *41* (17), 6129-6136.
67. Müller, L.; Reinnig, M. C.; Warnke, J.; Hoffmann, T., Unambiguous identification of esters as oligomers in secondary organic aerosol formed from cyclohexene and cyclohexene/ $\alpha$ -pinene ozonolysis. *Atmos. Chem. Phys.* **2008**, *8* (5), 1423-1433.
68. Sato, K.; Fujitani, Y.; Inomata, S.; Morino, Y.; Tanabe, K.; Ramasamy, S.; Hikida, T.; Shimono, A.; Takami, A.; Fushimi, A.; Kondo, Y.; Imamura, T.; Tanimoto, H.; Sugata, S., Studying volatility from composition, dilution, and heating measurements of secondary organic aerosols formed during  $\alpha$ -pinene ozonolysis. *Atmos. Chem. Phys.* **2018**, *18* (8), 5455-5466.

69. Laskin, A.; Laskin, J.; Nizkorodov, S. A., Mass spectrometric approaches for chemical characterisation of atmospheric aerosols: critical review of the most recent advances. *Environ. Chem.* **2012**, *9* (3), 163-189.
70. Cui, T.; Zeng, Z.; dos Santos, E. O.; Zhang, Z.; Chen, Y.; Zhang, Y.; Rose, C. A.; Budisulistiorini, S. H.; Collins, L. B.; Bodnar, W. M.; de Souza, R. A. F.; Martin, S. T.; Machado, C. M. D.; Turpin, B. J.; Gold, A.; Ault, A. P.; Surratt, J. D., Development of a hydrophilic interaction liquid chromatography (HILIC) method for the chemical characterization of water-soluble isoprene epoxydiol (IEPOX)-derived secondary organic aerosol. *Environ. Sci.: Process. Impacts* **2018**, *20* (11), 1524-1536.
71. Yee, L. D.; Isaacman-VanWertz, G.; Wernis, R. A.; Meng, M.; Rivera, V.; Kreisberg, N. M.; Hering, S. V.; Bering, M. S.; Glasius, M.; Upshur, M. A.; Bé, A. G.; Thomson, R. J.; Geiger, F. M.; Offenberg, J. H.; Lewandowski, M.; Kourttchev, I.; Kalberer, M.; de Sá, S.; Martin, S. T.; Alexander, M. L.; Palm, B. B.; Hu, W.; Campuzano-Jost, P.; Day, D. A.; Jimenez, J. L.; Liu, Y.; McKinney, K. A.; Artaxo, P.; Viegas, J.; Manzi, A.; Oliveira, M. B.; de Souza, R.; Machado, L. A. T.; Longo, K.; Goldstein, A. H., Observations of sesquiterpenes and their oxidation products in central Amazonia during the wet and dry seasons. *Atmos. Chem. Phys.* **2018**, *18*, 10433-10457.
72. Ault, A. P.; Axson, J. L., Atmospheric Aerosol Chemistry: Spectroscopic and Microscopic Advances. *Anal. Chem.* **2017**, *89* (1), 430-452.
73. Müller, L.; Reinnig, M. C.; Hayen, H.; Hoffmann, T., Characterization of oligomeric compounds in secondary organic aerosol using liquid chromatography coupled to electrospray ionization Fourier transform ion cyclotron resonance mass spectrometry. *Rapid Commun. Mass Spectrom.* **2009**, *23* (7), 971-979.
74. van Eijck, A.; Opatz, T.; Taraborrelli, D.; Sander, R.; Hoffmann, T., New tracer compounds for secondary organic aerosol formation from  $\beta$ -caryophyllene oxidation. *Atmos. Environ.* **2013**, *80*, 122-130.
75. Yasmeeen, F.; Vermeylen, R.; Szmigielski, R.; Iinuma, Y.; Böge, O.; Herrmann, H.; Maenhaut, W.; Claeys, M., Terpenylic acid and related compounds: precursors for dimers in secondary organic aerosol from the ozonolysis of alpha- and beta-pinene. *Atmos. Chem. Phys.* **2010**, *10* (19), 9383-9392.
76. Somorjai, G. A.; Li, Y., Impact of surface chemistry. *Proc. Natl. Acad. Sci.* **2011**, *108* (3), 917-924.
77. Adamson, A. W.; Gast, A. P., *Physical Chemistry of Surfaces*. 6th ed.; Wiley: New York, 1997.
78. Upshur, M. A.; Strick, B. F.; McNeill, V. F.; Thomson, R. J.; Geiger, F. M., Climate-relevant physical properties of molecular constituents for isoprene-derived secondary organic aerosol material. *Atmos. Chem. Phys.* **2014**, *14* (19), 10731-10740.

79. Sharma, N.; China, S.; Bhandari, J.; Gorkowski, K.; Dubey, M.; Zaveri, R. A.; Mazzoleni, C., Physical Properties of Aerosol Internally Mixed With Soot Particles in a Biogenically Dominated Environment in California. *Geophys. Res. Lett.* **2018**, *0* (0).
80. Stokes, G. Y.; Buchbinder, A. M.; Gibbs-Davis, J. M.; Scheidt, K. A.; Geiger, F. M., Heterogeneous Ozone Oxidation Reactions of 1-Pentene, Cyclopentene, Cyclohexene, and a Menthenol Derivative Studied by Sum Frequency Generation. *J. Phys. Chem. A* **2008**, *112* (46), 11688-11698.
81. Stokes, G. Y.; Buchbinder, A. M.; Gibbs-Davis, J. M.; Scheidt, K. A.; Geiger, F. M., Chemically diverse environmental interfaces and their reactions with ozone studied by sum frequency generation. *Vib. Spectrosc* **2009**, *50* (1), 86-98.
82. Nozière, B.; Baduel, C.; Jaffrezo, J.-L., The dynamic surface tension of atmospheric aerosol surfactants reveals new aspects of cloud activation. *Nature Commun.* **2014**, *5*, 3335.
83. Ruehl, C. R.; Davies, J. F.; Wilson, K. R., An interfacial mechanism for cloud droplet formation on organic aerosols. *Science* **2016**, *351* (6280), 1447-1450.
84. McNeill, V. F.; Sareen, N.; Schwier, A. N., Surface-Active Organics in Atmospheric Aerosols. In *Atmospheric and Aerosol Chemistry*, McNeill, F. V.; Ariya, A. P., Eds. Springer Berlin Heidelberg: Berlin, Heidelberg, 2014; pp 201-259.
85. Sareen, N.; Schwier, A. N.; Lathem, T. L.; Nenes, A.; McNeill, V. F., Surfactants from the gas phase may promote cloud droplet formation. *Proc. Natl. Acad. Sci.* **2013**, *110* (8), 2723-2728.
86. Gill, P. S.; Graedel, T. E.; Weschler, C. J., Organic films on atmospheric aerosol particles, fog droplets, cloud droplets, raindrops, and snowflakes. *Reviews of Geophysics* **1983**, *21* (4), 903-920.
87. Zhang, Q.; Jimenez, J. L.; Canagaratna, M. R.; Allan, J. D.; Coe, H.; Ulbrich, I.; Alfarra, M. R.; Takami, A.; Middlebrook, A. M.; Sun, Y. L.; Dzepina, K.; Dunlea, E.; Docherty, K.; DeCarlo, P. F.; Salcedo, D.; Onasch, T.; Jayne, J. T.; Miyoshi, T.; Shimojo, A.; Hatakeyama, S.; Takegawa, N.; Kondo, Y.; Schneider, J.; Drewnick, F.; Borrmann, S.; Weimer, S.; Demerjian, K.; Williams, P.; Bower, K.; Bahreini, R.; Cottrell, L.; Griffin, R. J.; Rautiainen, J.; Sun, J. Y.; Zhang, Y. M.; Worsnop, D. R., Ubiquity and dominance of oxygenated species in organic aerosols in anthropogenically-influenced Northern Hemisphere midlatitudes. *Geophys. Res. Lett.* **2007**, *34* (13), n/a-n/a.
88. Kourtev, I.; Ruuskanen, T. M.; Keronen, P.; Sogacheva, L.; Dal Maso, M.; Reissell, A.; Chi, X.; Vermeylen, R.; Kulmala, M.; Maenhaut, W.; Claeys, M., Determination of isoprene and  $\alpha$ - $\beta$ -pinene oxidation products in boreal forest aerosols from Hyytiälä, Finland: diel variations and possible link with particle formation events. *Plant Biology* **2008**, *10* (1), 138-149.

89. Vestenius, M.; Hellén, H.; Levula, J.; Kuronen, P.; Helminen, K. J.; Nieminen, T.; Kulmala, M.; Hakola, H., Acidic reaction products of monoterpenes and sesquiterpenes in atmospheric fine particles in a boreal forest. *Atmos. Chem. Phys.* **2014**, *14* (15), 7883-7893.
90. Gómez-González, Y.; Surratt, J. D.; Cuyckens, F.; Szmigielski, R.; Vermeylen, R.; Jaoui, M.; Lewandowski, M.; Offenberg, J. H.; Kleindienst, T. E.; Edney, E. O.; Blockhuys, F.; Van Alsenoy, C.; Maenhaut, W.; Claeys, M., Characterization of organosulfates from the photooxidation of isoprene and unsaturated fatty acids in ambient aerosol using liquid chromatography/(-) electrospray ionization mass spectrometry. *J. Mass Spectrom.* **2008**, *43* (3), 371-382.
91. Gao, S.; Surratt, J. D.; Knipping, E. M.; Edgerton, E. S.; Shahgholi, M.; Seinfeld, J. H., Characterization of polar organic components in fine aerosols in the southeastern United States: Identity, origin, and evolution. *J. Geophys. Res. Atmos.* **2006**, *111* (D14), n/a-n/a.
92. Baduel, C.; Nozière, B.; Jaffrezo, J.-L., Summer/winter variability of the surfactants in aerosols from Grenoble, France. *Atmos. Environ.* **2012**, *47*, 413-420.
93. Wu, Y.; Li, W.; Xu, B.; Li, X.; Wang, H.; McNeill, V. F.; Rao, Y.; Dai, H.-L., Observation of Organic Molecules at the Aerosol Surface. *J. Phys. Chem. Lett.* **2016**, *7* (12), 2294-2297.
94. Woo, J. L.; Kim, D. D.; Schwier, A. N.; Li, R.; McNeill, V. F., Aqueous aerosol SOA formation: impact on aerosol physical properties. *Faraday Discuss.* **2013**, *165* (0), 357-367.
95. Ehn, M.; Thornton, J. A.; Kleist, E.; Sipila, M.; Junninen, H.; Pullinen, I.; Springer, M.; Rubach, F.; Tillmann, R.; Lee, B.; Lopez-Hilfiker, F.; Andres, S.; Acir, I.-H.; Rissanen, M.; Jokinen, T.; Schobesberger, S.; Kangasluoma, J.; Kontkanen, J.; Nieminen, T.; Kurten, T.; Nielsen, L. B.; Jorgensen, S.; Kjaergaard, H. G.; Canagaratna, M.; Maso, M. D.; Berndt, T.; Petaja, T.; Wahner, A.; Kerminen, V.-M.; Kulmala, M.; Worsnop, D. R.; Wildt, J.; Mentel, T. F., A large source of low-volatility secondary organic aerosol. *Nature* **2014**, *506* (7489), 476-479.
96. Bracco, G.; Holst, B., *Surface Science Techniques*. Springer Berlin Heidelberg: 2013.
97. Oura, K.; Lifshits, V. G.; Saranin, A. A.; Zotov, A. V.; Katayama, M., *Surface Science: An Introduction*. Springer Berlin Heidelberg: 2013.
98. Mocellin, A.; Gomes, A. H. d. A.; Araújo, O. C.; de Brito, A. N.; Björneholm, O., Surface Propensity of Atmospherically Relevant Amino Acids Studied by XPS. *J. Phys. Chem. B* **2017**, *121* (16), 4220-4225.
99. Rella, S.; Malitesta, C., X-ray photoelectron spectroscopy characterization of aerosol particles in Antarctica. *Antarctic Science* **2015**, *27* (5), 493-499.

100. Song, J.; Peng, P. a., Surface Characterization of Aerosol Particles in Guangzhou, China: A Study by XPS. *Aerosol Sci. Technol.* **2009**, *43* (12), 1230-1242.
101. Wang, B.; Knopf, D. A.; China, S.; Arey, B. W.; Harder, T. H.; Gilles, M. K.; Laskin, A., Direct observation of ice nucleation events on individual atmospheric particles. *Phys. Chem. Chem. Phys.* **2016**, *18* (43), 29721-29731.
102. Virtanen, A.; Joutsensaari, J.; Koop, T.; Kannosto, J.; Yli-Pirilä, P.; Leskinen, J.; Mäkelä, J. M.; Holopainen, J. K.; Pöschl, U.; Kulmala, M.; Worsnop, D. R.; Laaksonen, A., An amorphous solid state of biogenic secondary organic aerosol particles. *Nature* **2010**, *467* (7317), 824-827.
103. Sui, X.; Zhou, Y.; Zhang, F.; Chen, J.; Zhu, Z.; Yu, X.-Y., Deciphering the aqueous chemistry of glyoxal oxidation with hydrogen peroxide using molecular imaging. *Phys. Chem. Chem. Phys.* **2017**, *19* (31), 20357-20366.
104. Sui, X.; Zhou, Y.; Zhang, F.; Zhang, Y.; Chen, J.; Zhu, Z.; Yu, X.-Y., ToF-SIMS characterization of glyoxal surface oxidation products by hydrogen peroxide: A comparison between dry and liquid samples. *Surf. Interface Anal.* **2018**, *50* (10), 927-938.
105. Bondy, A. L.; Kirpres, R. M.; Merzel, R. L.; Pratt, K. A.; Banasxak Holl, M. M.; Ault, A. P., Atomic Force Microscopy-Infrared Spectroscopy of Individual Atmospheric Aerosol Particles: Subdiffraction Limit Vibrational Spectroscopy and Morphological Analysis. *Anal. Chem.* **2017**, *89*, 5897-8598.
106. Li, K.; Wang, W.; Ge, M.; Li, J.; Wang, D., Optical properties of secondary organic aerosols generated by photooxidation of aromatic hydrocarbons. *Sci. Rep.* **2014**, *4*, 4922.
107. Craig, R. L.; Bondy, A. L.; Ault, A. P., Surface Enhanced Raman Spectroscopy Enables Observations of Previously Undetectable Secondary Organic Aerosol Components at the Individual Particle Level. *Anal. Chem.* **2015**, *87* (15), 7510-7514.
108. Sivaprakasam, V.; Hart, M. B.; Eversole, J. D., Surface Enhanced Raman Spectroscopy of Individual Suspended Aerosol Particles. *J. Phys. Chem. C* **2017**, *121* (40), 22326-22334.
109. Li, S.; Du, L.; Wei, Z.; Wang, W., Aqueous-phase aerosols on the air-water interface: Response of fatty acid Langmuir monolayers to atmospheric inorganic ions. *The Science of the total environment* **2017**, *580*, 1155-1161.
110. Reddy, S. K.; Thiriaux, R.; Wellen Rudd, B. A.; Lin, L.; Adel, T.; Joutsuka, T.; Geiger, F. M.; Allen, H. C.; Morita, A.; Paesani, F., Bulk Contributions Modulate the Sum-Frequency Generation Spectra of Water on Model Sea-Spray Aerosols. *Chem* **2018**, *4* (7), 1629-1644.
111. Qian, Y.; Deng, G.-h.; Rao, Y., In Situ Chemical Analysis of the Gas–Aerosol Particle Interface. *Anal. Chem.* **2018**, *90*, 10967-10973.

112. Ault, A. P.; Zhao, D.; Ebben, C. J.; Tauber, M. J.; Geiger, F. M.; Prather, K. A.; Grassian, V. H., Raman microspectroscopy and vibrational sum frequency generation spectroscopy as probes of the bulk and surface compositions of size-resolved sea spray aerosol particles. *Phys. Chem. Chem. Phys.* **2013**, *15* (17), 6206-6214.
113. Glasius, M.; Goldstein, A. H., Recent Discoveries and Future Challenges in Atmospheric Organic Chemistry. *Environ. Sci. Technol.* **2016**, *50* (6), 2754-2764.
114. Bé, A. G.; Chase, H. M.; Liu, Y.; Upshur, M. A.; Zhang, Y.; Tuladhar, A.; Chase, Z. A.; Bellcross, A. D.; Wang, H.-F.; Wang, Z.; Batista, V. S.; Martin, S. T.; Thomson, R. J.; Geiger, F. M., Atmospheric  $\beta$ -Caryophyllene-Derived Ozonolysis Products at Interfaces. *ACS Earth Space Chem.* **2019**, *3* (2), 158-169.
115. Ye, Q.; Upshur, M. A.; Robinson, E. S.; Geiger, F. M.; Sullivan, R. C.; Thomson, R. J.; Donahue, N. M., Following Particle-Particle Mixing in Atmospheric Secondary Organic Aerosols by Using Isotopically Labeled Terpenes. *Chem* **2018**, *4* (2), 318-333.
116. Zhang, X.; Lambe, A. T.; Upshur, M. A.; Brooks, W. A.; Gray Bé, A.; Thomson, R. J.; Geiger, F. M.; Surratt, J. D.; Zhang, Z.; Gold, A.; Graf, S.; Cubison, M. J.; Groessl, M.; Jayne, J. T.; Worsnop, D. R.; Canagaratna, M. R., Highly Oxygenated Multifunctional Compounds in  $\alpha$ -Pinene Secondary Organic Aerosol. *Environ. Sci. Technol.* **2017**, *51* (11), 5932-5940.
117. Bates, K. H.; Crouse, J. D.; St. Clair, J. M.; Bennett, N. B.; Nguyen, T. B.; Seinfeld, J. H.; Stoltz, B. M.; Wennberg, P. O., Gas Phase Production and Loss of Isoprene Epoxydiols. *J. Phys. Chem. A* **2014**, *118* (7), 1237-1246.
118. Surratt, J. D.; Kroll, J. H.; Kleindienst, T. E.; Edney, E. O.; Claeys, M.; Sorooshian, A.; Ng, N. L.; Offenberg, J. H.; Lewandowski, M.; Jaoui, M.; Flagan, R. C.; Seinfeld, J. H., Evidence for Organosulfates in Secondary Organic Aerosol. *Environ. Sci. Technol.* **2007**, *41* (2), 517-527.
119. Wang, Y.-C.; Ma, Y.; Li, X.; Kuang, B. Y.; Huang, C.; Tong, R.; Yu, J. Z., Monoterpene and sesquiterpene  $\alpha$ -hydroxy organosulfates: Synthesis, MS/MS characteristics, and ambient presence. *Environ. Sci. Technol.* **2019**.

**Chapter 2 references.**

1. Ng, N. L.; Canagaratna, M. R.; Zhang, Q.; Jimenez, J. L.; Tian, J.; Ulbrich, I. M.; Kroll, J. H.; Docherty, K. S.; Chhabra, P. S.; Bahreini, R.; Murphy, S. M.; Seinfeld, J. H.; Hildebrandt, L.; Donahue, N. M.; DeCarlo, P. F.; Lanz, V. A.; Prévôt, A. S. H.; Dinar, E.; Rudich, Y.; Worsnop, D. R., Organic aerosol components observed in Northern Hemispheric datasets from Aerosol Mass Spectrometry. *Atmos. Chem. Phys.* **2010**, *10* (10), 4625-4641.
2. Baltensperger, U.; Kalberer, M.; Dommen, J.; Paulsen, D.; Alfarra, M. R.; Coe, H.; Fisseha, R.; Gascho, A.; Gysel, M.; Nyeki, S.; Sax, M.; Steinbacher, M.; Prevot, A. S. H.; Sjogren, S.; Weingartner, E.; Zenobi, R., Secondary organic aerosols from anthropogenic and biogenic precursors. *Farad. Discuss.* **2005**, *130*, 265-278.
3. Ebben, C. J.; Shrestha, M.; Martinez, I. S.; Corrigan, A. L.; Frossard, A. A.; Song, W. W.; Worton, D. R.; Petäjä, T.; Williams, J.; Russell, L. M.; Kulmala, M.; Goldstein, A. H.; Artaxo, P.; Martin, S. T.; Thomson, R. J.; Geiger, F. M., Organic Constituents on the Surfaces of Aerosol Particles from Southern Finland, Amazonia, and California Studied by Vibrational Sum Frequency Generation. *J. Phys. Chem. A* **2012**, *116* (32), 8271-8290.
4. Hallquist, M.; Wenger, J. C.; Baltensperger, U.; Rudich, Y.; Simpson, D.; Claeys, M.; Dommen, J.; Donahue, N. M.; George, C.; Goldstein, A. H.; Hamilton, J. F.; Herrmann, H.; Hoffmann, T.; Iinuma, Y.; Jang, M.; Jenkin, M. E.; Jimenez, J. L.; Kiendler-Scharr, A.; Maenhaut, W.; McFiggans, G.; Mentel, T. F.; Monod, A.; Prévôt, A. S. H.; Seinfeld, J. H.; Surratt, J. D.; Szmigielski, R.; Wildt, J., The formation, properties and impact of secondary organic aerosol: current and emerging issues. *Atmos. Chem. Phys.* **2009**, *9* (14), 5155-5236.
5. Williams, J.; Crowley, J.; Fischer, H.; Harder, H.; Martinez, M.; Petäjä, T.; Rinne, J.; Bäck, J.; Boy, M.; Dal Maso, M.; Hakala, J.; Kajos, M.; Keronen, P.; Rantala, P.; Aalto, J.; Aaltonen, H.; Paatero, J.; Vesala, T.; Hakola, H.; Levula, J.; Pohja, T.; Herrmann, F.; Auld, J.; Mesarchaki, E.; Song, W.; Yassaa, N.; Nölscher, A.; Johnson, A. M.; Custer, T.; Sinha, V.; Thieser, J.; Pouvesle, N.; Taraborrelli, D.; Tang, M. J.; Bozem, H.; Hosaynali-Beygi, Z.; Axinte, R.; Oswald, R.; Novelli, A.; Kubistin, D.; Hens, K.; Javed, U.; Trawny, K.; Breitenberger, C.; Hidalgo, P. J.; Ebben, C. J.; Geiger, F. M.; Corrigan, A. L.; Russell, L. M.; Ouwersloot, H. G.; Vilà-Guerau de Arellano, J.; Ganzeveld, L.; Vogel, A.; Beck, M.; Bayerle, A.; Kampf, C. J.; Bertelmann, M.; Köllner, F.; Hoffmann, T.; Valverde, J.; González, D.; Riekkola, M. L.; Kulmala, M.; Lelieveld, J., The summertime Boreal forest field measurement intensive (HUMPPA-COPEC-2010): an overview of meteorological and chemical influences. *Atmos. Chem. Phys.* **2011**, *11* (20), 10599-10618.
6. Beck, M.; Hoffmann, T., A detailed MSn study for the molecular identification of a dimer formed from oxidation of pinene. *Atmos. Environ.* **2015**.
7. Goldstein, A. H.; Galbally, I. E., Known and Unexplored Organic Constituents in the Earth's Atmosphere. *Environ. Sci. Technol.* **2007**, *41* (5), 1514-1521.

8. Galbally, I. E.; Lawson, S. J.; Weeks, I. A.; Bentley, S. T.; Gillett, R. W.; Meyer, M.; Goldstein, A. H., Volatile organic compounds in marine air at Cape Grim, Australia. *Environ. Chem.* **2007**, *4* (3), 178-182.
9. Riipinen, I.; Pierce, J. R.; Yli-Juuti, T.; Nieminen, T.; Häkkinen, S.; Ehn, M.; Junninen, H.; Lehtipalo, K.; Petäjä, T.; Slowik, J.; Chang, R.; Shantz, N. C.; Abbatt, J.; Leitch, W. R.; Kerminen, V. M.; Worsnop, D. R.; Pandis, S. N.; Donahue, N. M.; Kulmala, M., Organic condensation: a vital link connecting aerosol formation to cloud condensation nuclei (CCN) concentrations. *Atmos. Chem. Phys.* **2011**, *11* (8), 3865-3878.
10. Carlton, A. G.; Wiedinmyer, C.; Kroll, J. H., A review of Secondary Organic Aerosol (SOA) formation from isoprene. *Atmos. Chem. Phys.* **2009**, *9* (14), 4987-5005.
11. McNeill, V. F.; Sareen, N.; Schwier, A. N., Surface-Active Organics in Atmospheric Aerosols. In *Atmospheric and Aerosol Chemistry*, McNeill, F. V.; Ariya, A. P., Eds. Springer Berlin Heidelberg: Berlin, Heidelberg, 2014; pp 201-259.
12. Köhler, H., The nucleus in and the growth of hygroscopic droplets. *Trans. Faraday Soc.* **1936**, *32*, 1152-1161.
13. Liu, P.; Song, M.; Zhao, T.; Gunthe, S. S.; Ham, S.; He, Y.; Qin, Y. M.; Gong, Z.; Amorim, J. C.; Bertram, A. K.; Martin, S. T., Resolving the mechanisms of hygroscopic growth and cloud condensation nuclei activity for organic particulate matter. *Nature Commun.* **2018**, *9* (1), 4076.
14. Sareen, N.; Schwier, A. N.; Lathem, T. L.; Nenes, A.; McNeill, V. F., Surfactants from the gas phase may promote cloud droplet formation. *Proc. Natl. Acad. Sci.* **2013**, *110* (8), 2723-2728.
15. Sorjamaa, R.; Svenningsson, B.; Raatikainen, T.; Henning, S.; Bilde, M.; Laaksonen, A., The role of surfactants in Köhler theory reconsidered. *Atmos. Chem. Phys.* **2004**, *4* (8), 2107-2117.
16. Li, Z.; Williams, A. L.; Rood, M. J., Influence of Soluble Surfactant Properties on the Activation of Aerosol Particles Containing Inorganic Solute. *Journal of the Atmospheric Sciences* **1998**, *55* (10), 1859-1866.
17. Moore, R. H.; Ingall, E. D.; Sorooshian, A.; Nenes, A., Molar mass, surface tension, and droplet growth kinetics of marine organics from measurements of CCN activity. *Geophys. Res. Lett.* **2008**, *35* (7), n/a-n/a.
18. Petters, M. D.; Kreidenweis, S. M.; Prenni, A. J.; Sullivan, R. C.; Carrico, C. M.; Koehler, K. A.; Ziemann, P. J., Role of molecular size in cloud droplet activation. *Geophys. Res. Lett.* **2009**, *36* (22).

19. Prenni, A. J.; Petters, M. D.; Kreidenweis, S. M.; DeMott, P. J.; Ziemann, P. J., Cloud droplet activation of secondary organic aerosol. *J. Geophys. Res. Atmos.* **2007**, *112*, D10223.
20. Wex, H.; Petters, M. D.; Carrico, C. M.; Hallbauer, E.; Massling, A.; McMeeking, G. R.; Poulain, L.; Wu, Z.; Kreidenweis, S. M.; Stratmann, F., Towards closing the gap between hygroscopic growth and activation for secondary organic aerosol: Part 1 – Evidence from measurements. *Atmos. Chem. Phys.* **2009**, *9* (12), 3987-3997.
21. Good, N.; Topping, D. O.; Duplissy, J.; Gysel, M.; Meyer, N. K.; Metzger, A.; Turner, S. F.; Baltensperger, U.; Ristovski, Z.; Weingartner, E.; Coe, H.; McFiggans, G., Widening the gap between measurement and modelling of secondary organic aerosol properties? *Atmos. Chem. Phys.* **2010**, *10* (6), 2577-2593.
22. Renbaum-Wolff, L.; Song, M.; Marcolli, C.; Zhang, Y.; Liu, P. F.; Grayson, J. W.; Geiger, F. M.; Martin, S. T.; Bertram, A. K., Observations and implications of liquid–liquid phase separation at high relative humidities in secondary organic material produced by  $\alpha$ -pinene ozonolysis without inorganic salts. *Atmos. Chem. Phys.* **2016**, *16* (12), 7969-7979.
23. Shulman, M. L.; Jacobson, M. C.; Carlson, R. J.; Synovec, R. E.; Young, T. E., Dissolution behavior and surface tension effects of organic compounds in nucleating cloud droplets. *Geophys. Res. Lett.* **1996**, *23* (3), 277-280.
24. Ruehl, C. R.; Davies, J. F.; Wilson, K. R., An interfacial mechanism for cloud droplet formation on organic aerosols. *Science* **2016**, *351* (6280), 1447-1450.
25. Petters, M. D.; Kreidenweis, S. M., A single parameter representation of hygroscopic growth and cloud condensation nucleus activity. *Atmos. Chem. Phys.* **2007**, *7* (8), 1961-1971.
26. Upshur, M. A.; Strick, B. F.; McNeill, V. F.; Thomson, R. J.; Geiger, F. M., Climate-relevant physical properties of molecular constituents for isoprene-derived secondary organic aerosol material. *Atmos. Chem. Phys.* **2014**, *14* (19), 10731-10740.
27. Nozière, B.; Baduel, C.; Jaffrezo, J.-L., The dynamic surface tension of atmospheric aerosol surfactants reveals new aspects of cloud activation. *Nature Commun.* **2014**, *5*, 3335.
28. Atkinson, R.; Arey, J., Atmospheric Chemistry of Biogenic Organic Compounds. *Acc. Chem. Res.* **1998**, *31* (9), 574-583.
29. Shu, Y.; Atkinson, R., Atmospheric lifetimes and fates of a series of sesquiterpenes. *J. Geophys. Res. Atmos.* **1995**, *100* (D4), 7275-7281.
30. Bonn, B.; Moortgat, G. K., Sesquiterpene ozonolysis: Origin of atmospheric new particle formation from biogenic hydrocarbons. *Geophys. Res. Lett.* **2003**, *30* (11), 1585.

31. Goldstein, A. H.; McKay, M.; Kurpius, M. R.; Schade, G. W.; Lee, A.; Holzinger, R.; Rasmussen, R. A., Forest thinning experiment confirms ozone deposition to forest canopy is dominated by reaction with biogenic VOCs. *Geophys. Res. Lett.* **2004**, *31*, L22106.
32. Ehn, M.; Thornton, J. A.; Kleist, E.; Sipila, M.; Junninen, H.; Pullinen, I.; Springer, M.; Rubach, F.; Tillmann, R.; Lee, B.; Lopez-Hilfiker, F.; Andres, S.; Acir, I.-H.; Rissanen, M.; Jokinen, T.; Schobesberger, S.; Kangasluoma, J.; Kontkanen, J.; Nieminen, T.; Kurten, T.; Nielsen, L. B.; Jorgensen, S.; Kjaergaard, H. G.; Canagaratna, M.; Maso, M. D.; Berndt, T.; Petaja, T.; Wahner, A.; Kerminen, V.-M.; Kulmala, M.; Worsnop, D. R.; Wildt, J.; Mentel, T. F., A large source of low-volatility secondary organic aerosol. *Nature* **2014**, *506* (7489), 476-479.
33. Sakulyanontvittaya, T.; Duhl, T.; Wiedinmyer, C.; Helmig, D.; Matsunaga, S.; Potosnak, M.; Milford, J.; Guenther, A., Monoterpene and Sesquiterpene Emission Estimates for the United States. *Environ. Sci. Technol.* **2008**, *42* (5), 1623-1629.
34. Helmig, D.; Ortega, J.; Duhl, T.; Tanner, D.; Guenther, A.; Harley, P.; Wiedinmyer, C.; Milford, J.; Sakulyanontvittaya, T., Sesquiterpene Emissions from Pine Trees – Identifications, Emission Rates and Flux Estimates for the Contiguous United States. *Environ. Sci. Technol.* **2007**, *41* (5), 1545-1553.
35. Winterhalter, R.; Herrmann, F.; Kanawati, B.; Nguyen, T. L.; Peeters, J.; Vereecken, L.; Moortgat, G. K., The gas-phase ozonolysis of  $\beta$ -caryophyllene ( $C_{15}H_{24}$ ). Part I: an experimental study. *Phys. Chem. Chem. Phys.* **2009**, *11* (21), 4152-4172.
36. Jaoui, M.; Lewandowski, M.; Kleindienst, T. E.; Offenberg, J. H.; Edney, E. O.,  $\beta$ -caryophyllinic acid: An atmospheric tracer for  $\beta$ -caryophyllene secondary organic aerosol. *Geophys. Res. Lett.* **2007**, *34*, L05816.
37. Parshintsev, J.; Nurmi, J.; Kilpeläinen, I.; Hartonen, K.; Kulmala, M.; Riekkola, M.-L., Preparation of  $\beta$ -caryophyllene oxidation products and their determination in ambient aerosol samples. *Anal. Bioanal. Chem.* **2008**, *390* (3), 913-919.
38. Jaoui, M.; Leungsakul, S.; Kamens, R. M., Gas and Particle Products Distribution from the Reaction of  $\beta$ -Caryophyllene with Ozone. *J. Atmos. Chem.* **2003**, *45* (3), 261-287.
39. Hartonen, K.; Parshintsev, J.; Vilja, V.-P.; Tiala, H.; Knuuti, S.; Lai, C. K.; Riekkola, M.-L., Gas chromatographic vapor pressure determination of atmospherically relevant oxidation products of  $\beta$ -caryophyllene and  $\alpha$ -pinene. *Atmos. Environ.* **2013**, *81*, 330-338.
40. van Eijck, A.; Opatz, T.; Taraborrelli, D.; Sander, R.; Hoffmann, T., New tracer compounds for secondary organic aerosol formation from  $\beta$ -caryophyllene oxidation. *Atmos. Environ.* **2013**, *80*, 122-130.

41. Fu, P.; Kawamura, K.; Chen, J.; Barrie, L. A., Isoprene, Monoterpene, and Sesquiterpene Oxidation Products in the High Arctic Aerosols during Late Winter to Early Summer. *Environ. Sci. Technol.* **2009**, *43* (11), 4022-4028.
42. Lewandowski, M.; Jaoui, M.; Offenberg, J. H.; Kleindienst, T. E.; Edney, E. O.; Sheesley, R. J.; Schauer, J. J., Primary and Secondary Contributions to Ambient PM in the Midwestern United States. *Environ. Sci. Technol.* **2008**, *42* (9), 3303-3309.
43. Kleindienst, T. E.; Jaoui, M.; Lewandowski, M.; Offenberg, J. H.; Lewis, C. W.; Bhawe, P. V.; Edney, E. O., Estimates of the contributions of biogenic and anthropogenic hydrocarbons to secondary organic aerosol at a southeastern US location. *Atmos. Environ.* **2007**, *41* (37), 8288-8300.
44. Bouvier-Brown, N. C.; Goldstein, A. H.; Gilman, J. B.; Kuster, W. C.; de Gouw, J. A., In-situ ambient quantification of monoterpenes, sesquiterpenes, and related oxygenated compounds during BEARPEX 2007: implications for gas- and particle-phase chemistry. *Atmos. Chem. Phys.* **2009**, *9* (15), 5505-5518.
45. Lee, A.; Goldstein, A. H.; Kroll, J. H.; Ng, N. L.; Varutbangkul, V.; Flagan, R. C.; Seinfeld, J. H., Gas-phase products and secondary aerosol yields from the photooxidation of 16 different terpenes. *J. Geophys. Res. Atmos.* **2006**, *111*, D17305.
46. Lee, A.; Goldstein, A. H.; Keywood, M. D.; Gao, S.; Varutbangkul, V.; Bahreini, R.; Ng, N. L.; Flagan, R. C.; Seinfeld, J. H., Gas-phase products and secondary aerosol yields from the ozonolysis of ten different terpenes. *J. Geophys. Res. Atmos.* **2006**, *111*, D07302.
47. Li, Y. J.; Chen, Q.; Guzman, M. I.; Chan, C. K.; Martin, S. T., Second-generation products contribute substantially to the particle-phase organic material produced by  $\beta$ -caryophyllene ozonolysis. *Atmos. Chem. Phys.* **2011**, *11* (1), 121-132.
48. Chan, M. N.; Surratt, J. D.; Chan, A. W. H.; Schilling, K.; Offenberg, J. H.; Lewandowski, M.; Edney, E. O.; Kleindienst, T. E.; Jaoui, M.; Edgerton, E. S.; Tanner, R. L.; Shaw, S. L.; Zheng, M.; Knipping, E. M.; Seinfeld, J. H., Influence of aerosol acidity on the chemical composition of secondary organic aerosol from beta-caryophyllene. *Atmos. Chem. Phys.* **2011**, *11* (4), 1735-1751.
49. Vestenius, M.; Hellén, H.; Levula, J.; Kuronen, P.; Helminen, K. J.; Nieminen, T.; Kulmala, M.; Hakola, H., Acidic reaction products of monoterpenes and sesquiterpenes in atmospheric fine particles in a boreal forest. *Atmos. Chem. Phys.* **2014**, *14* (15), 7883-7893.
50. Wyche, K. P.; Monks, P. S.; Smallbone, K. L.; Hamilton, J. F.; Alfara, M. R.; Rickard, A. R.; McFiggans, G. B.; Jenkin, M. E.; Bloss, W. J.; Ryan, A. C.; Hewitt, C. N.; MacKenzie, A. R., Mapping gas-phase organic reactivity and concomitant secondary organic aerosol formation: chemometric dimension reduction techniques for the deconvolution of complex atmospheric data sets. *Atmos. Chem. Phys.* **2015**, *15* (14), 8077-8100.

51. Nozière, B.; Kalberer, M.; Claeys, M.; Allan, J.; D'Anna, B.; Decesari, S.; Finessi, E.; Glasius, M.; Grgić, I.; Hamilton, J. F.; Hoffmann, T.; Iinuma, Y.; Jaoui, M.; Kahnt, A.; Kampf, C. J.; Kourttchev, I.; Maenhaut, W.; Marsden, N.; Saarikoski, S.; Schnelle-Kreis, J.; Surratt, J. D.; Szidat, S.; Szmigielski, R.; Wisthaler, A., The Molecular Identification of Organic Compounds in the Atmosphere: State of the Art and Challenges. *Chem. Rev.* **2015**, *115* (10), 3919-3983.
52. Tuckermann, R.; Cammenga, H. K., The surface tension of aqueous solutions of some atmospheric water-soluble organic compounds. *Atmos. Environ.* **2004**, *38* (36), 6135-6138.
53. Li, X.; Hede, T.; Tu, Y.; Leck, C.; Ågren, H., Surface-Active cis-Pinonic Acid in Atmospheric Droplets: A Molecular Dynamics Study. *J. Phys. Chem. Lett.* **2010**, *1* (4), 769-773.
54. von Szyszkowski, B., Experimentelle Studien über kapillare Eigenschaften der wasserigen Lösungen von Fettsäuren. (Experimental studies of the capillary properties of aqueous solutions of fatty acids). *Z. Phys. Chem.* **1908**, *64*, 385-414.
55. Meissner, H. P.; Michaels, A. S., Surface Tensions of Pure Liquids and Liquid Mixtures. *Industrial & Engineering Chemistry* **1949**, *41* (12), 2782-2787.
56. Henning, S.; Rosenørn, T.; D'Anna, B.; Gola, A. A.; Svenningsson, B.; Bilde, M., Cloud droplet activation and surface tension of mixtures of slightly soluble organics and inorganic salt. *Atmos. Chem. Phys.* **2005**, *5* (2), 575-582.
57. Sareen, N.; Schwier, A. N.; Shapiro, E. L.; Mitroo, D.; McNeill, V. F., Secondary organic material formed by methylglyoxal in aqueous aerosol mimics. *Atmos. Chem. Phys.* **2010**, *10* (3), 997-1016.
58. Cruz, C. N.; Pandis, S. N., The effect of organic coatings on the cloud condensation nuclei activation of inorganic atmospheric aerosol. *J. Geophys. Res. Atmos.* **1998**, *103* (D11), 13111-13123.
59. Xi Yuan, H.; Rosen, M. J., Dynamic surface tension of aqueous surfactant solutions: I. Basic parameters. *J. Colloid Interface Sci.* **1988**, *124* (2), 652-659.
60. Engelhart, G. J.; Asa-Awuku, A.; Nenes, A.; Pandis, S. N., CCN activity and droplet growth kinetics of fresh and aged monoterpene secondary organic aerosol. *Atmos. Chem. Phys.* **2008**, *8* (14), 3937-3949.
61. Prisle, N. L.; Asmi, A.; Topping, D.; Partanen, A. I.; Romakkaniemi, S.; Dal Maso, M.; Kulmala, M.; Laaksonen, A.; Lehtinen, K. E. J.; McFiggans, G.; Kokkola, H., Surfactant effects in global simulations of cloud droplet activation. *Geophys. Res. Lett.* **2012**, *39* (5), L05802.

62. Gérard, V.; Nozière, B.; Baduel, C.; Fine, L.; Frossard, A. A.; Cohen, R. C., Anionic, Cationic, and Nonionic Surfactants in Atmospheric Aerosols from the Baltic Coast at Askö, Sweden: Implications for Cloud Droplet Activation. *Environ. Sci. Technol.* **2016**, *50* (6), 2974-2982.
63. Asa-Awuku, A.; Engelhart, G. J.; Lee, B. H.; Pandis, S. N.; Nenes, A., Relating CCN activity, volatility, and droplet growth kinetics of  $\beta$ -caryophyllene secondary organic aerosol. *Atmos. Chem. Phys.* **2009**, *9* (3), 795-812.
64. Huff Hartz, K. E.; Rosenørn, T.; Ferchak, S. R.; Raymond, T. M.; Bilde, M.; Donahue, N. M.; Pandis, S. N., Cloud condensation nuclei activation of monoterpene and sesquiterpene secondary organic aerosol. *J. Geophys. Res. Atmos.* **2005**, *110*, D14208.
65. Frosch, M.; Bilde, M.; Nenes, A.; Praplan, A. P.; Jurányi, Z.; Dommen, J.; Gysel, M.; Weingartner, E.; Baltensperger, U., CCN activity and volatility of  $\beta$ -caryophyllene secondary organic aerosol. *Atmos. Chem. Phys.* **2013**, *13* (4), 2283-2297.
66. Tang, X.; Cocker Iii, D. R.; Asa-Awuku, A., Are sesquiterpenes a good source of secondary organic cloud condensation nuclei (CCN)? Revisiting  $\beta$ -caryophyllene CCN. *Atmos. Chem. Phys.* **2012**, *12* (18), 8377-8388.
67. Morris, H. S.; Grassian, V. H.; Tivanski, A. V., Humidity-dependent surface tension measurements of individual inorganic and organic submicrometre liquid particles. *Chem. Sci.* **2015**, *6* (5), 3242-3247.
68. Bzdek, B. R.; Power, R. M.; Simpson, S. H.; Reid, J. P.; Royall, C. P., Precise, contactless measurements of the surface tension of picolitre aerosol droplets. *Chem. Sci.* **2016**, *7* (1), 274-285.
69. Ebben, C. J.; Strick, B. F.; Upshur, M. A.; Chase, H. M.; Achtyl, J. L.; Thomson, R. J.; Geiger, F. M., Towards the identification of molecular constituents associated with the surfaces of isoprene-derived secondary organic aerosol (SOA) particles. *Atmos. Chem. Phys.* **2014**, *14* (5), 2303-2314.
70. Ho, J.; Psciuk, B. T.; Chase, H. M.; Rudshteyn, B.; Upshur, M. A.; Fu, L.; Thomson, R. J.; Wang, H.-F.; Geiger, F. M.; Batista, V. S., Sum Frequency Generation Spectroscopy and Molecular Dynamics Simulations Reveal a Rotationally Fluid Adsorption State of  $\alpha$ -Pinene on Silica. *J. Phys. Chem. C* **2016**, *120*, 12578-12589.
71. Chase, H. M.; Ho, J.; Upshur, M. A.; Thomson, R. J.; Batista, V. S.; Geiger, F. M., Unanticipated Stickiness of  $\alpha$ -Pinene. *J. Phys. Chem. A* **2017**, *121* (17), 3239-3246.

**Chapter 3 references.**

1. Corrigan, C. E.; Novakov, T., Cloud condensation nucleus activity of organic compounds: a laboratory study. *Atmos. Environ.* **1999**, *33* (17), 2661-2668.
2. Cruz, C. N.; Pandis, S. N., The effect of organic coatings on the cloud condensation nuclei activation of inorganic atmospheric aerosol. *J. Geophys. Res. Atmos.* **1998**, *103* (D11), 13111-13123.
3. Duplissy, J.; Gysel, M.; Alfarra, M. R.; Dommen, J.; Metzger, A.; Prevot, A. S. H.; Weingartner, E.; Laaksonen, A.; Raatikainen, T.; Good, N.; Turner, S. F.; McFiggans, G.; Baltensperger, U., Cloud forming potential of secondary organic aerosol under near atmospheric conditions. *Geophys. Res. Lett.* **2008**, *35* (3), L03818.
4. Facchini, M. C.; Mircea, M.; Fuzzi, S.; Charlson, R. J., Cloud albedo enhancement by surface-active organic solutes in growing droplets. *Nature* **1999**, *401* (6750), 257-259.
5. Frosch, M.; Bilde, M.; DeCarlo, P. F.; Jurányi, Z.; Tritscher, T.; Dommen, J.; Donahue, N. M.; Gysel, M.; Weingartner, E.; Baltensperger, U., Relating cloud condensation nuclei activity and oxidation level of  $\alpha$ -pinene secondary organic aerosols. *J. Geophys. Res. Atmos.* **2011**, *116* (D22), D22212.
6. Gill, P. S.; Graedel, T. E.; Weschler, C. J., Organic films on atmospheric aerosol particles, fog droplets, cloud droplets, raindrops, and snowflakes. *Reviews of Geophysics* **1983**, *21* (4), 903-920.
7. Huff Hartz, K. E.; Rosenørn, T.; Ferchak, S. R.; Raymond, T. M.; Bilde, M.; Donahue, N. M.; Pandis, S. N., Cloud condensation nuclei activation of monoterpene and sesquiterpene secondary organic aerosol. *J. Geophys. Res. Atmos.* **2005**, *110* (D14), D14208.
8. McNeill, V. F.; Sareen, N.; Schwier, A. N., Surface-Active Organics in Atmospheric Aerosols. In *Atmospheric and Aerosol Chemistry*, McNeill, F. V.; Ariya, A. P., Eds. Springer Berlin Heidelberg: Berlin, Heidelberg, 2014; pp 201-259.
9. Nozière, B.; Baduel, C.; Jaffrezo, J.-L., The dynamic surface tension of atmospheric aerosol surfactants reveals new aspects of cloud activation. *Nature Commun.* **2014**, *5*, 3335.
10. Prenni, A. J.; Petters, M. D.; Kreidenweis, S. M.; DeMott, P. J.; Ziemann, P. J., Cloud droplet activation of secondary organic aerosol. *J. Geophys. Res. Atmos.* **2007**, *112* (D10), D10223.
11. Prisle, N. L.; Asmi, A.; Topping, D.; Partanen, A. I.; Romakkaniemi, S.; Dal Maso, M.; Kulmala, M.; Laaksonen, A.; Lehtinen, K. E. J.; McFiggans, G.; Kokkola, H., Surfactant effects in global simulations of cloud droplet activation. *Geophys. Res. Lett.* **2012**, *39* (5), L05802.

12. Ruehl, C. R.; Davies, J. F.; Wilson, K. R., An interfacial mechanism for cloud droplet formation on organic aerosols. *Science* **2016**, *351* (6280), 1447-1450.
13. Sareen, N.; Schwier, A. N.; Lathem, T. L.; Nenes, A.; McNeill, V. F., Surfactants from the gas phase may promote cloud droplet formation. *Proc. Natl. Acad. Sci.* **2013**, *110* (8), 2723-2728.
14. Shrestha, M.; Zhang, Y.; Ebben, C. J.; Martin, S. T.; Geiger, F. M., Vibrational sum frequency generation spectroscopy of secondary organic material produced by condensational growth from alpha-pinene ozonolysis. *J. Phys. Chem. A* **2013**, *117* (35), 8427-8436.
15. Tolocka, M. P.; Heaton, K. J.; Dreyfus, M. A.; Wang, S.; Zordan, C. A.; Saul, T. D.; Johnston, M. V., Chemistry of Particle Inception and Growth during  $\alpha$ -Pinene Ozonolysis. *Environ. Sci. Technol.* **2006**, *40* (6), 1843-1848.
16. Wang, J.; Wexler, A. S., Adsorption of organic molecules may explain growth of newly nucleated clusters and new particle formation. *Geophys. Res. Lett.* **2013**, *40* (11), 2834-2838.
17. George, C.; Ammann, M.; D'Anna, B.; Donaldson, D. J.; Nizkorodov, S. A., Heterogeneous Photochemistry in the Atmosphere. *Chem. Rev.* **2015**, *115* (10), 4218-4258.
18. Wu, Y.; Li, W.; Xu, B.; Li, X.; Wang, H.; McNeill, V. F.; Rao, Y.; Dai, H.-L., Observation of Organic Molecules at the Aerosol Surface. *J. Phys. Chem. Lett.* **2016**, *7* (12), 2294-2297.
19. Ellison, G. B.; Tuck, A. F.; Vaida, V., Atmospheric processing of organic aerosols. *J. Geophys. Res. Atmos.* **1999**, *104* (D9), 11633-11641.
20. Kairaliyeva, T.; Aksenenko, E. V.; Mucic, N.; Makievski, A. V.; Fainerman, V. B.; Miller, R., Surface Tension and Adsorption Studies by Drop Profile Analysis Tensiometry. *J. Surf. Deterg.* **2017**, (20), 1225-1241.
21. Bé, A. G.; Upshur, M. A.; Liu, P.; Martin, S. T.; Geiger, F. M.; Thomson, R. J., Cloud Activation Potentials for Atmospheric  $\alpha$ -Pinene and  $\beta$ -Caryophyllene Ozonolysis Products. *ACS Cent. Sci.* **2017**, *3* (7), 715-725.
22. Jaoui, M.; Lewandowski, M.; Kleindienst, T. E.; Offenber, J. H.; Edney, E. O.,  $\beta$ -caryophyllinic acid: An atmospheric tracer for  $\beta$ -caryophyllene secondary organic aerosol. *Geophys. Res. Lett.* **2007**, *34* (5), L05816.
23. Parshintsev, J.; Nurmi, J.; Kilpeläinen, I.; Hartonen, K.; Kulmala, M.; Riekkola, M.-L., Preparation of  $\beta$ -caryophyllene oxidation products and their determination in ambient aerosol samples. *Anal. Bioanal. Chem.* **2008**, *390* (3), 913-919.

24. Hellén, H.; Praplan, A. P.; Tykkä, T.; Ylivinkka, I.; Vakkari, V.; Bäck, J.; Petäjä, T.; Kulmala, M.; Hakola, H., Long-term measurements of volatile organic compounds highlight the importance of sesquiterpenes for the atmospheric chemistry of a boreal forest. *Atmos. Chem. Phys.* **2018**, *18* (19), 13839-13863.
25. Yee, L. D.; Isaacman-VanWertz, G.; Wernis, R. A.; Meng, M.; Rivera, V.; Kreisberg, N. M.; Hering, S. V.; Bering, M. S.; Glasius, M.; Upshur, M. A.; Bé, A. G.; Thomson, R. J.; Geiger, F. M.; Offenberg, J. H.; Lewandowski, M.; Kourtchev, I.; Kalberer, M.; de Sá, S.; Martin, S. T.; Alexander, M. L.; Palm, B. B.; Hu, W.; Campuzano-Jost, P.; Day, D. A.; Jimenez, J. L.; Liu, Y.; McKinney, K. A.; Artaxo, P.; Viegas, J.; Manzi, A.; Oliveira, M. B.; de Souza, R.; Machado, L. A. T.; Longo, K.; Goldstein, A. H., Observations of sesquiterpenes and their oxidation products in central Amazonia during the wet and dry seasons. *Atmos. Chem. Phys.* **2018**, *18*, 10433-10457.
26. Jaoui, M.; Leungsakul, S.; Kamens, R. M., Gas and Particle Products Distribution from the Reaction of  $\beta$ -Caryophyllene with Ozone. *J. Atmos. Chem.* **2003**, *45* (3), 261-287.
27. Winterhalter, R.; Herrmann, F.; Kanawati, B.; Nguyen, T. L.; Peeters, J.; Vereecken, L.; Moortgat, G. K., The gas-phase ozonolysis of  $\beta$ -caryophyllene (C<sub>15</sub>H<sub>24</sub>). Part I: an experimental study. *Phys. Chem. Chem. Phys.* **2009**, *11* (21), 4152-4172.
28. Hartonen, K.; Parshintsev, J.; Vilja, V.-P.; Tiala, H.; Knuuti, S.; Lai, C. K.; Riekkola, M.-L., Gas chromatographic vapor pressure determination of atmospherically relevant oxidation products of  $\beta$ -caryophyllene and  $\alpha$ -pinene. *Atmos. Environ.* **2013**, *81*, 330-338.
29. van Eijck, A.; Opatz, T.; Taraborrelli, D.; Sander, R.; Hoffmann, T., New tracer compounds for secondary organic aerosol formation from  $\beta$ -caryophyllene oxidation. *Atmos. Environ.* **2013**, *80*, 122-130.
30. Ebben, C. J.; Shrestha, M.; Martinez, I. S.; Corrigan, A. L.; Frossard, A. A.; Song, W. W.; Worton, D. R.; Petäjä, T.; Williams, J.; Russell, L. M.; Kulmala, M.; Goldstein, A. H.; Artaxo, P.; Martin, S. T.; Thomson, R. J.; Geiger, F. M., Organic Constituents on the Surfaces of Aerosol Particles from Southern Finland, Amazonia, and California Studied by Vibrational Sum Frequency Generation. *J. Phys. Chem. A* **2012**, *116* (32), 8271-8290.
31. Ebben, C. J.; Martinez, I. S.; Shrestha, M.; Buchbinder, A. M.; Corrigan, A. L.; Guenther, A.; Karl, T.; Petäjä, T.; Song, W. W.; Zorn, S. R.; Artaxo, P.; Kulmala, M.; Martin, S. T.; Russell, L. M.; Williams, J.; Geiger, F. M., Contrasting organic aerosol particles from boreal and tropical forests during HUMPPA-COPEC-2010 and AMAZE-08 using coherent vibrational spectroscopy. *Atmos. Chem. Phys.* **2011**, *11* (20), 10317-10329.
32. Fu, L.; Chen, S.-L.; Wang, H.-F., Validation of Spectra and Phase in Sub-1 cm<sup>-1</sup> Resolution Sum-Frequency Generation Vibrational Spectroscopy through Internal Heterodyne Phase-Resolved Measurement. *J. Phys. Chem. B* **2016**, *120* (8), 1579-1589.

33. Geiger, F. M., Second Harmonic Generation, Sum Frequency Generation, and  $\chi(3)$ : Dissecting Environmental Interfaces with a Nonlinear Optical Swiss Army Knife. *Annu. Rev. Phys. Chem.* **2009**, *60* (1), 61-83.
34. K. Kemnitz, K. B., J. M. Hicks, G. R. Pinto, K. B. Eisenthal, T. F. Heinz, The Phase of Second-Harmonic Light Generated at an Interface and its Relation to Absolute Molecular Orientation. *Chem. Phys. Lett.* **1986**, *131* (45), 285-290.
35. Ault, A. P.; Axson, J. L., Atmospheric Aerosol Chemistry: Spectroscopic and Microscopic Advances. *Anal. Chem.* **2017**, *89* (1), 430-452.
36. Ault, A. P.; Zhao, D.; Ebben, C. J.; Tauber, M. J.; Geiger, F. M.; Prather, K. A.; Grassian, V. H., Raman microspectroscopy and vibrational sum frequency generation spectroscopy as probes of the bulk and surface compositions of size-resolved sea spray aerosol particles. *Phys. Chem. Chem. Phys.* **2013**, *15* (17), 6206-6214.
37. Ault, A. P.; Moffet, R. C.; Baltrusaitis, J.; Collins, D. B.; Ruppel, M. J.; Cuadra-Rodriguez, L. A.; Zhao, D.; Guasco, T. L.; Ebben, C. J.; Geiger, F. M.; Bertram, T. H.; Prather, K. A.; Grassian, V. H., Size-Dependent Changes in Sea Spray Aerosol Composition and Properties with Different Seawater Conditions. *Environ. Sci. Technol.* **2013**, *47* (11), 5603-5612.
38. Ebben, C. J.; Ault, A. P.; Ruppel, M. J.; Ryder, O. S.; Bertram, T. H.; Grassian, V. H.; Prather, K. A.; Geiger, F. M., Size-Resolved Sea Spray Aerosol Particles Studied by Vibrational Sum Frequency Generation. *J. Phys. Chem. A* **2013**, *117* (30), 6589-6601.
39. Williams, J.; Crowley, J.; Fischer, H.; Harder, H.; Martinez, M.; Petäjä, T.; Rinne, J.; Bäck, J.; Boy, M.; Dal Maso, M.; Hakala, J.; Kajos, M.; Keronen, P.; Rantala, P.; Aalto, J.; Aaltonen, H.; Paatero, J.; Vesala, T.; Hakola, H.; Levula, J.; Pohja, T.; Herrmann, F.; Auld, J.; Mesarchaki, E.; Song, W.; Yassaa, N.; Nölscher, A.; Johnson, A. M.; Custer, T.; Sinha, V.; Thieser, J.; Pouvesle, N.; Taraborrelli, D.; Tang, M. J.; Bozem, H.; Hosaynali-Beygi, Z.; Axinte, R.; Oswald, R.; Novelli, A.; Kubistin, D.; Hens, K.; Javed, U.; Trawny, K.; Breitenberger, C.; Hidalgo, P. J.; Ebben, C. J.; Geiger, F. M.; Corrigan, A. L.; Russell, L. M.; Ouwersloot, H. G.; Vilà-Guerau de Arellano, J.; Ganzeveld, L.; Vogel, A.; Beck, M.; Bayerle, A.; Kampf, C. J.; Bertelmann, M.; Köllner, F.; Hoffmann, T.; Valverde, J.; González, D.; Riekkola, M. L.; Kulmala, M.; Lelieveld, J., The summertime Boreal forest field measurement intensive (HUMPPA-COPEC-2010): an overview of meteorological and chemical influences. *Atmos. Chem. Phys.* **2011**, *11* (20), 10599-10618.
40. Ebben, C. J.; Strick, B. F.; Upshur, M. A.; Chase, H. M.; Achtyl, J. L.; Thomson, R. J.; Geiger, F. M., Towards the identification of molecular constituents associated with the surfaces of isoprene-derived secondary organic aerosol (SOA) particles. *Atmos. Chem. Phys.* **2014**, *14* (5), 2303-2314.
41. Kasparian, J.; Wolf, J. P., Ultrafast laser spectroscopy and control of atmospheric aerosols. *Phys. Chem. Chem. Phys.* **2012**, *14* (26), 9291-9300.

42. Qian, Y.; Deng, G.-h.; Rao, Y., In Situ Chemical Analysis of the Gas–Aerosol Particle Interface. *Anal. Chem.* **2018**, *90*, 10967-10973.
43. Upshur, M. A.; Strick, B. F.; McNeill, V. F.; Thomson, R. J.; Geiger, F. M., Climate-relevant physical properties of molecular constituents for isoprene-derived secondary organic aerosol material. *Atmos. Chem. Phys.* **2014**, *14* (19), 10731-10740.
44. Shrestha, M.; Zhang, Y.; Upshur, M. A.; Liu, P.; Blair, S. L.; Wang, H.-f.; Nizkorodov, S. A.; Thomson, R. J.; Martin, S. T.; Geiger, F. M., On Surface Order and Disorder of  $\alpha$ -Pinene-Derived Secondary Organic Material. *J. Phys. Chem. A* **2015**, *119* (19), 4609-4617.
45. Gao, Y.; Hall, W. A.; Johnston, M. V., Molecular Composition of Monoterpene Secondary Organic Aerosol at Low Mass Loading. *Environ. Sci. Technol.* **2010**, *44* (20), 7897-7902.
46. Zhang, Y.; Sanchez, M. S.; Douet, C.; Wang, Y.; Bateman, A. P.; Gong, Z.; Kuwata, M.; Renbaum-Wolff, L.; Sato, B. B.; Liu, P. F.; Bertram, A. K.; Geiger, F. M.; Martin, S. T., Changing shapes and implied viscosities of suspended submicron particles. *Atmos. Chem. Phys.* **2015**, *15* (14), 7819-7829.
47. Tasoglou, A.; Pandis, S. N., Formation and chemical aging of secondary organic aerosol during the  $\beta$ -caryophyllene oxidation. *Atmos. Chem. Phys.* **2015**, *15* (11), 6035-6046.
48. Jokinen, T.; Kausiala, O.; Garmash, O.; Peräkylä, O.; Junninen, H.; Schobesberger, S.; Yan, C.; Sipilä, M.; Rissanen, M., Production of highly oxidized organic compounds from ozonolysis of  $\beta$ -caryophyllene: Laboratory and field measurements. *Boreal Environ. Res.* **2016**, *21*, 262-273.
49. Watry, M. B., M. G.; Richmond, G. L. Applied Spectroscopy, 55 (321A-340A) 2001., Probing Molecular Structure at Liquid Surfaces with Vibrational Sum Frequency Spectroscopy. *Appl. Spectrosc.* **2001**, *55*, 321A-340A.
50. Buchbinder, A. M.; al, e., Method for Evaluating Vibrational Mode Assignments in Surface-Bound Cyclic Hydrocarbons Using Sum-Frequency Generation. *J. Phys. Chem. C* **2011**, *115*, 18284-18294.
51. Buchbinder, A. M.; Ray, N. A.; Lu, J.; Van Duyne, R. P.; Stair, P. C.; Weitz, E.; Geiger, F. M., Displacement of Hexanol by the Hexanoic Acid Overoxidation Product in Alcohol Oxidation on a Model Supported Palladium Nanoparticle Catalyst. *J. Am. Chem. Soc.* **2011**, *133* (44), 17816-17823.
52. Esenturk, O.; Walker, R. A., Surface Structure at Hexadecane and Halo-hexadecane Liquid/Vapor Interfaces. *J. Phys. Chem. B* **2004**, *108* (30), 10631-10635.

53. Velarde, L.; Zhang, X.-y.; Lu, Z.; Joly, A. G.; Wang, Z.; Wang, H.-f., Communication: Spectroscopic Phase and Lineshapes in High-Resolution Broadband Sum Frequency Vibrational Spectroscopy: Resolving Interfacial Inhomogeneities Of "Identical" Molecular Groups. *J. Chem. Phys.* **2011**, *135* (24), 241102.
54. Mifflin, A. L.; Velarde, L.; Ho, J.; Psciuk, B. T.; Negre, C. F.; Ebben, C. J.; Upshur, M. A.; Lu, Z.; Strick, B. F.; Thomson, R. J.; Batista, V. S.; Wang, H.-F.; Geiger, F. M., Accurate Lineshapes from Sub-1 cm<sup>-1</sup> Resolution Sum Frequency Generation Vibrational Spectroscopy of  $\alpha$ -Pinene at Room Temperature. *J. Phys. Chem. A* **2015**, *119*, 1292-1302.
55. Upshur, M. A.; Chase, H. M.; Strick, B. F.; Ebben, C. J.; Fu, L.; Wang, H.; Thomson, R. J.; Geiger, F. M., Vibrational Mode Assignment of  $\alpha$ -Pinene by Isotope Editing: One Down, Seventy-One To Go. *J. Phys. Chem. A* **2016**, *120* (17), 2684-2690.
56. Stokes, G. Y.; Buchbinder, A. M.; Gibbs-Davis, J. M.; Scheidt, K. A.; Geiger, F. M., Heterogeneous Ozone Oxidation Reactions of 1-Pentene, Cyclopentene, Cyclohexene, and a Menthenol Derivative Studied by Sum Frequency Generation. *J. Phys. Chem. A* **2008**, *112* (46), 11688-11698.
57. Buchbinder, A. M.; Weitz, E.; Geiger, F. M., Pentane, Hexane, Cyclopentane, Cyclohexane, 1-Hexene, 1-Pentene, cis-2-Pentene, Cyclohexene, and Cyclopentene at Vapor/ $\alpha$ -Alumina and Liquid/ $\alpha$ -Alumina Interfaces Studied by Broadband Sum Frequency Generation. *J. Phys. Chem. C* **2010**, *114* (1), 554-566.
58. Doğangün, M.; Ohno, P. E.; Liang, D.; McGeachy, A. C.; Bé, A. G.; Dalchand, N.; Li, T.; Cui, Q.; Geiger, F. M., Hydrogen-Bond Networks near Supported Lipid Bilayers from Vibrational Sum Frequency Generation Experiments and Atomistic Simulations. *J. Phys. Chem. B* **2018**, *122* (18), 4870-4879.
59. Adhikari, N. M.; Premadasa, U. I.; Cimat, K. L. A., Sum frequency generation vibrational spectroscopy of methacrylate-based functional monomers at the hydrophilic solid-liquid interface. *Phys. Chem. Chem. Phys.* **2017**, *19* (32), 21818-21828.
60. Levitas, V. I.; Samani, K., Size and mechanics effects in surface-induced melting of nanoparticles. *Nature Commun.* **2011**, *2*, 284.
61. Makkonen, L., Surface Melting of Ice. *J. Phys. Chem. B* **1997**, *101* (32), 6196-6200.
62. Zhang, Z.; Guo, Y.; Lu, Z.; Velarde, L.; Wang, H.-f., Resolving Two Closely Overlapping -CN Vibrations and Structure in the Langmuir Monolayer of the Long-Chain Nonadecanenitrile by Polarization Sum Frequency Generation Vibrational Spectroscopy. *J. Phys. Chem. C* **2012**, *116* (4), 2976-2987.
63. Martinez, I. S.; Peterson, M. D.; Ebben, C. J.; Hayes, P. L.; Artaxo, P.; Martin, S. T.; Geiger, F. M., On molecular chirality within naturally occurring secondary organic

- aerosol particles from the central Amazon basin. *Phys. Chem. Chem. Phys.* **2011**, *13*, 12114-12122.
64. Ebben, C. J.; Zorn, S. R.; Lee, S.-B.; Artaxo, P.; Martin, S. T.; Geiger, F. M., Stereochemical Transfer to Atmospheric Aerosol Particles Accompanying the Oxidation of Biogenic Volatile Organic Compound. *Geophys. Res. Lett.* **2011**, *38*, L16807.
65. Wang, H.-F., Sum frequency generation vibrational spectroscopy (SFG-VS) for complex molecular surfaces and interfaces: Spectral lineshape measurement and analysis plus some controversial issues. *Prog. Surf. Sci.* **2016**, *91*, 155-182.
66. Fu, L.; Chen, S.-L.; Gan, W.; Wang, H.-F., Cross-propagation sum-frequency generation vibrational spectroscopy. *Chin. J. Chem. Phys.* **2016**, *29*, 70.
67. Chen, S.-L.; Fu, L.; Gan, W.; Wang, H.-F., Homogeneous and inhomogeneous broadenings and the Voigt line shapes in the phase-resolved and intensity sum-frequency generation vibrational spectroscopy. *J. Chem. Phys.* **2016**, *144*, 034704.
68. Mathi, P.; Jagatap, B. N.; Mondal, J. A., Heterodyne-Detected Sum Frequency Generation Study of Adsorption of I<sup>-</sup> at Model Paint–Water Interface and Its Relevance to Post-Nuclear Accident Scenario. *J. Phys. Chem. C* **2017**, *121* (14), 7993-8001.
69. Shen, Y. R., Phase-Sensitive Sum Frequency Spectroscopy. *Annu. Rev. Phys. Chem.* **2013**, *64*, 129-150.
70. Nihonyanagi, S.; Mondal, J. A.; Yamaguchi, S.; Tahara, T., Structure and Dynamics of Interfacial Water Structure Studied by Heterodyne-Detected Vibrational-Sum Frequency Generation. *Annu. Rev. Phys. Chem.* **2013**, *64*, 579-603.
71. Chase, H. M.; Chen, S.; Fu, L.; Upshur, M. A.; Rudshiteyn, B.; Thomson, R. J.; Wang, H.-F.; Batista, V. S.; Geiger, F. M., Orientations of nonlocal vibrational modes from combined experimental and theoretical sum frequency spectroscopy. *Chem. Phys. Lett.* **2017**, *683*, 199-204.
72. Chase, H. M.; Rudshiteyn, B.; Psciuk, B. T.; Upshur, M. A.; Strick, B. F.; Thomson, R. J.; Batista, V. S.; Geiger, F. M., Assessment of DFT for Computing Sum Frequency Generation Spectra of an Epoxydiol and a Deuterated Isotopologue at Fused Silica/Vapor Interfaces. *J. Phys. Chem. B* **2016**, *120*, 1919-1927.
73. Becke, A. D., Density - Functional Thermochemistry. III. The Role of Exact Exchange. *J. Chem. Phys.* **1993**, *98* (7), 5648-5652.
74. Lee, C.; Yang, W.; Parr, R. G., Development of the Colle-Salvetti Correlation-Energy Formula into a Functional of the Electron Density. *Phys. Rev. B* **1988**, *37* (2), 785.

75. Stephens, P.; Devlin, F.; Chabalowski, C.; Frisch, M. J., *Ab initio* Calculation of Vibrational Absorption and Circular Dichroism Spectra Using Density Functional Force Fields. *J. Phys. Chem.* **1994**, *98* (45), 11623-11627.
76. Ditchfield, R.; Hehre, W. J.; Pople, J. A., Self - Consistent Molecular - Orbital Methods. IX. An Extended Gaussian - Type Basis for Molecular - Orbital Studies of Organic Molecules. *J. Chem. Phys.* **1971**, *54* (2), 724-728.
77. Frisch, M. J.; Trucks, G. W.; Schlegel, H. B.; Scuseria, G. E.; Robb, M. A.; Cheeseman, J. R.; Scalmani, G.; Barone, V.; Mennucci, B.; Petersson, G. A.; Nakatsuji, H.; Caricato, M.; Li, X.; Hratchian, H. P.; Izmaylov, A. F.; Bloino, J.; Zheng, G.; Sonnenberg, J. L.; Hada, M.; Ehara, M.; Toyota, K.; Fukuda, R.; Hasegawa, J.; Ishida, M.; Nakajima, T.; Honda, Y.; Kitao, O.; Nakai, H.; Vreven, T.; Montgomery, J. A., Jr.; Peralta, J. E.; Ogliaro, F.; Bearpark, M.; Heyd, J. J.; Brothers, E.; Kudin, K. N.; Staroverov, V. N.; Keith, T.; Kobayashi, R.; Normand, J.; Raghavachari, K.; Rendell, A.; Burant, J. C.; Iyengar, S. S.; Tomasi, J.; Cossi, M.; Rega, N.; Millam, J. M.; Klene, M.; Knox, J. E.; Cross, J. B.; Bakken, V.; Adamo, C.; Jaramillo, J.; Gomperts, R.; Stratmann, R. E.; Yazyev, O.; Austin, A. J.; Cammi, R.; Pomelli, C.; Ochterski, J. W.; Martin, R. L.; Morokuma, K.; Zakrzewski, V. G.; Voth, G. A.; Salvador, P.; Dannenberg, J. J.; Dapprich, S.; Daniels, A. D.; Farkas, O.; Foresman, J. B.; Ortiz, J. V.; Cioslowski, J.; Fox, D. J. *Gaussian 09*, rev. C.01; Gaussian Inc.: Wallingford, CT, 2010.
78. Ho, J.; Psciuk, B. T.; Chase, H. M.; Rudshteyn, B.; Upshur, M. A.; Fu, L.; Thomson, R. J.; Wang, H.-F.; Geiger, F. M.; Batista, V. S., Sum Frequency Generation Spectroscopy and Molecular Dynamics Simulations Reveal a Rotationally Fluid Adsorption State of  $\alpha$ -Pinene on Silica. *J. Phys. Chem. C* **2016**, *120*, 12578-12589.
79. Chase, H. M.; Ho, J.; Upshur, M. A.; Thomson, R. J.; Batista, V. S.; Geiger, F. M., Unanticipated Stickiness of  $\alpha$ -Pinene. *J. Phys. Chem. A* **2017**, *121* (17), 3239-3246.
80. Li, Y. J.; Chen, Q.; Guzman, M. I.; Chan, C. K.; Martin, S. T., Second-generation products contribute substantially to the particle-phase organic material produced by  $\beta$ -caryophyllene ozonolysis. *Atmos. Chem. Phys.* **2011**, *11* (1), 121-132.
81. Cui, T.; Zeng, Z.; dos Santos, E. O.; Zhang, Z.; Chen, Y.; Zhang, Y.; Rose, C. A.; Budisulistiorini, S. H.; Collins, L. B.; Bodnar, W. M.; de Souza, R. A. F.; Martin, S. T.; Machado, C. M. D.; Turpin, B. J.; Gold, A.; Ault, A. P.; Surratt, J. D., Development of a hydrophilic interaction liquid chromatography (HILIC) method for the chemical characterization of water-soluble isoprene epoxydiol (IEPOX)-derived secondary organic aerosol. *Environ. Sci.: Process. Impacts* **2018**, *20* (11), 1524-1536.
82. Ehn, M.; Thornton, J. A.; Kleist, E.; Sipila, M.; Junninen, H.; Pullinen, I.; Springer, M.; Rubach, F.; Tillmann, R.; Lee, B.; Lopez-Hilfiker, F.; Andres, S.; Acir, I.-H.; Rissanen, M.; Jokinen, T.; Schobesberger, S.; Kangasluoma, J.; Kontkanen, J.; Nieminen, T.; Kurten, T.; Nielsen, L. B.; Jorgensen, S.; Kjaergaard, H. G.; Canagaratna, M.; Maso, M. D.; Berndt, T.; Petaja, T.; Wahner, A.; Kerminen, V.-M.; Kulmala, M.; Worsnop, D. R.;

- Wildt, J.; Mentel, T. F., A large source of low-volatility secondary organic aerosol. *Nature* **2014**, *506* (7489), 476-479.
83. Zhang, X.; McVay, R. C.; Huang, D. D.; Dalleska, N. F.; Aumont, B.; Flagan, R. C.; Seinfeld, J. H., Formation and evolution of molecular products in  $\alpha$ -pinene secondary organic aerosol. *Proc. Natl. Acad. Sci.* **2015**, *112* (46), 14168-14173.
84. Zhang, X.; Lambe, A. T.; Upshur, M. A.; Brooks, W. A.; Gray Bé, A.; Thomson, R. J.; Geiger, F. M.; Surratt, J. D.; Zhang, Z.; Gold, A.; Graf, S.; Cubison, M. J.; Groessl, M.; Jayne, J. T.; Worsnop, D. R.; Canagaratna, M. R., Highly Oxygenated Multifunctional Compounds in  $\alpha$ -Pinene Secondary Organic Aerosol. *Environ. Sci. Technol.* **2017**, *51* (11), 5932-5940.
85. Richters, S.; Herrmann, H.; Berndt, T., Highly Oxidized RO<sub>2</sub> Radicals and Consecutive Products from the Ozonolysis of Three Sesquiterpenes. *Environ. Sci. Technol.* **2016**, *50* (5), 2354-2362.
86. Docherty, K. S.; Wu, W.; Lim, Y. B.; Ziemann, P. J., Contributions of Organic Peroxides to Secondary Aerosol Formed from Reactions of Monoterpenes with O<sub>3</sub>. *Environ. Sci. Technol.* **2005**, *39* (11), 4049-4059.
87. Krapf, M.; El Haddad, I.; Bruns, Emily A.; Molteni, U.; Daellenbach, Kaspar R.; Prévôt, André S. H.; Baltensperger, U.; Dommen, J., Labile Peroxides in Secondary Organic Aerosol. *Chem* **2016**, *1* (4), 603-616.
88. Li, H.; Chen, Z.; Huang, L.; Huang, D., Organic peroxides' gas-particle partitioning and rapid heterogeneous decomposition on secondary organic aerosol. *Atmos. Chem. Phys.* **2016**, *16* (3), 1837-1848.
89. Pagonis, D.; Ziemann, P. J., Chemistry of hydroperoxycarbonyls in secondary organic aerosol. *Aerosol Sci. Technol.* **2018**, *52* (10), 1178-1193.
90. Li, Y. J.; Liu, P.; Gong, Z.; Wang, Y.; Bateman, A. P.; Bergoend, C.; Bertram, A. K.; Martin, S. T., Chemical Reactivity and Liquid/Nonliquid States of Secondary Organic Material. *Environ. Sci. Technol.* **2015**, *49* (22), 13264-13274.

**Chapter 4 references.**

1. Donaldson, D. J.; Valsaraj, K. T., Adsorption and Reaction of Trace Gas-Phase Organic Compounds on Atmospheric Water Film Surfaces: A Critical Review. *Environ. Sci. Technol.* **2010**, *44* (3), 865-873.
2. Hallquist, M.; Wenger, J. C.; Baltensperger, U.; Rudich, Y.; Simpson, D.; Claeys, M.; Dommen, J.; Donahue, N. M.; George, C.; Goldstein, A. H.; Hamilton, J. F.; Herrmann, H.; Hoffmann, T.; Iinuma, Y.; Jang, M.; Jenkin, M. E.; Jimenez, J. L.; Kiendler-Scharr, A.; Maenhaut, W.; McFiggans, G.; Mentel, T. F.; Monod, A.; Prévôt, A. S. H.; Seinfeld, J. H.; Surratt, J. D.; Szmigielski, R.; Wildt, J., The formation, properties and impact of secondary organic aerosol: current and emerging issues. *Atmos. Chem. Phys.* **2009**, *9* (14), 5155-5236.
3. Reid, J. P.; Bertram, A. K.; Topping, D. O.; Laskin, A.; Martin, S. T.; Petters, M. D.; Pope, F. D.; Rovelli, G., The viscosity of atmospherically relevant organic particles. *Nature Commun.* **2018**, *9* (1), 956.
4. Shrestha, M.; Zhang, Y.; Upshur, M. A.; Liu, P.; Blair, S. L.; Wang, H.-f.; Nizkorodov, S. A.; Thomson, R. J.; Martin, S. T.; Geiger, F. M., On Surface Order and Disorder of  $\alpha$ -Pinene-Derived Secondary Organic Material. *J. Phys. Chem. A* **2015**, *119* (19), 4609-4617.
5. Li, Y. J.; Liu, P.; Gong, Z.; Wang, Y.; Bateman, A. P.; Bergoend, C.; Bertram, A. K.; Martin, S. T., Chemical Reactivity and Liquid/Nonliquid States of Secondary Organic Material. *Environ. Sci. Technol.* **2015**, *49* (22), 13264-13274.
6. Liu, P.; Song, M.; Zhao, T.; Gunthe, S. S.; Ham, S.; He, Y.; Qin, Y. M.; Gong, Z.; Amorim, J. C.; Bertram, A. K.; Martin, S. T., Resolving the mechanisms of hygroscopic growth and cloud condensation nuclei activity for organic particulate matter. *Nature Commun.* **2018**, *9* (1), 4076.
7. Abramson, E.; Imre, D.; Beranek, J.; Wilson, J.; Zelenyuk, A., Experimental determination of chemical diffusion within secondary organic aerosol particles. *Phys. Chem. Chem. Phys.* **2013**, *15* (8), 2983-2991.
8. Chu, Y.; Cheng, T. F.; Gen, M.; Chan, C. K.; Lee, A. K. Y.; Chan, M. N., Effect of Ozone Concentration and Relative Humidity on the Heterogeneous Oxidation of Linoleic Acid Particles by Ozone: An Insight into the Interchangeability of Ozone Concentration and Time. *ACS Earth Space Chem.* **2019**, *3* (5), 779-788.
9. Li, H.; Chen, Z.; Huang, L.; Huang, D., Organic peroxides' gas-particle partitioning and rapid heterogeneous decomposition on secondary organic aerosol. *Atmos. Chem. Phys.* **2016**, *16* (3), 1837-1848.

10. O'Brien, R. E.; Wang, B.; Kelly, S. T.; Lundt, N.; You, Y.; Bertram, A. K.; Leone, S. R.; Laskin, A.; Gilles, M. K., Liquid-Liquid Phase Separation in Aerosol Particles: Imaging at the Nanometer Scale. *Environ. Sci. Technol.* **2015**, *49* (8), 4995-5002.
11. Renbaum-Wolff, L.; Song, M.; Marcolli, C.; Zhang, Y.; Liu, P. F.; Grayson, J. W.; Geiger, F. M.; Martin, S. T.; Bertram, A. K., Observations and implications of liquid-liquid phase separation at high relative humidities in secondary organic material produced by  $\alpha$ -pinene ozonolysis without inorganic salts. *Atmos. Chem. Phys.* **2016**, *16* (12), 7969-7979.
12. Song, M.; Liu, P.; Martin, S. T.; Bertram, A. K., Liquid-liquid phase separation in particles containing secondary organic material free of inorganic salts. *Atmos. Chem. Phys.* **2017**, *17* (18), 11261-11271.
13. Zuend, A.; Seinfeld, J. H., Modeling the gas-particle partitioning of secondary organic aerosol: the importance of liquid-liquid phase separation. *Atmos. Chem. Phys.* **2012**, *12* (9), 3857-3882.
14. Qiu, Y.; Molinero, V., Morphology of Liquid-Liquid Phase Separated Aerosols. *J. Am. Chem. Soc.* **2015**, *137* (33), 10642-10651.
15. Ruehl, C. R.; Davies, J. F.; Wilson, K. R., An interfacial mechanism for cloud droplet formation on organic aerosols. *Science* **2016**, *351* (6280), 1447-1450.
16. Tang, X.; Cocker III, D. R.; Asa-Awuku, A., Are sesquiterpenes a good source of secondary organic cloud condensation nuclei (CCN)? Revisiting  $\beta$ -caryophyllene CCN. *Atmos. Chem. Phys.* **2012**, *12* (18), 8377-8388.
17. Bé, A. G.; Upshur, M. A.; Liu, P.; Martin, S. T.; Geiger, F. M.; Thomson, R. J., Cloud Activation Potentials for Atmospheric  $\alpha$ -Pinene and  $\beta$ -Caryophyllene Ozonolysis Products. *ACS Cent. Sci.* **2017**, *3* (7), 715-725.
18. Nozière, B.; Kalberer, M.; Claeys, M.; Allan, J.; D'Anna, B.; Decesari, S.; Finessi, E.; Glasius, M.; Grgić, I.; Hamilton, J. F.; Hoffmann, T.; Iinuma, Y.; Jaoui, M.; Kahnt, A.; Kampf, C. J.; Kourtchev, I.; Maenhaut, W.; Marsden, N.; Saarikoski, S.; Schnelle-Kreis, J.; Surratt, J. D.; Szidat, S.; Szmigielski, R.; Wisthaler, A., The Molecular Identification of Organic Compounds in the Atmosphere: State of the Art and Challenges. *Chem. Rev.* **2015**, *115* (10), 3919-3983.
19. Gérard, V.; Nozière, B.; Baduel, C.; Fine, L.; Frossard, A. A.; Cohen, R. C., Anionic, Cationic, and Nonionic Surfactants in Atmospheric Aerosols from the Baltic Coast at Askö, Sweden: Implications for Cloud Droplet Activation. *Environ. Sci. Technol.* **2016**, *50* (6), 2974-2982.
20. Sareen, N.; Schwier, A. N.; Lathem, T. L.; Nenes, A.; McNeill, V. F., Surfactants from the gas phase may promote cloud droplet formation. *Proc. Natl. Acad. Sci.* **2013**, *110* (8), 2723-2728.

21. Riipinen, I.; Rastak, N.; Pandis, S. N., Connecting the solubility and CCN activation of complex organic aerosols: a theoretical study using solubility distributions. *Atmos. Chem. Phys.* **2015**, *15* (11), 6305-6322.
22. McNeill, V. F.; Sareen, N.; Schwier, A. N., Surface-Active Organics in Atmospheric Aerosols. In *Atmospheric and Aerosol Chemistry*, McNeill, F. V.; Ariya, A. P., Eds. Springer Berlin Heidelberg: Berlin, Heidelberg, 2014; pp 201-259.
23. Bzdek, B. R.; Power, R. M.; Simpson, S. H.; Reid, J. P.; Royall, C. P., Precise, contactless measurements of the surface tension of picolitre aerosol droplets. *Chem. Sci.* **2016**, *7* (1), 274-285.
24. Boyer, H. C.; Dutcher, C. S., Atmospheric Aqueous Aerosol Surface Tensions: Isotherm-Based Modeling and Biphasic Microfluidic Measurements. *J. Phys. Chem. A* **2017**, *121* (25), 4733-4742.
25. Wingen, L. M.; Finlayson-Pitts, B. J., Probing surfaces of atmospherically relevant organic particles by easy ambient sonic-spray ionization mass spectrometry (EASI-MS). *Chem. Sci.* **2019**, *10* (3), 884-897.
26. Burrows, S. M.; Gobrogge, E.; Fu, L.; Link, K.; Elliott, S. M.; Wang, H.; Walker, R., OCEANFILMS-2: Representing coadsorption of saccharides in marine films and potential impacts on modeled marine aerosol chemistry. *Geophys. Res. Lett.* **2016**, *43* (15), 8306-8313.
27. Link, K. A.; Spurzem, G. N.; Tuladhar, A.; Chase, Z.; Wang, Z.; Wang, H.; Walker, R. A., Organic Enrichment at Aqueous Interfaces: Cooperative Adsorption of Glucuronic Acid to DPPC Monolayers Studied with Vibrational Sum Frequency Generation. *J. Phys. Chem. A* **2019**, *123* (26), 5621-5632.
28. Schill, R. S.; Burrows, M. S.; Hasencz, S. E.; Stone, A. E.; Bertram, H. T., The Impact of Divalent Cations on the Enrichment of Soluble Saccharides in Primary Sea Spray Aerosol. *Atmosphere* **2018**, *9* (12), 476.
29. Morris, H. S.; Grassian, V. H.; Tivanski, A. V., Humidity-dependent surface tension measurements of individual inorganic and organic submicrometre liquid particles. *Chem. Sci.* **2015**, *6* (5), 3242-3247.
30. Henning, S.; Rosenørn, T.; D'Anna, B.; Gola, A. A.; Svenningsson, B.; Bilde, M., Cloud droplet activation and surface tension of mixtures of slightly soluble organics and inorganic salt. *Atmos. Chem. Phys.* **2005**, *5* (2), 575-582.
31. Tuckermann, R.; Cammenga, H. K., The surface tension of aqueous solutions of some atmospheric water-soluble organic compounds. *Atmos. Environ.* **2004**, *38* (36), 6135-6138.

32. Shulman, M. L.; Jacobson, M. C.; Carlson, R. J.; Synovec, R. E.; Young, T. E., Dissolution behavior and surface tension effects of organic compounds in nucleating cloud droplets. *Geophys. Res. Lett.* **1996**, *23* (3), 277-280.
33. Sareen, N.; Schwier, A. N.; Shapiro, E. L.; Mitroo, D.; McNeill, V. F., Secondary organic material formed by methylglyoxal in aqueous aerosol mimics. *Atmos. Chem. Phys.* **2010**, *10* (3), 997-1016.
34. Upshur, M. A.; Strick, B. F.; McNeill, V. F.; Thomson, R. J.; Geiger, F. M., Climate-relevant physical properties of molecular constituents for isoprene-derived secondary organic aerosol material. *Atmos. Chem. Phys.* **2014**, *14* (19), 10731-10740.
35. Facchini, M. C.; Decesari, S.; Mircea, M.; Fuzzi, S.; Loglio, G., Surface tension of atmospheric wet aerosol and cloud/fog droplets in relation to their organic carbon content and chemical composition. *Atmos. Environ.* **2000**, *34* (28), 4853-4857.
36. Nozière, B.; Baduel, C.; Jaffrezo, J.-L., The dynamic surface tension of atmospheric aerosol surfactants reveals new aspects of cloud activation. *Nature Commun.* **2014**, *5*, 3335.
37. Kiss, G.; Tombácz, E.; Hansson, H.-C., Surface Tension Effects of Humic-Like Substances in the Aqueous Extract of Tropospheric Fine Aerosol. *J. Atmos. Chem.* **2005**, *50* (3), 279-294.
38. Reddy, S. K.; Thiriaux, R.; Wellen Rudd, B. A.; Lin, L.; Adel, T.; Joutsuka, T.; Geiger, F. M.; Allen, H. C.; Morita, A.; Paesani, F., Bulk Contributions Modulate the Sum-Frequency Generation Spectra of Water on Model Sea-Spray Aerosols. *Chem* **2018**, *4* (7), 1629-1644.
39. Link, K. A.; Hsieh, C.-Y.; Tuladhar, A.; Chase, Z.; Wang, Z.; Wang, H.; Walker, R. A., Vibrational studies of saccharide-induced lipid film reorganization at aqueous/air interfaces. *Chem. Phys.* **2018**, *512*, 104-110.
40. Kleber, J.; Laß, K.; Friedrichs, G., Quantitative Time-Resolved Vibrational Sum Frequency Generation Spectroscopy as a Tool for Thin Film Kinetic Studies: New Insights into Oleic Acid Monolayer Oxidation. *J. Phys. Chem. A* **2013**, *117* (33), 7863-7875.
41. Voss, L. F.; Hadad, C. M.; Allen, H. C., Competition between Atmospherically Relevant Fatty Acid Monolayers at the Air/Water Interface. *J. Phys. Chem. B* **2006**, *110* (39), 19487-19490.
42. Bé, A. G.; Chase, H. M.; Liu, Y.; Upshur, M. A.; Zhang, Y.; Tuladhar, A.; Chase, Z. A.; Bellcross, A. D.; Wang, H.-F.; Wang, Z.; Batista, V. S.; Martin, S. T.; Thomson, R. J.; Geiger, F. M., Atmospheric  $\beta$ -Caryophyllene-Derived Ozonolysis Products at Interfaces. *ACS Earth Space Chem.* **2019**, *3* (2), 158-169.

43. Fu, L.; Chen, S.-L.; Wang, H.-F., Validation of Spectra and Phase in Sub-1  $\text{cm}^{-1}$  Resolution Sum-Frequency Generation Vibrational Spectroscopy through Internal Heterodyne Phase-Resolved Measurement. *J. Phys. Chem. B* **2016**, *120* (8), 1579-1589.
44. Tuladhar, A.; Chase, Z. A.; Baer, M. D.; Legg, B. A.; Tao, J.; Zhang, S.; Winkelman, A. D.; Wang, Z.; Mundy, C. J.; De Yoreo, J. J.; Wang, H.-f., Direct Observation of the Orientational Anisotropy of Buried Hydroxyl Groups inside Muscovite Mica. *J. Am. Chem. Soc.* **2019**, *141* (5), 2135-2142.
45. Velarde, L.; Zhang, X.-y.; Lu, Z.; Joly, A. G.; Wang, Z.; Wang, H.-f., Communication: Spectroscopic phase and lineshapes in high-resolution broadband sum frequency vibrational spectroscopy: Resolving interfacial inhomogeneities of “identical” molecular groups. *J. Chem. Phys.* **2011**, *135* (24), 241102.
46. Wang, H.-F.; Velarde, L.; Gan, W.; Fu, L., Quantitative Sum-Frequency Generation Vibrational Spectroscopy of Molecular Surfaces and Interfaces: Lineshape, Polarization, and Orientation. *Annu. Rev. Phys. Chem.* **2015**, *66* (1), 189-216.
47. Nihonyanagi, S.; Yamaguchi, S.; Tahara, T., Direct evidence for orientational flip-flop of water molecules at charged interfaces: a heterodyne-detected vibrational sum frequency generation study. *J. Chem. Phys.* **2009**, *130* (20), 204704.
48. Yamaguchi, S., Development of single-channel heterodyne-detected sum frequency generation spectroscopy and its application to the water/vapor interface. *J. Chem. Phys.* **2015**, *143* (3), 034202.
49. Esenturk, O.; Walker, R. A., Surface vibrational structure at alkane liquid/vapor interfaces. *J. Chem. Phys.* **2006**, *125*, 174701.
50. Esenturk, O.; Walker, R. A., Surface Structure at Hexadecane and Halo-hexadecane Liquid/Vapor Interfaces. *J. Phys. Chem. B* **2004**, *108* (30), 10631-10635.
51. Surratt, J. D.; Murphy, S. M.; Kroll, J. H.; Ng, N. L.; Hildebrandt, L.; Sorooshian, A.; Szmigielski, R.; Vermeylen, R.; Maenhaut, W.; Claeys, M.; Flagan, R. C.; Seinfeld, J. H., Chemical Composition of Secondary Organic Aerosol Formed from the Photooxidation of Isoprene. *J. Phys. Chem. A* **2006**, *110* (31), 9665-9690.
52. Zhang, Z.; Zheng, D.-s.; Guo, Y.; Wang, H.-f., Water penetration/accommodation and phase behaviour of the neutral langmuir monolayer at the air/water interface probed with sum frequency generation vibrational spectroscopy (SFG-VS). *Phys. Chem. Chem. Phys.* **2009**, *11* (6), 991-1002.
53. Chase, H. M.; Psciuk, B. T.; Strick, B. L.; Thomson, R. J.; Batista, V. S.; Geiger, F. M., Beyond Local Group Modes in Vibrational Sum Frequency Generation. *J. Phys. Chem. A* **2015**, *119* (14), 3407-3414.

54. Dalchand, N.; Doğangün, M.; Ohno, P. E.; Ma, E.; Martinson, A. B. F.; Geiger, F. M., Perturbation of Hydrogen-Bonding Networks over Supported Lipid Bilayers by Poly(allylamine hydrochloride). *J. Phys. Chem. B* **2019**, *123* (19), 4251-4257.
55. Doğangün, M.; Ohno, P. E.; Liang, D.; McGeachy, A. C.; Bé, A. G.; Dalchand, N.; Li, T.; Cui, Q.; Geiger, F. M., Hydrogen-Bond Networks near Supported Lipid Bilayers from Vibrational Sum Frequency Generation Experiments and Atomistic Simulations. *J. Phys. Chem. B* **2018**, *122* (18), 4870-4879.
56. Ohno, P. E.; Wang, H.-f.; Paesani, F.; Skinner, J. L.; Geiger, F. M., Second-Order Vibrational Lineshapes from the Air/Water Interface. *J. Phys. Chem. A* **2018**, *122* (18), 4457-4464.
57. Gonella, G.; Lütgebaucks, C.; de Beer, A. G. F.; Roke, S., Second Harmonic and Sum-Frequency Generation from Aqueous Interfaces Is Modulated by Interference. *J. Phys. Chem. C* **2016**, *120* (17), 9165-9173.
58. Ohno, P. E.; Saslow, S. A.; Wang, H.-f.; Geiger, F. M.; Eienthal, K. B., Phase-referenced nonlinear spectroscopy of the  $\alpha$ -quartz/water interface. *Nat. Commun.* **2016**, *7*, 13587.
59. Ohno, P. E.; Wang, H.-f.; Geiger, F. M., Second-order spectral lineshapes from charged interfaces. *Nat. Commun.* **2017**, *8* (1), 1032.
60. Du, Q.; Superfine, R.; Freysz, E.; Shen, Y. R., Vibrational spectroscopy of water at the vapor/water interface. *Phys. Rev. Lett.* **1993**, *70* (15), 2313-2316.
61. Brown, M. G.; Raymond, E. A.; Allen, H. C.; Scatena, L. F.; Richmond, G. L., The Analysis of Interference Effects in the Sum Frequency Spectra of Water Interfaces. *J. Phys. Chem. A* **2000**, *104* (45), 10220-10226.
62. Morita, A.; Hynes, J. T., A theoretical analysis of the sum frequency generation spectrum of the water surface. *Chem. Phys.* **2000**, *258* (2), 371-390.
63. Richmond, G. L., Molecular Bonding and Interactions at Aqueous Surfaces as Probed by Vibrational Sum Frequency Spectroscopy. *Chem. Rev.* **2002**, *102* (8), 2693-2724.
64. Allen, H. C.; Raymond, E. A.; Richmond, G. L., Non-linear vibrational sum frequency spectroscopy of atmospherically relevant molecules at aqueous solution surfaces. *Curr. Opin. Colloid Interface Sci.* **2000**, *5* (1-2), 74-80.
65. Allen, H. C.; Raymond, E. A.; Richmond, G. L., Surface Structural Studies of Methanesulfonic Acid at Air /Aqueous Solution Interfaces Using Vibrational Sum Frequency Spectroscopy. *J. Phys. Chem. A* **2001**, *105* (9), 1649-1655.
66. Jungwirth, P.; Tobias, D. J., Specific Ion Effects at the Air/Water Interface. *Chem. Rev.* **2006**, *106* (4), 1259-1281.

67. Liu, D.; Ma, G.; Levering, L. M.; Allen, H. C., Vibrational Spectroscopy of Aqueous Sodium Halide Solutions and Air–Liquid Interfaces: Observation of Increased Interfacial Depth. *J. Phys. Chem. B* **2004**, *108* (7), 2252-2260.
68. Shultz, M. J.; Baldelli, S.; Schnitzer, C.; Simonelli, D., Aqueous Solution/Air Interfaces Probed with Sum Frequency Generation Spectroscopy. *J. Phys. Chem. B* **2002**, *106* (21), 5313-5324.
69. Feng, R.-r.; Guo, Y.; Lü, R.; Velarde, L.; Wang, H.-f., Consistency in the Sum Frequency Generation Intensity and Phase Vibrational Spectra of the Air/Neat Water Interface. *J. Phys. Chem. A* **2011**, *115* (23), 6015-6027.
70. Gan, W.; Wu, D.; Zhang, Z.; Feng, R.-r.; Wang, H.-f., Polarization and experimental configuration analyses of sum frequency generation vibrational spectra, structure, and orientational motion of the air/water interface. *J. Chem. Phys.* **2006**, *124* (11), 114705.
71. Wei, X.; Shen, Y. R., Motional Effect in Surface Sum-Frequency Vibrational Spectroscopy. *Phys. Rev. Lett.* **2001**, *86* (21), 4799-4802.
72. Casper, C. B.; Verreault, D.; Adams, E. M.; Hua, W.; Allen, H. C., Surface Potential of DPPC Monolayers on Concentrated Aqueous Salt Solutions. *J. Phys. Chem. B* **2016**, *120* (8), 2043-2052.
73. Boamah, M. D.; Ohno, P. E.; Lozier, E.; Van Ardenne, J.; Geiger, F. M., Specifics about Specific Ion Adsorption from Heterodyne-Detected Second Harmonic Generation. *J. Phys. Chem. B* **2019**, *123* (27), 5848-5856.
74. Ohno, P. E.; Chang, H.; Spencer, A. P.; Liu, Y.; Boamah, M. D.; Wang, H.-f.; Geiger, F. M., Beyond the Gouy–Chapman Model with Heterodyne-Detected Second Harmonic Generation. *J. Phys. Chem. Lett.* **2019**, *10* (10), 2328-2334.
75. Bé, A. G.; Upshur, M. A.; Liu, P.; Martin, S. T.; Geiger, F. M.; Thomson, R. J., Cloud Activation Potentials for Atmospheric  $\alpha$ -Pinene and  $\beta$ -Caryophyllene Ozonolysis Products. *ACS Cent. Sci.* **2017**, *3* (7), 715-725.
76. Ebben, C. J.; Strick, B. F.; Upshur, M. A.; Chase, H. M.; Achtyl, J. L.; Thomson, R. J.; Geiger, F. M., Towards the identification of molecular constituents associated with the surfaces of isoprene-derived secondary organic aerosol (SOA) particles. *Atmos. Chem. Phys.* **2014**, *14* (5), 2303-2314.
77. Conboy, J. C.; Messmer, M. C.; Richmond, G. L., Dependence of Alkyl Chain Conformation of Simple Ionic Surfactants on Head Group Functionality As Studied by Vibrational Sum-Frequency Spectroscopy. *J. Phys. Chem. B* **1997**, *101* (34), 6724-6733.
78. Stokes, G. Y.; Buchbinder, A. M.; Gibbs-Davis, J. M.; Scheidt, K. A.; Geiger, F. M., Chemically diverse environmental interfaces and their reactions with ozone studied by sum frequency generation. *Vib. Spectrosc* **2009**, *50* (1), 86-98.

79. Chase, H. M.; Chen, S.; Fu, L.; Upshur, M. A.; Rudshiteyn, B.; Thomson, R. J.; Wang, H.-F.; Batista, V. S.; Geiger, F. M., Orientations of nonlocal vibrational modes from combined experimental and theoretical sum frequency spectroscopy. *Chem. Phys. Lett.* **2017**, *683*, 199-204.
80. Mathi, P.; Jagatap, B. N.; Mondal, J. A., Heterodyne-Detected Sum Frequency Generation Study of Adsorption of I<sup>-</sup> at Model Paint–Water Interface and Its Relevance to Post-Nuclear Accident Scenario. *J. Phys. Chem. C* **2017**, *121* (14), 7993-8001.
81. Nihonyanagi, S.; Mondal, J. A.; Yamaguchi, S.; Tahara, T., Structure and Dynamics of Interfacial Water Structure Studied by Heterodyne-Detected Vibrational-Sum Frequency Generation. *Annu. Rev. Phys. Chem.* **2013**, *64*, 579-603.
82. Gurau, M. C.; Lim, S.-M.; Castellana, E. T.; Albertorio, F.; Kataoka, S.; Cremer, P. S., On the Mechanism of the Hofmeister Effect. *J. Am. Chem. Soc.* **2004**, *126* (34), 10522-10523.
83. Rembert, K. B.; Paterová, J.; Heyda, J.; Hilty, C.; Jungwirth, P.; Cremer, P. S., Molecular Mechanisms of Ion-Specific Effects on Proteins. *J. Am. Chem. Soc.* **2012**, *134* (24), 10039-10046.
84. Scheu, R.; Chen, Y.; de Aguiar, H. B.; Rankin, B. M.; Ben-Amotz, D.; Roke, S., Specific Ion Effects in Amphiphile Hydration and Interface Stabilization. *J. Am. Chem. Soc.* **2014**, *136* (5), 2040-2047.

**Chapter 5 references.**

1. Kroll, J. H.; Seinfeld, J. H., Chemistry of secondary organic aerosol: Formation and evolution of low-volatility organics in the atmosphere. *Atmos. Environ.* **2008**, *42* (16), 3593-3624.
2. Nozière, B.; Kalberer, M.; Claeys, M.; Allan, J.; D'Anna, B.; Decesari, S.; Finessi, E.; Glasius, M.; Grgić, I.; Hamilton, J. F.; Hoffmann, T.; Iinuma, Y.; Jaoui, M.; Kahnt, A.; Kampf, C. J.; Kourtchev, I.; Maenhaut, W.; Marsden, N.; Saarikoski, S.; Schnelle-Kreis, J.; Surratt, J. D.; Szidat, S.; Szmigielski, R.; Wisthaler, A., The Molecular Identification of Organic Compounds in the Atmosphere: State of the Art and Challenges. *Chem. Rev.* **2015**, *115* (10), 3919-3983.
3. Holopainen, J. K.; Kivimäenpää, M.; Nizkorodov, S. A., Plant-derived Secondary Organic Material in the Air and Ecosystems. *Trends Plant Sci.* **2017**, *22* (9), 744-753.
4. Ault, A. P.; Axson, J. L., Atmospheric Aerosol Chemistry: Spectroscopic and Microscopic Advances. *Anal. Chem.* **2017**, *89* (1), 430-452.
5. Chen, Q.; Liu, Y.; Donahue, N. M.; Shilling, J. E.; Martin, S. T., Particle-Phase Chemistry of Secondary Organic Material: Modeled Compared to Measured O:C and H:C Elemental Ratios Provide Constraints. *Environ. Sci. Technol.* **2011**, *45* (11), 4763-4770.
6. Gao, Y.; Hall, W. A.; Johnston, M. V., Molecular Composition of Monoterpene Secondary Organic Aerosol at Low Mass Loading. *Environ. Sci. Technol.* **2010**, *44* (20), 7897-7902.
7. Liu, P.; Song, M.; Zhao, T.; Gunthe, S. S.; Ham, S.; He, Y.; Qin, Y. M.; Gong, Z.; Amorim, J. C.; Bertram, A. K.; Martin, S. T., Resolving the mechanisms of hygroscopic growth and cloud condensation nuclei activity for organic particulate matter. *Nature Commun.* **2018**, *9* (1), 4076.
8. Song, M.; Liu, P.; Martin, S. T.; Bertram, A. K., Liquid-liquid phase separation in particles containing secondary organic material free of inorganic salts. *Atmos. Chem. Phys.* **2017**, *17* (18), 11261-11271.
9. Canagaratna, M. R.; Jimenez, J. L.; Kroll, J. H.; Chen, Q.; Kessler, S. H.; Massoli, P.; Hildebrandt Ruiz, L.; Fortner, E.; Williams, L. R.; Wilson, K. R.; Surratt, J. D.; Donahue, N. M.; Jayne, J. T.; Worsnop, D. R., Elemental ratio measurements of organic compounds using aerosol mass spectrometry: characterization, improved calibration, and implications. *Atmos. Chem. Phys.* **2015**, *15* (1), 253-272.
10. Chan, M. N.; Surratt, J. D.; Chan, A. W. H.; Schilling, K.; Offenberg, J. H.; Lewandowski, M.; Edney, E. O.; Kleindienst, T. E.; Jaoui, M.; Edgerton, E. S.; Tanner, R. L.; Shaw, S. L.; Zheng, M.; Knipping, E. M.; Seinfeld, J. H., Influence of aerosol acidity

- on the chemical composition of secondary organic aerosol from  $\beta$ -caryophyllene. *Atmos. Chem. Phys.* **2011**, *11* (4), 1735-1751.
11. Wang, Y.; Ma, Y.; Li, X.; Kuang, B. Y.; Huang, C.; Tong, R.; Yu, J. Z., Monoterpene and Sesquiterpene  $\alpha$ -Hydroxy Organosulfates: Synthesis, MS/MS Characteristics, and Ambient Presence. *Environ. Sci. Technol.* **2019**, *53* (21), 12278-12290.
  12. van Eijck, A.; Opatz, T.; Taraborrelli, D.; Sander, R.; Hoffmann, T., New tracer compounds for secondary organic aerosol formation from  $\beta$ -caryophyllene oxidation. *Atmos. Environ.* **2013**, *80*, 122-130.
  13. Chan, M. N.; Surratt, J. D.; Chan, A. W. H.; Schilling, K.; Offenberg, J. H.; Lewandowski, M.; Edney, E. O.; Kleindienst, T. E.; Jaoui, M.; Edgerton, E. S.; Tanner, R. L.; Shaw, S. L.; Zheng, M.; Knipping, E. M.; Seinfeld, J. H., Influence of aerosol acidity on the chemical composition of secondary organic aerosol from  $\beta$ -caryophyllene. *Atmos. Chem. Phys.* **2011**, *11* (4), 1735-1751.
  14. Zuend, A.; Seinfeld, J. H., Modeling the gas-particle partitioning of secondary organic aerosol: the importance of liquid-liquid phase separation. *Atmos. Chem. Phys.* **2012**, *12* (9), 3857-3882.
  15. Freedman, M. A., Phase separation in organic aerosol. *Chem. Soc. Rev.* **2017**, *46* (24), 7694-7705.
  16. O'Brien, R. E.; Wang, B.; Kelly, S. T.; Lundt, N.; You, Y.; Bertram, A. K.; Leone, S. R.; Laskin, A.; Gilles, M. K., Liquid-Liquid Phase Separation in Aerosol Particles: Imaging at the Nanometer Scale. *Environ. Sci. Technol.* **2015**, *49* (8), 4995-5002.
  17. Ebben, C. J.; Martinez, I. S.; Shrestha, M.; Buchbinder, A. M.; Corrigan, A. L.; Guenther, A.; Karl, T.; Petäjä, T.; Song, W. W.; Zorn, S. R.; Artaxo, P.; Kulmala, M.; Martin, S. T.; Russell, L. M.; Williams, J.; Geiger, F. M., Contrasting organic aerosol particles from boreal and tropical forests during HUMPPA-COPEC-2010 and AMAZE-08 using coherent vibrational spectroscopy. *Atmos. Chem. Phys.* **2011**, *11* (20), 10317-10329.
  18. Shrestha, M.; Zhang, Y.; Upshur, M. A.; Liu, P.; Blair, S. L.; Wang, H.-f.; Nizkorodov, S. A.; Thomson, R. J.; Martin, S. T.; Geiger, F. M., On Surface Order and Disorder of  $\alpha$ -Pinene-Derived Secondary Organic Material. *J. Phys. Chem. A* **2015**, *119* (19), 4609-4617.
  19. Stokes, G. Y.; Buchbinder, A. M.; Gibbs-Davis, J. M.; Scheidt, K. A.; Geiger, F. M., Chemically diverse environmental interfaces and their reactions with ozone studied by sum frequency generation. *Vib. Spectrosc* **2009**, *50* (1), 86-98.
  20. Chase, H. M.; Ho, J.; Upshur, M. A.; Thomson, R. J.; Batista, V. S.; Geiger, F. M., Unanticipated Stickiness of  $\alpha$ -Pinene. *J. Phys. Chem. A* **2017**, *121* (17), 3239-3246.

21. Liu, Y.; Chase, H. M.; Geiger, F. M., Partially (resp. fully) reversible adsorption of monoterpenes (resp. alkanes and cycloalkanes) to fused silica. *J. Chem. Phys.* **2019**, *150* (7), 074701.
22. Doğangün, M.; Ohno, P. E.; Liang, D.; McGeachy, A. C.; Bé, A. G.; Dalchand, N.; Li, T.; Cui, Q.; Geiger, F. M., Hydrogen-Bond Networks near Supported Lipid Bilayers from Vibrational Sum Frequency Generation Experiments and Atomistic Simulations. *J. Phys. Chem. B* **2018**, *122* (18), 4870-4879.
23. Bé, A. G.; Liu, Y.; Tuladhar, A.; Bellcross, A. D.; Wang, Z.; Thomson, R. J.; Geiger, F. M., Surface-Active  $\beta$ -Caryophyllene Oxidation Products at the Air/Aqueous Interface. *ACS Earth Space Chem.* **2019**, *3* (9), 1740-1748.
24. Reid, J. P.; Bertram, A. K.; Topping, D. O.; Laskin, A.; Martin, S. T.; Petters, M. D.; Pope, F. D.; Rovelli, G., The viscosity of atmospherically relevant organic particles. *Nature Commun.* **2018**, *9* (1), 956.
25. Ewing, G. E., Ambient Thin Film Water on Insulator Surfaces. *Chem. Rev.* **2006**, *106* (4), 1511-1526.
26. Shrestha, M.; Zhang, Y.; Ebben, C. J.; Martin, S. T.; Geiger, F. M., Vibrational sum frequency generation spectroscopy of secondary organic material produced by condensational growth from alpha-pinene ozonolysis. *J. Phys. Chem. A* **2013**, *117* (35), 8427-8436.
27. Zhang, Y.; Liu, P.; Gong, Z.; Geiger, F. M.; Martin, S. T., Production and Measurement of Organic Particulate Matter in a Flow Tube Reactor. *J Vis Exp* **2018**, (142), e55684.
28. Aljawhary, D.; Lee, A. K. Y.; Abbatt, J. P. D., High-resolution chemical ionization mass spectrometry (ToF-CIMS): application to study SOA composition and processing. *Atmos. Meas. Tech.* **2013**, *6* (11), 3211-3224.
29. Ebben, C. J.; Strick, B. F.; Upshur, M. A.; Chase, H. M.; Achtyl, J. L.; Thomson, R. J.; Geiger, F. M., Towards the identification of molecular constituents associated with the surfaces of isoprene-derived secondary organic aerosol (SOA) particles. *Atmos. Chem. Phys.* **2014**, *14* (5), 2303-2314.
30. Li, Y. J.; Chen, Q.; Guzman, M. I.; Chan, C. K.; Martin, S. T., Second-generation products contribute substantially to the particle-phase organic material produced by  $\beta$ -caryophyllene ozonolysis. *Atmos. Chem. Phys.* **2011**, *11* (1), 121-132.
31. Kristensen, K.; Watne, Å. K.; Hammes, J.; Lutz, A.; Petäjä, T.; Hallquist, M.; Bilde, M.; Glasius, M., High-Molecular Weight Dimer Esters Are Major Products in Aerosols from  $\alpha$ -Pinene Ozonolysis and the Boreal Forest. *Environ. Sci. Technol. Lett.* **2016**, *3* (8), 280-285.

32. Zhang, X.; McVay, R. C.; Huang, D. D.; Dalleska, N. F.; Aumont, B.; Flagan, R. C.; Seinfeld, J. H., Formation and evolution of molecular products in  $\alpha$ -pinene secondary organic aerosol. *Proc. Natl. Acad. Sci.* **2015**, *112* (46), 14168-14173.
33. Upshur, M. A.; Chase, H. M.; Strick, B. F.; Ebben, C. J.; Fu, L.; Wang, H.; Thomson, R. J.; Geiger, F. M., Vibrational Mode Assignment of  $\alpha$ -Pinene by Isotope Editing: One Down, Seventy-One To Go. *J. Phys. Chem. A* **2016**, *120* (17), 2684-2690.
34. Ebben, C. J.; Shrestha, M.; Martinez, I. S.; Corrigan, A. L.; Frossard, A. A.; Song, W. W.; Worton, D. R.; Petäjä, T.; Williams, J.; Russell, L. M.; Kulmala, M.; Goldstein, A. H.; Artaxo, P.; Martin, S. T.; Thomson, R. J.; Geiger, F. M., Organic Constituents on the Surfaces of Aerosol Particles from Southern Finland, Amazonia, and California Studied by Vibrational Sum Frequency Generation. *J. Phys. Chem. A* **2012**, *116* (32), 8271-8290.
35. de Sá, S. S.; Rizzo, L. V.; Palm, B. B.; Campuzano-Jost, P.; Day, D. A.; Yee, L. D.; Wernis, R.; Isaacman-VanWertz, G.; Brito, J.; Carbone, S.; Liu, Y. J.; Sedlacek, A.; Springston, S.; Goldstein, A. H.; Barbosa, H. M. J.; Alexander, M. L.; Artaxo, P.; Jimenez, J. L.; Martin, S. T., Contributions of biomass-burning, urban, and biogenic emissions to the concentrations and light-absorbing properties of particulate matter in central Amazonia during the dry season. *Atmos. Chem. Phys.* **2019**, *19* (12), 7973-8001.
36. Martin, S. T.; Artaxo, P.; Machado, L. A. T.; Manzi, A. O.; Souza, R. A. F.; Schumacher, C.; Wang, J.; Andreae, M. O.; Barbosa, H. M. J.; Fan, J.; Fisch, G.; Goldstein, A. H.; Guenther, A.; Jimenez, J. L.; Pöschl, U.; Silva Dias, M. A.; Smith, J. N.; Wendisch, M., Introduction: Observations and Modeling of the Green Ocean Amazon (GoAmazon2014/5). *Atmos. Chem. Phys.* **2016**, *16* (8), 4785-4797.
37. Kalberer, M.; Paulsen, D.; Sax, M.; Steinbacher, M.; Dommen, J.; Prevot, A. S. H.; Fisseha, R.; Weingartner, E.; Frankevich, V.; Zenobi, R.; Baltensperger, U., Identification of polymers as major components of atmospheric organic aerosols. *Science* **2004**, *303*, 1659-1662.
38. Müller, L.; Reinnig, M. C.; Warnke, J.; Hoffmann, T., Unambiguous identification of esters as oligomers in secondary organic aerosol formed from cyclohexene and cyclohexene/ $\alpha$ -pinene ozonolysis. *Atmos. Chem. Phys.* **2008**, *8* (5), 1423-1433.
39. Gao, Y.; Hall IV, W. A.; Johnston, M. V., Molecular Composition of Monoterpene Secondary Organic Aerosol at Low Mass Loadings. *Env. Sci. Technol. in press* **2010**.
40. Yasmeeen, F.; Vermeylen, R.; Szmigielski, R.; Linuma, Y.; Boege, O.; Herrmann, H.; Maenhaut, W.; Claeys, M., Terpenylic acid and related compounds: precursors for dimers in secondary organic aerosol from the ozonolysis of  $\alpha$ - and  $\beta$ -pinene. *ACP* **2010**, *10*, 10865-10888.
41. Glasius, M.; Goldstein, A. H., Recent Discoveries and Future Challenges in Atmospheric Organic Chemistry. *Environ. Sci. Technol.* **2016**, *50* (6), 2754-2764.

42. Jang, M.; Czoschke, N. M.; Lee, S.; Kamens, R. M., Heterogeneous Atmospheric Aerosol Production by Acid-Catalyzed Particle-Phase Reactions. *Science* **2002**, *298* (5594), 814-817.
43. Vaden, T. D.; Imre, D.; Beranek, J.; Shrivastava, M.; Zelenyuk, A., Evaporation kinetics and phase of laboratory and ambient secondary organic aerosol. *Proc. Natl. Acad. Sci. U. S. A.* **2011**, *108* (6), 2190-2195, S2190/1-S2190/5.
44. Boyd, C. M.; Nah, T.; Xu, L.; Berkemeier, T.; Ng, N. L., Secondary Organic Aerosol (SOA) from Nitrate Radical Oxidation of Monoterpenes: Effects of Temperature, Dilution, and Humidity on Aerosol Formation, Mixing, and Evaporation. *Environ. Sci. Technol.* **2017**, *51* (14), 7831-7841.
45. Roldin, P.; Liao, L.; Mogensen, D.; Dal Maso, M.; Rusanen, A.; Kerminen, V. M.; Mentel, T. F.; Wildt, J.; Kleist, E.; Kiendler-Scharr, A.; Tillmann, R.; Ehn, M.; Kulmala, M.; Boy, M., Modelling the contribution of biogenic volatile organic compounds to new particle formation in the Jülich plant atmosphere chamber. *Atmos. Chem. Phys.* **2015**, *15* (18), 10777-10798.
46. Vander Wall, A. C.; Lakey, P. S. J.; Rossich Molina, E.; Perraud, V.; Wingen, L. M.; Xu, J.; Soulsby, D.; Gerber, R. B.; Shiraiwa, M.; Finlayson-Pitts, B. J., Understanding interactions of organic nitrates with the surface and bulk of organic films: implications for particle growth in the atmosphere. *Environ. Sci.: Processes Impacts* **2018**, *20* (11), 1593-1610.
47. Stropoli, S. J.; Miner, C. R.; Hill, D. R.; Elrod, M. J., Assessing Potential Oligomerization Reaction Mechanisms of Isoprene Epoxydiols on Secondary Organic Aerosol. *Environ. Sci. Technol.* **2019**, *53* (1), 176-184.
48. DePalma, J. W.; Horan, A. J.; Hall Iv, W. A.; Johnston, M. V., Thermodynamics of oligomer formation: implications for secondary organic aerosol formation and reactivity. *Phys. Chem. Chem. Phys.* **2013**, *15* (18), 6935-6944.
49. Hall, W. A.; Johnston, M. V., Oligomer Content of  $\alpha$ -Pinene Secondary Organic Aerosol. *Aerosol Sci. Technol.* **2011**, *45* (1), 37-45.
50. Kristensen, K.; Enggrob, K. L.; King, S. M.; Worton, D. R.; Platt, S. M.; Mortensen, R.; Rosenoern, T.; Surratt, J. D.; Bilde, M.; Goldstein, A. H.; Glasius, M., Formation and occurrence of dimer esters of pinene oxidation products in atmospheric aerosols. *Atmos. Chem. Phys.* **2013**, *13* (7), 3763-3776.
51. Witkowski, B.; Gierczak, T., Early stage composition of SOA produced by  $\alpha$ -pinene/ozone reaction:  $\alpha$ -Acyloxyhydroperoxy aldehydes and acidic dimers. *Atmos. Environ.* **2014**, *95*, 59-70.
52. Liggió, J.; Li, S. M., A new source of oxygenated organic aerosol and oligomers. *Atmos. Chem. Phys.* **2013**, *13* (6), 2989-3002.

53. Hall, W. I. V.; Johnston, M., Oligomer Formation Pathways in Secondary Organic Aerosol from MS and MS/MS Measurements with High Mass Accuracy and Resolving Power. *J. Am. Soc. Mass Spectrom.* **2012**, *23* (6), 1097-1108.
54. Tolocka, M. P.; Jang, M.; Ginter, J. M.; Cox, F. J.; Kamens, R. M.; Johnston, M. V., Formation of Oligomers in Secondary Organic Aerosol. *Environ. Sci. Technol.* **2004**, *38* (5), 1428-1434.
55. Nozière, B.; Córdova, A., A Kinetic and Mechanistic Study of the Amino Acid Catalyzed Aldol Condensation of Acetaldehyde in Aqueous and Salt Solutions. *J. Phys. Chem. A* **2008**, *112* (13), 2827-2837.
56. Claus, R. E.; Schreiber, S. L., Ozonolytic Cleavage of Cyclohexene to Terminally Differentiated Products: Methyl 6-Oxoheptanoate, 6,6-Dimethoxyhexanal, Methyl 6,6-Dimethoxyheptanoate. In *Organic Syntheses*, John Wiley & Sons, Inc.: 2003.
57. Rodríguez, J. B., Gros, E. G., Caram, J. A., & Marschoff, C. M., Ritter reaction on terpenoids. IV. Remarkable tendency to produce 3-aza-bicyclo[3.3.1]non-2-ene systems from mono and sesquiterpenes. *Tetrahedron Lett.* **1995**, *36* (43), 7825-7828.
58. Sui, X.; Zhou, Y.; Zhang, F.; Zhang, Y.; Chen, J.; Zhu, Z.; Yu, X.-Y., ToF-SIMS characterization of glyoxal surface oxidation products by hydrogen peroxide: A comparison between dry and liquid samples. *Surf. Interface Anal.* **2018**, *50* (10), 927-938.
59. Bé, A. G.; Upshur, M. A.; Liu, P.; Martin, S. T.; Geiger, F. M.; Thomson, R. J., Cloud Activation Potentials for Atmospheric  $\alpha$ -Pinene and  $\beta$ -Caryophyllene Ozonolysis Products. *ACS Cent. Sci.* **2017**, *3* (7), 715-725.
60. Lee, S.-G.,  $\alpha$ -Pinene and myrtenol: complete  $^1\text{H}$  NMR assignment. *Magn. Reson. Chem.* **2002**, *40* (4), 311-312.

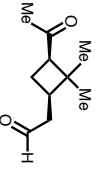
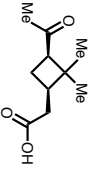
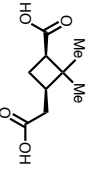
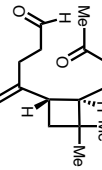
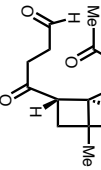
## APPENDIX 1

### Supplementary Interfacial Tension Data

**Portions of this chapter appear in the supporting information for the following publication with permission from the American Chemical Society:**

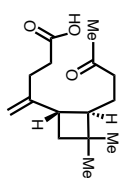
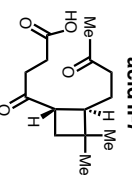
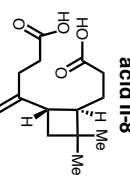
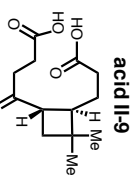
Bé, A. G.; Upshur, M. A.; Liu, P.; Martin, S. T.; Geiger, F. M.; Thomson, R. J., Cloud Activation Potentials for Atmospheric  $\alpha$ -Pinene and  $\beta$ -Caryophyllene Ozonolysis Products. *ACS Cent. Sci.* **2017**, *3* (7), 715–725.

Table A1.1. Optimized fitting parameters for kinetics of interfacial tension and equilibration timescale calculations.

compound	conc. (mM)	$\eta$	$S_0$ (mN m <sup>-1</sup> )	$S_m$ (mN m <sup>-1</sup> )	$t_{m,lab}$ (s)	$D_{drop}$ (mm)	$t_{eq,1 \mu m}$ (s)
 pinonaldehyde II-1	0.1	1.06±0.25 (0.75±1.69)	72.63±0.07 (74.30±0.46)	68.94±1.91 (73.32±1.86)	841±716 (n.d. *)	2.21±0.03 (2.18±0.04)	3.20×10 <sup>-4</sup> (n.d. *)
	0.5	1.00±0.34 (0.98±0.46)	71.77±0.08 (72.83±0.17)	70.54±0.32 (70.45±1.22)	257±123 (395±382)	2.29±0.01 (2.15±0.02)	1.03×10 <sup>-4</sup> (1.71×10 <sup>-4</sup> )
	1	0.82±0.55 (0.98±0.24)	71.30±0.25 (71.21±0.20)	64.68±12.55 (67.10±0.81)	n.d. * (269±99)	2.24±0.02 (2.14±0.06)	n.d. * (1.18×10 <sup>-4</sup> )
	5	n.d. *	66.05±1.53	60.09±12.96	n.d. *	2.21±0.02	n.d. *
	10	0.49±0.14	60.87±0.32	57.75±0.46	101±34	2.13±0.02	4.42×10 <sup>-5</sup>
 pinonic acid II-2	1	1.05±0.34 (0.78±0.33)	71.40±0.06 (71.65±0.12)	69.94±0.59 (68.53±2.75)	453±324 (n.d. *)	2.27±0.02 (2.04±0.09)	1.99×10 <sup>-4</sup> (5.05×10 <sup>-4</sup> )
	5	1.20±0.93 (0.86±0.19)	68.55±0.05 (65.04±0.08)	68.15±0.30 (62.08±0.89)	n.d. * (538±344)	2.23±0.04 (2.04±0.08)	n.d. * (2.59×10 <sup>-4</sup> )
	10	0.82±0.52	65.09±0.09	64.26±0.58	n.d. *	2.19±0.04	n.d. *
	20	0.65±0.53	61.71±0.27	60.02±1.34	n.d. *	2.16±0.04	n.d. *
	30	0.61±0.46	59.39±0.14	58.28±0.96	n.d. *	2.13±0.07	n.d. *
 pinic acid II-3	1	1.81±0.53 (1.65±1.06)	71.28±0.07 (74.49±0.15)	70.32±0.13 (73.43±0.37)	200±32 (222±96)	2.26±0.02 (2.19±0.07)	7.85×10 <sup>-5</sup> (9.25×10 <sup>-5</sup> )
	5	0.59±0.20 (0.79±0.22)	70.50±0.20 (69.76±0.22)	66.75±1.54 (65.27±1.35)	n.d. * (386±264)	2.22±0.02 (2.13±0.14)	n.d. * (1.70×10 <sup>-4</sup> )
	10	1.27±0.10 (1.00±0.09)	67.04±0.07 (66.62±0.09)	63.28±0.16 (62.98±0.17)	192±12 (156±13)	2.11±0.05 (2.10±0.03)	8.61×10 <sup>-5</sup> (7.10×10 <sup>-5</sup> )
	20	0.98±0.23 (0.67±0.08)	62.87±0.21 (61.57±0.16)	59.16±0.54 (56.44±0.47)	194±12 (211±46)	2.04±0.05 (2.04±0.02)	8.95×10 <sup>-5</sup> (1.01×10 <sup>-4</sup> )
	30	0.44±0.20 (0.55±0.36)	62.13±0.90 (58.32±0.69)	53.41±3.71 (52.72±3.93)	n.d. * (n.d. *)	2.08±0.04 (1.94±0.08)	n.d. * (n.d. *)
 β-caryophyllene aldehyde II-4	0.01	0.56±0.23 (1.24±0.35)	70.16±0.21 (73.12±0.21)	68.46±0.47 (70.87±0.21)	173±122 (105±20)	2.25±0.04 (2.10±0.04)	6.84×10 <sup>-5</sup> (4.75×10 <sup>-5</sup> )
	0.1	0.59±0.20 (0.51±0.19)	62.44±0.15 (60.12±0.30)	60.02±0.88 (57.06±0.86)	n.d. * (231±190)	2.18±0.08 (2.03±0.01)	n.d. * (1.13×10 <sup>-4</sup> )
	0.2	0.47±0.09 (0.51±0.13)	57.98±0.21 (55.40±0.22)	48.55±3.57 (51.55±0.91)	n.d. * (353±265)	2.08±0.11 (1.95±0.03)	n.d. * (1.86×10 <sup>-4</sup> )
	0.5	0.47±0.15	50.93±0.22	46.83±1.72	n.d. *	1.99±0.14	n.d. *
	1	0.65±0.22	47.03±0.11	45.24±0.66	425±423	1.95±0.01	2.24×10 <sup>-4</sup>
 β-caryophyllone aldehyde II-5	0.01	n.d. * (n.d. *)	72.55±1.44 (74.50±0.07)	73.21±4.64 (74.97±1.44)	n.d. * (n.d. *)	2.23±0.05 (2.17±0.10)	n.d. * (n.d. *)
	0.1	n.d. * (0.75±0.27)	71.86±0.06 (72.71±0.14)	71.61±0.69 (71.02±0.46)	n.d. * (232±142)	2.17±0.07 (2.15±0.05)	n.d. * (1.00×10 <sup>-4</sup> )
	0.2	1.22±0.47 (0.73±0.22)	71.01±0.05 (70.17±0.16)	68.45±3.04 (64.72±3.13)	n.d. * (n.d. *)	2.18±0.05 (2.07±0.04)	n.d. * (n.d. *)
	0.5	1.83±0.37 (0.70±0.11)	68.94±0.04 (65.56±0.15)	67.62±0.18 (60.53±0.75)	293±47 (349±130)	2.14±0.02 (2.03±0.02)	1.27×10 <sup>-4</sup> (1.69×10 <sup>-4</sup> )
	1	0.88±0.12 (0.90±0.08)	66.21±0.07 (61.52±0.09)	62.52±0.64 (56.76±0.30)	488±177 (229±28)	2.14±0.02 (2.03±0.03)	2.12×10 <sup>-4</sup> (1.12×10 <sup>-4</sup> )

\* = due to large uncertainties on the point estimates

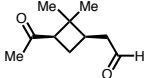
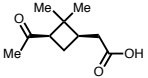
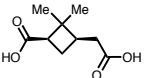
Table A1.1 (continued). Optimized fitting parameters for kinetics of interfacial tension and equilibration timescale calculations.

compound	conc. (mM)	n	S <sub>0</sub> (mN m <sup>-1</sup> )	S <sub>m</sub> (mN m <sup>-1</sup> )	t <sub>m,lab</sub> (s)	D <sub>drop</sub> (mm)	t <sub>eq,1</sub> μm (s)
 <b>β-caryophyllonic acid II-6</b>	0.01	n.d.* (1.80±0.91)	72.45±0.05 (73.32±0.10)	72.18±1.11 (72.82±0.05)	n.d.* (83±25)	2.17±0.05 (2.13±0.07)	n.d.* (3.65x10 <sup>-5</sup> )
	0.1	1.99±1.13 (0.50±0.13)	71.49±0.14 (64.18±0.42)	70.74±0.10 (60.39±0.48)	114±32 (77±21)	2.25±0.01 (2.02±0.05)	4.80x10 <sup>-5</sup> (3.75x10 <sup>-5</sup> )
	0.2	0.44±0.20 (n.d.*)	66.21±0.29 (54.51±1.96)	60.44±4.90 (54.11±2.96)	n.d.* (n.d.*)	2.18±0.03 (1.97±0.05)	n.d.* (n.d.*)
	0.5	0.51±0.11 (0.55±0.20)	56.62±0.25 (49.09±0.18)	51.93±0.85 (46.04±1.39)	272±148 (n.d.*)	2.01±0.03 (1.87±0.03)	1.34x10 <sup>-4</sup> (n.d.*)
	1	0.71±0.15	52.14±0.09	48.43±1.20	774±623	1.97±0.02	3.97x10 <sup>-4</sup>
 <b>β-caryophyllonic acid II-7</b>	0.01	n.d.* (1.23±0.70)	71.96±0.24 (74.21±0.09)	72.23±2.03 (n.d.*)	n.d.* (n.d.*)	2.21±0.05 (2.14±0.10)	n.d.* (n.d.*)
	0.1	1.08±0.28 (0.93±0.37)	72.11±0.08 (73.68±0.09)	69.82±0.72 (71.55±1.40)	441±241 (n.d.*)	2.25±0.06 (2.08±0.01)	1.74x10 <sup>-4</sup> (n.d.*)
	0.2	1.07±0.06 (2.00±1.21)	71.37±0.07 (71.39±0.26)	63.09±0.39 (70.33±0.10)	314±26 (71±26)	2.25±0.01 (2.07±0.05)	1.29x10 <sup>-4</sup> (3.31x10 <sup>-5</sup> )
	0.5	0.95±0.02 (0.95±0.23)	68.12±0.14 (67.30±0.29)	56.41±0.06 (58.48±2.56)	45±1 (460±259)	2.09±0.01 (2.02±0.01)	2.07x10 <sup>-5</sup> (2.26x10 <sup>-4</sup> )
	1	0.64±0.02 (1.17±0.09)	63.50±0.38 (62.20±0.19)	48.89±0.09 (51.60±0.52)	14±1 (209±16)	2.00±0.03 (1.99±0.01)	7.21x10 <sup>-6</sup> (1.05x10 <sup>-4</sup> )
 <b>β-caryophyllinic acid II-8</b>	0.01	n.d.* (2.00±0.65)	72.98±0.09 (75.18±0.09)	72.75±0.08 (74.35±0.06)	137±86 (113±18)	2.29±0.01 (2.16±0.02)	5.22x10 <sup>-5</sup> (4.84x10 <sup>-5</sup> )
	0.1	n.d.* (0.99±0.11)	72.46±0.03 (71.49±0.13)	n.d.* (63.09±1.19)	n.d.* (453±120)	2.23±0.05 (2.13±0.06)	n.d.* (2.00x10 <sup>-4</sup> )
	0.2	0.84±0.20 (0.68±0.09)	70.88±0.13 (64.10±0.12)	66.70±1.41 (56.18±1.66)	569±413 (881±479)	2.20±0.06 (2.08±0.06)	2.36x10 <sup>-4</sup> (4.08x10 <sup>-4</sup> )
	0.5	0.94±0.09 (0.68±0.16)	60.05±0.07 (53.95±0.20)	56.40±0.26 (48.47±1.58)	242±32 (519±91)	2.07±0.03 (1.92±0.05)	1.12x10 <sup>-4</sup> (2.81x10 <sup>-4</sup> )
	1	0.78±0.10 (0.60±0.14)	52.29±0.10 (46.10±0.13)	48.44±0.37 (41.36±1.91)	249±52 (n.d.*)	1.99±0.04 (1.84±0.20)	1.26x10 <sup>-4</sup> (n.d.*)
 <b>β-caryophyllinic acid II-9</b>	0.01	n.d.* (n.d.*)	72.49±0.03 (74.47±0.03)	72.34±3.31 (73.28±9.14)	n.d.* (n.d.*)	2.21±0.01 (2.15±0.02)	n.d.* (n.d.*)
	0.1	n.d.* (0.95±0.91)	71.77±0.84 (74.30±0.15)	71.81±2.16 (73.96±0.10)	n.d.* (66±55)	2.18±0.02 (2.20±0.03)	n.d.* (2.82x10 <sup>-5</sup> )
	0.2	2.00±1.20 (0.99±0.18)	71.69±0.05 (73.81±0.08)	71.37±0.07 (70.05±0.97)	180±51 (546±259)	2.16±0.01 (2.17±0.01)	7.73x10 <sup>-5</sup> (2.36x10 <sup>-4</sup> )
	0.5	0.91±0.27 (1.29±0.04)	70.62±0.22 (69.41±0.06)	65.48±1.85 (60.95±0.13)	456±332 (185±4)	2.10±0.04 (2.11±0.02)	2.07x10 <sup>-4</sup> (8.33x10 <sup>-5</sup> )
	1	0.93±0.05 (0.89±0.03)	66.89±0.12 (64.52±0.12)	60.72±0.13 (54.64±0.12)	91±4 (83±2)	2.07±0.02 (1.97±0.03)	4.21x10 <sup>-5</sup> (4.28x10 <sup>-5</sup> )

\* = due to large uncertainties on the point estimates

**Table A1.2.** (A) Equilibrium surface tension for  $\alpha$ -pinene-derived oxidation products at 0–30 mM in H<sub>2</sub>O and 1.0 M (NH<sub>4</sub>)<sub>2</sub>SO<sub>4</sub> (values in parentheses). All values have units of mN m<sup>-1</sup>. [Asterisk (\*) notes that value was not obtained due to insolubility at the indicated concentration.] (B) Fitting parameters (a and b), cross-sectional area of the surfactant molecules at the surface ( $\omega$ ), and free energy of adsorption ( $\Delta G_{ads}^{\circ}$ ) for the  $\alpha$ -pinene-derived oxidation products obtained from Szyszkowski-Langmuir equation,<sup>1-2</sup> where  $T$  is the laboratory temperature,  $\sigma_{blank}$  is the average surface tension of the blank solution, and  $\sigma$  is the minimum surface tension at each concentration  $C$  (in mM) measured. [SEP denotes standard error exceeds point estimate.]

**A**

Conc. (mM)	pinonaldehyde II-1	pinonic acid II-2	pinic acid II-3
0	73.29±0.15 (74.16±0.13)	71.90±0.11 (74.52±0.09)	72.66±0.28 (74.52±0.09)
1	69.40±0.33 (68.54±0.36)	70.57±0.07 (70.42±0.12)	70.31±0.08 (73.51±0.30)
5	63.61±0.31 (N/A*)	68.27±0.10 (63.48±0.11)	68.63±0.14 (67.16±0.28)
10	58.66±0.10 (N/A*)	64.59±0.08 (N/A*)	64.00±0.16 (63.71±0.11)
20	N/A* (N/A*)	60.68±0.17 (N/A*)	60.02±0.12 (58.16±0.08)
30	N/A* (N/A*)	58.79±0.19 (N/A*)	57.46±0.29 (55.21±0.28)

**B** Szyszkowski-Langmuir equation fit parameters:  
 $\sigma = \sigma_{blank} - aT \ln(1 + bC)$  where  $a = R/\omega$  and  $b = K_{ads}$

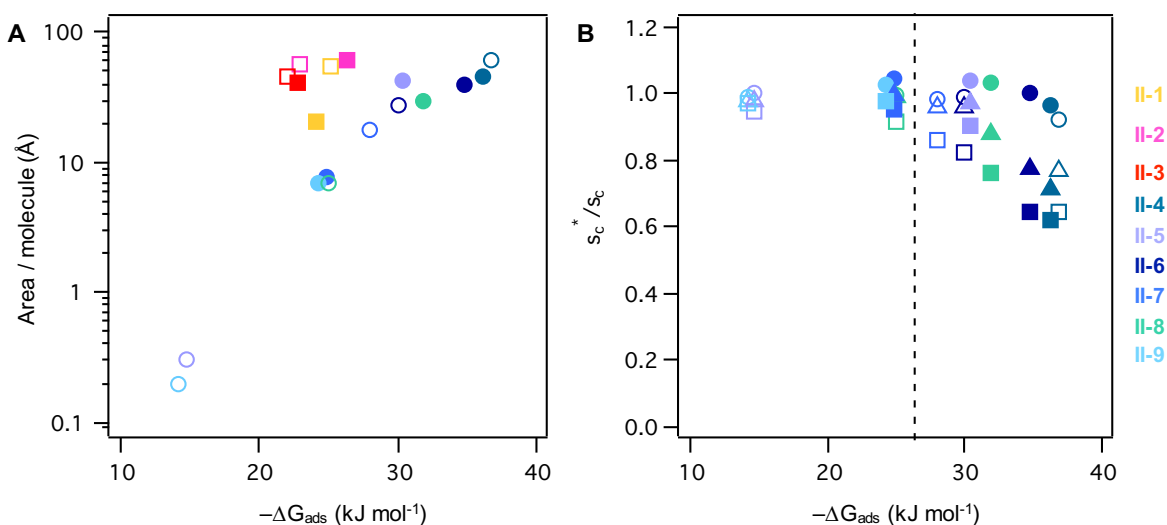
	pinonaldehyde II-1	pinonic acid II-2	pinic acid II-3
$a$ (mN m <sup>-1</sup> K <sup>-1</sup> )	0.026 ± 0.007 (0.067 ± SEP)	0.024 ± 0.004 (0.022 ± N/A)	0.030 ± 0.008 (0.034 ± 0.004)
$b$ (L mmol <sup>-1</sup> )	0.53 ± 0.30 (0.36 ± SEP)	0.21 ± 0.08 (0.89 ± N/A)	0.16 ± 0.08 (0.21 ± 0.05)
$\omega$ (Å <sup>2</sup> molec <sup>-1</sup> )	54.0 ± 15.5 (20.7 ± SEP)	57.2 ± 10.7 (61.8 ± N/A)	45.7 ± 12.4 (40.8 ± 4.7)
$-\Delta G_{ads}^{\circ}$ (kJ mol <sup>-1</sup> )	25.1 ± 1.4 (24.1 ± SEP)	22.9 ± 0.9 (26.3 ± N/A)	22.1 ± 1.2 (22.8 ± 0.6)

**Table A1.3.** (A) Equilibrium surface tension for  $\beta$ -caryophyllene-derived oxidation products at 0–1 mM in H<sub>2</sub>O and 1.0 M (NH<sub>4</sub>)<sub>2</sub>SO<sub>4</sub> (values in parentheses). All values have units of mN m<sup>-1</sup>. [Asterisk (\*) notes that value was not obtained due to insolubility at the indicated concentration.] (B) Fitting parameters (a and b), cross-sectional area of the surfactant molecules at the surface ( $\omega$ ), and free energy of adsorption ( $\Delta G_{ads}^{\circ}$ ) for the  $\beta$ -caryophyllene-derived oxidation products obtained from Szyszkowski-Langmuir equation,<sup>1-2</sup> where  $T$  is the laboratory temperature,  $\sigma_{blank}$  is the average surface tension of the blank solution, and  $\sigma$  is the minimum surface tension at each concentration  $C$  (in mM) measured. [SEP denotes standard error exceeds point estimate.]

Conc. (mM)	$\beta$ -caryophyllene aldehyde II-4	$\beta$ -nocaryophyllone aldehyde II-5	$\beta$ -caryophyllonic acid II-6	$\beta$ -nocaryophyllonic acid II-7	$\beta$ -caryophyllinic acid II-8	$\beta$ -nocaryophyllinic acid II-9
0	73.14±0.20 (74.33±0.21)	72.90±0.14 (74.78±0.19)	73.08±0.37 (74.16±0.13)	73.01±0.16 (74.52±0.09)	72.78±0.17 (74.65±0.13)	72.76±0.09 (75.33±0.09)
0.01	68.99±0.08 (71.13±0.35)	72.87±0.16 (74.77±0.07)	72.31±0.10 (72.88±0.07)	72.11±0.08 (74.97±0.30)	72.77±0.14 (74.33±0.16)	72.48±0.14 (74.18±0.22)
0.1	61.04±0.08 (58.18±0.07)	71.72±0.11 (71.54±0.11)	70.69±0.39 (61.38±0.07)	70.76±0.11 (72.69±0.09)	72.32±0.16 (66.72±0.10)	71.69±0.16 (73.98±0.13)
0.2	54.58±0.08 (53.19±0.06)	70.14±0.14 (67.96±0.13)	64.13±0.10 (54.47±0.06)	65.91±0.14 (70.50±0.69)	68.73±0.09 (60.68±0.07)	71.41±0.13 (71.85±0.10)
0.5	49.04±0.06 (N/A*)	67.94±0.15 (62.49±0.16)	53.81±0.07 (47.62±0.06)	57.32±0.07 (62.33±0.34)	57.52±0.08 (51.14±0.34)	67.84±0.40 (62.56±0.13)
1	46.01±0.05 (N/A*)	64.19±0.12 (58.10±0.09)	50.46±0.08 (N/A*)	50.10±0.07 (54.07±0.27)	49.72±0.09 (44.10±0.06)	61.60±0.10 (56.08±0.09)

<b>B</b> Szyszkowski-Langmuir equation fit parameters: $\sigma = \sigma_{blank} - aT \ln(1 + bC)$ where $a = R/\omega$ and $b = K_{ads}$						
$a$ (mN m <sup>-1</sup> K <sup>-1</sup> )	0.022 ± 0.003 (0.030 ± 0.003)	4.099 ± SEP (0.033 ± 0.005)	0.050 ± 0.025 (0.034 ± 0.005)	0.077 ± 0.029 (0.178 ± 0.131)	0.197 ± SEP (0.047 ± 0.004)	6.047 ± SEP (0.203 ± SEP)
$b$ (L mmol <sup>-1</sup> )	64.6 ± 24.8 (51.4 ± 10.4)	0.007 ± SEP (4.7 ± 1.4)	4.0 ± 3.5 (28.3 ± 9.3)	1.8 ± 0.9 (0.5 ± 0.4)	0.508 ± SEP (8.5 ± 1.6)	0.006 ± SEP (0.4 ± SEP)
$\omega$ (Å <sup>2</sup> molec <sup>-1</sup> )	61.7 ± 7.1 (45.5 ± 3.9)	0.3 ± SEP (42.0 ± 7.0)	27.6 ± 13.7 (40.1 ± 5.5)	17.9 ± 6.7 (7.8 ± 5.7)	7.0 ± SEP (29.5 ± 2.7)	0.2 ± SEP (6.8 ± SEP)
$-\Delta G_{ads}^{\circ}$ (kJ mol <sup>-1</sup> )	36.8 ± 0.9 (36.2 ± 0.6)	14.7 ± SEP (30.4 ± 0.8)	30.0 ± 2.1 (34.8 ± 0.8)	28.0 ± 1.3 (24.9 ± 2.1)	25.0 ± SEP (31.9 ± 0.5)	14.2 ± SEP (24.2 ± SEP)



**Figure A1.1.** (A) Area per molecule adsorbed at the air/water interface of pendant drops as a function of the free energy of adsorption obtained from the Szyszkowski-Langmuir equation. Results are for solutions in water (empty symbols) and 1 M ammonium sulfate (filled symbols) for the  $\alpha$ -pinene (squares) and the  $\beta$ -caryophyllene (circles) series ([Pinonaldehyde (**II-1**), pinonic acid (**II-2**), pinic acid (**II-3**),  $\beta$ -caryophyllene aldehyde (**II-4**),  $\beta$ -nocaryophyllone aldehyde (**II-5**),  $\beta$ -caryophyllonic acid (**II-6**),  $\beta$ -nocaryophyllonic acid (**II-7**),  $\beta$ -caryophyllinic acid (**II-8**),  $\beta$ -nocaryophyllinic acid (**II-9**)]. (B) Supersaturation ratio as a function of free energy of adsorption of the  $\beta$ -caryophyllene series studied here. Results are for solutions in water (empty symbols) and 1 M ammonium sulfate (filled symbols) for concentrations of 0.01 (circles), 0.1 (triangles), and 0.2 (squares) mmol/L.  $\beta$ -Caryophyllene aldehyde (**II-4**) and  $\beta$ -caryophyllonic acid (**II-6**) were insoluble at 1 mM in 1 M ammonium sulfate and therefore are not shown.

**Appendix 1 references.**

1. Saien, J.; Bahrami, M., Understanding the effect of different size silica nanoparticles and SDS surfactant mixtures on interfacial tension of n-hexane–water. *J. Mol. Liq.* **2016**, *224*, Part A, 158-164.
2. Adamson, A. W.; Gast, A. P., *Physical Chemistry of Surfaces*. 6th ed.; Wiley: New York, 1997.

## APPENDIX 2

### Supplementary SFG Spectroscopy Data

**Portions of this chapter appear in the supporting information for the following publications with permission from the American Chemical Society:**

Bé, A. G.; Chase, H. M.; Liu, Y.; Upshur, M. A.; Zhang, Y.; Tuladhar, A.; Chase, Z. A.; Bellcross, A. D.; Wang, H.-F.; Wang, Z.; Batista, V. S.; Martin, S. T.; Thomson, R. J.; Geiger, F. M., Atmospheric  $\beta$ -Caryophyllene-Derived Ozonolysis Products at Interfaces. *ACS Earth Space Chem.* **2019**, 3 (2), 158–169.

Bé, A. G.; Liu, Y.; Tuladhar, A.; Bellcross, A. D.; Wang, Z.; Thomson, R. J.; Geiger, F. M., Surface-Active  $\beta$ -Caryophyllene Oxidation Products at the Air/Aqueous Interface. *ACS Earth Space Chem.* **2019**, 3 (9), 1740–1748.

## Chapter 3 Appendix

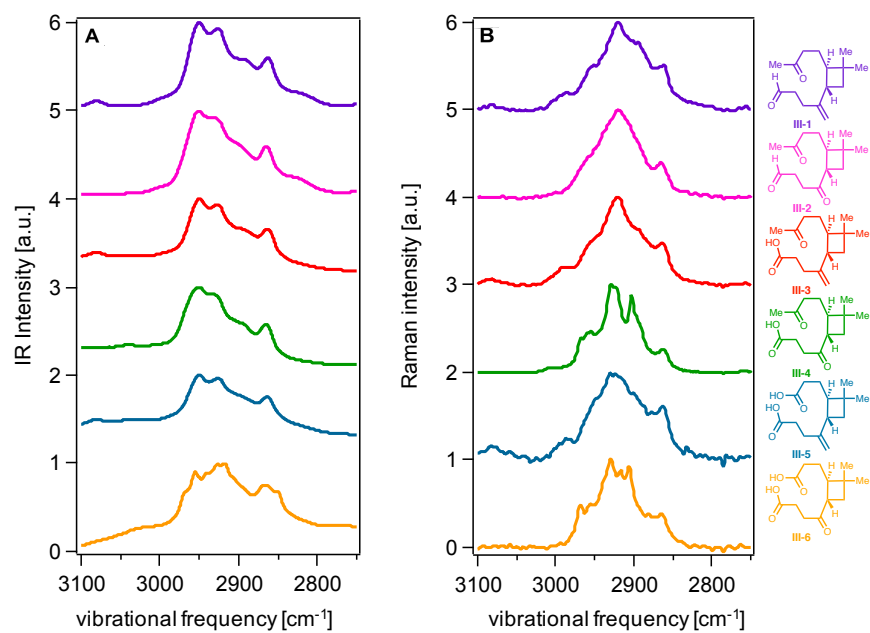


**Figure A2.1.** (A) IR and (B) Raman spectra of synthesized oxidation products **III-1–III-6**.

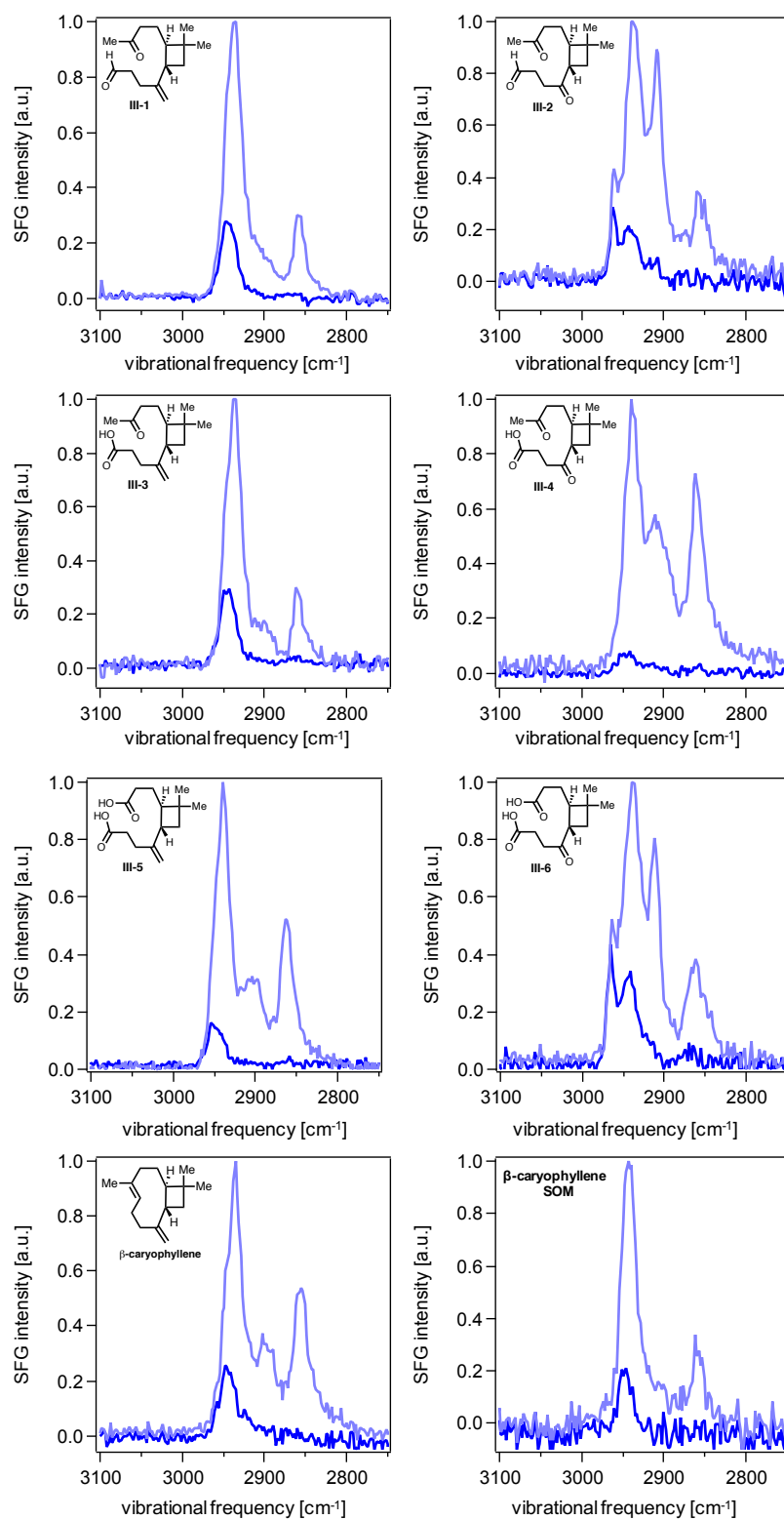


**Figure A2.2.** HR *ppp*- (dark blue) and *ssp*-polarized (light blue) SFG spectra of spin-coated samples and SOM on fused silica normalized to the highest intensity in the *ssp*-polarized spectra.

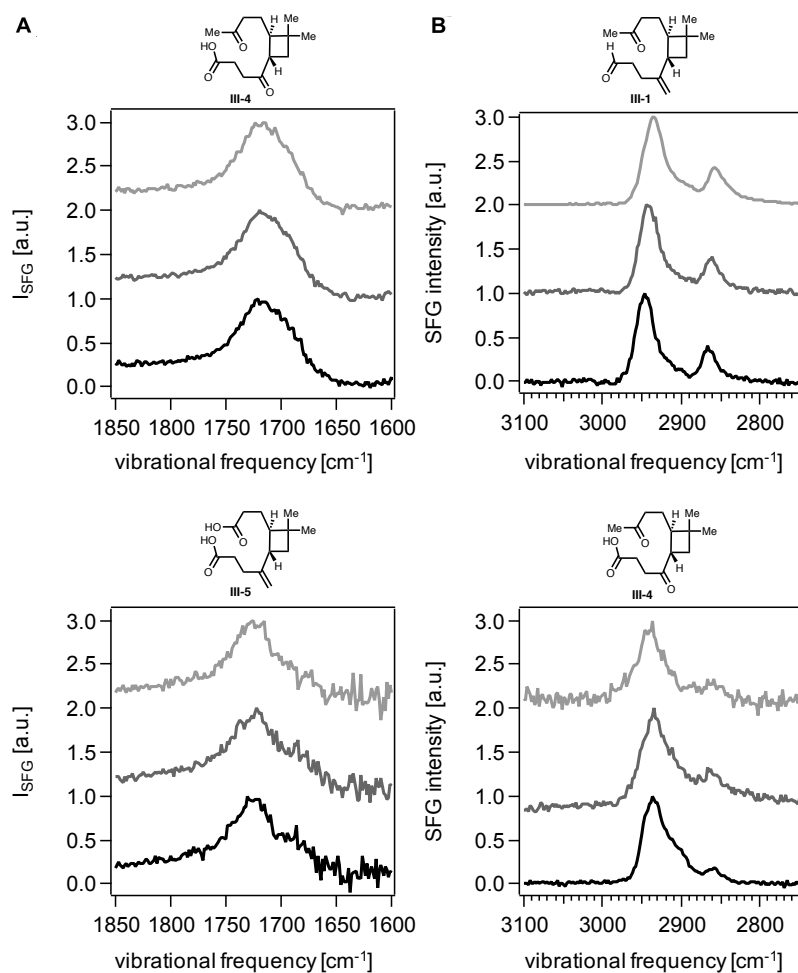


**Figure A2.3.** Representative triplicates of individual *ssp*-polarized SFG spectra of (A) spin-coated compounds **III-4** (top) and **III-5** (bottom) on CaF<sub>2</sub> in C=O region. (B) Standard resolution spectra of vapor phase compounds **III-1** (top) and **III-4** (bottom) in contact with fused silica in the C–H region. Maximum intensities have been normalized to 1 and offset for clarity.

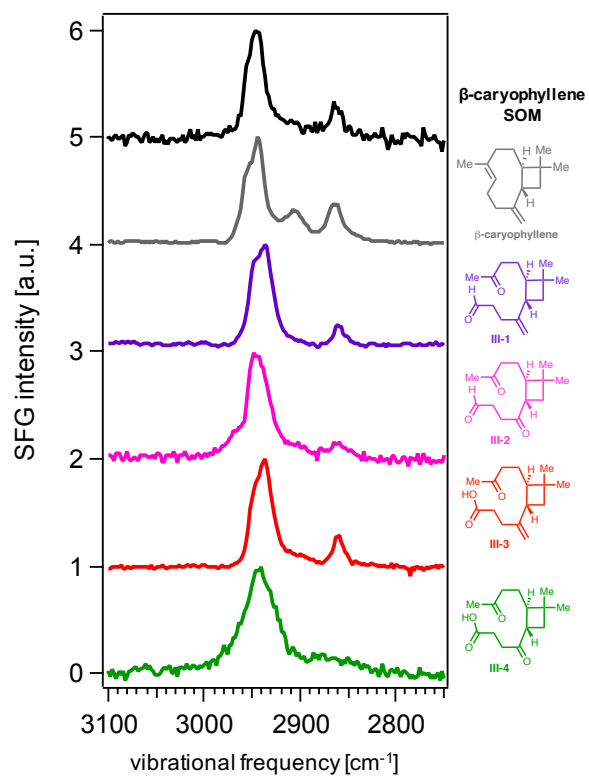


**Figure A2.4.** HR *ssp*-polarized spectra of vapor-phase of oxidation products on fused silica and comparison to SOM (black trace) in C–H region. Due to extremely low vapor-phase signal from compounds **III-5** and **III-6**, spectra were not collected. Maximum intensities have been normalized to 1 and offset for clarity.

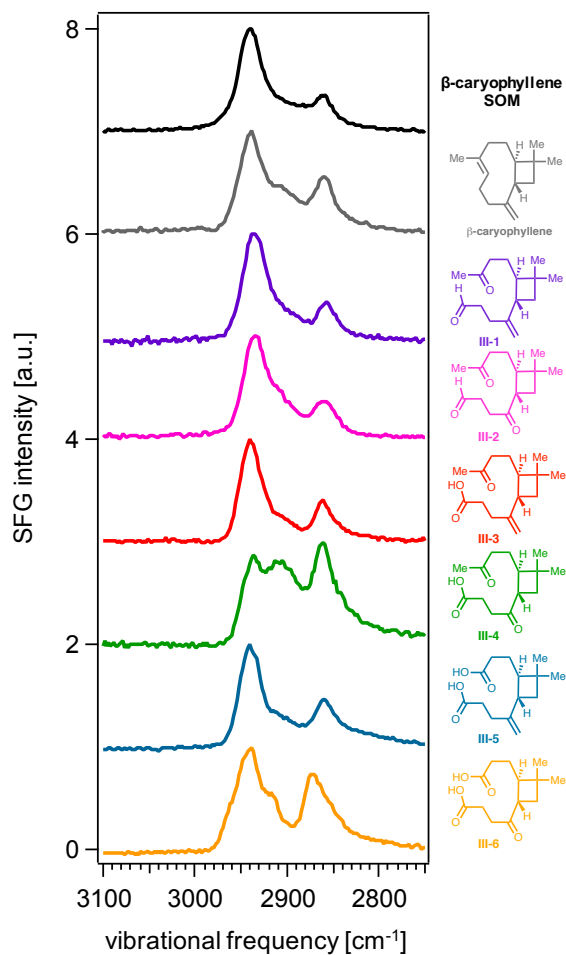


**Figure A2.5.** Standard resolution *ssp*-polarized spectra of spin-coated oxidation products on fused silica and comparison to SOM (black trace) in C–H region. Maximum intensities have been normalized to 1 and offset for clarity.

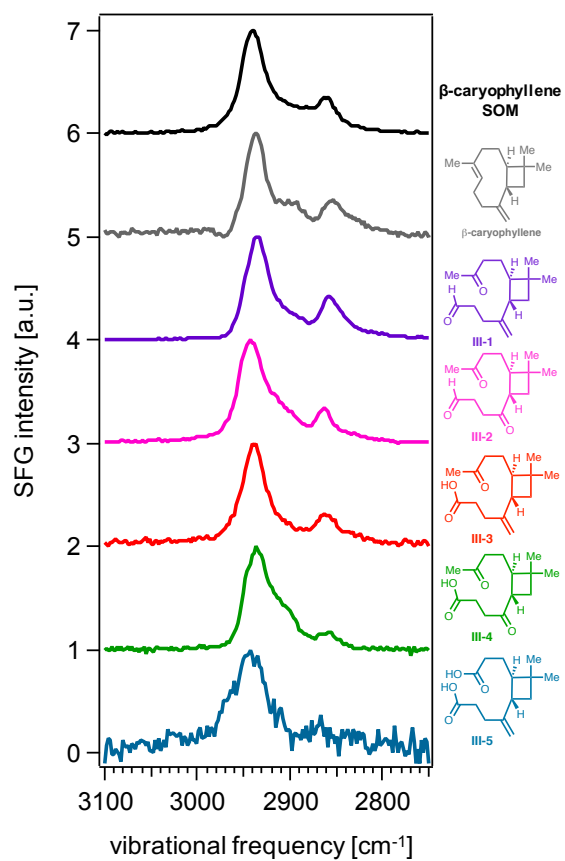


**Figure A2.6.** Standard resolution *ssp*-polarized spectra of spin-coated oxidation products on fused silica and comparison to SOM (black trace) in C–H region. Maximum intensities have been normalized to 1 and offset for clarity.

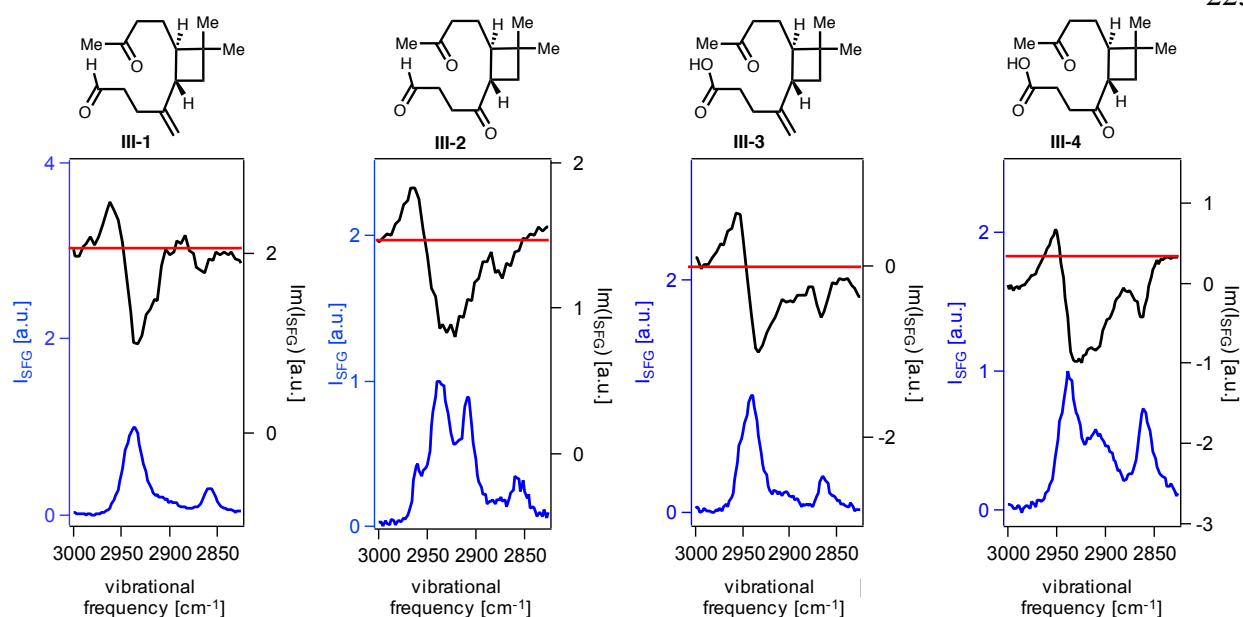


**Figure A2.7.** High resolution *ssp*-polarized SFG intensity spectra (blue trace) of compounds **III-1–III-4** (spin-coated on fused silica) and imaginary parts of the respective spectra (offset, black trace) obtained from measurements of the compounds spin-coated onto  $\alpha$ -quartz. Note that discrepancies were observed between the spectra acquired for **III-2** on fused silica versus  $\alpha$ -quartz, emphasizing that for **III-2** in particular, there may be a dependence in the structural organization within the spin-coated layer on these two substrates that is not observed for the other compounds.

**A2.1. Phase-resolved analysis to deduce the orientation of the four-membered ring on  $\beta$ -caryophyllene aldehyde.** The intensity of the SFG signal observed in the interference SFG spectrum is expressed as

$$I \propto 2\chi_{\text{Quartz}}^{(2)}\chi_{S,Im}^{(2)} \quad (\text{A2.1}),$$

which is the direct interference term from quartz and the sample. z-Cut  $\alpha$ -quartz has  $D_3$  symmetry,<sup>1</sup> therefore the nonlinear quartz response in the *ssp* polarization is given by

$$\vec{\chi}_{\text{Quartz},ssp}^{(2)} \propto \chi_{YYZ} \propto -\beta_{xxx} \cos \phi \quad (\text{A2.2})$$

where  $\phi$  is the azimuthal angle of quartz. Therefore, when  $\phi=0^\circ$ , the quartz term  $\vec{\chi}_{\text{Quartz},ssp}^{(2)}$  is negative in sign in the *ssp* polarization combination. Based on the DFT calculations, the peak at  $\sim 2940 \text{ cm}^{-1}$  that is negative in sign is attributed to the  $\text{CH}_2$  symmetric stretching motion within the four-membered ring. This calculated frequency agrees reasonably with recently reported vibrational mode assignments of strained methylene stretches within  $\alpha$ -pinene as determined by DFT<sup>2</sup> and HR-BB SFG spectroscopy.<sup>3</sup> For the symmetric stretch of a  $\text{C}_{2v}$  group that is facing away from the surface, it is known that its nonlinear response is given by:<sup>4</sup>

$$\chi_{YYZ,ss} \propto (\beta_{xxz} + \beta_{yyz} + \beta_{zzz}) \quad (\text{A2.3})$$

Therefore, the negative peak in the interference spectrum associated with the symmetric stretching motion when  $\phi_{\text{Quartz}}=0^\circ$  indicates that the methylene group on the four-membered ring faces *away* from the surface. The peak near  $2860 \text{ cm}^{-1}$  is also negative in sign, and we can identify the orientation of the methyl groups attached to the four-membered ring. The peak in this region appears to be negative when quartz rotational angle is  $0^\circ$ . Assuming the  $\text{CH}_3$  group has full  $\text{C}_{3v}$  symmetry, and invoking the notion that if a group bearing  $\text{C}_{3v}$  symmetry is facing

away from the surface, the nonlinear contribution of the symmetric stretch in the *ssp* polarization combination is given by:<sup>4-5</sup>

$$\chi_{YYZ,ss} \propto \beta_{zzz} \quad (\text{A2.4})$$

Therefore, the negative interference peak indicates that the CH<sub>3</sub> group is facing away from the surface.

## Chapter 4 Appendix

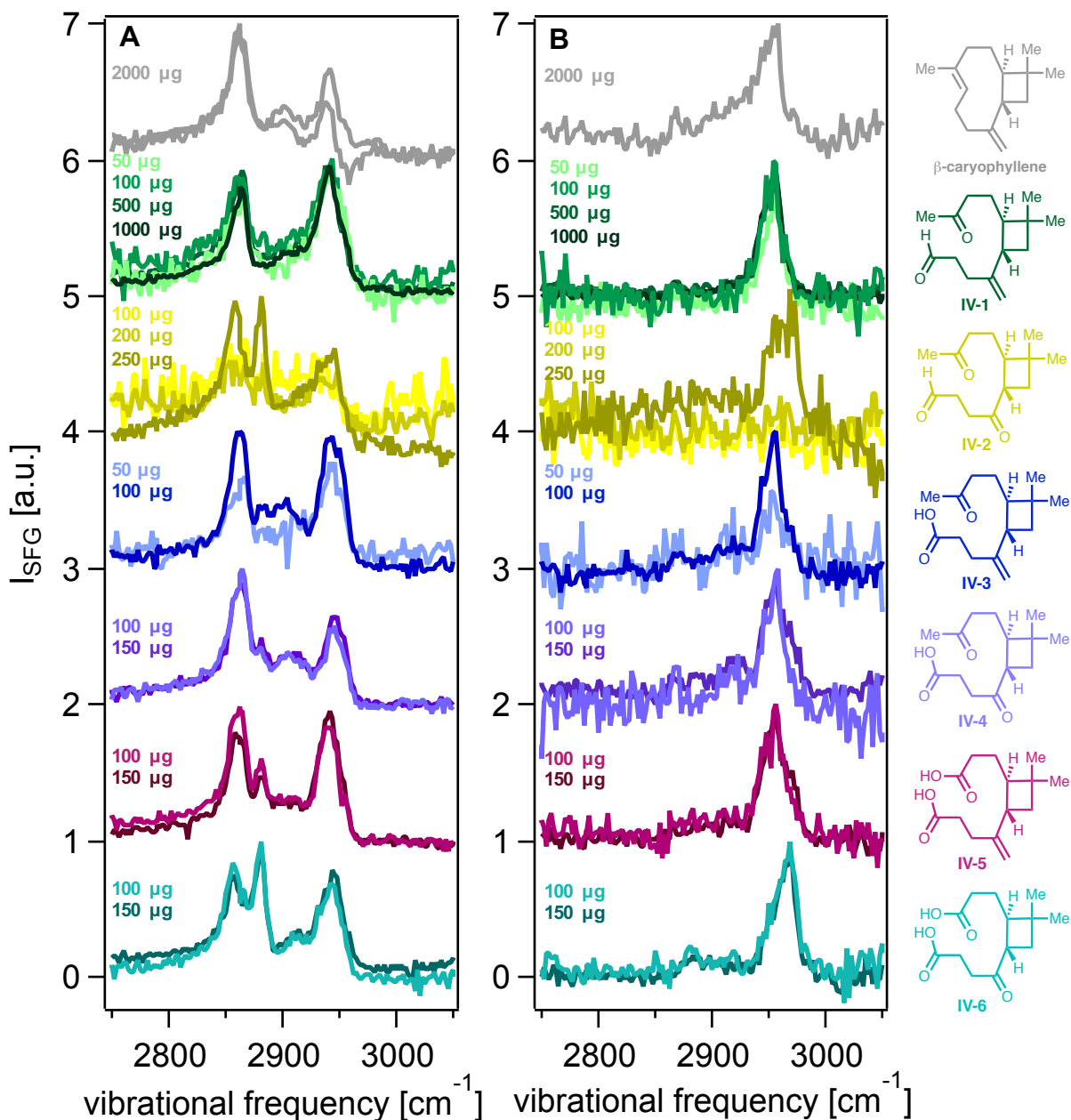


**Figure A2.8.** Individual (A) *ssp*- and (B) *ppp*-polarized HR SFG spectra of  $\beta$ -caryophyllene oxidation products at varying amounts of sample spread on the surface of 1 M  $(\text{NH}_4)_2\text{SO}_4$  (aq) collected in the C–H region. Each spectrum is an average of triplicate or quadruplet spectra.

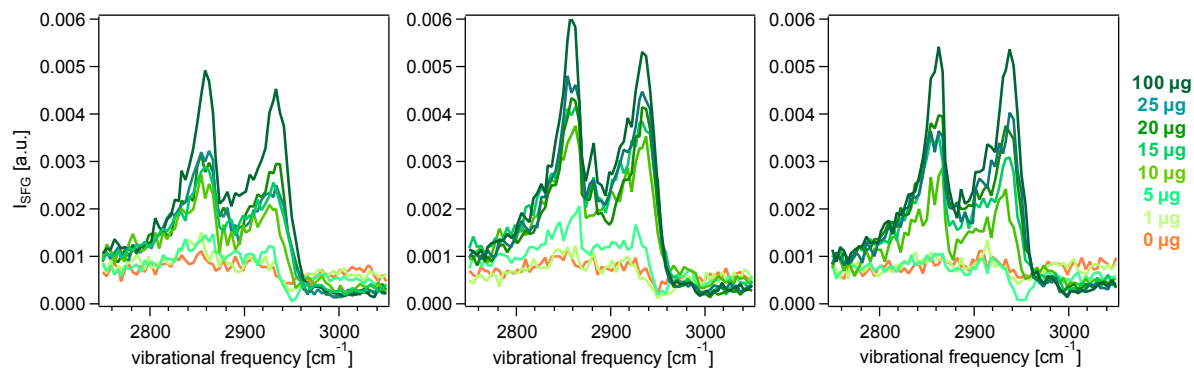


**Figure A2.9.** Individual *ssp*-polarized SFG spectra of  $\beta$ -caryophyllene aldehyde (IV-1) on 1 M  $(\text{NH}_4)_2\text{SO}_4$  (aq) at varying sample amounts (0–100  $\mu\text{g}$ ) collected in the C–H region.

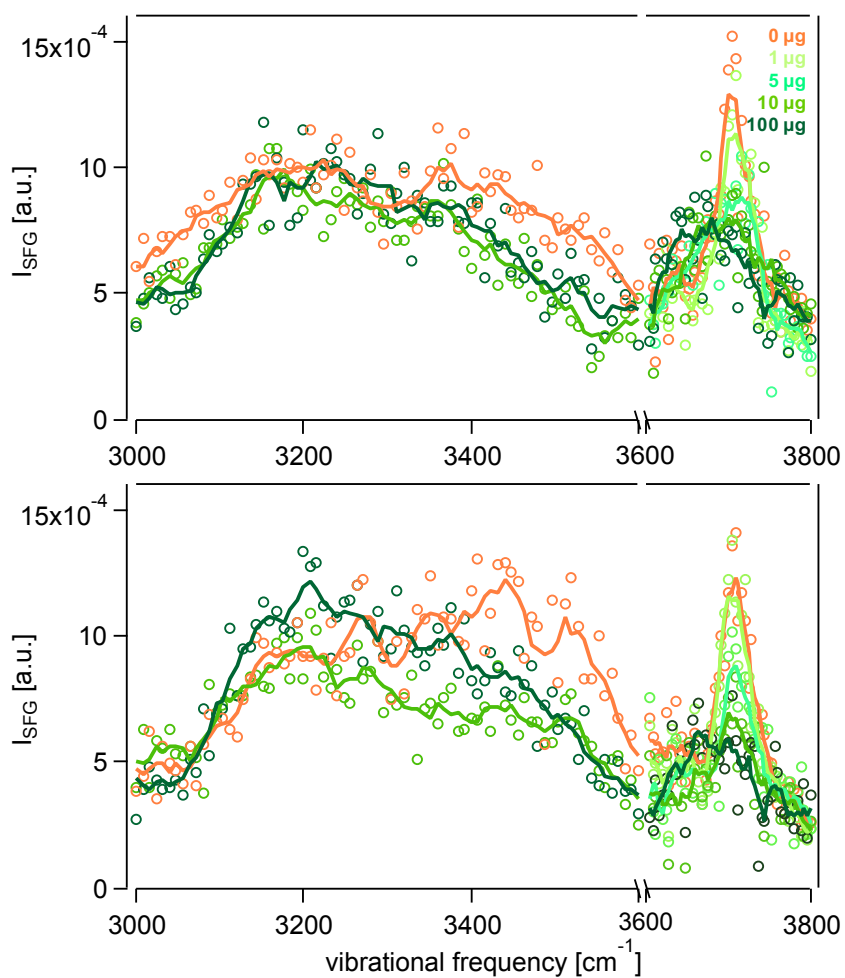


**Figure A2.10.** Individual *ssp*-polarized SFG spectra in the O–H stretching region of  $\beta$ -caryophyllene aldehyde (**IV-1**) on 1 M  $(\text{NH}_4)_2\text{SO}_4$  (aq) at varying sample amounts (0–100  $\mu\text{g}$ ).

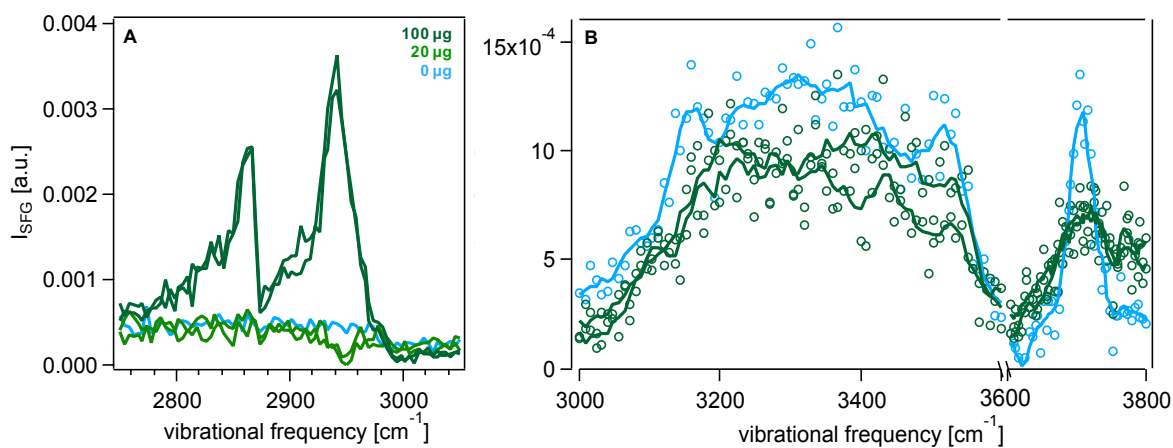


**Figure A2.11.** Duplicate *ssp*-polarized SFG spectra in the (A) C–H region and (B) O–H stretching region of  $\beta$ -caryophyllene aldehyde (**IV-1**) on neat water at 0, 20, and 100  $\mu\text{g}$ .

**Appendix 2 references.**

1. Hore, D. K.; Hamamoto, M. Y.; Richmond, G. L., Mid-infrared second-order susceptibility of  $\alpha$ -quartz and its application to visible-infrared surface sum-frequency spectroscopy. *J. Chem. Phys.* **2004**, *121* (24), 12589-12594.
2. Ho, J.; Psciuk, B. T.; Chase, H. M.; Rudshteyn, B.; Upshur, M. A.; Fu, L.; Thomson, R. J.; Wang, H.-F.; Geiger, F. M.; Batista, V. S., Sum Frequency Generation Spectroscopy and Molecular Dynamics Simulations Reveal a Rotationally Fluid Adsorption State of  $\alpha$ -Pinene on Silica. *J. Phys. Chem. C* **2016**, *120*, 12578-12589.
3. Mifflin, A. L.; Velarde, L.; Ho, J.; Psciuk, B. T.; Negre, C. F.; Ebben, C. J.; Upshur, M. A.; Lu, Z.; Strick, B. F.; Thomson, R. J.; Batista, V. S.; Wang, H.-F.; Geiger, F. M., Accurate Lineshapes from Sub-1  $\text{cm}^{-1}$  Resolution Sum Frequency Generation Vibrational Spectroscopy of  $\alpha$ -Pinene at Room Temperature. *J. Phys. Chem. A* **2015**, *119*, 1292-1302.
4. Wang, H.-F.; Gan, W.; Lu, R.; Rao, Y.; Wu, B. H., Quantitative Spectral and Orientational Analysis in Surface Sum Frequency Generation Vibrational Spectroscopy (SFG-VS). *Int. Rev. Phys. Chem.* **2005**, *24* (2), 191-256.
5. Wang, H.-F.; Velarde, L.; Gan, W.; Fu, L., Quantitative Sum-Frequency Generation Vibrational Spectroscopy of Molecular Surfaces and Interfaces: Lineshape, Polarization, and Orientation. *Annu. Rev. Phys. Chem.* **2015**, *66* (1), 189-216.

## Ariana Gray Bé

6218 N Lakewood Ave, Chicago, IL 60660 | agraybe@gmail.com | 216-659-8824

### EDUCATION

- Northwestern University** SEPT. 2015–DEC. 2019  
*Ph.D. in Chemistry*, GPA: 3.86/4.00 Evanston, IL
- Kellogg School of Management** JUNE–AUG. 2019  
 Management for Scientists & Engineers Certification Program
- Northwestern Center for Civic Engagement** APRIL–JUNE 2019  
 Graduate Engagement Opportunities Internship & Practicum
- Denison University** AUG. 2011–MAY 2015  
*B.S. in Chemistry, Minor in Vocal Music Performance*  
*magna cum laude*, GPA: 3.87/4.00 Granville, OH

### RESEARCH

- Graduate Student Researcher** NOV. 2015–DEC. 2019  
*Advisors: Prof. Regan Thomson & Prof. Franz Geiger* Northwestern University
- Probed the surface physicochemistry of biogenic aerosol particles to offer molecular insights into aerosol–climate interactions
  - Bridged together the disciplines of synthetic organic chemistry, surface spectroscopy, & atmospheric science
  - Collaborated with 12 research institutions within the US & internationally: Traveled to 2 labs to carry out on-site experiments, synthesized molecular reference standards for 6 collaborations, & self-initiated 1 new collaboration
  - Mentor 2 graduate students & previously 1 undergraduate in organic synthesis, surface tensiometry, & nonlinear spectroscopy
  - Manage group meeting schedule, troubleshoot spectrometers, & have previously served as safety designate for research labs
- Summer Research Assistant** JUNE 2015–AUG. 2015  
*Advisor: Prof. Michael Wasielewski* Northwestern University
- Synthesized photoactive aromatic hydrocarbons for singlet fission analysis by ultra-fast transient absorption spectroscopy
- Undergraduate Student Researcher** NOV. 2012–MAY 2015  
*Advisor: Prof. Joseph Reczek* Denison University
- Synthesized polycyclic aromatic molecules & incorporated them into self-assembling donor–acceptor columnar liquid crystals

- Examined structure–property relationships of donor–acceptor columnar liquid crystals for organic photovoltaic applications
- Trained 1 undergraduate & 1 high school student in liquid crystalline materials characterization techniques

---

 HONORS
 

---

<b>National Science Foundation Graduate Research Fellowship</b>	SEPT. 2016–SEPT. 2019
<b>Phi Beta Kappa Honor Society</b>	MAY 2015–PRESENT
<b>Sigma Xi Scientific Research Honor Society</b>	JAN. 2015–PRESENT
<b>Gordon Research Conference Young Investigator Award</b>	JUNE 2018
<b>Northwestern Building on Diversity PPG Diversity Award</b>	DEC. 2017
<b>Northwestern Presidential Fellowship Finalist (1 of 2 Chemistry nominees)</b>	NOV. 2017
<b>Denison Department of Chemistry &amp; Biochemistry Ebaugh Award</b>	APRIL 2015
<b>ACS Division of Inorganic Chemistry Undergraduate Award</b>	APRIL 2015
<b>Columbus Local ACS section Chemistry Achievement Award</b>	APRIL 2015
<b>ACS Division of Organic Chemistry Travel Award</b>	MARCH 2015
<b>Anderson Research Assistantship Award in the Sciences</b>	JUNE 2014–AUG. 2014
<b>E. Stanley Melick Chemistry Scholar</b>	SEPT. 2014–MAY 2015
<b>Denison Chemistry Emeritus Faculty Scholarship</b>	JAN. 2014–MAY 2015
<b>Denison Gillingham Award</b>	SEPT. 2013–MAY 2015
<b>Denison Tyree/Paragon Half-Tuition Merit Scholarship</b>	SEPT. 2011–MAY 2015
<b>Denison Dept. of Music Karl Eschman Memorial Scholarship</b>	SEPT. 2011–MAY 2015

---

 PUBLICATIONS
 

---

- Bé, A. G.**,<sup>‡</sup> Liu, Y.;<sup>‡</sup> Tuladhar, A.; Bellcross, A. D.; Wang, Z.; Thomson, R. J.; Geiger, F. M. Surface-Active  $\beta$ -Caryophyllene Oxidation Products at the Air/Aqueous Interface. *ACS Earth Space Chem.* **2019**, *3* (9), 1740–1748.
- Upshur, M. A.;<sup>‡</sup> Vega, M. M.;<sup>‡</sup> **Bé, A. G.**,<sup>‡</sup> Chase, H. M.; Zhang, Y.; Tuladhar, A.; Chase, Z. A.; Fu, L.; Ebben, C. J.; Wang, Z.; Martin, S. T.; Geiger, F. M.; Thomson, R. J. Synthesis & Surface Spectroscopy of  $\alpha$ -Pinene Isotopologues & their Corresponding Secondary Organic Material. *Chem. Sci.* **2019**, *10* (36), 8390–8398.
- Bé, A. G.**,<sup>‡</sup> Chase, H. M.;<sup>‡</sup> Liu, Y.; Upshur, M. A.; Zhang, Y.; Tuladhar, A.; Chase, Z. A.; Bellcross, A. D.; Wang, H.-F.; Wang, Z.; Batista, V. S.; Martin, S. T.; Thomson, R. J.; Geiger, F. M. Atmospheric  $\beta$ -Caryophyllene-Derived Ozonolysis Products at Interfaces. *ACS Earth Space Chem.* **2019**, *3*, 158–169.
- Yee, L. D.; Isaacman-VanWertz, G.; Wernis, R. A.; Meng, M.; Rivera, V.; Kreisberg, N. M.; Hering, S. V.; Bering, M. S.; Glasius, M.; Upshur, M. A.; **Bé, A. G.**; Thomson, R. J.; Geiger, F. M.; Offenberg, J. H.; Lewandowski, M.; Kourtchev, I.; Kalberer, M.; de Sá, S.; Martin, S. T.; Alexander, M. L.; Palm, B. B.; Hu, W.; Campuzano-Jost, P.; Day, D. A.; Jimenez, J. L.; Liu, Y.; McKinney, K. A.; Artaxo, P.; Viegas, J.; Manzi, A.; Oliveira, M. B.;

- de Souza, R.; Machado, L. A. T.; Longo, K.; Goldstein, A. H., Observations of Sesquiterpenes & their Oxidation Products in Central Amazonia During the Wet & Dry Seasons. *Atmos. Chem. Phys.* **2018**, *18*, 10433–10457.
- Doğangün, M.; Ohno, P. E.; Liang, D.; McGeachy, A. C.; **Bé, A. G.**; Dalchand, N.; Li, T.; Cui, Q.; Geiger, F. M., Hydrogen-Bond Networks Near Supported Lipid Bilayers from Vibrational Sum Frequency Generation Experiments & Atomistic Simulations. *J. Phys. Chem. B* **2018**, *122*, 4870–4879.
- Bé, A. G.**; Upshur, M. A.; Liu, P.; Martin, S. T.; Geiger, F. M.; Thomson, R. J. Cloud Activation Potentials for Atmospheric  $\alpha$ -Pinene &  $\beta$ -Caryophyllene Ozonolysis Products. *ACS Cent. Sci.* **2017**, *3*, 715–725.
- Zhang, X.; Lambe, A. T.; Upshur, M. A.; Brooks, W. A.; **Bé, A. G.**; Thomson, R. J.; Geiger, F. M.; Surratt, J. D.; Zhang, Z.; Gold, A.; Graf, S.; Cubison, M. J.; Groessl, M.; Jayne, J. T.; Worsnop, D. R.; Canagaratna, M. R. Highly Oxygenated Multifunctional Compounds in  $\alpha$ -Pinene Secondary Organic Aerosol. *Env. Sci. Technol.* **2017**, *51*, 5932–5940.
- Bé, A. G.**; Tran, C.; Sechrist, R.; Reczek, J. J. Strongly Dichroic Organic Films via Controlled Assembly of Modular Aromatic Charge-Transfer Liquid Crystals. *Org. Lett.* **2015**, *17*, 4834–4837.
- Thompson, A. C.; Grimm, H. M.; **Bé, A. G.**; McKnight, K. J.; Reczek, J. J. Efficient Bromination of Naphthalene Dianhydride & Microwave Assisted Synthesis of Core-Brominated Naphthalene Diimides. *Synth. Comm.* **2015**, *45*, 1127–1136.

## LEADERSHIP & OUTREACH

### Northwestern Building on Diversity (NU Bond)

JULY 2017–DEC. 2019

#### Co-Leader

Northwestern University

- Coordinate Faces of Science seminar series showcasing scientists for both their science achievements & diversity efforts
- Organize community workshops to discuss social identity & promote inclusivity within the Department of Chemistry
- Volunteer at Museum of Science & Industry Black Creativity Program & present hands-on chemistry demonstrations
- Write & edit grant applications for sponsorship & funding of NUBonD events

### Women in Science & Engineering Research (WISER)

SEPT. 2016–AUG. 2019

#### Various Board Roles

Northwestern University

- Vice-President (2018–2019): Plan professional development events for STEM women & write grant applications
- Outreach Volunteer (2018): Presented on famous female scientists at HerStory event at Museum of Science & Industry
- Events Coordinator (2017–2018): Managed event planning & other logistics for WISER

workshops & seminars

- Publicity Chair (2016–2017): Enhanced WISER's social media presence & advertised upcoming events

**Phi Lambda Upsilon (PLU) Chemistry Honorary Society** SEPT. 2017–DEC. 2019  
*Social Chair & Member* Northwestern University

- Co-Social Chair (2017–2018): Organized monthly PLU events to promote cohort bonding & community building within the Dept. of Chemistry
- Selected to speak on PLU panel for first-year graduate students entitled “Choosing a Research Group” (5/300 selected)
- Elected to serve on decision committee for Lambert award given to a second year graduate student (3/60 selected)

**CHEMunity Mentoring Program** JULY 2017–DEC. 2019  
*Graduate Student Mentor* Northwestern University

- Advise incoming students on lab selection process, graduate classes, TA responsibilities, & life as an NU graduate student

**Environmental Law & Policy Center (ELPC)** APRIL 2019–JUNE 2019  
*Intern through Northwestern Center for Civic Engagement* ELPC headquarters, Chicago, IL

- Worked on Air Quality Team to improve & expand community PM2.5 monitoring programing in Chicago & the Midwest
- Mapped & analyzed satellite PM2.5 data using ArcGIS to pinpoint poor air quality regions in need of ELPC monitoring

**Denison Department of Chemistry & Biochemistry** SEPT. 2014–MAY 2015  
*Senior Department Fellow* Denison University

- Awarded senior fellow for Dept. of Chemistry & Biochemistry (2/35 selected)
- Served as a student leader for the department & liaison connecting students to faculty

**Denison Chemical Society** SEPT. 2014–MAY 2015  
*Vice-President* Denison University

- Coordinated department community events & science outreach events in the Greater Columbus area for students ages 6 to 18

## TEACHING

**Co-Instructor, Weinberg Bridge II Program** SEPT. 2018  
*Preparation in organic chemistry* Northwestern University

**Private Student Tutor** JAN. 2015–AUG. 2019  
*Undergraduate general & organic chemistry* Northwestern University

**Laboratory Teaching Assistant** SEPT. 2015–JULY 2016  
*Undergraduate organic chemistry* Northwestern University

<b>Laboratory Teaching Assistant</b> <i>General, organic, bio, &amp; analytical chemistry</i>	SEPT. 2012–MAY 2015 Denison University
<b>Academic Support &amp; Enrichment Tutor</b> <i>General &amp; organic chemistry</i>	JAN. 2013–MAY 2015 Denison University
<b>Dept. of Chemistry &amp; Biochemistry Tutor</b> <i>General chemistry, organic chemistry, &amp; biochemistry</i>	JAN. 2015–MAY 2015 Denison University

---

**CONFERENCES & PRESENTATIONS**

<b>ACS National Meeting</b> <i>Oral Presentation (Physical Division)</i>	AUG. 2019 San Diego, CA
<b>Pacific Conference on Spectroscopy &amp; Dynamics</b> <i>Poster Presentation – Awarded Graduate School &amp; PLU Travel Grants</i>	JAN. 2019 San Diego, CA
<b>AVS International Symposium</b> <i>Invited Oral Presentation</i>	OCT. 2018 Long Beach, CA
<b>GRC: Biogenic Hydrocarbons &amp; the Atmosphere</b> <i>Invited Oral Presentation – Young Investigator Award Winner</i>	JUNE 2018 Les Diablerets, Switzerland
<b>AGU Annual Meeting</b> <i>Poster Presentation – NU BonD PPG Diversity Travel Awardee</i>	DEC. 2017 New Orleans, LA
<b>Chautauqua on Nonlinear Optics</b> <i>Workshop &amp; Lightning Talk Presentation</i>	JUNE 2017 West Lafayette, IN
<b>Chicago Organic Symposium</b> <i>Poster Presentation</i>	OCT. 2016 Chicago, IL
<b>ACS National Meeting</b> <i>Poster Presentation (Organic Division)</i>	MARCH 2015 Denver, CO
<b>ACS National Meeting</b> <i>Poster Presentation (Chemical Education Division)</i>	MARCH 2014 Dallas, TX

## Ladder Polyether Polymers Enabled by Biomimetic Epoxide-Opening Cascades

Ariana Gray Bé

### **Abstract.**

Ladder polymers are an intriguing class of macromolecules comprised of consecutively fused two-bond ring linkages. While ladder polymers have been a subject of research interests for over fifty years, polymers in this class are largely limited to structures consisting of aromatic building blocks. With the goal of expanding upon the current synthetic methods available to synthesize ladder polymers, this proposal seeks to add a novel structural scaffold to the polymer chemistry toolbox through the design and development of a new class of non-aromatic macromolecules, termed ladder polyether polymers. The proposed ladder polyether polymer architecture contains an unprecedented aliphatic backbone comprised of fused, alternating cyclic tetrahydropyran rings. Here, we outline a synthetic methodology for accessing these polymers by leveraging biomimetic epoxide-opening cascades, analogous to those proposed in the biosynthetic pathway of the marine ladder polyether small molecule family. Through an iterative design, synthesis, and characterization strategy, this proposal seeks to explore the fundamental structure–property relationships of this new class of ladder polyether polymers to assess their currently unrealized functionalities.

## 1. Introduction, background, and significance of the research.

**1.1. A new structural scaffold for the polymer chemistry toolbox.** Expanding synthetic methodologies to access new polymer architectures with unexplored structure–property relationships is requisite for advancing the rational design and development of functional polymeric materials.<sup>1,2</sup> Distinct from the majority of polymer structures, which consist of repeat units connected through one bond, ladder polymers are an intriguing class of macromolecules comprised of consecutive backbone units fused together via two bonds.<sup>1, 3-4</sup> Such fused ring linkages lead to restricted conformational freedom, and the resulting rigidity of these polymers has been predicted to impart increased resistance to thermal, chemical, and/or mechanical degradation than their linear counterparts.<sup>1,3-5</sup> However, ladder polymers remain challenging to synthesize, and their intrinsic rigidity leads to poor solubility that continues to hamper comprehensive structural characterization and well as necessary processing for various applications.<sup>1, 6</sup> Furthermore, although ladder polymers have been a subject of research interests for over fifty years, polymers in this class are largely limited to structures consisting of aromatic building blocks in either non-conjugated (i.e. kinked) and conjugated (i.e. planar) structural motifs, which are predominantly designed for applications in gas separation membranes or organic electronics, respectively (**Figure 1A**).<sup>1, 6-8</sup> Therefore, expanding upon the current synthetic methods to synthesize ladder polymers remains critical to both addressing the aforementioned current limitations and diversifying the polymer structures within this elusive class of materials.

To meet this challenge, the proposed work focuses on developing a synthetic approach to access a new class of polymers containing an aliphatic backbone comprised of fused, alternating cyclic tetrahydropyran (THP) rings — ladder polyether polymers. The unique combination between ladder polymer and polyether properties make the proposed scaffold an attractive new

target architecture. For instance, we predict that the proposed ladder polyether polymers would exhibit increased structural flexibility compared to previously synthesized ladder polymers, as ladder polymers containing aliphatic cyclohexyl and cyclooctyl rings have been found to possess semi-flexible backbones with partial bending freedom.<sup>9-10</sup> By preserving the contiguous ladder backbone, the proposed ladder polyethers would concurrently offer a more rigid alternative to existing polyethers — namely, epoxy resins and linear polymers, such as polyethylene glycol (PEG), polypropylene glycol (PPG), and polytetrahydrofuran (**Figure 1B**) — which are highly flexible and relatively noncrystalline.<sup>2, 11-12</sup> Additionally, hydrophilicity induced by the ether bridges in polyethers cannot be matched by a purely carbon-based backbone, thus potentially leading to improved solubility in polar environments.<sup>2</sup> Such desirable characteristics in the proposed ladder polyether polymers (**Figure 1C**) will ultimately enable new functionality within traditional polyether applications across the pharmaceutical, cosmetic, and biomedical worlds.

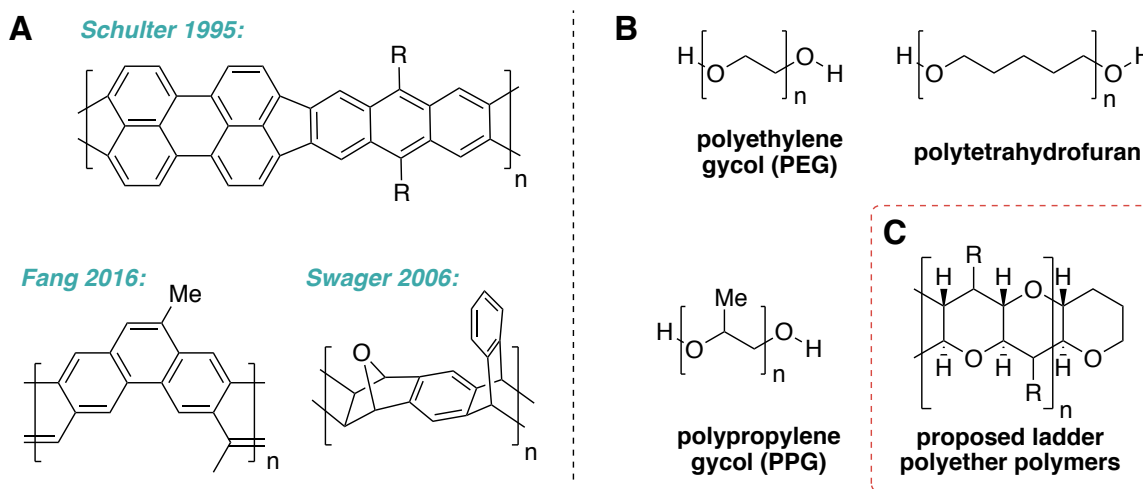


**Figure 1.** Examples of (A) previously reported ladder polymers<sup>1, 6-8</sup> and (B) prevalently used polyether polymers. (C) Proposed ladder polyether polymer structure.

**1.2. Biomimetic polymer synthesis inspired by ladder polyether natural products.** The methodology to synthesize ladder polyether polymers outlined herein is motivated by the

biosynthesis of cyclic polyether natural products, an intriguing class of bioactive compounds comprised of one or more ether rings ranging from 5- to 9-membered in size.<sup>13-14</sup> Cyclic polyether natural products are derived from the polyketide biosynthetic pathway, and it is believed that late-stage modifications of the polyketide chain give rise to the distinctive polyether frameworks in these molecules.<sup>13-15</sup> Isolated from both terrestrial and marine sources, small molecule natural products bearing cyclic polyether motifs include polyether ionophores, marine ladder polyethers, and plant-derived Annonaceous acetogenins.<sup>14, 16</sup>

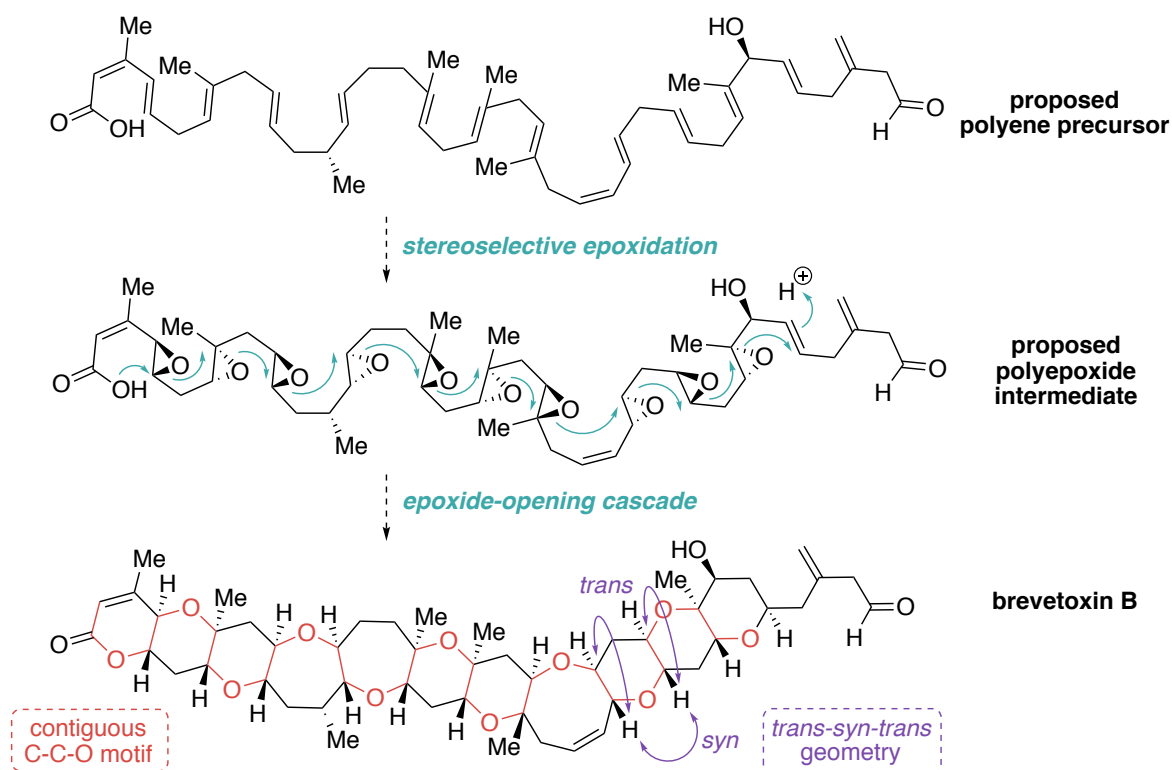


**Figure 2.** Speculated epoxide-opening cascade in the biosynthesis of marine ladder polyethers and structure of brevetoxin B, an example natural product in this class of small molecules (figure adapted from refs. 16 and 17).<sup>16-17</sup>

Interestingly, the marine ladder polyether class of natural products uniquely exhibit a double-stranded *trans-syn-trans* ladder framework comprised of a contiguously fused ring system with alternating ether bridges,<sup>13, 15-16, 18-19</sup> which is the structural scaffold of interest in this work.

In the late-stage biosynthetic pathway of marine ladder polyethers, it is speculated that a mono-oxygenase enzyme catalyzes an asymmetric epoxidation on either the *Re* or the *Si* face of a precursor polyene containing all *trans* double bonds. Subsequently, the stereochemically uniform polyepoxide intermediate (with all-(R,R) or all-(S,S) *trans*-epoxides) undergoes an intramolecular cyclization via a cascade of S<sub>N</sub>2 epoxide openings.<sup>13-14, 16</sup> Inspired by this proposed biosynthesis of the marine ladder polyether natural product family, this proposal seeks to apply analogous epoxide-opening cascades to the development of a new ladder polyether polymer architecture.

## **2. Scientific objectives.**

The overarching objective of this proposed work is to develop a methodology to utilize biomimetic epoxide-opening cascades in the design, synthesis, and characterization of a new class of ladder polyether polymeric materials. Specifically, we aim to synthesize a suite of polymers that contain the unprecedented polycyclic ether backbone by leveraging epoxide-opening cascades, analogous to those proposed in the biosynthetic pathway of ladder polyether small molecules. The proposed method design would enable chemically diverse polymer architectures to be assembled by adding ring substituents and/or changing backbone ring size according to the desired polymer property and functionality. Provided that the reaction methodology is accomplishable, we subsequently aim to iteratively characterize the fundamental structure–property relationships of this new class of ladder polyether polymers to assess their potential for materials and biological applications.

## **3. Previous work.**

Given that proposed synthetic route to the desired ladder polyether polymer architecture hinges on accomplishing the post-polymerization biomimetic epoxide-opening cascade, a brief overview of literature precedent for mechanistic postulations and method developments related to

this key transformation follows. As mentioned above, the distinct stereochemically uniform contiguously fused THP backbone of marine ladder polyethers is believed to arise from a series of  $S_N2$  epoxide-opening events originating from a polyepoxide intermediate. While this proposed epoxide-opening cascade mechanism, originally put forth by Nakanishi and coworkers,<sup>20-21</sup> accounts for the characteristic O-C-C backbone and *trans-syn* topography in these molecules, it is predicted to proceed via disfavored 6-*endo*-tet ring closures that violate Baldwin's rules for ring-closing reactions (**Figure 3A**).<sup>14, 17, 22</sup> According to Baldwin's rules, intramolecular epoxide-opening favors formation the *spiro 5-exo*-tet transition state, as is observed in the terrestrial polyether natural products (i.e. *Streptomyces*-produced polyether ionophores and plant-derived Annonaceous acetogenins).<sup>13-16</sup>

Consequently, inquiries into how *endo*-selective cascades in marine ladder polyether biosynthesis overcome the inherent bias for smaller rings in epoxide-opening reactions have revealed several mechanistic postulations. Among them, it has been proposed that an epoxide hydrolase-type enzyme may direct each *endo*-closure,<sup>14, 19</sup> that the unique combination of substrate and solvent conditions may influence the anti-Baldwin outcome,<sup>17, 23</sup> and that a starter ring scaffold may initiate the traditionally unfavorable mechanism.<sup>17, 24-25</sup> With dual motivations to investigate the discussed mechanistic questions and to develop methodologies towards the total synthesis of marine ladder polyether natural products, the groups of Murai,<sup>26</sup> Jamison,<sup>17, 24-25, 27</sup> McDonald,<sup>28</sup> and Floreancig<sup>29</sup> have reported various methods to perform 6-*endo*-tet-selective epoxide-opening cascades.

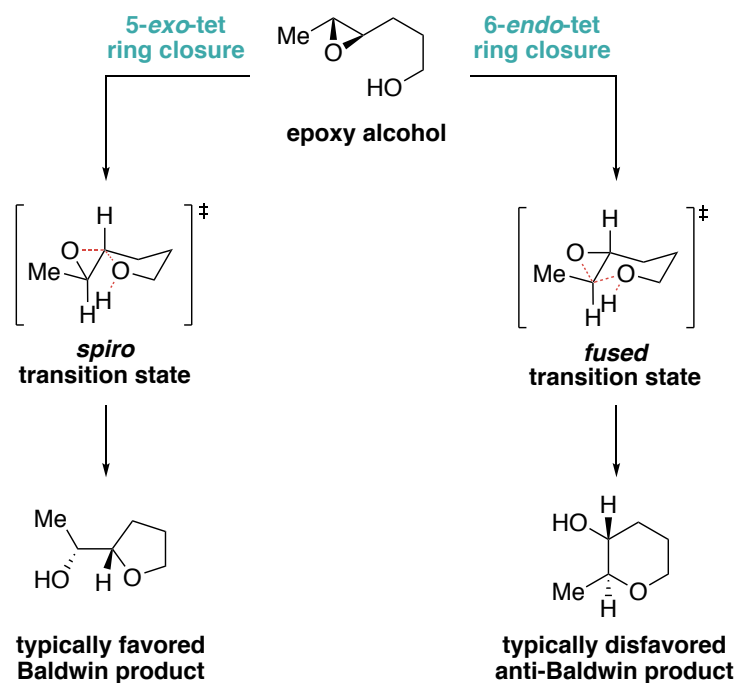


**Figure 3.** Outcome of expected products for intramolecular cyclization of an epoxy alcohol via epoxide opening (figure adapted from refs. 16 and 17).<sup>16-17</sup>

While the majority of strategies have relied on directing groups in conjunction with Lewis or Brønsted acid activators,<sup>22, 24, 26, 28-29</sup> Jamison and coworkers extensively reported on method development for epoxide-opening cascades using a “directing-group-free” approach involving a templated system and neutral water as the reaction promoter.<sup>17</sup> Subjecting a THP-templated epoxy alcohol to a range of Brønsted and Lewis acids and bases, solvents, and additives, Jamison and coworkers discovered that the selectivity for the *endo*-closed THP product over the *exo*-closed THF product increased significantly in polar protic solvents compared to less polar or aprotic solvents.<sup>17</sup> Interestingly, neutral deionized water was found to impart the highest rate acceleration and THP:THF selectivity (>10:1) of all reaction conditions screened (**Figure 3B**).<sup>17</sup> A follow up kinetic study on this water-promoted *endo*-selective epoxide-opening cascade of a THP-templated epoxy alcohol demonstrated that the transformation proceeds via a stepwise mechanism, rather

than a concerted pathway, and becomes both faster and more selective (THP:THF regioselectivity = 19:1) following the first cyclization.<sup>23</sup>

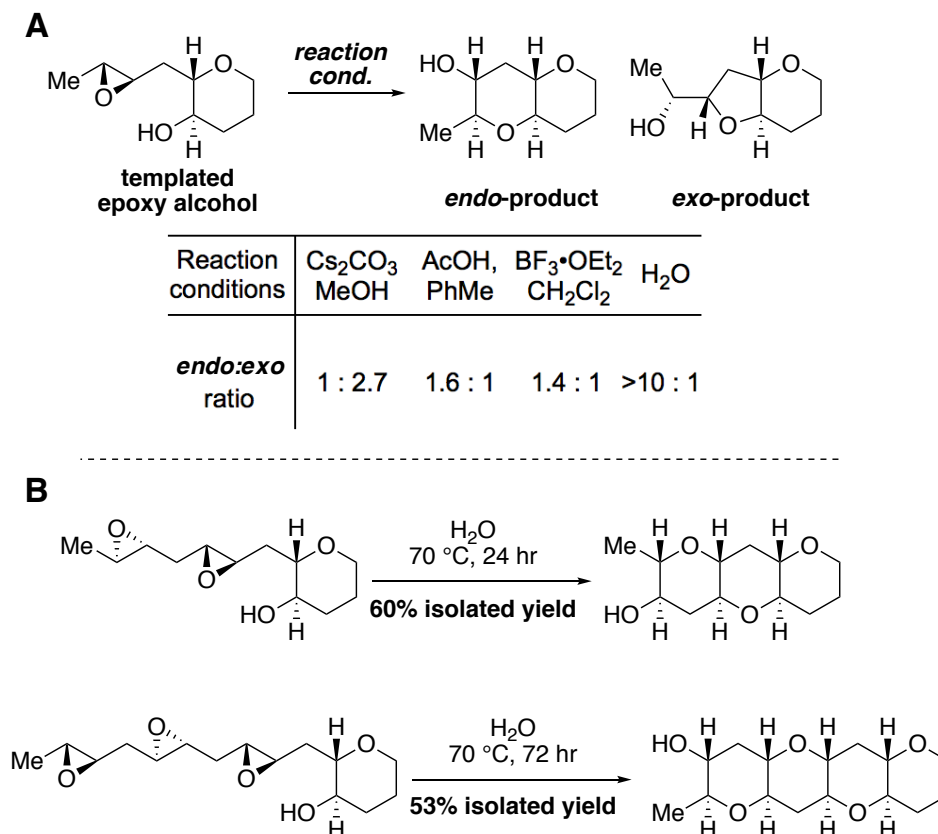


**Figure 4.** Overview of work by Jamison and coworkers on (A) screening reaction conditions for epoxide-opening of templated epoxy alcohol and (B) H<sub>2</sub>O-promoted epoxide-opening cascades.<sup>16-17</sup>

Taken together, their findings highlight that (1) selectivities and yields are significantly improved by appending a tetrahydropyran “template” to the epoxide chain, suggesting that a template may serve as a proxy for conformational constraints imposed by an enzyme active site, and (2) water is an important promoter in the anti-Baldwin cascade mechanism, implying that epoxide activation upon hydrogen-bonding to water is a key promoter in the biosynthesis of marine ladder polyether natural products.<sup>17, 23</sup> The latter is also interesting given that, in contrast to land-derived polyethers, which predominantly contain unfused *exo*-rings, polyether natural products produced in aqueous, marine environments distinctly contain the fused ladder framework produced

via *endo*-selective epoxide opening.<sup>14, 17</sup> Inspired by such findings reported by the Jamison lab, this proposal seeks to apply analogous water-promoted epoxide-opening cascades in the synthesis of new ladder polyether polymers.

#### 4. Proposed research.

In order to test the discussed methodology by Jamison and coworkers on epoxide-opening cascades for use in the development of ladder polyether polymers, a stereouniform precursor polyepoxy alcohol that is poised to undergo the desired intramolecular cyclization must first be synthesized. Thus, the overall proposed synthetic route utilizes the following: (1) ring opening metathesis polymerization (ROMP) of a cyclopropene monomer with end functionalization using a masked aldehyde terminating agent to furnish a 1,4-polyene, (2) post-polymerization modifications, namely an aldehyde reduction and a stereoselective epoxidation, and (3) the key epoxide-opening cascade promoted by water (**Figure 5**).

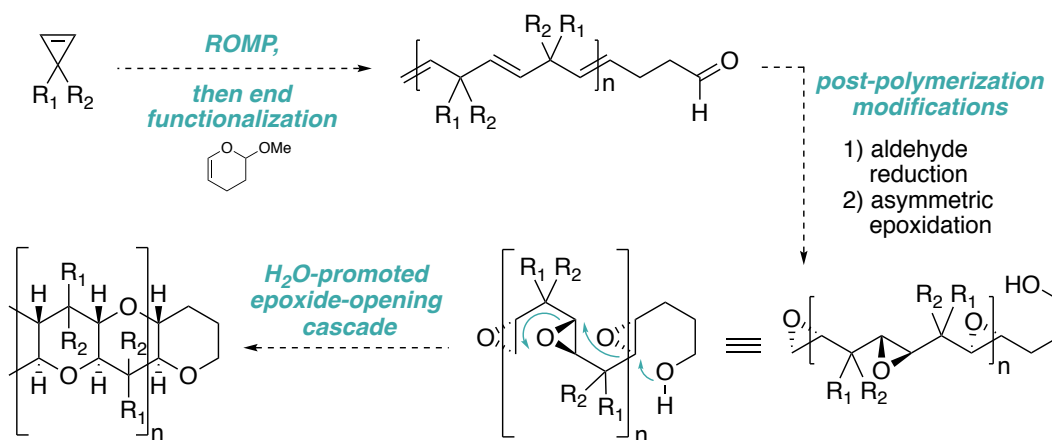


**Figure 5.** Proposed synthetic route for the development of ladder polyether polymers.

**4.1. Cyclopropene ring opening metathesis polymerization.** To synthesize the desired 1,4-polyene, we propose to carry out ROMP of various substituted cyclopropane monomers. Methods for the synthesis of a wide range of 1,2- and 3,3-disubstituted cyclopropenes that are stable at ambient conditions have been previously established.<sup>30</sup> ROMP of disubstituted cyclopropenes

using both molybdenum<sup>31</sup> and ruthenium<sup>32</sup> catalysts has recently been shown to yield 1,4-polyenes with controllable molecular weights and low polydispersities.<sup>31-32</sup> Given the anticipated instabilities of some cyclopropene monomers, potential for structural defects (e.g. branching, crosslinking), and challenges with improving molar mass distributions, we will iteratively explore a range of substituted cyclopropene monomers, solvent conditions, and ROMP catalysts to optimize the polymerization event. To set the stage for the final epoxide-opening cascade, an end-capping hydroxyl moiety is also needed. Functional terminating agents leading to aldehyde end-functional ROMP polymers have recently been reported by Kilbinger and coworkers.<sup>33</sup> In particular, the terminating agent, 2-methoxy-3,4-dihydro-2H-pyran (MDHP), which is commercially available, has been shown to regioselectively add to propagating ruthenium carbenes and subsequently undergo spontaneous decomposition into an aldehyde end group on a polymer chain (**Figure 6**).<sup>33</sup>

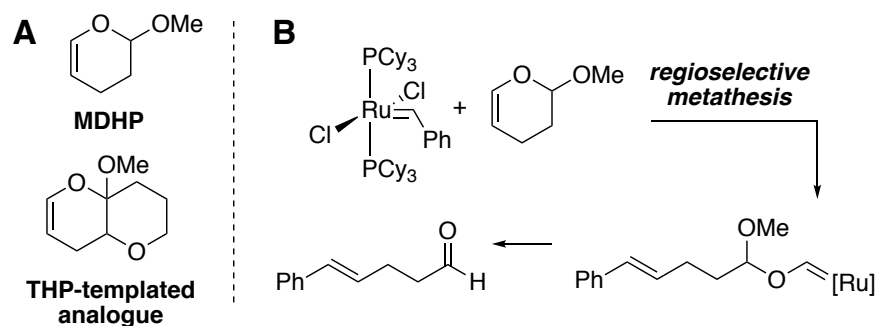


**Figure 6.** (A) Proposed terminating agents for (B) aldehyde end functionalization of ROMP polymers reported by Kilbinger and coworkers (figure adapted from ref. 33).<sup>33</sup>

The nature of the terminating agent is will be closely evaluated, beginning with MDHP and subsequently moving to a “templated” analogue, due to the aforementioned expected improvements in regioselectivities and yields. If the aldehyde end group is found to be reactive or otherwise unstable to the polymerization conditions, or if challenges arise with the regioselective

formation of the Fischer carbene and acetal decomposition to aldehyde, we will explore alternative nucleophilic end groups, such as a primary amine end group or a piperidine template.

**4.2. Post-polymerization modifications.** Provided that the desired 1,4-polyene could be furnished, we next propose to carry out a post-polymerization reduction of the aldehyde end group, followed by a stereoselective epoxidation of the polyene to yield the desired stereouniform polyepoxide intermediate for the key epoxide-opening/intramolecular cyclization cascade. For the stereoselective epoxidation step, we will begin by employing a fructose-derived ketone and Oxone mediated approach reported by Shi and coworkers,<sup>34</sup> which was previously used by Jamison and coworkers in their epoxide-opening method development studies.<sup>17</sup> While we do not anticipate challenges to arise during these modification steps, if unforeseen issues arise, a diverse host of conditions for aldehyde reductions as well as stereoselective epoxidations (e.g. Sharpless conditions, vanadium-catalyzed epoxidations, dioxirane-based approaches, etc.) exist for achieving the proposed post-polymerization reaction sequence.<sup>27, 35</sup>

**4.3. Epoxide-opening cascade leading to intramolecular cyclization.** At this stage, the polyepoxide polymer is poised to undergo the key biomimetic epoxide-opening cascade to afford the desired ladder polyether architecture. We will begin by comparing the THP-templated and non-templated analogues in aqueous conditions, to determine if the THP-template provides the expected enhancement in regioselectivity and yield.<sup>17</sup> Comparing across a range of pH and ionic strength values, we will evaluate if neutral deionized water is the optimal promoter for the intramolecular cyclization, as was previously reported.<sup>17</sup> If achieving notable regioselectivities, reaction rates, or yields for the epoxide-opening cascades prove to be challenging, we will turn to alternative methods using a traceless directing group, which have also been reported by the Jamison lab.<sup>22</sup>

**4.4. Characterization and further synthetic modifications.** With an initial ladder polyether polymer suite in hand, various polymer characterization techniques will be employed to determine the molecular structure and stability, molecular mass, thermal properties, persistence length and other mechanical properties, morphology, and multicomponent mixture characteristics, such as phase separation and compatibility with other materials (**Figure 7**). Key characterization techniques will include NMR, IR, MS (e.g. MALDI), GPC, DSC, TGA, viscometry, electron microscopies, scanning probe microscopies, and DMA, among other tools.

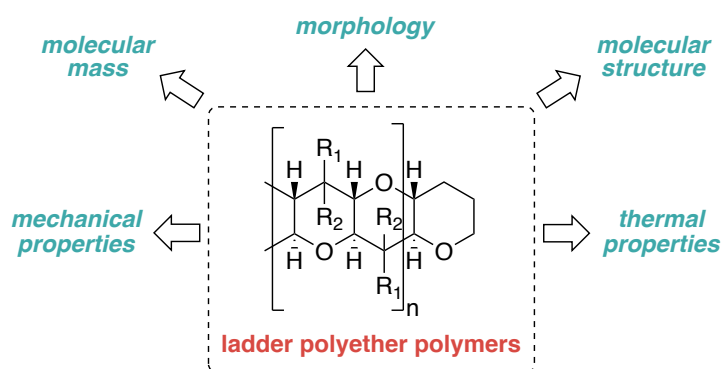


**Figure 7.** Overview of ladder polyether polymer characterization and analysis.

While we expect the synthesized ladder polyether polymers to have improved solubility over previously synthesized hydrocarbon-based ladder polymers, it is possible that solubility issues could make traditional polymer characterization methods difficult to carry out. Additionally, unanticipated complications, such as polymer instability during analysis could arise, making characterization challenging. We will address such contingencies as they arise by modifying the ring substituents as desired. Overall, the generalizability of this methodology will be investigated to include a variety of substituted cycloalkane starting monomers, which would yield a diverse array of polymer structures with targeted structure–property–function relationships.

## 5. Summary and conclusions.

The proposed work has detailed a synthetic method for accessing a new class of polymers, termed ladder polyether polymers, which contain an unprecedented polymer backbone comprised of a contiguously fused ring system with alternating ether bridges. This polymer architecture is inspired by the unique core scaffold of the marine ladder polyether natural product family and their proposed biosynthesis, via an endo-selective water-promoted epoxide-opening cascade leading to intramolecular cyclization. Our proposed synthetic route involves ROMP of a cyclopropene monomer with end functionalization using a masked aldehyde terminating agent to furnish an aldehyde end-capped 1,4-polyene that can be subsequently reduced, followed by a post-polymerization stereoselective epoxidation, and a final epoxide-opening cascade promoted by water to yield the desired ladder polyether polymer structure. The discussed methodology may be amenable to adjusting polymer structure through modifications to the ring substituents as well as ring size, enabling control over structure-dependent polymer properties and functions. The successful synthesis and characterization of ladder polyether polymers would likely lead to discovery of their currently unrealized uses in pharmaceutical, cosmetic, raw industrial materials, and biomedical applications.

**References.**

1. Teo, Y. C.; Lai, H. W. H.; Xia, Y., Synthesis of Ladder Polymers: Developments, Challenges, and Opportunities. *Chem. Eur. J.* **2017**, *23* (57), 14101-14112.
2. Herzberger, J.; Niederer, K.; Pohlit, H.; Seiwert, J.; Worm, M.; Wurm, F. R.; Frey, H., Polymerization of Ethylene Oxide, Propylene Oxide, and Other Alkylene Oxides: Synthesis, Novel Polymer Architectures, and Bioconjugation. *Chem. Rev.* **2016**, *116* (4), 2170-2243.
3. Zou, Y.; Ji, X.; Cai, J.; Yuan, T.; Stanton, D. J.; Lin, Y.-H.; Naraghi, M.; Fang, L., Synthesis and Solution Processing of a Hydrogen-Bonded Ladder Polymer. *Chem* **2017**, *2* (1), 139-152.
4. Mehta, G.; Viswanath, M. B.; Kunwar, A. C., Characterization of [n]-Ladderanes of Unprecedented Length: A New Record for Fused Carbocyclic Arrays. *J. Org. Chem.* **1994**, *59* (21), 6131-6132.
5. Gao, X.; Friščić, T.; MacGillivray, L. R., Supramolecular Construction of Molecular Ladders in the Solid State. *Angew. Chem. Int. Ed.* **2004**, *43* (2), 232-236.
6. Chen, Z.; Amara, J. P.; Thomas, S. W.; Swager, T. M., Synthesis of a Novel Poly(iptycene) Ladder Polymer. *Macromolecules* **2006**, *39* (9), 3202-3209.
7. Lee, J.; Rajeeva, B. B.; Yuan, T.; Guo, Z.-H.; Lin, Y.-H.; Al-Hashimi, M.; Zheng, Y.; Fang, L., Thermodynamic synthesis of solution processable ladder polymers. *Chem. Sci.* **2016**, *7* (2), 881-889.
8. Schlicke, B.; Schirmer, H.; Schlüter, A.-D., Unsaturated ladder polymers: Structural variations and improved molecular weights. *Adv. Mater.* **1995**, *7* (6), 544-546.
9. Wegener, S.; Muellen, K., New ladder polymers via repetitive Diels-Alder reaction under high pressure. *Macromolecules* **1993**, *26* (12), 3037-3040.
10. Pollmann, M.; Muellen, K., Semiflexible Ribbon-type Structures via Repetitive Diels-Alder Cycloaddition. Cage Formation versus Polymerization. *J. Am. Chem. Soc.* **1994**, *116* (6), 2318-2323.
11. Kawai, F.; Schink, B., The Biochemistry of Degradation of Polyethers. *Crit. Rev. Biotechnol.* **1987**, *6* (3), 273-307.
12. Jin, F.-L.; Li, X.; Park, S.-J., Synthesis and application of epoxy resins: A review. *J. Ind. Eng. Chem.* **2015**, *29*, 1-11.
13. Vilotijevic, I.; Jamison, T. F., Epoxide-Opening Cascades in the Synthesis of Polycyclic Polyether Natural Products. *Angew. Chem. Int. Ed.* **2009**, *48* (29), 5250-5281.

14. Gallimore, A. R., The biosynthesis of polyketide-derived polycyclic ethers. *Nat. Prod. Rep.* **2009**, *26* (2), 266-280.
15. Gallimore, A. R.; Spencer, J. B., Stereochemical Uniformity in Marine Polyether Ladders—Implications for the Biosynthesis and Structure of Maitotoxin. *Angew. Chem. Int. Ed.* **2006**, *45* (27), 4406-4413.
16. Vilotijevic, I.; Jamison, T. F., Synthesis of marine polycyclic polyethers via endo-selective epoxide-opening cascades. *Mar. Drugs* **2010**, *8* (3), 763-809.
17. Vilotijevic, I.; Jamison, T. F., Epoxide-Opening Cascades Promoted by Water. *Science* **2007**, *317* (5842), 1189-1192.
18. Bourdelais, A. J.; Jacocks, H. M.; Wright, J. L. C.; Bigwarfe, P. M.; Baden, D. G., A New Polyether Ladder Compound Produced by the Dinoflagellate *Karenia brevis*. *J. Nat. Prod.* **2005**, *68* (1), 2-6.
19. Hotta, K.; Chen, X.; Paton, R. S.; Minami, A.; Li, H.; Swaminathan, K.; Mathews, I. I.; Watanabe, K.; Oikawa, H.; Houk, K. N.; Kim, C.-Y., Enzymatic catalysis of anti-Baldwin ring closure in polyether biosynthesis. *Nature* **2012**, *483*, 355-359.
20. Lin, Y.-Y.; Risk, M.; Ray, S. M.; Van Engen, D.; Clardy, J.; Golik, J.; James, J. C.; Nakanishi, K., Isolation and structure of brevetoxin B from the "red tide" dinoflagellate *Ptychodiscus brevis* (*Gymnodinium breve*). *J. Am. Chem. Soc.* **1981**, *103* (22), 6773-6775.
21. Lee, M. S.; Qin, G.; Nakanishi, K.; Zagorski, M. G., Biosynthetic studies of brevetoxins, potent neurotoxins produced by the dinoflagellate *Gymnodinium breve*. *J. Am. Chem. Soc.* **1989**, *111* (16), 6234-6241.
22. Heffron, T. P.; Simpson, G. L.; Merino, E.; Jamison, T. F., Ladder Polyether Synthesis via Epoxide-Opening Cascades Directed by a Disappearing Trimethylsilyl Group. *J. Org. Chem.* **2010**, *75* (8), 2681-2701.
23. Morten, C. J.; Byers, J. A.; Jamison, T. F., Evidence That Epoxide-Opening Cascades Promoted by Water Are Stepwise and Become Faster and More Selective After the First Cyclization. *J. Am. Chem. Soc.* **2011**, *133* (6), 1902-1908.
24. Heffron, T. P.; Jamison, T. F., SiMe<sub>3</sub>-Based Homologation–Epoxidation–Cyclization Strategy for Ladder THP Synthesis. *Org. Lett.* **2003**, *5* (13), 2339-2342.
25. Simpson, G. L.; Heffron, T. P.; Merino, E.; Jamison, T. F., Ladder Polyether Synthesis via Epoxide-Opening Cascades Using a Disappearing Directing Group. *J. Am. Chem. Soc.* **2006**, *128* (4), 1056-1057.
26. Fujiwara, K.; Tokiwano, T.; Murai, A., La(otf)<sub>3</sub>-catalyzed 6-endo epoxide opening of 4, 5-epoxy-4-methoxymethyl-1-hexanols. *Tetrahedron Lett.* **1995**, *36* (44), 8063-8066.

27. Czabaniuk, L. C.; Jamison, T. F., Hydroxyl-Substituted Ladder Polyethers via Selective Tandem Epoxidation/Cyclization Sequence. *Org. Lett.* **2015**, *17* (4), 774-777.
28. McDonald, F. E.; Wang, X.; Do, B.; Hardcastle, K. I., Synthesis of Oxepanes and trans-Fused Bisoxepanes via Biomimetic, endo-Regioselective Tandem Oxacyclizations of Polyepoxides. *Org. Lett.* **2000**, *2* (18), 2917-2919.
29. Wan, S.; Gunaydin, H.; Houk, K. N.; Floreancig, P. E., An Experimental and Computational Approach to Defining Structure/Reactivity Relationships for Intramolecular Addition Reactions to Bicyclic Epoxonium Ions. *J. Am. Chem. Soc.* **2007**, *129* (25), 7915-7923.
30. Zhu, Z.-B.; Wei, Y.; Shi, M., Recent developments of cyclopropene chemistry. *Chem. Soc. Rev.* **2011**, *40* (11), 5534-5563.
31. Singh, R.; Czekelius, C.; Schrock, R. R., Living Ring-Opening Metathesis Polymerization of Cyclopropenes. *Macromolecules* **2006**, *39* (4), 1316-1317.
32. Elling, B. R.; Su, J. K.; Xia, Y., Ring-opening metathesis polymerization of 1,2-disubstituted cyclopropenes. *Chem. Commun.* **2016**, *52* (58), 9097-9100.
33. Nagarkar, A. A.; Kilbinger, A. F. M., End functional ROMP polymers via degradation of a ruthenium Fischer type carbene. *Chem. Sci.* **2014**, *5* (12), 4687-4692.
34. Tu, Y.; Wang, Z.-X.; Shi, Y., An Efficient Asymmetric Epoxidation Method for trans-Olefins Mediated by a Fructose-Derived Ketone. *J. Am. Chem. Soc.* **1996**, *118* (40), 9806-9807.
35. Heravi, M. M.; Lashaki, T. B.; Poorahmad, N., Applications of Sharpless asymmetric epoxidation in total synthesis. *Tetrahedron: Asymmetry* **2015**, *26* (8), 405-495.